UNIVERSITY OF SOUTHAMPTON

FACULTY OF NATURAL AND ENVIRONMENTAL SCIENCES

Chemistry

Design of Hybrid Nanomaterials as Sustainable Heterogeneous Oxidation Catalysts

by

Christopher Stephen Hinde

Thesis for the degree of Doctor of Philosophy

April 2015

UNIVERSITY OF SOUTHAMPTON

ABSTRACT

FACULTY OF NATURAL AND ENVIRONMENTAL SCIENCES

Chemistry

Thesis for the degree of Doctor of Philosophy

DESIGN OF HYBRID NANOMATERIALS AS SUSTAINABLE HETEROGENEOUS OXIDATION CATALYSTS

Christopher Stephen Hinde

Anion exchange properties of a microporous copper chlorophosphate have been exploited to demonstrate, for the first time, a method for generating monodisperse and uncapped noble metal nanoparticles by thermal extrusion. Confirmed initially by structural characterisation with PXRD, SEM and TEM studies, the microporous framework supported Au, Pt and Pd nanoparticles were shown to activate molecular oxygen for the environmentally benign oxidation of benzyl alcohol to benzaldehyde. Probing of the kinetic properties demonstrated contrasting catalytic features for each of the NP catalysts, with the Pt NP catalyst showing heightened activity and a propensity for selectivity toward benzaldehyde.

In-depth physico-chemical analysis of the metal NP catalysts revealed a dependence of the activation/extrusion parameters to the activity and catalytic properties of the resulting materials. Utilising X-ray techniques such as XAS (EXAFS and XANES) and XPS, coupled with the investigation of catalytic properties toward aerobic oxidation of vanillyl alcohol to vanillin, it was established that reduction in the presence of H_2 at moderate temperatures is a much more efficient process to calcination in air at much higher temperatures, to afford the complete extrusion of complex anions for active NP formation. Structure-property correlations were harnessed to rationalise the superior catalytic properties of the Pt catalyst compared with the Au and Pd

counterparts, exposing the extent of extrusion and revealing a contrast in the nature of complex anion-support interactions.

To further exemplify the scope of hybrid metal nanoparticle/microporous nanomaterials in the pursuit of new, efficient, green and industrially applicable catalysts, the highly robust UiO-66 type MOFs have been utilised as NP hosts for tandem catalytic applications. A facile method of NP deposition on UiO-66 has been demonstrated using established colloidal synthesis methods with PVP, to generate active Au NP materials for the selective oxidation of cinnamyl alcohol to cinnamaldehyde using simple peroxides. By introducing amine functionality to the MOF with 2-aminoterephthalic acid to form the isoreticular NH_2-UiO-66 as a host for Au NPs, an effective catalyst for the two step process involving the aforementioned oxidation with subsequent Knoevenagel condensation reaction (coupling the aldehyde with an activated methylene compound at the $-NH_2$ sites on the MOF) has been achieved in good yield.

Table of Contents

List of Tables

List of Schemes

List of Figures

DECLARATION OF AUTHORSHIP

I, Christopher Stephen Hinde

declare that this thesis and the work presented in it are my own and has been generated by me as the result of my own original research.

Design of Hybrid Nanomaterials as Sustainable Heterogeneous Oxidation Catalysts

I confirm that:

1. This work was done wholly or mainly while in candidature for a research degree at this University;
2. Where any part of this thesis has previously been submitted for a degree or any other qualification at this University or any other institution, this has been clearly stated;
3. Where I have consulted the published work of others, this is always clearly attributed;
4. Where I have quoted from the work of others, the source is always given. With the exception of such quotations, this thesis is entirely my own work;
5. I have acknowledged all main sources of help;
6. Where the thesis is based on work done by myself jointly with others, I have made clear exactly what was done by others and what I have contributed myself;
7. Parts of this work have been published as:

    - C. S. Hinde, S. Van Aswegen, G. Collins, J. D. Holmes, T. S. A. Hor and R. Raja, *Dalton Trans.*, **2013**, 42, 12600.
    - C. S. Hinde, D. Ansovini, P. P. Wells, G. Collins, S. V. Aswegen, J. D. Holmes, T. S. A. Hor and R. Raja, *ACS Catal.*, **2015**, 5, 3807.

Signed: .....

Date: .....

Acknowledgements

I have been lucky enough in the course of this PhD to carry out my research across two countries, the UK and Singapore, and gain a wider knowledge and awareness of a global research landscape in chemistry, materials science, chemical engineering and related fields. My eyes have truly been opened from a cultural and professional point of view through my one and a half years based in Singapore, and for that I will always be grateful.

In that vein, I would like to express my heartfelt gratitude to Dr Robert Raja, my PhD supervisor at the University of Southampton for inspiring me in my undergraduate studies and encouraging me to pursue doctoral studies in the area of materials chemistry and catalysis. I would also like to thank him for his encouragements to apply for the A*STAR scholarship and be a representative for him, the department and the university at IMRE in Singapore.

For the opportunities he provided during my time at IMRE, I would also like to thank my co-supervisor, Prof. Andy Hor. It was a pleasure to be able to work with him and the members of his research group. To Dr Wenhua Zhang, I'd also like to express my gratitude for his mentorship during my initial months at IMRE before he moved back to China for bigger and better things.

At the outset of my PhD, it would have been difficult to learn the ropes without many existing characters within the Raja group; I learnt a lot from all and appreciated the friendships that came with that. I particularly appreciated the encouragements from David Xuereb, in addition to the mutual love of wine and champagne that he and I shared. It was also great to make a good friend and colleague in Matthew Potter who challenged me in many ways to be a better scientist and researcher. Special thanks should also go to his wife, Emma, who helped to host many social events, becoming one of the group and also a good friend.

To those in the group with whom I've worked closely and had the honour of writing papers with; Davide Ansovini, Sivan Van Aswegen and Arran Gill, thanks for your time and efforts in some often frustrating periods. Thanks also go to external collaborators who have faithfully delivered to deadlines to add significant value to my research: Dr Gillian Collins and Prof. Justin Holmes at University College Cork, Ireland and Dr Peter Wells at the UK Catalysis Hub.

Acknowledgements

For my time in Singapore, I would like to thank Benny Chew for not only being my work colleague, but for being my lunch *khaki* and Singaporean brother; who kept me motivated and sustained even through the tough times, whether in the laboratory or dealing with politics of a new place. I'd also like to thank Andre Dürrbeck for being a fellow European at IMRE; to reminisce of home and also be an avenue to vent frustrations.

Outside of work, I would also love to thank my friends at YAM from Westside Anglican Church in Singapore who became my adopted family and made my whole experience so much more exciting. For teaching me some Singlish, some useful Chinese phrases, showing me the local food and of course for your spiritual support, 谢谢你! I have no doubt that you have all had a positive influence on my research: The Liow family (Zhong Fa, Ivy, Ethan and Eunice), the Low family (Reggie, Cindy, Zoanne and Zoelle), Mee Cheng, Becky ("*Trouble*"), Candice, Diane, Joanie, Janice, Casie, Jun Hoong, Adrian and Michael. As much as my research gave me something for my brain to pursue in Singapore, extra special recognition goes to Mee Cheng, who gave my heart something to pursue, adding an extra dimension to my time abroad and life in general.

In the UK, I'd also like to recognise my close friends and the spiritual support they gave from my undergraduate days and through to my PhD; James Pritchard, Adam Collett, Patrick Noonan, Luke O'Dowd, Steve Price and Dave Callaghan.

It would be difficult to make acknowledgements without sending a special thanks to my Mum, Vivienne, who I give most of the credit to for helping me to achieve my highest potential and which has led to the eventual submission of this thesis. Without her parental guidance and support, I wouldn't have been the driven and motivated person that I am today.

Abbreviations

BE	Binding Energy
BET	Brunauer-Emmett-Teller (Gas Adsorption)
BP	Boiling Point
CN	Coordination Number
COP	Covalent Organic Polymer
CuClP	Copper Chlorophosphate
DMF	N,N'-Dimethylformamide
EELS	Electron Energy Loss Spectroscopy
EDX	Energy Dispersive X-ray Spectroscopy
EXAFS	Extended X-Ray Absorption Fine Structure
FESEM	Field Emission Gun Scanning Electron Microscope
FID	Flame Ionisation Detector
FT-IR	Fourier Transform – Infrared Spectroscopy
GC	Gas Chromatography/Chromatograph
GC-MS	Gas Chromatography-Mass Spectrometry
HAADF	High Angle Annular Dark Field Imaging
HAP	Hydroxyapatite
HKUST	Hong Kong University of Science and Technology
HT	Hydrotalcite
ICP-OES	Inductively-Coupled Plasma – Optical Emission Spectroscopy
KE	Kinetic Energy
LSPR	Localised Surface Plasmon Resonance
MCM	Mobil Crystalline Material
MIL	Material Institut Lavoisier
MOF	Metal-Organic Framework

MS	Mass Spectrometry
NP	Nanoparticle
PCP	Porous Coordination Polymer
PSM	Post-Synthetic Modification
PTFE	Polytetrafluoroethene
PXRD	Powder X-Ray Diffraction
RBF	Round Bottom Flask
RT	Room Temperature
SEM	Scanning Electron Microscopy
SPR	Surface Plasmon Resonance
STEM	Scanning Transmission Electron Microscopy
TBHP	*tert*-Butyl Hydroperoxide
TCD	Thermal Conductivity Detector
TEM	Transmission Electron Microscopy
TGA	Thermogravimetric Analysis
TON	Turnover Number
TOF	Turnover Frequency
TS-1	Titanosilicate-1
UiO	Universitetet i Oslo
XANES	X-Ray Absorption Near-Edge Spectroscopy
XAS	X-Ray Absorption Spectroscopy
XPS	X-Ray Photoelectron Spectroscopy
XRD	X-Ray Diffraction
ZIF	Zeolitic Imidazolate Framework

Chapter 1: Introduction

1.1 Catalysis

It is hard to imagine a modern world that isn't dependent on the chemical industry and catalysis in some form. Catalysis is an essential tool used in a variety of applications including the production of plastics, the manufacture of fuels, the removal of chemical pollutants and even within processes in our own bodies.[1] Shriver and Atkins[2] define a catalyst as "*a substance that increases the rate of a reaction but is not itself consumed*" and estimate that processes dependent on catalysts contribute to one-sixth of the value of all manufactured goods in industrialised countries, with 90 % requiring a catalyst at some point in their production. Furthermore, Ertl *et al*. describe the catalyst as being "the heart of a chemical process".[3] As such, design and utilisation of catalysts is therefore an essential branch of research that is necessary for modern development of industrial chemistry.

The concept of a catalyst was first explored in the early 19th century when Sir Humphry Davy and Michael Faraday examined the role of platinum in preventing explosions in coal mines from the candles used to light the tunnels.[4] Despite a very limited understanding of chemistry, atoms and molecules, they were able to establish that the platinum was acting to catalyse termination reactions to prevent the explosions. These discoveries and theories laid the foundations for the field of catalysis. The terms *catalyst* and *catalysis* as we know them were first coined by Berzelius in 1835 in review of the above works and other similar contributions.[5]

1.1.1 Mechanisms and Fundamental Theory

In a typical reaction profile, both thermodynamic and kinetic properties are described to demonstrate whether a chemical reaction can occur and at what rate it will proceed. The thermodynamics of a system can be ascertained from the energy levels of both the reactants and the products. If the energy of the products is less than the energy of the reactants, then the reaction is said to be spontaneous and will have a negative value for the Gibbs free energy (ΔG) at a set temperature and pressure (Figure 1.1).[6-7] The concept of Gibbs free energy

was first described by J. W. Gibbs in the late 19th century[6] and can be summarised in (Equation 1.1).

$$\Delta G = \Delta H - T\Delta S \qquad \textbf{Equation 1.1}$$

Gibbs postulated that the change in energies were dependent not just on enthalpy, but changes in entropy too. In most cases, exothermic reactions will have negative Gibbs free energies due to the negative change in enthalpy, however a reaction may also be spontaneous if there is an increase in entropy.

The kinetics of a reaction are defined by the energy barrier that a reaction must pass through to convert reactants to products and dictated by the lowest energy transition state. This is more commonly known as the activation energy (E_a). The level of the activation energy affects the rate at which a reaction will occur. If the activation energy is high, the reaction will occur at a much slower rate than for a relatively lower activation energy. The role of a catalyst is to reduce this energy barrier and thus increase the rate of a reaction as earlier described; we can therefore establish that catalysis is a purely kinetic phenomenon.

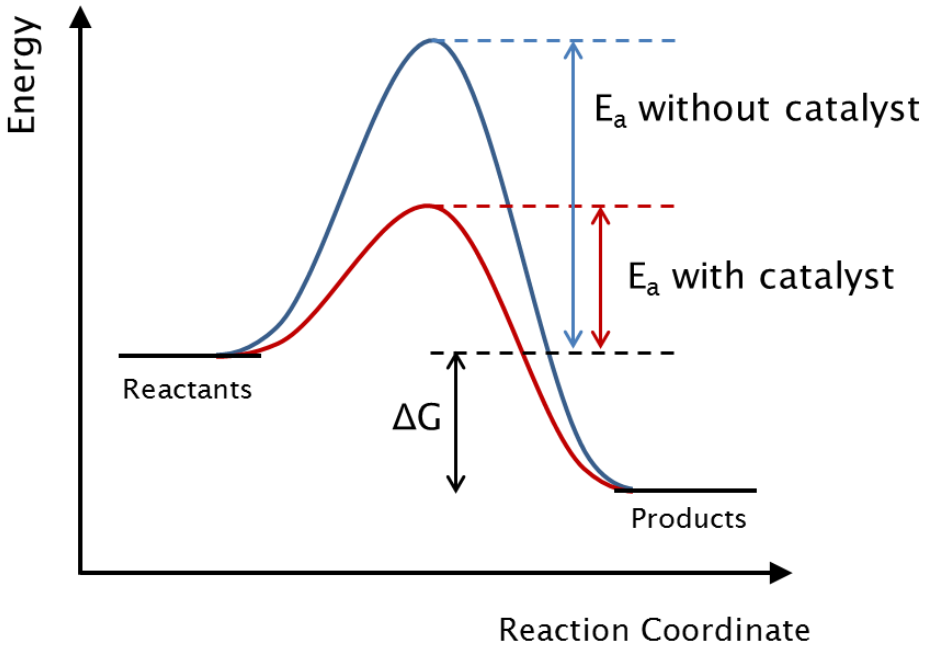

Figure 1.1 Energy diagram of reactions with and without a catalyst

Catalysts can reduce the activation energy in a variety of ways,[4] some of which include:

- Helping to initiate reactions
- Stabilising intermediates of a reaction
- Holding reactants in close proximity to one another
- Holding reactants in the right configuration
- Donating and accepting electrons
- Stretching and weakening bonds

Mechanisms of catalytic action are usually represented in a 'catalytic cycle' that illustrates the concept that the catalyst material is returned to the initial active state after one reaction has taken place. This then leaves the catalyst to continue around the cycle until all of the original substrate has been converted into the product.

A general mechanism involves the association or adsorption of the substrate(s) to the catalyst, followed by the chemical transformation and finishing with the disassociation or desorption of the product(s) (Figure 1.2). In specific cases, this mechanism may become more complex depending on the nature of the catalyst, the number of substrates and the degree of transformations that need to occur in the reaction.

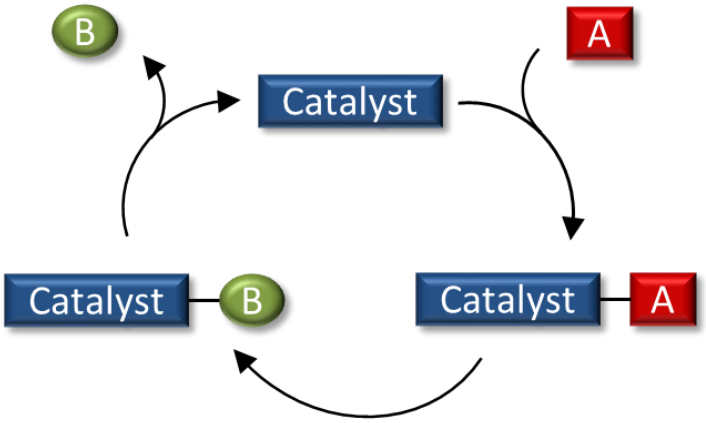

Figure 1.2 A general catalytic cycle

Mass transfer is also a consideration in a catalytic mechanism and describes the movement of substrates and products to and from the catalyst respectively.[4] In homogeneous systems with good mixing, mass transfer is usually efficient and has little effect on the rates of reactions, although mobility through the reaction medium may be impeded due to low

concentrations, viscosity or poor solvent choice. Mass transfer becomes more of an obstacle in heterogeneous systems where, in most cases, the catalyst is quite bulky and mixing is not quite as simple: diffusion of substrates to the catalyst surface becomes a limiting factor. To minimise diffusion effects, it is possible to control catalyst particle sizes, surface area, methods of mixing and design of reactor systems.

Monitoring the progressions of a reaction, or the rate of a reaction, can give a plethora of information about the mechanisms and kinetic processes by which a reaction occurs. Experimentally, it is well known that the concentrations of the reaction components as well as the temperature can have a large effect on the rate of a reaction. In simple reactions, the rate of reaction is proportional to the concentration of the reactants raised to a power, also known as the order.

$$rate = k\,[A][B] \qquad \textbf{Equation 1.2}$$

In the example Equation 1.2, the rate of the reaction is first-order with respect to the concentration of A and B, and second-order overall. The rate constant is denoted *k* and is a function of the reaction conditions. The temperature dependence of a reaction can be measured by the Arrhenius equation (Equation 1.3) which quantifies the relationship between the rate constant and the temperature, where A is the pre-exponential factor, E_a is the activation energy and R is the ideal gas constant.

$$k = A\,e^{-(\frac{E_a}{RT})} \qquad \textbf{Equation 1.3}$$

By rearranging the Arrhenius equation (Equation 1.4), it is possible to see that a plot of ln k against 1/T will produce a straight line graph that makes it possible to calculate the activation energy of the reaction under a set of experimental conditions, as well as the pre-exponential factor. This is an effective way of being able to compare whether changes in experimental conditions are beneficial or detrimental to the kinetics of the reaction, or more

specifically the effectiveness of different types of catalysts on the same reaction.

$$\ln k = \ln A - \frac{E_a}{RT} \qquad \textbf{Equation 1.4}$$

1.1.1.1 Heterogeneous and Homogeneous Catalysis

As defined by Sheldon,[8] catalysts can be broadly divided into four sub-categories; homogenous, heterogeneous, organocatalysts and biocatalysts, each of which come with their own benefits and limitations. It can be argued that organocatalysts and biocatalysts fall under the brackets of hetero- or homogeneous catalysts, but the separation is mostly in view of their eventual application, with the former two being more traditional branches of industrial chemical catalysis.

Table 1.1 General advantages and disadvantages of homogeneous and heterogeneous catalysts

Property	Homogeneous	Heterogeneous
Operating Phase	Liquid	Solid, liquid or gas
Operating Temperature	Low; limited by solvent operating conditions	Limited only by thermal stability of catalyst
Diffusivity	High rates of diffusion	Reduced diffusivity by low mobility of catalyst
Separation	Generally complex and expensive	Usually straightforward and cheaper
Recyclability	Expensive treatment of spent catalyst	Facile although regeneration may be necessary
Active Sites	Well defined with precise control on chemical and electronic environments	Less well defined with more complex methods required for chemical and electronic control
Reaction Mechanisms	Direct methods provide simple tools for deciphering mechanisms	Often require indirect methods and less routine characterisation

These classes are defined by the phase of a catalyst with respect to the reaction medium. Homogeneous catalysis describes reactions where the catalyst is in the same phase as the reaction medium, most commonly in solution with a dissolved catalyst species. Conversely, heterogeneous catalysis describes processes where the catalyst is in a different phase to the reaction medium; the most common example would be the use of solid materials for liquid or gas-phase reactions. Some of the general advantages and disadvantages of heterogeneous and homogeneous catalysts are outlined in Table 1.1. The exploitation of organocatalysis in key reactions for pharmaceutically significant processes is a relatively new area of research where the properties of organic molecules can be exploited for complex transformations including, but not exclusive to, isomerisations and asymmetric reactions. Biocatalysis refers mostly to enzymes or molecular materials employed within biological processes in natural or synthetic systems, with some recent utilisation in the chemical industry such as the biosynthesis of niacin (Vitamin B_3).[9]

In most industrial chemical processes where catalysts are employed, heterogeneous catalysts are generally preferred over homogeneous[10] with an estimated usage ratio of 3:1 respectively. This is for a variety of reasons, the most important of which is the ability to collect and recycle solid catalysts using cheap and easy methods such as filtration.[4] Despite solid catalysts being generally less active than homogeneous catalysts, the economical and practical benefits in large scale projects outweigh this disadvantage. A solid material also provides a platform by which to control and engineer isolated active sites and the surrounding environment with great ease and reproducibility, in contrast with bulk functional surfaces.

1.1.1.2 Active sites

The concept of the *active site* is most commonly associated with enzymes, but as biology's natural catalysts, this concept is not unique to enzymes, but applicable to all catalysts. The active site is the location on the catalyst at which a substrate can bind to undergo a chemical transformation (Figure 1.3). For homogeneous catalytic reactions, this is often the metal-centre of an organometallic compound (Figure 1.3 A), and for organocatalysts, the functional group at which binding occurs. The surrounding chemical

environment is also considered part of the active site as they can have direct effects on the outcome of the reaction. For example, in the synthesis of natural products or fine chemicals, stereocontrol of the products is essential and so the choice of ligands on an organometallic catalyst can be opportunistically selected for their steric influence or ability to introduce asymmetry or chirality to a product.[11]

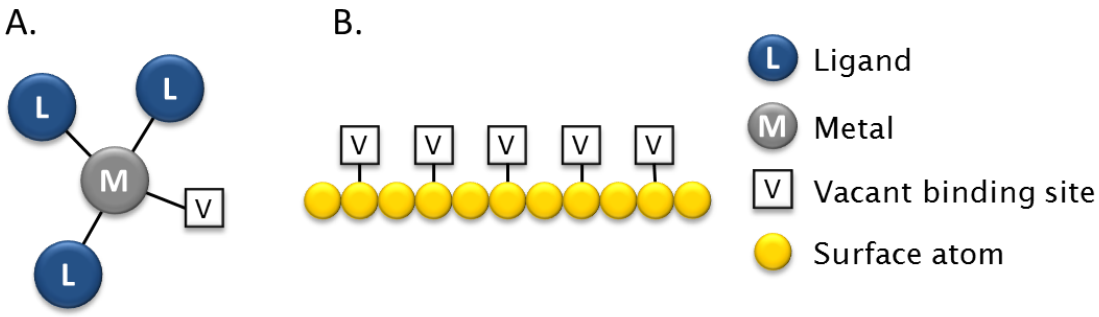

Figure 1.3 Active sites in homogeneous organometallic (A) and surfaces (B) catalysts

Active sites are a little more difficult to determine for surface catalysts (Figure 1.3 B) as the binding sites are often not well defined.[12] Approximations can be made to determine how many accessible sites are available on a surface based on the substrate that is being used. As such, where a high degree of stereo-control is required, homogeneous catalysts tend to be the catalysts of choice. To gain the benefits of heterogeneous catalysts, it is also possible to employ the use of porous materials and/or immobilise the intricate homogeneous catalyst to solid supports.

1.1.1.3 Immobilisation Concepts

Immobilisation concepts have been one effective way in which homogeneous catalysts can be optimised for scale-up processes.[12] By anchoring homogeneous active sites such as organic molecules, organometallic species or metals to a solid support, it can be possible to maintain the functionality of the catalyst. In some cases, a price is often paid with a reduction in activity due to the increased effects of mass transfer and the reliance on diffusion of reactants and products to and from the immobilised catalyst respectively.[4] In some cases, serendipitously or otherwise, synergistic properties can be

established between the active species and support that can enhance the activity of a catalyst.[13-16]

Depending on the species to be immobilised and the ability of the support to facilitate immobilisation (e.g. hydrophobicity, hydrophilicity, functionalization), there are an assortment of ways in which the immobilisation can be achieved. These can include, but are not limited to, covalent bonding through linkers[12, 17-20] and electrostatic interactions.[13, 20-21] If a porous support is used, it is also possible to encapsulate the active species within the support structure.[20, 22]

1.1.1.4 Reactions at Surfaces

As described earlier, typical heterogeneous reactions occur on a solid catalyst in the liquid or gas-phase. As such, it is important to understand the mechanisms by which reactions occur on solid surfaces. With the catalytic cycle in mind, the general mechanism can be broken down into a few steps beginning with adsorption of reactants through favourable surface-adsorbate interactions, surface diffusion to bring the reactants in close proximity, chemical transformations facilitated by the surface properties and finishing with desorption of products[23] (Figure 1.4).

The mechanism can vary slightly depending on whether the active site is, for example, the surface of a metal or an isolated organometallic species. With the latter, surface diffusion becomes less of an issue, but adsorption at the specific site plays a bigger role. Desorption of species from the surface of a catalyst is, of course, essential to regenerate a vacant site for subsequent cycles of the reaction to occur. Strong associations of molecules to surfaces that cannot be desorbed lead to surface poisoning and deactivation of the catalyst. A typical example is the strong affinity of carbon monoxide to surfaces of platinum in fuel cells.[24] In some cases, catalyst materials can be regenerated through thermal treatments, however this is less than ideal as it requires further steps and more resources and energy.

Reactions at surfaces between two reactants proceed via two generally accepted mechanisms or variations thereof.[23] The Langmuir-Hinshelwood mechanism details a reaction that occurs between two surface adsorbed species and the Eley-Rideal mechanism, a reaction that occurs between one adsorbed species and one in the gas-phase (Figure 1.5 and Figure 1.6). Whilst

these mechanisms are described as gas-phase heterogeneous reactions, they can be extrapolated to also apply to liquid-phase systems.

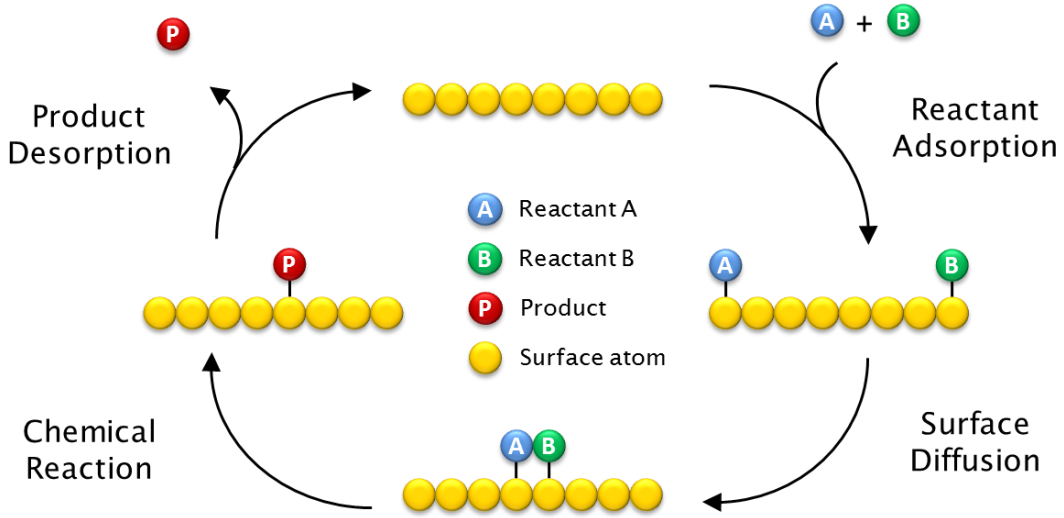

Figure 1.4 General mechanism of surface reactions

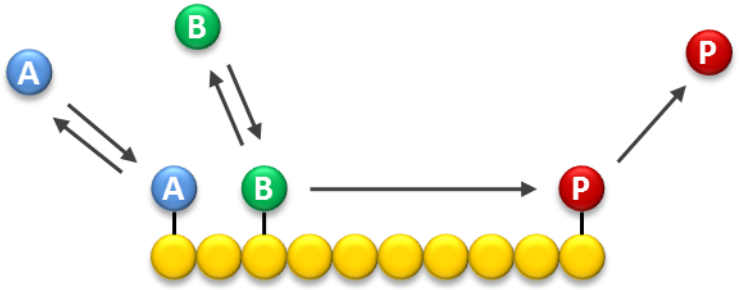

Figure 1.5 Langmuir-Hinshelwood reaction mechanism on a surface (A and B, reactants; P, product)

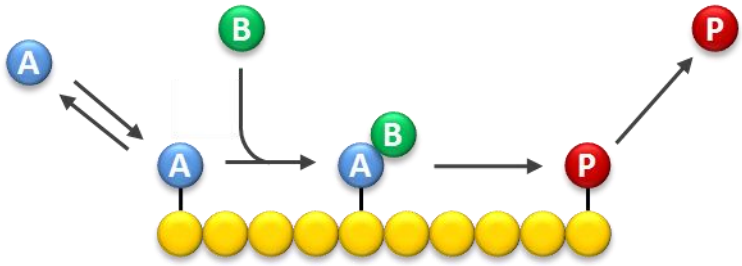

Figure 1.6 Eley-Rideal reaction mechanism on a surface

As our understanding of the molecular structures and functions of catalyst materials increase, so too does the potential for rational design and modification of catalyst properties such as activity and selectivity.[23]

1.1.1.5 Measurement of Activity

Measuring the activity of catalysts, especially heterogeneous catalysts, in a quantifiable way that is widely comparable can be a challenge as the nature of the active species can vary from surfaces to isolated atoms or complexes. Catalytic data are often quoted in the literature as conversion vs time; however these do not take into account the efficiency of the catalyst itself. It has become more common place to quote activity of catalysts using turnover numbers (TONs) or turnover frequencies (TOFs).[25] The former is a measure of mole conversion with respect to the number of active sites present while the latter is this ratio per unit of time (Equation 1.5 and Equation 1.6).

$$Turnover\ Number = \frac{substrate\ conversion\ (mol)}{active\ sites\ (mol)} \qquad \textbf{Equation 1.5}$$

$$Turnover\ Frequency\ = \frac{turnover\ number}{unit\ of\ time} \qquad \textbf{Equation 1.6}$$

Counting active sites for atomically isolated species is relatively simple and equal to the molar quantity of the species present. Quantifying the active sites for surfaces is a little more problematic as each atom may not be equivalent to an active site. As such, approximations need to be made and sometimes the molar quantity is still used, or if possible to calculate, the surface atomic quantities can be used.

Even if some approximations are made (and explicitly stated), calculation of TONs and TOFs provide many advantages.[25] As long as reaction conditions are kept the same, these values should be reproducible by different researchers in different locations within reasonable experimental error. They are a good check to make sure that the material is indeed catalytic by having multiple turnovers per site, and are a good way to compare against catalysts in current use or in recent literature.

Whilst TONs and TOFs are a good measure of activity with respect to conversion of a substrate, they give little information on the effectiveness of a catalyst to produce a desired product. A catalyst can have a significant value for a TON, but produce a large mix of products that would prove to be an inefficient process. Of course, in any situation where one product is required, complete selectivity toward that product would be necessary for an efficient reaction. In this vein, measurements of selectivity and yield are used to evaluate a catalyst's ability to produce a single product.

$$Selectivity\ (\%) = 100\ \times \frac{product\ (mol)}{converted\ substrate\ (mol)} \qquad \textbf{Equation 1.7}$$

$$Yield\ (\%) =\ 100 \times \frac{product\ (mol)}{substrate_{initial}\ (mol)} \qquad \textbf{Equation 1.8}$$

To add a caveat, the yield calculated in Equation 1.8 is only valid when a quantitative mass balance (MB) can be achieved i.e. when (assuming conversion of A to B) the combined moles of detectable components at a time, *t*, after the start of a reaction is equal to that of the starting substrate. Sometimes loss of substrate by routes other than the formation of a product which are undetectable can occur (decomposition, formation of non-volatile compounds etc.). In this case, the real yield is a factor of the mass balance as shown in Equation 1.9.

$$Yield\ (\%) = 100\ \times \frac{product\ (mol)}{converted\ substrate\ (mol)} \times MB \qquad \textbf{Equation 1.9}$$

1.1.2 Catalysis in Industry

As alluded to in *section 1.1*, catalysis has found significance and value in industrial chemistry. In fact, Chiusoli *et al.*[26] go as far as to say that "Generally, the value of catalysis lies not in the catalyst itself but in the products or effects they produce", showing how much importance is placed on the process and

end products that catalysts can have such an effect on. Catalysts add value in a few different ways including reduction of manufacturing costs (e.g. energy and resource requirements), increase in quality and purity of chemicals, production of novel chemicals and reduction of waste products or emissions.[26] For example, catalytic converters are now fitted to almost every vehicle manufactured in the world.[11] The precious metal based catalysts are designed to oxidise carbon monoxide and unburnt hydrocarbons to carbon dioxide and water, and nitrous oxides to molecular nitrogen, reducing emissions by up to 90 %.[26] The catalytic cracking of crude oil was used as early as the 1930's when Houdry used simple silica/alumina catalysts. This, along with further catalytic processes such as isomerisation, reforming, hydrotreating and hydrocracking, have increased the volume of gasoline fuel that can be obtained from a barrel of crude oil by 50 %.[26]

As well as these examples, catalysts are intrinsic to the production of commodity petrochemicals including monomers for the polymer industry (high volume plastics, for example, polystyrene, polyvinyl chloride (PVC) and polyethylene terephthalate (PET)); fine-chemicals such as pharmaceuticals, agrochemicals, flavours and fragrances; and environmental processes for waste clean-up or regeneration and reforming of exhaust gases.[26]

1.1.2.1 Sustainable Chemistry

With the increasing social, political and economic pressure for all areas of business and industries to take greater care over human effects on the environment, sustainable or "green" chemistry looks to tackle the negative impact of the chemical industry[8].

Green chemistry focuses on the design, manufacture, and use of chemicals and chemical processes that have little or no pollution potential, or environmental risk and are both economically and technologically feasible.[11, 27-28] It is widely accepted that green chemistry can be summarised by 12 principles[29] listed in Table 1.2.

Table 1.2 Principles of Green Chemistry

No.	Principle
1.	Waste prevention is better than treatment or clean-up

No.	Principle
2.	Chemical syntheses should maximise the incorporation of all starting materials
3.	Chemical syntheses ideally should use and generate non-hazardous substances
4.	Chemical products should be designed to be nontoxic
5.	Catalysts are superior to reagents
6.	The use of auxiliaries should be minimised
7.	Energy demands in chemical syntheses should be minimised
8.	Raw materials should be increasingly renewable
9.	Derivations should be minimised
10.	Chemical products should break down into innocuous products
11.	Chemical processes require better control
12.	Substances should have minimum potential for accidents

It is interesting to note that principle 5 identifies the use of catalysts as intrinsic towards green/sustainable chemistry and should be preferred over stoichiometric reagents. It is also noteworthy that catalysts can be employed in many ways to achieve the goals of most of the other principles listed. For example, a catalyst can be used to reduce the waste products in a reaction as identified for principle 1. It is therefore not unsurprising that catalysts have been described as "the key to sustainable chemistry".[27]

Some catalysts are already employed with these themes in mind (recall the use of catalytic converters in the previous section), however with so many different processes, a lot more can be done. Another example includes the use of catalysts to convert sustainable feed-stocks such as biomass to biofuels which also exemplifies a process that converts waste into useful and valuable materials. It is important for catalysts to not only increase productivity of a target reaction, but to attempt to do so in a more sustainable way. As a result, sustainability will be a key aim for this project.

1.1.2.2 Oxidation Catalysis

Oxidation chemistry is vitally important in the chemicals industry, owing to the fact that production of chemicals is largely based on hydrocarbon feed-stocks with products often containing large quantities of oxygen.[11] Traditionally, oxidations have been performed in industry using stoichiometric inorganic oxidising agents such as MnO_2 and CrO_3 or harsh acids like H_2SO_4 and HNO_3.[11, 30-32] The employment of these reagents leads to hazardous and toxic conditions which are environmentally polluting and corrosive, requiring specialist equipment. Atmospheric oxygen is by far the cheapest and most abundant oxidising agent available,[33] notwithstanding its environmentally benign nature;[34] however oxidations with O_2 are generally far less selective than with other reagents. On the other hand, because O_2 is a gaseous reagent, it requires some investment that becomes financially viable only when production of a target chemical exceeds 10^4 to 10^5 tons per annum which can be a deterrent.[30, 35] If employment of a catalyst can overcome some of these costs by activating O_2 under milder conditions, this route becomes significantly more attractive. With these factors in mind, it is not unsurprising that selective oxidation reactions with sustainable systems are often a significant challenge for the fine chemical industry.

There are existing industrial processes that are able to utilise molecular oxygen, but these are often done in the gas phase and therefore require high temperatures and energy consumption. Examples include the oxidation of methanol to formaldehyde which is performed at 600-720 °C using the BASF process and 350-450 °C using the Formox process (Perstorp).[30] Oxygen is also used in the industrial oxidation of *o*-xylene to phthalic anhydride with a vanadium oxide catalyst[36] as in Scheme 1.1.[35] There is enormous scope for the development of catalysts and processes that can utilise benign O_2 in mild reaction conditions.

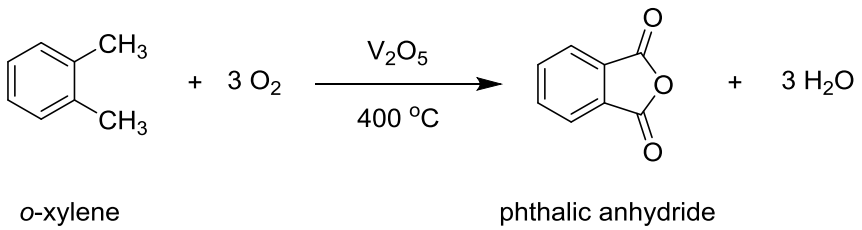

Scheme 1.1 Formation of phthalic anhydride by aerobic oxidation of *o*-xylene of a vanadium oxide catalyst

One of the most well-known commercial heterogeneous catalysts associated with oxidation chemistry is TS-1, a catalyst used first by Enichem in the early 1990s.[11] TS-1 is a microporous titanosilicate and is useful in oxidation reactions particularly involving hydrogen peroxide as an oxidant; the synthesis of hydroquinone being one important example (Scheme 1.2).[11]

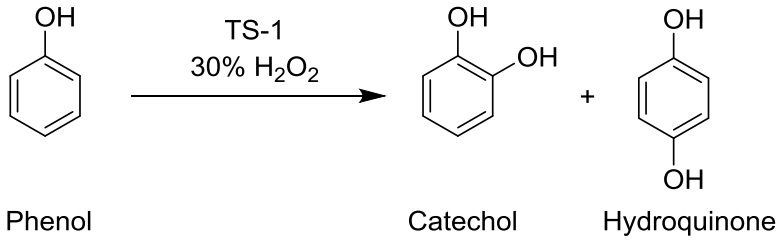

Scheme 1.2 Oxidation of phenol by hydrogen peroxide of TS-1 to form catechol and hydroquinone

Aldehydes are important chemicals in the flavours and fragrances sector and are produced in large quantities each year through oxidation reactions (specifically dehydrogenative oxidation of alcohols).[37-39] They are also inherently reactive due to the polar nature of the carbonyl group that allows for facile nucleophilic addition, oxidation or reduction of the molecule, and particularly acidic hydrogens on the α-carbon leading to condensation reactions.[37] As such, the energy involved in the oxidation of aliphatic or alcoholic substrates often leads to the over-oxidation of the aldehyde to acids or esters and hence low yields for the aldehyde products.[32] It is imperative, therefore, to design new catalyst materials that can provide a kinetic pathway to obtaining aldehyde products in good yield with benign reagents and mild conditions.

Oxidation reactions can occur via homolytic or heterolytic mechanisms although it is generally accepted that most heterogeneous oxidation catalysts using metals or metal-oxide surfaces occur via a heterolytic pathway.[30] It is

more common for homogeneous catalysts or immobilised complexes to proceed via a homolytic pathway.

1.2 Nanoparticles as Catalysts

Some heterogeneous catalysts such as metal-oxides rely on surface reactions to function. As such, the available surface area is a key property of a solid catalyst where in theory, the larger the surface area, the more potential sites for adsorption and reaction. Two major strategies exist in the engineering of solid catalysts to enhance the surface areas; firstly, it is possible to create a porous material so that substrates can gain access to an internal surface area. Secondly, one can reduce the particle size of the catalyst so that the surface area to bulk ratio is increased. If these strategies are performed on the nanoscale, then high surface area, functional nanomaterials can be created.

Nanoparticles are a subclass of nanomaterials defined by their dimensions in the low nanometre range (1-100 nm).[40] These are often crystalline materials that can be single or multiphasic and are mostly metallic or metal oxide materials though not exclusively. Nanoparticles have been identified as promising catalysts, where the presence of metals, in full or part, act as active sites for a variety of chemical transformations. Noble metal nanoparticles have been of particular interest due to their unique physical properties derived from quantum effects associated with the size of the particles which will be described in section 1.2.1. Although not limited to these applications, gold nanoparticles have been particularly successful in oxidation reactions and activation of simple oxidants;[41-47] platinum nanoparticles have also shown promise in oxidation reactions,[48-51] hydrogenation reactions,[51-54] and photocatalytic applications,[55-56] whereas palladium has been applied broadly in oxidations,[57-60] hydrogenation reactions[61] and other synthetic organic processes (e.g. Heck and Suzuki C-C couplings).[62-63] As well as these noble metal nanoparticle catalysts, other examples of metal used in nanoparticle catalysis include silver,[64-65] cobalt,[66-68] copper,[69-70] iron[71-73] and others.[40] Other interesting properties of nanoparticles have allowed them to be utilised in the medical field as drug delivery systems and contrast agents for magnetic resonance imaging (MRI),[74] electrochemical sensors[75], biosensors[76] and antimicrobial agents.[64]

Photocatalysis is a topical area of research with efforts to utilise sustainable and renewable energy sources such as solar energy.[77-78] One of the major drawbacks in some semi-conductor photocatalysts is that the rate of recombination of generated electron-hole pairs is often too high to attain desirable quantum efficiencies.[79-81] Using nanoparticles of semi-conductor materials, or highly nanoporous materials, can increase the effective surface area and thus increase the chances that excited electrons or holes will react rather than recombine.[80, 82-83] Iron oxide nanoparticles, magnetite (Fe_3O_4) being the most popular, have also recently been used to develop materials and catalysts with magnetic properties that can make recovery of catalysts even more facile with the use of a magnetic field.[84-86] These are just a few examples of how nanoparticles are playing a role in in a diverse range of applications and catalysis.

It is also possible to prepare ultra-small metal nanoparticles termed *clusters* with sizes less than 1 nm and often only containing up to 20 atoms (although this is not yet well defined in the literature).[87-95] They are often prepared using organometallic precursors with small ligands such as phenyl groups or coordinated carbon monoxide, then activated by calcination to remove the organic components and leave the bare cluster as an active species. They can be easily prepared as multimetallic entities and used for isomerisations, metathesis reactions, hydrogenations, dehydrogenations and many others.[96] As the electronic properties of clusters more closely resemble that of single unit complexes rather than a typical nanoparticle, their mechanisms of action can be quite different and more similar to organometallic compounds. Clusters can also be employed as precursors to larger nanoparticles, with reduction of metal salts often forming clusters as intermediate states.

1.2.1 Metal Nanoparticles and the Quantum Size Effect

With catalysis in mind, metal nanoparticles have really found a niche owing to their high catalytic activities that stem from the change in surface properties with respect to their bulk metals. These changes in physical and chemical properties are known as quantum size effects, and can be rationalised by the conception that nanoparticles are an intermediate state between bulk metals and atomic metals.[21, 97-98] As such, the energy levels of the material are split from their continuum conduction and valence bands, although they maintain a

certain level a degeneracy, caused by the energy overlap from the presence of a low quantity of adjacent atoms.[99] A schematic example of energy level splitting for gold nanoparticles can be seen in Figure 1.7.

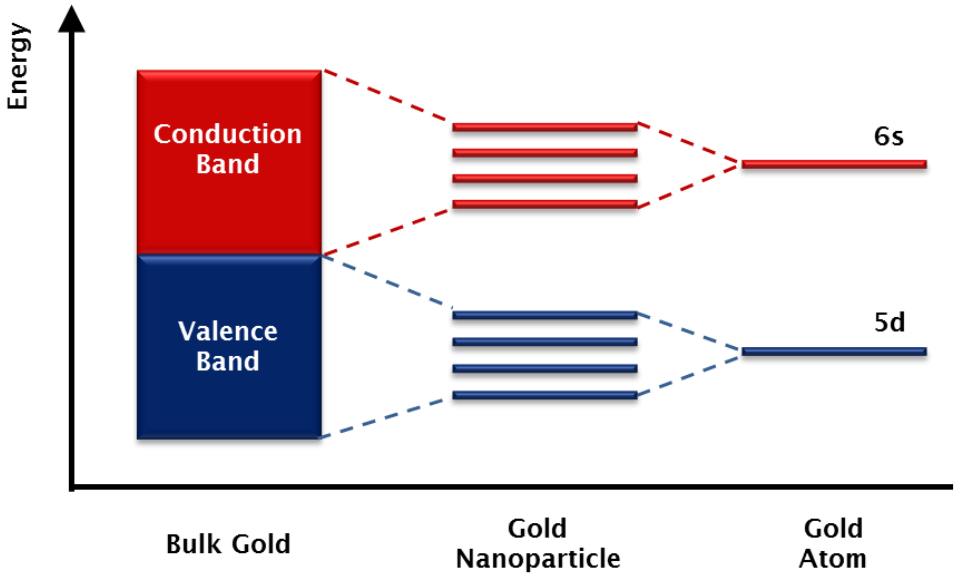

Figure 1.7 Energy level diagram with splitting of bulk, nanoparticulate and atomic gold species

As the size of the particles drop, the surface/volume ratio increases significantly below 10 nm, with more than 50 % of constituent atoms being on the surface of particles less than 3 nm.[100] With the reduction in particle size, individual surface atoms in a particle experience a net inward force caused by attraction of the central atoms but which is not compensated by atoms above them; this leads to a decrease in the interatomic distances of the atoms in a nanoparticle.[21] The lack of neighbouring atoms on the surfaces allow for a greater degree of freedom and vibration in their locations that can be detected by a lowering of the melting temperature.[21] It is hypothesised that the atoms with low coordination numbers, that is those at surfaces, corners and edges, with higher degrees of freedom are the key to increased chemical reactivity for these reasons.[97, 99]

1.2.2 Localised Surface Plasmon Resonance (LSPR)

Surface plasmon resonance (SPR) is a phenomenon that occurs on metallic surfaces when incident light of defined frequencies causes oscillations in the free conduction electrons. The precise depth of penetration of these

interactions depends on the wavelength of the incident light and the physical properties of the metal, but is limited to an ultrathin sheet in the nanometre range close to the surface.[101] As specific frequencies excite the resonant oscillations, they are absorbed and the components of the resulting reflected light are therefore changed. If the absorbed frequencies happen to be in the visible region, then colour changes are perceived. The colours of bulk gold and copper, for example, are due to SPR effects.

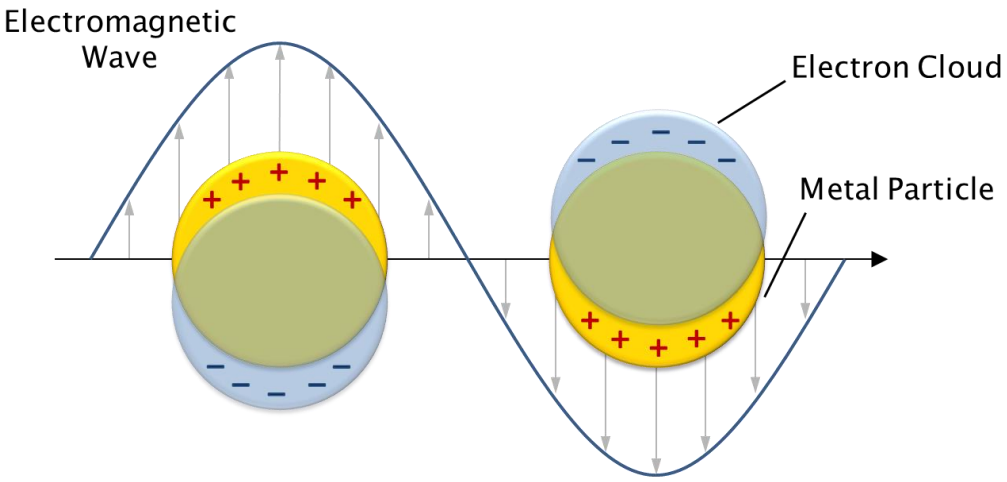

Figure 1.8 Schematic representation of localised surface plasmon resonance (LSPR) in a nanoparticle.

Localised surface plasmon resonance (LSPR) is an extension of this phenomenon to metal nanoparticles. Where the dimensions of the nanoparticles are smaller than the wavelength of light and penetration depth of the electromagnetic waves, certain frequencies of light are able to excite conduction electrons across the whole particle, causing oscillations of the complete electron cloud and development of alternating charges on opposite surfaces (Figure 1.8).[101-103] Dampening effects are caused by the oscillating polarisation that produces an opposing electric field to the excitation field and is observed through light scattering and generation of heat.[101] All these factors contribute towards characteristic LSPR excitation frequencies that are different to normal SPR excitation frequencies of bulk metals. Although this phenomenon occurs in metals, the visual effects are only significant in gold and silver nanoparticles where the LSPR excitation frequencies are in the visible or near-infrared regions.[64-65, 101]

LSPR is sensitive to anything that can affect the polarisation potential of a nanoparticle. These can include changes to the composition, size and shape of the molecule, as well as the surrounding environment and any adsorbed species.

Whilst LSPR is not intrinsic to the catalytic activity of a nanoparticle, it is an optical phenomenon that is related to the relativistic electronic properties that do contribute to chemical reactivity. As such LSPR can be a good tool for characterising synthesised nanoparticle catalysts and changes in electronic properties when extra species are adsorbed or bound to the surface of the nanoparticle. This has also led to nanoparticles being utilised in many sensing applications.[64]

1.2.3 Control of Size and Shape

As previously described, the unique properties of nanoparticles – optical, physical and chemical – are largely derived from the size and shape, and related quantum size effects. Therefore, it is imperative when designing nanoparticle materials for catalytic applications, that a high degree of control over the size and shape of the particles is attained. Herein lies one of the biggest challenges for the industrial materials chemist. If the size distribution of nanoparticles in a catalyst batch is broad, it is likely that a proportion of catalyst will be rendered inactive for the intended application. If the catalyst batch contains a homogeneous distribution of particular size and shape, this optimises the desired physical and chemical properties of the nanoparticles that are necessary for maximum efficiency in a designated process.

Nanoparticles are relatively unstable forms of metals due to their high surface energies, tending toward aggregation into larger bulk materials over time. As a result, the nanoparticle needs to be stabilised in some way. There are two main strategies for nanoparticle stabilisation; firstly it is possible to create colloidal dispersions of gold in the liquid phase,[100] or secondly, nanoparticles can be immobilised on solid surfaces to form a heterogeneous material.[100] The latter will be discussed further in *Section 1.2.4*.

Nanoparticle colloids can be formed with a variety of different stabilising agents including a range of surfactants, coordinating small organic molecules such as citrates or with polymers such as polyvinyl alcohol (PVA) or

polyvinylpyrrolidone (PVP)[54] as in Figure 1.9.[104] The small organic molecule stabilising agents act like surfactants to cap the surfaces of the nanoparticles, preventing aggregation and limiting the growth of nucleating particles. The polymer stabilising agents effectively 'wrap' around the particle to prevent the aggregation and particle growth as before. It is thought that the heteroatoms on the pendant groups of the polymers act to coordinate the polymer to the surface of the nanoparticle through dipolar interactions.[105-106] In both cases, the sizes of the nanoparticles can be tuned by changing the concentration of stabilising agent relative to the metal.

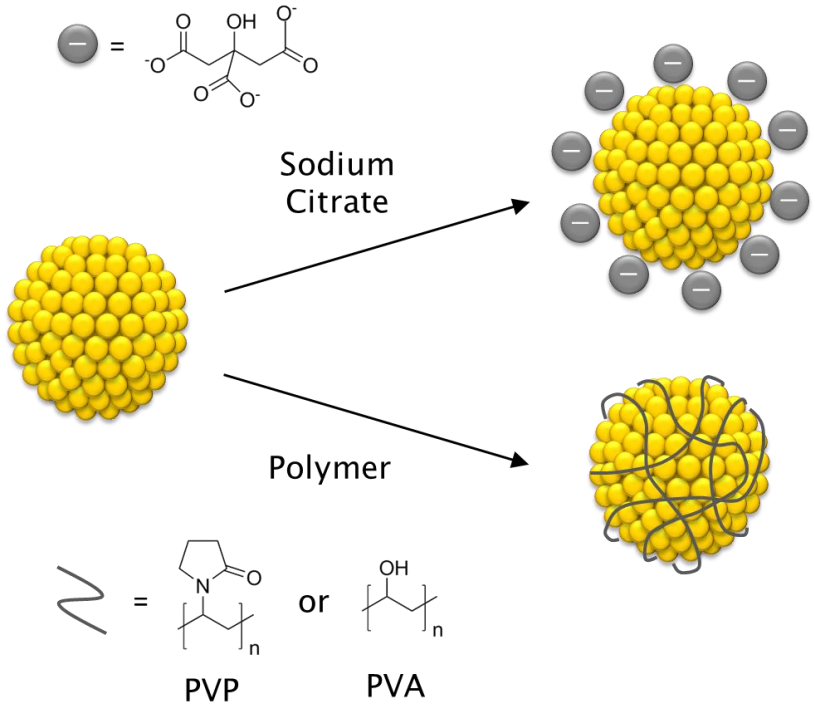

Figure 1.9 Stabilisation of metal nanoparticles through capping agents

In addition to controlling the size, it is possible to control more of the synthesis parameters to gain more of a handle on the shape of nanoparticle formation. As an example, the use of CTAB (cetyltrimethylammonium bromide) as a surfactant along with ascorbic acid and gold seed-clusters allows for the formation of nanorods.[107] This effect can be rationalised by the fact that some adsorbates can preferentially coordinate to some facets over others and encourage anisotropic growth of the particle. Preferential binding of capping agents can be attributed to the differing surface energies of the respective crystal facets, the binding mode of the capping molecule or a combination of both.

1.2.4 Synthesis and Immobilisation of Nanoparticles

Colloidal nanoparticle solutions are not ideal for catalytic systems. Although they act as heterogeneous catalysts and provide a surface on which a chemical reaction may take place, the stability of the colloidal sols make collection and recycling of the nanoparticles difficult.[100] To combat this, a variety of different techniques have been established in recent years to immobilise nanoparticles onto solid supports.[108] The supports range from metal-oxides to porous materials and a thorough discussion on supports can be found in section 1.2.5. With the need to control particle size and shape distributions, these methods have met with varied success.

The general synthetic pathway involves the reduction of metal salts from dilute aqueous or organic media in the presence of, or with subsequent deposition on, larger particles of solid materials. Reduction in the liquid phase is often done with strong reducing agents such as sodium borohydride or hydrazine, where monodispersity and kinetic control are maintained by operating in high dilution, and thus preventing aggregation.[100] Alternatively, reductions can be performed on dry precursors in the gas-phase using H_2. An evaluation of the most common synthetic methods follows.

1.2.4.1 Impregnation

$$HAuCl_4 + H_2O + Support \xrightarrow[ii)\ thermal\ reduction\ (H_2)]{i)\ dry} Au/Support$$

Scheme 1.3 Example scheme for generation of immobilised Au NPs by impregnation methods

Impregnation methods are arguably the simplest methods of synthesising immobilised nanoparticle catalysts.[108-109] The process involves wetting the surface of a powdered solid with an aqueous solution of the metal salts (often chlorides). The material is then dried, leaving the metal precursors impregnated on the surface of the support (Scheme 1.3). Subsequent reduction is performed by thermal treatment of the material in the presence of hydrogen to form the metal nanoparticles. Because this is a simple method, it has the advantage that it can be applied to many different solid supports as long as

they are stable under the reducing conditions. However, large particles in excess of 10 nm and a broad size distribution are commonly observed. Larger particles are formed because of the high probability of nanoparticle sintering under elevated temperatures and in the presence of chlorides. In addition, excess chloride ions may remain on the surface of the material and could interfere with any catalytic process which the material may be used in.[108]

In a modified method, the pH of the metal salt solution is reduced below the point of zero-charge (PZC) of the support to encourage electrostatic interactions between the charged metal salts and the acidified surface of the support. This allows for washing of the material to remove excess chloride and maintain nanoparticle loading before reduction and formation of the nanoparticles. This modification is an improvement but fails to remove all excess chlorides, and is dependent on the properties of the support thus introducing extra limitations.[108]

1.2.4.2 Deposition-Precipitation Strategy

$$HAuCl_4 + H_2O + Support \xrightarrow[ii)\ collect\ and\ dry]{i)\ adjust\ pH\ with\ base;\ Heat\ \sim 80\ ℃} Au/Support$$

Scheme 1.4 Example scheme for generation of immobilised Au NPs by DP methods

Deposition-precipitation (DP) methods are the most commonly used for preparation of gold nanoparticle catalysts. There are a few variations, but the theory is based around the formation of nanoparticles by mediation of the solution pH under slightly elevated temperatures (Scheme 1.4). In a fixed pH system first proposed by Haruta *et al.*,[49, 108, 110] a solution containing the metal salt and solid support is adjusted to pH 7-8 by the addition of NaOH and successive stirring at 70-80 °C for 1 hour. This method is applicable to supports with higher PZCs than required for the pH mediated impregnation method described in the previous section and eliminates the problems associated with thermal reduction. The disadvantage is that quantitative deposition of the metal is difficult with maximum loadings not exceeding ~1 wt %.[108]

An alternative method exploits the *in-situ* degradation of urea at 80 °C that results in a steady rise in pH over time. First established by Geus *et al.*,[111] this method gives greater control over particle size; where the rise in pH can occur over a period of 16 hours, the reaction can be stopped at any time to achieve different sized particles. Loadings can also be achieved up to 8 wt %.[108]

1.2.4.3 Colloidal Deposition

$$HAuCl_4 + H_2O + SA \xrightarrow{NaBH_4\ reduction} Au\ NP\ sol$$

$$\xrightarrow[ii)\ collect\ and\ dry]{i)\ add\ support\ and\ stir} Au/Support$$

Scheme 1.5 Example scheme for generation of immobilised Au NPs by colloidal sol deposition methods (SA – Stabilising agent)

The previous synthesis methods have focused on the direct synthesis of nanoparticles on the surface, external or internal, of various solid materials. Colloidal deposition (sometimes called sol immobilisation) reverses the process by pre-forming the nanoparticles as a colloid in solution, most commonly with polymer stabilising agents, before subsequent deposition to the surface of the support (Scheme 1.5).[108] This technique takes advantage of the nanoparticle size control that can be attained through the use of polymers which is often a problem in the direct synthesis approaches. Deposition often requires simple immersion of the solid support into the colloidal suspension of nanoparticles. Adhesion of the metal colloid to the surface can occur through interactions of the support with the nanoparticles as before, in which case the PZCs of the support still need to be taken into account, or through interactions of the support with the stabilising agent. For example, where negatively charged stabilisers are used (e.g. citrates), electrostatic interactions can aid adhesion, and polymer stabilisers can form interactions between functional groups such as carboxylic acids. The main disadvantages of this method is that after deposition, the polymer stabilisers remain on the surface of the nanoparticle, blocking potential adsorption sites for catalytic reactions.

This method has been the preferred method for the preparation of highly active, bimetallic gold-based nanoparticle catalysts by Hutchings *et al.*[112-113] and many others.

1.2.4.4 Encapsulation

Impregnation and DP deposition methods can be used to synthesise well dispersed metal nanoparticles on surfaces, however if the interactions between the surfaces and the nanoparticles aren't sufficient, then the mobility of the nanoparticles can increase during a catalytic process leading to sintering and leaching. This can limit the lifetime and recyclability of catalysts. Colloidal deposition can increase the strength of interactions with the surface, but can reduce the accessible surface areas of the nanoparticles. A strategy of overcoming a lot of these drawbacks is the idea of encapsulation; the embedding of nanoparticles within a porous framework. By encapsulating nanoparticles within the pores of a porous material, they are physically prevented from migrating and thus leaching, aggregation and sintering can be greatly reduced if not eliminated completely. Although it is possible to embed nanoparticles within an amorphous porous material such as a silica,[108] the recent literature shows a trend toward the use of nanoporous crystalline materials and the exploitation of additional functionality for hybrid materials and applications.[114] With the use of crystalline porous supports, it is possible to achieve much better control over the location and thus the chemical and physical environment around the nanoparticles.

$$Porous\ Support + HAuCl_4 + H_2O \xrightarrow[ii)\ thermal\ reduction\ (H_2)]{i)\ collect\ and\ dry} Au@Support$$

Scheme 1.6 Example scheme for generation of encapsulated Au NPs by "ship in a bottle" methods

Two approaches present themselves; growth of nanoparticles within a preformed microporous material (also called "ship-in-a-bottle"), or growth of a porous material around preformed nanoparticles.[115] The desired conditions and nature of the porous support can dictate which of these methods is most

suitable. Although there is no hard and fast rule, if the pores of the material are relatively large, then it may be more feasible to synthesise the framework first as shown in Scheme 1.6, as there will be minimal internal stress on the framework caused by the continual growth of the nanoparticles. In the recent case presented by Wen *et al.*,[116] a porous material with mesoporous cages and internal amine functionality was first synthesised and used to encapsulate platinum nanoparticles. The large cavities and presence of the amine functionality aided in the internal adsorption of metal salts before reduction to form encapsulated nanoparticles for photocatalytic applications. Difficulties with this approach are that it can be difficult to control the size and shape of nanoparticles, some particles may form on the external surface of the support and there could be some degradation to the immediate area around the point of nucleation for the metal nanoparticle.

$$HAuCl_4 + H_2O + SA \xrightarrow{NaBH_4\ reduction} Au\ NP\ sol$$

$$\xrightarrow[ii)\ synthesise\ support]{i)\ add\ support\ precursors} Au@Support$$

Scheme 1.7 Example scheme for generation of encapsulated Au NPs by sequential growth of support (SA – Stabilising agent)

The opposite approach of pre-synthesising the nanoparticles (Scheme 1.7) can be much better for tuning the sizes and shapes as for the colloidal deposition route. However, the process is a lot more difficult as interactions between the support precursors and the metals must be just right to encourage sequential growth of the support around the nanoparticles rather than self-nucleation to form separate entities. The synthesis conditions of both the nanoparticles and support must also be compatible. Lu *et al.*,[117] presented a strategy for the encapsulation of gold nanoparticles in a nanoporous material by this method. They first prepared a gold colloid using PVP as a polymer-stabiliser which acted in two capacities; firstly, to restrict particle growth and form a stable colloid as expected, but also to encourage interactions between the precursors of the support and encourage overgrowth. This method is not restricted by particle

size and can in theory be used to encapsulate nanoparticles of all shapes and sizes provided the conditions are right.

1.2.4.5 Multimetallic Nanoparticles

The majority of research on nanoparticle catalysts has been performed on particles containing a single metal. As the understanding of the reactive chemical origin of these catalysts expands, both in general and within specific processes, we can intuitively design more complex systems as superior catalysts. The more recent literature has been exploring the use of multimetallic particles in catalysis to further improve the reactions by fine tuning the physical and electronic properties. Bimetallic nanoparticle catalysts gained research momentum just before the turn of the century,[118] however a lot of the research was in the observation of new catalytic properties with minimal understanding or explanation as to their origin.

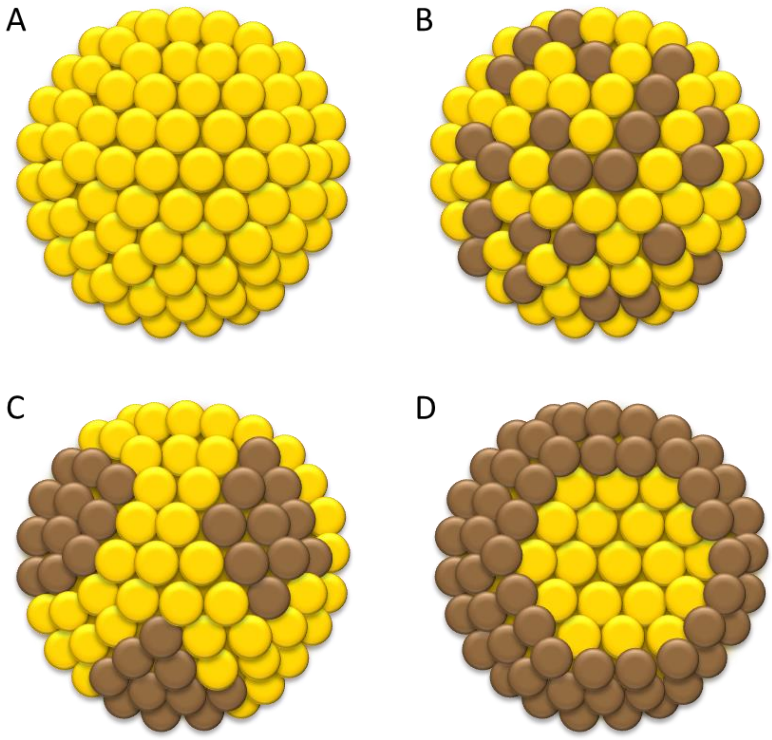

Figure 1.10 Configurations of bimetallic nanoparticles; monometallic mixture (A), alloy (B), cluster-in-cluster (C) and core-shell (D).

As more detailed and precise characterisation techniques have been applied to analysing nanoparticle catalysts, it was discovered that bimetallic particles could take on a variety of different morphologies depending on the precursors

and synthetic conditions employed. Possible compositions include a simple combination of two or more types of discrete monometallic nanoparticles, alloys where the metals are randomly distributed throughout the particle, cluster-in-cluster where distinct regions of each metal are randomly distributed within a particle and core-shell structures with one metal on the surface and another in the centre[119] (Figure 1.10).

Alloyed particles can generally be prepared through simultaneous reduction of two metal-salts, with nucleation and growth of particles being non-specific to metal location. Core-shell particles can be prepared through epitaxial growth by sequential reduction of a second metal onto preformed monometallic seed crystals.

Whilst there are an array of different metal combinations with nickel, cobalt, copper, ruthenium, rhodium, silver, gold, platinum, palladium and others[120-132] that have been prepared and reported in the literature, the combination of gold and palladium has shown to be synergistic in a range of different catalytic processes,[133] particularly in oxidation reactions.[134-141] Methods have been established to generate bimetallic gold-palladium systems of all different morphologies with varying catalytic properties.[113]

1.2.5 Host Materials

A few properties should be considered when selecting host supports for nanoparticle based catalysts. First and foremost, the support must be able to form reasonable interactions with the nanoparticles so as to generate monodisperse isolated sites with good adhesion. The support must also be stable in the nanoparticle synthesis conditions or be able to be synthesised in the presence of nanoparticles, and lastly should remain stable under catalytic reaction conditions, maintaining nanoparticle adhesion and site isolation. These properties are essential for a support to act as an inert heterogeneous host, however it is also possible for the support to behave favourably by increasing the activity of a catalyst or even playing an intrinsic role in the activation of substrate molecules. Spillover, for example, was a phenomenon that was observed when adsorbed species on an active surface can migrate (or "spillover") to the surface of an otherwise inert adjacent material. This is true of examples where palladium nanoparticles supported on TiO_2 can facilitate

spillover of adsorbed oxygen species from the nanoparticle to the surface of a titania support.[142] In addition, it has been noted that different metal oxide supports can either enhance or reduce the activity of gold nanoparticle toward the aerobic oxidation of carbon monoxide and other substrates.[143-145]

In earlier research, noble metal nanoparticles were commonly supported on dense phase metal oxides such as titania,[44, 49, 140, 146] silica,[109, 147-148] ceria,[147, 149] zirconia,[147, 150-151] alumina[147, 152] and magnesia.[153-154] Deposition relied on electrostatic interactions as governed by the support PZC discussed earlier in *Section 1.2.4*. Research on these materials is still ongoing, but there is a drive to explore the effects of new supports with interesting features that can act synergistically or cooperatively in catalysis.

Nanoporous materials are already employed as catalysts in a variety of different applications[3, 155-156] and possess unique features that offer advantages as supports for metal nanoparticles over dense phase materials. They can be crystalline, amorphous with ordered pore structures or amorphous with random pore distribution and are categorised by the size of the pores within the frameworks; microporous materials have pores less than 2 nm, mesoporous between 2-50 nm, and macroporous anything with pores larger than 50 nm.[157] The porosity of the frameworks can offer internal cavities in which nanoparticles can be positioned; for larger pore materials, the increase in internal surface area can allow for higher nanoparticle loadings and greater chemical control of the restricted environment around the nanoparticles.[51] In smaller pore materials, the size of the pores can be used for templated growth of nanoparticles as well as encapsulation and size selective access to the nanoparticle surfaces.[114, 158] Where a porous material is charged, the internal metal counterions can act as nucleation sites for the growth of nanoparticles.[159-161] The following sections describe in more detail some of the porous materials that have been used as supports for nanoparticles.

1.2.5.1 Microporous Inorganic Frameworks

Inorganic materials with microporous architectures have been known for a long time, with zeolites being the most common crystalline examples.[162-163] Zeolites are hydrated microporous aluminosilicates composed of $[AlO_4]^{5-}$ and $[SiO_4]^{4-}$ tetrahedral building units and occur naturally, found in areas of igneous rock where historical volcanic activity provided the necessary temperatures and

pressures for formation.[155, 164] They are already heavily utilised as selective catalysts in the petrochemical industry, utilising their porous architectures for selectivity in reactions or separations.[156] Zeolites can be artificially synthesised using hydrothermal techniques where high temperatures and pressures are replicated in autoclaves.[164] The overall structure of a zeolite is $[Al_xSi_{1-x}O_4]^{x-}$ (with the level of aluminium not exceeding a threshold of 50 %)[165] and carries a net negative charge which is balanced by the presence of counter-ions; mostly protons or metals. As the counter-ions are held in the internal cavities of the structures through electrostatic interactions, ion exchange processes are well-known, revealing one characteristic property and application of the materials. Other microporous materials with similar topologies to zeolites but with different compositions are referred to as zeotypes (e.g. aluminophosphates and aluminogermanates).[162]

The ability of zeolites to exchange ions makes them a good precursor for supporting nanoparticles formed by reduction of the counter-ion. In a few examples, Ag^+ ions can be exchanged into the framework of mordenite or zeolite-Y and reduced to form isolated and well dispersed silver nanoparticles.[159-161] An alternative method of forming nanoparticles on zeolites is to perform the hydrothermal synthesis in the presence of a small amount of a metal salt. For example, one can load gold nanoparticles onto ZSM-5 and LSX zeolites by this method.[166] The reduction of gold is relatively facile and can be done in either reducing or oxidising conditions. As such, the hydrothermal treatments or subsequent calcinations are sufficient to generate the metallic gold species from the metal salts. Their relatively high porosity with surface area up to 600 m^2/g, thermal, chemical and even mechanical stability lend themselves as good potential hosts for nanoparticle encapsulation.[162] A disadvantage of zeolites as supports for deposited nanoparticles is lack of potential interactions between the crystal surfaces and the nanoparticles or respective stabilising agents.

1.2.5.2 Metal-Organic Frameworks

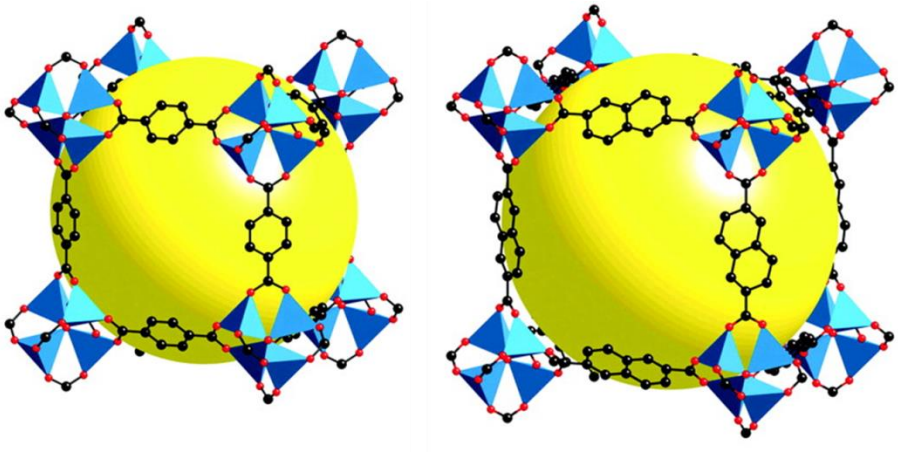

Figure 1.11 Isoreticular MOF-5 and IRMOF-8 with 1,4-benzenedicarboxylate and 2,6-napthalenedicarboxylate organic linkers respectively. From N. L. Rosi, J. Eckert, M. Eddaoudi, D. T. Vodak, J. Kim, M. O'Keeffe and O. M. Yaghi, *Science*, **2003**, 300, 1127. Reprinted with permission from AAAS.

Metal-organic frameworks (MOFs) are a class of crystalline porous materials and a type of porous coordination polymer constructed from metallic or metal-oxide nodes linked together by multitopic bridging organic ligands through coordinating functional groups such as carboxylates and/or heteroatoms such as nitrogen.[167-170] They are characteristic of having high internal surface areas due to the porosity and low density of the crystalline lattice and can, in a few cases, exceed values of 10,000 m^2/g.[171] The organic moieties in the framework are what separate them from traditional inorganic frameworks such as zeolites in terms of structure and properties, generally lending themselves toward more versatile tunability and functional design.[172-173] Functionality can be added to the organic linkers pre- or post-synthesis that can add properties suitable for gas storage,[174-177] molecular separation,[178-180] catalysis,[181-183] sensing,[180, 184-185] ion exchange[186-187] and drug delivery.[170, 188] Functionality can also be attained by exploiting coordinatively unsaturated metal centres that can bind substrate molecules for adsorption and/or catalytic processes.[189] The pore sizes of a MOF can be altered without changing the intrinsic structure of the framework in a technique known as isoreticular (same "net") synthesis.[190-191] By extending the physical length of a linker from 1,4-dicarboxylic acid to 2,6-napthalenedicarboxylic acid in MOF-5, for example, it is possible to open up

the pores of the framework whilst maintaining the same intrinsic connectivity (Figure 1.11).

As there is a diverse range of metals and organic ligands suitable for MOF synthesis, it is not unsurprising that an excess of 20,000 different MOF structures have been reported. With various applications in mind, thermal and chemical stability is an important property and many of these structures are not suitable.[192-193] It is interesting to note that the structures with more simple architectures (small organic ligands, strong coordinating groups, metals with simple geometries etc.) and synthesis conditions tend to be the most thermally stable with the most reported applications in the literature. A few examples of stable MOFs include MIL-53,[194] an aluminium terephthalate, MIL-101,[195] a chromium terephthalate, UiO-66,[196] a zirconium terephthalate, HKUST-1,[197] a copper trimesate and ZIF-8,[198] a zinc imidazolate, each with their own unique porous architectures. When considering MOFs as hosts for nanoparticles, the MOF must be stable and resistant to the synthesis conditions of the metal nanoparticles if constructed first and must also be stable to the chemical, thermal and mechanical parameters of the catalytic process it will be exposed to. The generally accepted terminology for nanoparticle supported MOFs is "NP/MOF" for deposited nanoparticles and "NP@MOF" for encapsulated nanoparticles although this is not always adhered to in the literature.

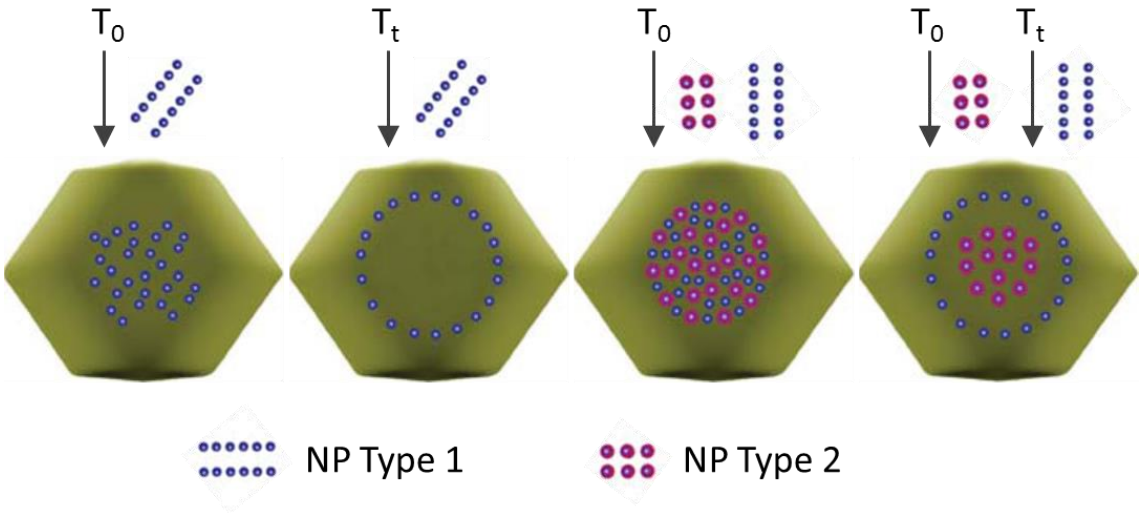

Figure 1.12 Positional control of nanoparticles in ZIF-8 crystals (T = time added to ZIF-8 synthesis). Adapted by permission from Macmillan Publishers Ltd: Nature Chemistry, G. Lu *et al.*, Issue 4, pages from 310, copyright 2012.

The surface of carboxylate-MOF crystals are decorated with free pendant carboxylic acid groups and the presence of heteroatoms in the organic linkers can both form electrostatic interactions with the surface of the nanoparticles, or with functional groups on stabilising agents around the nanoparticles.[199] The pores of MOFs also allow for the encapsulation of nanoparticles by reduction of metal salts in the pores of the framework, or sequential growth of the framework around pre-synthesised nanoparticles.[114, 200] The first method proves to be the most popular with the cavities being used to template the growth of the nanoparticle, however volatile organometallic precursors are often required to allow for effective diffusion of the precursor through the porous structure.[201] It was also noted that the growth of the nanoparticle can break down the MOF structure in the immediate area to form nanoparticles bigger than the cavity size, but still encapsulated.[199] A recent example of the latter method showed that is possible to gain positional control of the nanoparticles within a ZIF-8 crystal by introducing them to the synthesis at various stages of the crystal growth (Figure 1.12) with subsequent use as active catalysts for CO oxidation.[117]

Table 1.3 Summary of most common MOFs employed as hosts for noble metal based nanoparticles (Note: MOFs are denoted by their common abbreviations. The framework metal is given in parentheses.)

Metal NP	MOFs for encapsulation	MOFs for deposition
Au	ZIF-8(Zn),[117, 202] HKUST-1(Cu)[203]	ZIF-8(Zn),[204] MIL-53(Cr),[205] MIL-101(Cr),[205] MIL-101(Cr)-NH_2,[206] UiO-66(Zr),[207] IRMOF-3(Zn),[206] MIL-100(Fe)[208]
Pt	MOF-177(Zn),[201] MIL-101(Cr)[116]	UiO-66(Zr),[209] MIL-100(Fe)[208]
Pd	SNU-3(Zn),[210] MIL-101(Cr),[63] UiO-66(Zr),[211] IRMOF-3(Zn)[212]	MIL-53(Al)-NH_2,[213] ZIF-8(Zn),[214-215] UiO-66(Zr)-NH_2,[216] MIL-101(Cr)-SO_3H,[217] MIL-100(Fe)[208]
Au-Pd	MIL-101(Cr)[141]	MIL-101(Cr)[218]

Metal NP	MOFs for encapsulation	MOFs for deposition
Au-Ni	MIL-101(Cr)[219]	—
Pt-Pd	ZIF-8(Zn)[220]	—
Ag-Pd	—	MIL-101(Cr)[126]

Another example of subsequent growth of MOFs on preformed nanoparticles was demonstrated by Tsuruoka *et al.*[203] who successfully grew crystals of HKUST-1 around gold nanoparticles, showing that preferential growth on the capped nanoparticles was favoured due to the interactions between the nanoparticle stabiliser and the MOF precursors. Table 1.3 gives an overview of some MOFs used as hosts for noble metal based nanoparticles either by deposition on the crystal surfaces or by encapsulation within the pores. The hybrid nanomaterials are then used in a variety of catalytic applications[114] including selective oxidations,[201, 205] hydrogenations[217] and C-C coupling reactions.[63, 213]

As the nanoparticles and MOF support both have functional properties, it is also possible to envisage the use of these hybrid materials as multifunctional materials, with potential for tandem catalysis (with active sites both on the nanoparticles and MOF framework),[212] or for catalytic generation of H_2 and subsequent capture and storage within the porous framework.[141]

1.2.5.3 Mesoporous Materials

Materials with microporosity can often be limited in their applications by diffusion and mass transfer restrictions caused by the small range of molecules that can enter the pores. Mesoporous materials can also be employed for size selective reactions[156] but which can be applied to much larger molecules Mesoporous materials can also be employed for better diffusion kinetics in reactions with small molecules when compared with microporous materials, allowing the active site to reach a higher potential if diffusion becomes a rate limiting factor. Utilising materials with mesoporosity (pores between 2 and 50 nm) can aid facile access to the internal volume,[221] providing enough room for anchoring of active species such as organocatalysts which wouldn't be possible in a purely microporous material, and provide access to larger entities such as

drug molecules for a more diverse range of applications. Ordered amorphous silicas such as MCM-41,[222] possessing hexagonal channels with long range order but amorphous silica walls, have become popular mesoporous materials for the support of catalytic species including nanoparticles.[148, 223] It has also been demonstrated that mesoporosity can be introduced into microporous materials to form hierarchical functionality, where mesopores provide better diffusion potential, and functionality within the micropores can still be maintained.[221, 224] This can be achieved through templating and etching methods amongst others.[225]

There are many studies showing the use of gold nanoparticles on mesoporous materials such as MCM-41[226] for hydrogenation of 1-hexene,[148] adsorption of NO/CO,[166] and oxidation of CO.[227] Platinum nanoparticles have also been supported on mesoporous materials for hydrogenation reactions[51, 54, 228] and oxidation of hydrocarbons,[50] with palladium nanoparticles on similar supports also showing activity in similar reactions.[229-230]

1.2.6 Catalytic Oxidation Reactions with Noble Metal Nanoparticles

There are a range of different oxidation reactions that have been targeted by noble metal nanoparticle catalysts, some of which will be discussed further in this section, due to the propensity for nanoparticles to activate molecular oxygen and simple peroxides.[231] As discussed earlier, oxidation reactions are already performed on large scales in industry, so the target of new nanoparticle based materials is to achieve high activities at relatively mild conditions whilst maintaining high selectivity for a desired product. Herein lies the considerable challenge. Whether the reaction involves addition of oxygen to hydrocarbons, the dehydrogenative oxidation to form functional carbonyl compounds or coupling of molecules through oxygen rich functional groups such as ethers or esters, a nanoparticle catalyst must be designed and engineered with composition, support, chemical environment and reaction conditions in mind to facilitate this goal.

Regulating the size of nanoparticles is a key tool for engineering active catalysts and we have already established that large particles (>10 nm) have electronic properties closer to that of bulk metal and thus reduced catalytic

activity.[232] This also holds true for oxidation reactions with studies showing dramatically superior activity for nanoparticles of sizes between 1-3 nm. Gold nanoparticles supported on TiO_2 show a 3 times increase in TOFs for cinnamyl alcohol oxidation when particle sizes are dropped from 13 nm to 5 nm,[232] and similarly for Cr-MIL-101 supported gold nanoparticles, diameters of 2 nm showed TOFs two orders of magnitude higher than for particles of 10 nm.[233]

With activity in mind, the presence of stabilising ligands can also play an important role. As surface reactions are the consideration for mechanistic pathways of oxidation reactions on a nanoparticle surface, the presence of stabilising ligands can block adsorption of oxygen species and substrates acting in part as a surface 'poison'.[234] Whilst it is still possible to achieve respectable catalytic activity without the removal of the ligands, it has been identified that some treatments involving solvent washing can enhance catalytic performance through regulated removal by up to three times in CO oxidation reactions.[235] The complications with removing the stabilising ligands is that even after deposition of nanoparticles, the ligands still prevent surface mobility and aggregation of particles and so ligand removal can have detrimental effects to catalyst lifetimes. Partial ligand removal has been discussed as a compromise for increasing catalytic activity without significant detrimental effects. Whilst there are a few reports on removal of stabilising ligands, this is not yet a widely practised technique for immobilised metal nanoparticle catalysts.

The following sections summarise the latest research on some selected oxidation reactions with noble metal nanoparticle catalysts.

1.2.6.1 Oxidation of Carbon Monoxide

The oxidation of CO to CO_2 using O_2 is a common reaction reported in the literature and often described as a way of eliminating harmful CO to the less harmful CO_2 (although not totally environmentally benign) from exhaust gases.[236] It is also often used as a probe reaction for detecting activity of catalysts toward oxidation reactions and understanding the mechanism of oxidations of noble metal catalysts. Performed in the gas phase, the high mobility of reactants means that little attention is required on the mass transfer of the reaction, especially when nanoparticles are embedded within porous supports.

The reaction was first explored in the late 80s by Haruta *et al.*[237] when they discovered that activity for this reaction by supported gold nanoparticles could be achieved at temperatures as low as -70 °C. With simple molecules involved in this gas phase reaction, there has been a multitude of experimental and theoretical studies on how molecular oxygen is activated by gold nanoparticle catalysts for oxidation reactions. This debate is still hotly contested with a variety of different models proposed,[238-239] however there is an agreement that the activity can be greatly dependent on the nature of the support with one study proposing that interface sites between the gold and a titania support are the active site for generating active O_2 species.[239]

With this in mind, a great many supports have been tested for the gold nanoparticle catalysed aerobic CO oxidation, including, but not exclusive to, metal oxides[13, 46, 238-241] such as titania, silica, ceria, iron oxide, cobalt oxide, nickel oxide and magnesium oxide, zeolites[242-243] and metal-organic frameworks (MOFs).[22, 204] Although the original research has focused on gold nanoparticles, high activity for platinum and palladium nanoparticles for CO oxidation has also been reported.[22, 244-245]

1.2.6.2 Oxidation of Alcohols

The selective oxidation of alcohols is probably one of the biggest uses of nanoparticle catalysts today in the fine-chemicals industry. With nanoparticles showing an aptitude for activating simple benign oxidants like O_2 and some peroxides, the challenge is to achieve oxidations with maximum selectivity and therefore high yields of a single product. In the past, because harsh reaction conditions have been required to activate O_2 for use as an oxidant, the reactions have often been unselective and so produce large quantities of undesired by-products that end up as waste. Noble metal nanoparticle catalysts have shown promise in these selective oxidations of alcohol substrates and a summary of the most important reactions follows in Table 1.4, with more detailed catalytic properties in the following Table 1.5 to Table 1.10.

Whilst the lists are by no means exclusive, it demonstrates the wide breadth of research into heterogeneous nanoparticle catalysts for alcohol oxidations in an attempt to discover the best catalysts in terms of nanoparticle composition and nature of the support, but also to understand the mechanisms and structure-property relationships by which these catalysts operate. With this level of

understanding, it should be possible in the future to precisely design optimal catalysts for reactions of certain substrates with reaction conditions and desired target products in mind.

Table 1.4 Summary of noble metal nanoparticle catalysts used in selective oxidation of alcohols

Substrate	Structure	Product	NP Catalysts
Benzyl Alcohol	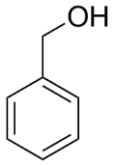	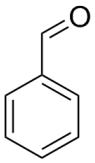	Au/zeolite Y,[246] Au/TS-1,[247] Au/Al_2O_3,[248] Au/C,[249] Au/TiO_2,[250-251] AuPt/TiO_2,[252] AuPd/TiO_2,[153, 252-253] AuPt/C,[252] Pd/COP-4,[245] AuPd/C,[252-254] AuPd/MgO,[153] Pd/HAP,[58] Pd/CeO_2[255]
Vanillyl Alcohol	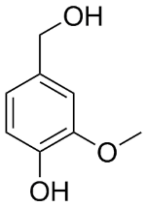	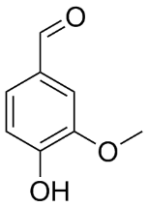	Pt/MOF-5,[256] Pt/C,[257-258] Pd/C[258]
Crotyl Alcohol	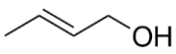	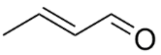	AuPd,[259-261] AuPd/TiO_2,[140, 153] AuPd/MgO[153]
Cinnamyl Alcohol	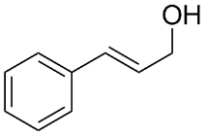	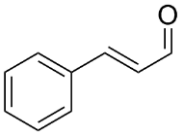	Au/TiO_2,[251] Pd/Al-SBA-15,[229] Pt/SiO_2,[262] Pd/HAP[58]
Glycerol	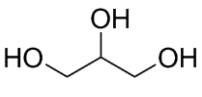	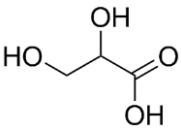	Au/C,[137, 263] Au/TiO_2,[263] Pd/C,[137] AuPd/TiO_2,[138] AuPd/C,[137-138] AuPt/MgO,[154] AuPd/MgO[154]
Cyclohexanol	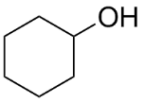	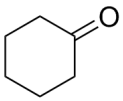	Au/TiO_2,[251] Au/HT,[264] Pd/CeO_2[255]

Table 1.5 Catalytic data of noble metal nanoparticle catalysts for benzyl alcohol oxidation

NP Catalyst	Oxidant	Conversion (%)	Benzaldehyde Selectivity (%)	Yield (%)	TOF[a] (h^{-1})
Au/Zeolite Y[246]	O_2	71.7	> 99	71.0	5.9
Au/TS-1[247]	H_2O_2	58.0	> 99	57.4	*12.2*
Au/Al_2O_3[248]	O_2	96.0	84.0	80.6	441.0
Au/C[249]	O_2	11.6	10.2	1.2	*2.9*
Au/C (NaOH)[249]	O_2	80.2	94.9	76.1	*20.2*
Au/TiO_2[250-251]	TBHP	63.1	79.2[b]	50.0	108.0
	H_2O_2	> 99	15.0[c]	14.9	*100.0*
$AuPt/TiO_2$[252]	TBHP	28.0	~12.0[c]	3.4	*75.8*
$AuPd/TiO_2$[153, 253]	O_2	88.0	77.0	67.8	6100
	O_2	32.8	71.6	23.5	8650
AuPt/C[252]	TBHP	22.0	~50.0[c]	11.0	*59.6*
Pd/COP-4[245]	O_2	32.0	57.1[d]	18.3	*303*
PdPt/C[252]	TBHP	17.0	~41.2[c]	7.0	*46.0*
AuPd/C[253-254]	O_2	94.7	67.0	63.4	-[e]
	O_2	6.0	75.1[b]	4.5	2430
AuPd/MgO[153]	O_2	33.0	98.0	32.3	2300
Pd/HAP[58]	O_2	> 99	99.0	98.0	*500*
Pd/CeO_2	O_2	82.1	62.9	51.6	*262.3*

[a] TOF values in italics are calculated from data reported in the literature. [b] By-product reported as benzyl benzoate. [c] By-product reported as benzoic acid. [e] By-product reported as toluene. [e] Unable to calculate from reported data.

Table 1.6 Catalytic data of noble metal nanoparticle catalysts for vanillyl alcohol oxidation

NP Catalyst	Oxidant	Conversion (%)	Vanillin Selectivity (%)	Yield (%)	TOF[a] (h^{-1})
Pt/MOF-5[256]	O_2	24.5	99.2	24.3	*4.9*
Pt/C[257-258]	O_2	94.8	94.9	90.0	*19.0*
	O_2	80.0	90.0[b]	72.0	*5.4*
Pd/C[258]	O_2	87.0	94.0[b]	81.8	*5.1*

[a] TOF data in italics are calculated from data reported in the literature. [b] Main by-product was vanillic acid.

Table 1.7 Catalytic data of noble metal nanoparticle catalysts for crotyl alcohol oxidation

NP Catalyst	Oxidant	Conversion (%)	Crotonaldehyde Selectivity (%)	Yield (%)	TOF[a] (h^{-1})
AuPd[259-261]	O_2	72.4	62.8	45.5	*60.3*
	O_2	36.9	73.0	26.9	*7.7*
	O_2	71.4	88.0	62.8	*92.8*
$AuPd/TiO_2$[140, 153]	O_2	18.0	45.0	8.1	920
	O_2	-[b]	85.0	-[b]	*2.5*[c]
AuPd/MgO[153]	O_2	12	47.0	5.6	1200

[a] TOF data in italics are calculated from data reported in the literature. [b] Data not provided in reference. [c] TOF calculated assuming 100 % conversion.

Table 1.8 Catalytic data of noble metal nanoparticle catalysts for cinnamyl alcohol oxidation

NP Catalyst	Oxidant	Conversion (%)	Cinnamaldehyde Selectivity (%)	Yield (%)	TOF[a] (h^{-1})
Au/TiO_2[251]	H_2O_2	> 99	> 99	98.0	*100*
Pt/SiO_2[262]	O_2	38.0	21.8	8.3	*88.9*
Pd/Al-SBA-15[229]	O_2	> 99	66.0	65.3	777.8
Pd/HAP[58]	O_2	91.0	87.0	79.2	*75.8*

[a] TOF data in italics are calculated from data reported in the literature.

Table 1.9 Catalytic data of noble metal nanoparticle catalysts for glycerol oxidation

NP Catalyst	Oxidant	Conversion (%)	Glyceric Acid Selectivity (%)	Yield (%)	TOF[a] (h^{-1})
Au/C[137, 263]	O_2	90.0	~55	49.5	*~850*
	O_2	6.8	67.0	4.6	*1088*
Au/TiO_2[263]	O_2	33.0	64.0	21.1	*5280*
AuPd/C[137-138]	O_2	90.0	63.0	56.7	*450*
	O_2	87.6	72.5	63.5	110
$AuPd/TiO_2$[138]	O_2	95.0	61.3	58.2	120
AuPd/MgO	O_2	14.5	74.4	10.8	*36.3*
AuPt/MgO	O_2	42.9	72.2	40.0	*107.3*
Pd/C[137]	O_2	90	~60	54.0	*~250*

[a] TOF data in italics are calculated from data reported in the literature.

Table 1.10 Catalytic data of noble metal nanoparticle catalysts for cyclohexanol oxidation

NP Catalyst	Oxidant	Conversion (%)	Cyclohexanone Selectivity (%)	Yield (%)	TOF[a] (h^{-1})
Au/TiO_2[251]	H_2O_2	87.0	>99	86.1	*87*
Pd/CeO_2[255]	O_2	57.8	98.2	56.8	*256.3*

[a] TOF data in italics are calculated from data reported in the literature.

Benzylic alcohols are important functional groups found in many pharmaceutical and fine-chemical intermediates and are often oxidised to aldehydes for the final products. Benzyl alcohol, the simplest of benzylic alcohols, is oxidised to benzaldehyde for its direct use in almond flavourings and as precursors for plastic additives, photographic chemicals and triphenyl methane dyes such as the leuco base of Malachite Green.[265-266] It is also employed as an intermediate toward antibiotic drugs such as chloramphenicol and ampicillin, and stimulants like ephedrine.[265] Vanillin, another aldehyde product formed by oxidation of a benzylic alcohol derivative (vanillyl alcohol),

is the single most highly produced synthetic flavouring and fragrance chemical in the world, with a global production in excess of 12k tons per annum.[38, 267] When natural extraction processes can only account for 0.1 % of the annual production of vanillin due to costs and resources, it is clear to see the demand for efficient processes to make up the difference.[267] Vanillin is also a highly coveted intermediate in the synthesis of L-3,4-dihydroxy-phenylalanine (L-DOPA), a key therapeutic agent used to combat Parkinson's disease.[267]

Benzaldehyde is commonly made in industry through the hydrolysis of benzal chloride or the oxidation of toluene; the former process involves the use of chlorinated starting materials, producing chlorinated waste and thus hazardous and not particularly environmentally friendly. The oxidation process from toluene is more environmentally benign, however the process is only driven to low conversion (10-20 %) to maintain partial oxidation of the toluene, whilst still only providing 40-60 % yields with myriad by-products that end up as waste.[265-266] The industrial production of vanillin from guaiacol already makes use of nanoparticle catalysts of platinum or palladium, however the process requires promoters of bismuth, lead or cadmium to achieve significant conversions. The process also produces a wide variety of over-oxidation products, relying on subsequent hydrogenation or hydrolysis reactions to convert by-products back to the target molecule. Even with these extra steps, yields of only 61 % are achieved.[258] There is great scope in both of these examples for improving the catalysts by careful design and engineering on the molecular scale, with manipulation of nanoparticle/support synergy showing a lot of promise as in Table 1.5 and Table 1.6. For example, bimetallic AuPd/TiO_2 catalysts are able to achieve impressive TOFs in excess of 6000, however because the reaction conditions were selected to maximise activity including solvent-free conditions and low catalyst rations, the yields are often low due to unreacted starting materials or by-product formation. Despite the high activity, this still poses challenges with regard to low E-factors (a measure of waste to product in kg) that would need to be resolved by difficult separations and isolation procedures. One could argue that it would be more economic to sacrifice on catalyst activity to some degree in order to achieve quantitative yields.

Although not produced on as large a scale as the benzylic aldehydes, allylic aldehydes such as crotonaldehyde and cinnamaldehyde are also produced for

the flavours and fragrances industry. Both chemicals are mostly produced by aldol condensation reactions that require basic catalysts with additional heavily basic conditions.[268-269] Waste streams of heavy organic by-products from the various reaction vessels are typically incinerated for disposal, which even after scrubbing, leads to emissions of greenhouse gases.[269] Simple, green oxidation methods from the respective alcohols provide an alternative route to production of these chemicals, providing the employed catalysts provide enough of an economic benefit and reduced hazardous reaction conditions. Although metal nanoparticles aren't yet used industrially for production of these chemicals, it is possible to see from Table 1.4, Table 1.7 and Table 1.8 that research is showing they are becoming competitively more viable as alternative catalysts. As well as application as a flavouring agent, crotonaldehyde is also used largely for the synthesis of sorbic acid, a food preservative, and Vitamin E. Crotonaldehyde-based intermediates also find wide use in a variety of pharmaceutical and agrochemicals, as well as additives in an assortment of polymers, resins and adhesives.[269] Cinnamaldehyde finds wider use as a flavouring agent as it carries the same spicy, sweet aroma of cinnamon, and as a fragrance used extensively in essential oils and air fresheners. Products that contain cinnamon flavourings range from baked goods and confectionary, to toothpastes and chewing gum.[268] Additionally, cinnamaldehyde finds use as a precursor toward compounds with anti-cancer properties.[270]

KA-oil (ketone/alcohol) is a mixture of cyclohexanol and cyclohexanone and produced in large quantities from the oxidation of cyclohexane. Whilst both are important fine-chemicals, that vast majority are either oxidised further to adipic acid, a major component of nylon-6,6, or oxidised entirely to cyclohexanone for subsequent conversion to ε-caprolactam via cyclohexanone oxime as intermediates in the production of nylon-6.[271-272] More than 97 % of the large scale production of cyclohexanone is used for the production of nylon products with an annual production in excess of 3 million tons;[272] an incredible demand with production efficiency and safety having a large influence on costs and environmental impact. Other minor uses include solvents for resins or polymers and building blocks for pharmaceuticals, insecticides and herbicides.[271-272] Metal nanoparticles have potential in selectively converting KA-oil to cyclohexanone in a clean and efficient way for effective use in the subsequent steps towards nylon-based products.

As can be seen from Table 1.4, nanoparticle catalysts have come a long way in developing more green and efficient ways of selectively oxidising some alcohols towards desired products, with scope to impact some of the industrial processes described. There still remains a challenge in developing catalyst materials that have the combined features of highly accessible nanoparticle surface areas (unblocked by capping agents), high adhesion to support surfaces, narrow size distributions, long lifetimes and recyclability with high activity and good selectivity under mild reaction conditions with benign reagents. Most nanoparticle catalysts are able to excel in a few of these areas, but tend to be limited by some others. If it is possible to break through these limitations, it may be possible to envisage the development of nanoparticle catalysts that are active enough to overcome any economic barriers to employing them directly in green industrial processes.

1.2.6.3 Oxidation of Hydrocarbons

Selective oxidation of hydrocarbons is a significant and more challenging reaction to achieve than for selective oxidation of alcohols. Activating C-H bonds requires more energy and with no functional groups to introduce electron deshielding effects and thus expose carbon centres for reaction, it can be difficult to target specific sites for oxidation.

Cyclohexane and toluene are very relevant industrial substrates and related to some of the alcohol oxidations listed in the previous section. Oxidation of toluene often yields benzaldehyde and benzoic acid, depending on the catalysts and conditions used, and can be a direct route to benzaldehyde from crude hydrocarbon sources rather than from benzyl alcohol. Recent examples of bimetallic gold-palladium nanoparticle catalysts have successfully activated the primary methyl C-H bond in toluene to allow for successful oxidation with O_2,[112] although in this case, the catalysts were selective towards the benzylbenzoate ester.

Table 1.11 Summary of noble metal nanoparticle catalysts used for oxidation of toluene and cyclohexane

Substrate	Structure	Product(s)	NP Catalysts
Toluene	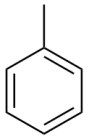	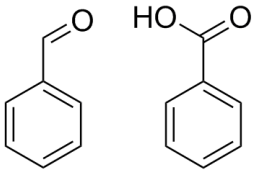	$AuPd/TiO_2$,[112, 273] AuPd/C,[112] Ag/WO_3,[274]
Cyclohexane		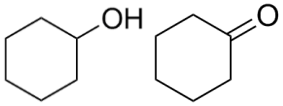	Au/C,[275] Au/CNT,[276] Au/TiO_2,[277] Au/MIL-101,[205] Au/SBA-15,[264] Au/HAP,[106, 278]
p-Xylene	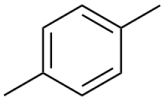	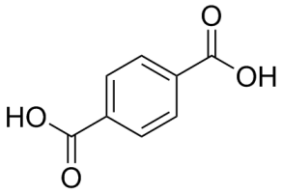	N/A

Table 1.12 Catalytic data of noble metal nanoparticle catalysts for toluene oxidation

NP Catalyst	Oxidant	Conversion (%)	Selectivity (%)		Yield[a] (%)	TOF[b] (h^{-1})
			Aldehyde	Acid		
$AuPd/TiO_2$[112, 273]	O_2	24.1	1.2[c]	2.8[c]	0.3	*32.7*
	TBHP	5.3	32.0	52.0	1.7	86.0
AuPd/C[112]	O_2	50.8	1.1[c]	4.5[c]	0.6	*68.8*
Ag/WO_3	H_2O_2	42.0	93.0	1.0	39.0	6.3

[a] Yield to benzaldehyde. [b] TOF data in italics are calculated from data reported in the literature. [c] Main product is benzylbenzoate.

As can be seen in more detail from the catalytic data in Table 1.12, the selectivity of products from the oxidation of toluene can be heavily dependent on the metal composition of the NPs, with bimetallic NPs favouring ester formation. The aerobic oxidation of cyclohexane is already a large industrial scale process as the main source of KA-oil (cyclohexanol and cyclohexanone) in

the multi-step process toward nylon products, although subsequent oxidation steps are required to convert the remaining cyclohexanol to cyclohexanone.

Table 1.13 Catalytic data of noble metal nanoparticle catalysts for cyclohexane oxidation

NP Catalyst	Oxidant	Conversion (%)	Selectivity (%)		KA-oil Yield (%)	TOF[a] (h^{-1})
			Alcohol	Ketone		
Au/C[275]	H_2O_2	1.7	76.5	23.5	1.7	*7.7*
Au/CNT[275-276]	H_2O_2	2.7	59.3	40.7	2.7	*17.7*
	TBHP/O_2	14.6	86.9	12.8	14.6	*6.1*
Au/TiO_2[277]	TBHP	26.0	60.0	15.0	19.5	-[b]
Au/MIL-101[205]	O_2	30.5	28.8	58.9	26.7	*3.3*
Au/SBA-15[264]	O_2	32.0	62.0	32.0	30.1	858
Au/HAP[106, 278]	TBHP/O_2	14.9	50.0	49.0	14.8	18500

[a] TOF data in italics are calculated from data reported in the literature. [b] Unable to calculate from reported data.

The mixture of alcohol and ketone products is generated because the intermediate cyclohexyl hydroperoxide, formed when the cyclohexane is couple with an activated O_2 species, can 'decompose' via different mechanisms to either of the products. The choice of catalyst can be chosen to gain a limited control over the ratio of the products by promoting one mechanistic pathway over the other. As the products are more reactive than cyclohexane, the industrial oxidation process must be kept to as low as 6 % conversion to prevent over-oxidation and formation of by-products with multiple additions of oxygen around the hydrocarbon ring. In contrast, as highlighted by the data in Table 1.13, a recent study showed that small clusters of gold supported on hydroxyapatite can achieve conversions closer to 15 % with > 99 % selectivity towards KA-oil and displaying impressive TOFs of 1.85 x 10^4 h^{-1},[278] thus exceeding the scope of that which is achieved in industry. Preliminary work examining the efficacy of Au NPs on porous materials such as MIL-101 and SBA-15 reveals that conversions in excess of 30 % can be achieved with reasonable yields of KA-oil (Table 1.13).

The production of terephthalic acid from *p*-xylene is another oxidation process with a lot of scope for exploiting the oxidation capabilities of noble metal

nanoparticles. Terephthalic acid is produced exclusively from oxidation of *p*-xylene in industry, commonly employing cobalt and manganese catalysts with large quantities of bromine in acetic acid as a solvent. The highly corrosive bromine - acetic acid environment requires reactors and equipment to be lined with titanium in some parts of the process which incurs significant costs and potential hazards. There are as of yet, no examples of the production of terephthalic acid using noble metal nanoparticles. The total oxidation of *p*-xylene can be problematic, with oxidation of the first methyl group being relatively facile, but the presence of the acid deactivating the second methyl group in the *para* position. The catalyst or conditions must be able to facilitate the activation of this intermediate for quantitative conversions. Another issue is the a later intermediate, 4-formylbenzoic acid, can co-crystallise with terephthalic acid due to being so similar in structure and properties and result in low purity or crude products that require further purification. The vast majority (> 90 %) of terephthalic acid is used in the production of polyesters such as poly(ethylene terephthalate) or PET which had a worldwide demand of 12.6 million tons in 1992. As of yet, there are no significant reports of nanoparticles used in this oxidation process, however given the activity of these catalyst for other hydrocarbon oxidation reactions, there is significant scope for the application of these catalyst towards this and other processes.

There is a large opportunity to explore the suitability of metal nanoparticles for these more challenging reactions given the high volume and high demand for these chemicals and their respective end-consumer products.

1.3 Aims and Discussion

1.3.1 Rationale for Development of NP Catalysts

The previous sections have highlighted the potential for nanoparticle catalysts in industrially significant selective oxidation reactions. These materials have the potential to increase the efficiency and productivity of oxidation processes, whilst also utilising environmentally benign oxidants to reveal less hazardous and greener solutions. In some cases, hybrid nanoparticle catalysts are already starting to exceed that which is achieved in industry today.

The literature has made it clear that the design of nanoparticle catalysts needs to be engineered with intellectual precision; with the metal composition, particle size and choice of support integral to the chemical properties of the synthesised materials in a given reaction. If metal nanoparticles are too large or small, for example, the catalytic activity and selectivity properties will be negatively affected. In any case, it has been established that the high surface energies associated with nanoparticulate noble metals resulting from quantum size effects, are essential for the activation of greener, but more benign reagents. The reported ability of supported noble metal NP catalysts to activate simple oxidants such as O_2, H_2O_2 and TBHP, as discussed in *Section 1.2.6*, make them ideal candidates for further development of sustainable industrial oxidation processes.

Current examples of these catalysts are able to excel in some properties that are required, but can be limited by others. For example, activity or selectivity in a reaction may be compromised due to capping of active surfaces or the need for harsh reaction conditions; the stability and lifetime can be limited due to collapse of the support, sintering or leaching of metal nanoparticles caused by weak adhesive interactions with the support can occur. One of the aims of this project will be to build on existing research, in terms of catalyst material design, to generate novel materials to attain enhanced productivity and sustainability, structural integrity of the support over the course of an oxidation reaction, and heightened interactions between the support and NPs to prevent sintering, aggregation or leaching that could render the catalyst inactive.

The role of the support has been largely limited to the opportunity for successful immobilisation, whether through surface electrostatic interactions or encapsulation within a porous architecture. Although some support effects have been observed on resulting catalytic properties of immobilised NPs, these have been largely serendipitous. Using the knowledge that has been reported on these, and related materials thus far, it should be possible to exploit these tools for effective design and engineering of the support at the molecular scale for enhanced interactions toward catalytic activity or multifunctionality.

1.3.2 Design, Characterisation and Implementation

In this project, the design of new nanoporous supports will be explored in the generation of novel hybrid nanoparticle catalyst materials to overcome some of these aforementioned limitations. The functional properties of the supports will be analysed and exploited for novel methods to generate highly active nanoparticles for oxidation reactions, or to act as secondary active sites for tandem/cascade reactions. In each case, the hybrid materials will be utilised in an attempt to increase productivity of a given reaction or process, whilst also increasing the sustainability and decreasing negative environmental impact through careful and selective choice of substrates and reaction conditions. To this end, one of the aims will be to attempt the generation of stable uncapped NPs, or with minor fractions of capping agents, in an attempt to liberate a higher degree of NP surface area as active sites for catalytic oxidation with O_2. Furthermore, the support of NPs on functional framework materials will be explored.

A combination of imaging techniques such as electron microscopy (SEM and TEM) will be applied for the analysis of the support and NP morphologies, as well as size distributions, with high resolution. In addition, bulk analysis methods such as PXRD, XPS, EXAFS and XANES will be used to thoroughly characterise NP supported materials to determine integrity of the support, and the nature of the metallic species, confirming the homogeneous distribution across a sample. Where applicable, N_2 adsorption studies and BET analysis will provide data on the porosity of support materials, and probe the ability to maintain structural properties over the course of NP loading and catalytic cycles. Comprehension of structural properties should aid in making informed

structure-property correlations, which should provide rationales toward how the materials could be further improved with respect to activity or stability.

Oxidation reactions will be carried out on industrially interesting reactions, using NP supported materials to investigate the activity with respect to that which is already reported in the literature. The merits of each NP/support combination against the applied oxidation reaction can be rationalised and compared to justify the advantages gained from the new methods or composite materials. In addition, the effect of the supports on the catalytic activity as well as additional functionality will be studied toward the oxidation reactions, and where possible, subsequent reactions in a tandem process. The contribution of each material and catalytic reaction will be evaluated for the contribution toward sustainability.

1.4 References

1 M. Bowker, *The Basis and Applications of Heterogeneous Catalysis*, Oxford University Press, New York, **1998**.
2 D. F. Shriver and P. W. Atkins, *Inorganic Chemistry*, 3rd ed., Oxford University Press, Oxford, **1999**.
3 G. Ertl, H. Knözinger and J. Weitkamp, *Preparation of Solid Catalysts*, Wiley-VCH, Weinheim, **1999**.
4 R. I. Masel, *Chemical Kinetics and Catalysis*, John Wiley & Sons, Inc., New York, **2001**.
5 J. M. Thomas and W. J. Thomas, *Introduction to the Principles of Heterogeneous Catalysis*, Academic Press, London, **1967**.
6 P. Atkins and J. de Paula, *Elements of Physical Chemistry*, 4th ed., Oxford University Press, Oxford, **2005**.
7 P. Atkins and J. de Paula, *Physical Chemistry*, 8th ed., Oxford University Press, Oxford, **2006**.
8 R. A. Sheldon, *Chem. Soc. Rev.,* **2012**, *41*, 1437.
9 L. Cantarella, A. Gallifuoco, A. Malandra, L. Martínková, A. Spera and M. Cantarella, *Enzyme Microb. Technol.,* **2011**, *48*, 345.
10 B. Cornils and W. A. Herrmann, *J. Catal.,* **2003**, *216*, 23.
11 M. Lancaster, *Green Chemistry: An Introductory Text*, Royal Society of Chemistry, Cambridge, **2002**.
12 P. Atkins, T. Overton, J. Rourke, M. Weller and F. Armstrong, *Inorganic Chemistry*, 4th ed., Oxford University Press, Oxford, **2006**.
13 M. Haruta and M. Daté, *Appl. Catal., A,* **2001**, *222*, 427.
14 J. Paterson, M. Potter, E. Gianotti and R. Raja, *Chem. Commun.,* **2011**, *47*, 517.
15 R. Raja, M. E. Potter and S. H. Newland, *Chem. Commun.,* **2014**, *50*, 5940.
16 M. E. Potter, A. J. Paterson and R. Raja, *ACS Catal.,* **2012**, *2*, 2446.
17 A. Corma and H. Garcia, *Adv. Synth. Catal.,* **2006**, *348*, 1391.
18 M. Heitbaum, F. Glorius and I. Escher, *Angew. Chem., Int. Ed.,* **2006**, *45*, 4732.
19 D. Xuereb, J. Dzierzak and R. Raja, Biomimetic Single-Site Heterogeneous Catalysts: Design Strategies and Catalytic Potential in *Heterogenized Homogeneous Catalysts for Fine Chemicals Production* (Eds.: P. Barbaro, F. Liguori), Springer, London, **2010**.
20 D. Macquarrie, Fine Chemicals Synthesis Through Heterogenized Catalysts: Scope, Challenges and Needs in *Heterogenized Homogeneous Catalysts for Fine Chemicals Production* (Eds.: P. Barbaro, F. Liguori), Springer, London, **2010**.
21 C. Louis and O. Pluchery, *Gold Nanoparticles for Physics, Chemistry and Biology*, Imperial College Press, London, **2012**.
22 A. Aijaz and Q. Xu, *J. Phys. Chem. Lett.,* **2014**, 1400.
23 G. A. Somorjai and Y. Lin, *Introduction to Surface Chemistry and Catalysis*, 2nd ed., John Wiley & Sons, Inc., Hoboken, **2010**.
24 Q. Li, R. He, J.-A. Gao, J. O. Jensen and N. J. Bjerrum, *J. Electrochem. Soc.,* **2003**, *150*, A1599.
25 M. Boudart, *Chem. Rev.,* **1995**, *95*, 661.
26 G. P. Chiusoli, P. M. Maitlis and F. Calderazzo, *Metal-Catalysis in Industrial Organic Processes*, Royal Society of Chemistry, Cambridge, **2006**.

27 F. Cavani and G. Centi, Sustainable Development and Chemistry in *Kirk-Othmer Encyclopedia of Chemical Technology*, John Wiley & Sons, Inc., **2011**.
28 G. Rothenberg, Catalysis in *Kirk-Othmer Encyclopedia of Chemical Technology*, John Wiley & Sons, Inc., **2010**.
29 P. T. Anastas and J. C. Warner, *Green Chemistry: Theory and Practice*, Oxford University Press, Oxford, UK, **1998**.
30 G. Franz and R. A. Sheldon, Oxidation in *Ullmann's Encyclopedia of Industrial Chemistry, Vol. 25*, 7th ed., Wiley-VCH Verlag GmbH & Co. KGaA, **2000**, pp. 543.
31 I. W. C. E. Arends and R. A. Sheldon, Modern Oxidation of Alcohols Using Environmentally Benign Oxidants in *Modern Oxidation Methods* (Ed.: J.-E. Bäckvall), Wiley-VCH Verlag GmbH & Co. KGaA, Weinheim, **2004**, pp. 83.
32 J. Clayden, N. Greeves, S. Warren and P. Wothers, *Organic Chemistry*, Oxford University Press, Oxford, **2001**.
33 M. G. Clerici and O. A. Kholdeeva, *Liquid Phase Oxidation via Heterogeneous Catalysis: Organic Synthesis and Industrial Applications*, John Wiley & Sons, Inc, Hoboken, **2013**.
34 A. Baiker and T. Mallat, *Catal. Sci. Technol.,* **2013**, *3*, 267.
35 M. J. Kirschner, Oxygen in *Ullmann's Encyclopedia of Industrial Chemistry*, Wiley-VCH Verlag GmbH & Co. KGaA, **2000**.
36 J. Haber and M. Witko, *J. Catal.,* **2003**, *216*, 416.
37 A. G. Abatjoglou and D. J. Miller, Aldehydes in *Kirk-Othmer Encyclopedia of Chemical Technology*, John Wiley & Sons, Inc., **2011**.
38 K.-G. Fahlbusch, F.-J. Hammerschmidt, J. Panten, W. Pickenhagen, D. Schatkowski, K. Bauer, D. Garbe and H. Surburg, Flavors and Fragrances in *Ullmann's Encyclopedia of Industrial Chemistry, Vol. 15*, 7th ed., Wiley-VCH Verlag GmbH & Co. KGaA, **2003**, pp. 73.
39 T. Mallat and A. Baiker, *Chem. Rev.,* **2004**, *104*, 3037.
40 R. J. White, R. Luque, V. L. Budarin, J. H. Clark and D. J. Macquarrie, *Chem. Soc. Rev.,* **2009**, *38*, 481.
41 C. H. Christensen and J. K. Nørskov, *Science,* **2010**, *327*, 278.
42 M. Haruta, *Gold Bull.,* **2004**, *37*, 27.
43 G. J. Hutchings and M. Haruta, *Appl. Catal., A,* **2005**, *291*, 2.
44 F. Porta, L. Prati, M. Rossi and G. Scari, *J. Catal.,* **2002**, *211*, 464.
45 T. V. Choudhary and D. W. Goodman, *Appl. Catal., A,* **2005**, *291*, 32.
46 W. Deng, J. D. Jesus, H. Saltsburg and M. Flytzani-Stephanopoulos, *Appl. Catal., A,* **2005**, *291*, 126.
47 Q. Fu, A. Weber and M. Flytzani-Stephanopoulos, *Catal. Lett.,* **2001**, *77*, 87.
48 S. H. Joo, J. Y. Park, C.-K. Tsung, Y. Yamada, P. Yang and G. A. Somorjai, *Nat. Mater.,* **2009**, *8*, 126.
49 G. R. Bamwenda, S. Tsubota, T. Nakamura and M. Haruta, *Catal. Lett.,* **1997**, *44*, 83.
50 Y. T. Lai, T. C. Chen, Y. K. Lan, B. S. Chen, J. H. You, C. M. Yang, N. C. Lai, J. H. Wu and C. S. Chen, *ACS Catal.,* **2014**, *4*, 3824.
51 J. Zhu, T. Wang, X. Xu, P. Xiao and J. Li, *Appl. Catal., B,* **2013**, *130–131*, 197.
52 Z. Guo, C. Xiao, R. V. Maligal-Ganesh, L. Zhou, T. W. Goh, X. Li, D. Tesfagaber, A. Thiel and W. Huang, *ACS Catal.,* **2014**, *4*, 1340.
53 K. M. Bratlie, H. Lee, K. Komvopoulos, P. Yang and G. A. Somorjai, *Nano Lett.,* **2007**, *7*, 3097.

54 H. Song, R. M. Rioux, J. D. Hoefelmeyer, R. Komor, K. Niesz, M. Grass, P. Yang and G. A. Somorjai, *J. Am. Chem. Soc.,* **2006**, *128*, 3027.
55 C. Wang, K. E. deKrafft and W. Lin, *J. Am. Chem. Soc.,* **2012**, *134*, 7211.
56 S. Sarina, H.-Y. Zhu, Q. Xiao, E. Jaatinen, J. Jia, Y. Huang, Z. Zheng and H. Wu, *Angew. Chem., Int. Ed.,* **2014**, n/a.
57 J. Muzart, *Tetrahedron,* **2003**, *59*, 5789.
58 K. Mori, T. Hara, T. Mizugaki, K. Ebitani and K. Kaneda, *J. Am. Chem. Soc.,* **2004**, *126*, 10657.
59 G. Chen, S. Wu, H. Liu, H. Jiang and Y. Li, *Green Chem.,* **2013**, *15*, 230.
60 Q. Zhang, W. Deng and Y. Wang, *Chem. Commun.,* **2011**, *47*, 9275.
61 M. R. Knecht and D. B. Pacardo, *Anal. Bioanal. Chem.,* **2010**, *397*, 1137.
62 G. Collins, M. Blömker, M. Osiak, J. D. Holmes, M. Bredol and C. O'Dwyer, *Chem. Mater.,* **2013**, *25*, 4312.
63 Y. Huang, Z. Lin and R. Cao, *Chem. Eur. J.,* **2011**, *17*, 12706.
64 C. Caro, P. M. Castillo, R. Klippstein, D. Pozo and A. P. Zadarenko, Silver Nanoparticles: Sensing and Imaging Applications in *Silver Nanoparticles* (Ed.: D. P. Perez), InTech, **2010**.
65 X. Meng, S. Tang and S. Vongehr, Synthesis, Growth Mechanisms and Tunable Optical and Catalytic Properties of Diverse Silver Nanstructures in *Silver Nanoparticles: Properties, Characterisation and Applications* (Ed.: A. E. Welles), Nova Science Publishers, Ic., New York, **2010**.
66 E. Escalera, M. A. Ballem, J. M. Córdoba, M.-L. Antti and M. Odén, *Powder Technol.,* **2012**, *221*, 359.
67 N. Shukla, E. B. Svedberg, J. Ell and A. J. Roy, *Mater. Lett.,* **2006**, *60*, 1950.
68 Y. Wang, H. Wu, Q. Zhang and Q. Tang, *Micro. Meso. Mater.,* **2005**, *86*, 38.
69 O. Akhavan and E. Ghaderi, *Surf. Coat. Technol.,* **2010**, *205*, 219.
70 D. Deng, Y. Cheng, Y. Jin, T. Qi and F. Xiao, *J. Mater. Chem.,* **2012**, *22*, 23989.
71 Y. Leng, K. Sato, J.-G. Li, T. Ishigaki, M. Iijima, H. Kamiya and T. Yoshida, *Powder Technol.,* **2009**, *196*, 80.
72 J. F. Sonnenberg and R. H. Morris, *ACS Catal.,* **2013**, *3*, 1092.
73 D. Karabelli, S. Ünal, T. Shahwan and A. E. Eroğlu, *Chem. Eng. J.,* **2011**, *168*, 979.
74 S. Månsson, E. Johansson, P. Magnusson, C.-M. Chai, G. Hansson, J. S. Petersson, F. Ståhlberg and K. Golman, *Eur Radiol,* **2006**, *16*, 57.
75 X. Hu and S. Dong, *J. Mater. Chem.,* **2008**, *18*, 1279.
76 G. J. Hutchings, *Chem. Commun.,* **2008**, *0*, 1148.
77 D. Ravelli, D. Dondi, M. Fagnoni and A. Albini, *Chem. Soc. Rev.,* **2009**, *38*, 1999.
78 B. Wardle, *Principles and Applications of Photochemistry*, Wiley, Hoboken, NJ, USA, **2009**.
79 T. L. Thompson and J. T. Yates, *Chem. Rev.,* **2006**, *106*, 4428.
80 A. Kubacka, M. Fernández-García and G. Colón, *Chem. Rev.,* **2011**, *112*, 1555.
81 A. Mills and S. Le Hunte, *J. Photochem. Photobiol., A,* **1997**, *108*, 1.
82 S. Rawalekar and T. Mokari, *Adv. Energy Mater.,* **2013**, *3*, 12.
83 W. Hou and S. B. Cronin, *Adv. Funct. Mater.,* **2013**, *23*, 1612.
84 D. Wang and D. Astruc, *Chem. Rev.,* **2014**, *114*, 6949.
85 H. W. Chen, A. Murugadoss, T. S. A. Hor and H. Sakurai, *Molecules,* **2010**, *16*, 149.

86 M. Shokouhimehr, K.-Y. Shin, J. S. Lee, M. J. Hackett, S. W. Jun, M. H. Oh, J. Jang and T. Hyeon, *J. Mater. Chem. A,* **2014**, *2*, 7593.
87 E. Gianotti, V. N. Shetti, M. Manzoli, J. A. L. Blaine, W. C. Pearl, R. D. Adams, S. Coluccia and R. Raja, *Chem. Eur. J.,* **2010**, *16*, 8202.
88 R. Raja, R. D. Adams, D. A. Blom, W. C. Pearl, E. Gianotti and J. M. Thomas, *Langmuir,* **2009**, *25*, 7200.
89 J. Meurig Thomas, R. D. Adams, E. M. Boswell, B. Captain, H. Gronbeck and R. Raja, *Faraday Discuss.,* **2008**, *138*, 301.
90 R. D. Adams, E. M. Boswell, B. Captain, A. B. Hungria, P. A. Midgley, R. Raja and J. M. Thomas, *Angew. Chem., Int. Ed.,* **2007**, *46*, 8182.
91 R. Raja, S. Hermans, D. S. Shephard, B. F. G. Johnson, G. Sankar, S. Bromley and J. Meurig Thomas, *Chem. Commun.,* **1999**, *0*, 1571.
92 S. Hermans, R. Raja, J. M. Thomas, B. F. G. Johnson, G. Sankar and D. Gleeson, *Angew. Chem., Int. Ed.,* **2001**, *40*, 1211.
93 R. Raja, T. Khimyak, J. M. Thomas, S. Hermans and B. F. G. Johnson, *Angew. Chem., Int. Ed.,* **2001**, *40*, 4638.
94 A. B. Hungria, R. Raja, R. D. Adams, B. Captain, J. M. Thomas, P. A. Midgley, V. Golovko and B. F. G. Johnson, *Angew. Chem., Int. Ed.,* **2006**, *45*, 4782.
95 J. Liu, K. S. Krishna, Y. B. Losovyj, S. Chattopadhyay, N. Lozova, J. T. Miller, J. J. Spivey and C. S. S. R. Kumar, *Chem. Eur. J.,* **2013**, *19*, 10201.
96 P. Buchwalter, J. Rosé and P. Braunstein, *Chem. Rev.,* **2014**, *115*, 28.
97 M.-S. Chen, Catalytically Active Gold Particles in *Handbook of Nanophysics: Nanoparticles and Quantum Dots* (Ed.: K. D. Sattler), CRC Press, Boca Raton, **2011**.
98 V. Voliani, *Update on Gold Nanoparticles: From Cathedral Windows to Nanomedicine*, Smithers Rapra, Shawbury, **2013**.
99 G. C. Bond, Introduction to the Physical and Chemical Properties of Gold in *Gold Nanoparticles for Physics, Chemistry and Biology* (Eds.: C. Louis, O. Pluchery), Imperial College Press, London, **2012**.
100 D. Seo and H. Song, Synthesis of Gold Nanoparticles in Liquid Phase in *Gold Nanoparticles for Physics, Chemistry and Biology* (Eds.: C. Louis, O. Pluchery), Imperial College Press, London, **2012**.
101 O. Pluchery, Optical Properties of Gold Nanoparticles in *Gold Nanoparticles for Physics, Chemistry and Biology* (Eds.: C. Louis, O. Pluchery), Imperial College Press, London, **2012**.
102 K. L. Kelly, E. Coronado, L. L. Zhao and G. C. Schatz, *J. Phys. Chem. B,* **2002**, *107*, 668.
103 W. J. Parak, L. Manna, F. C. Simmel, D. Gerion and P. Alivisatos, Quantum Dots in *Nanoparticles: From Theory to Application*, 2nd ed. (Ed.: G. Schmid), Wiley-VCH, Weinheim, **2010**.
104 T. Teranishi, I. Kiyokawa and M. Miyake, *Adv. Mater.,* **1998**, *10*, 596.
105 I. Pastoriza-Santos and L. M. Liz-Marzán, *Adv. Funct. Mater.,* **2009**, *19*, 679.
106 H. Tsunoyama, Y. Liu, T. Akita, N. Ichikuni, H. Sakurai, S. Xie and T. Tsukuda, *Catal. Surv. Asia,* **2011**, *15*, 230.
107 T. K. Sau and A. L. Rogach, Colloidal Synthesis of Noble Metal Nanoparticles of Complex Morphologies in *Complex-Shaped Metal Nanoparticles: Bottom-Up Syntheses and Applications* (Eds.: T. K. Sau, A. L. Rogach), Wiley-VCH Werlag & Co. KGaA, Weinheim, **2012**.
108 C. Louis, Chemical Preparation of Gold Nanoparticles on Surfaces in *Gold Nanoparticles for Physics, Chemistry and Biology* (Eds.: C. Louis, O. Pluchery), Imperial College Press, London, **2012**.

109 A. Barau, V. Budarin, A. Caragheorgheopol, R. Luque, D. Macquarrie, A. Prelle, V. Teodorescu and M. Zaharescu, *Catal. Lett.,* **2008**, *124*, 204.
110 M. Haruta, S. Tsubota, T. Kobayashi, H. Kageyama, M. J. Genet and B. Delmon, *J. Catal.,* **1993**, *144*, 175.
111 L. A. M. Hermans and J. W. Geus, Interaction Of Nickel Ions With Silica Supports During Deposition-Precipitation in *Stud. Surf. Sci. Catal., Vol. Volume 3* (Eds.: P. G. P. J. B. Delmon, G. Poncelet), Elsevier, **1979**, pp. 113.
112 L. Kesavan, R. Tiruvalam, M. H. A. Rahim, M. I. bin Saiman, D. I. Enache, R. L. Jenkins, N. Dimitratos, J. A. Lopez-Sanchez, S. H. Taylor, D. W. Knight, C. J. Kiely and G. J. Hutchings, *Science,* **2011**, *331*, 195.
113 G. J. Hutchings and C. J. Kiely, *Acc. Chem. Res.,* **2013**.
114 A. Dhakshinamoorthy and H. Garcia, *Chem. Soc. Rev.,* **2012**, *41*, 5262.
115 P. Hu, J. V. Morabito and C.-K. Tsung, *ACS Catal.,* **2014**, *4*, 4409.
116 M. Wen, K. Mori, T. Kamegawa and H. Yamashita, *Chem. Commun.,* **2014**, *50*, 11645.
117 G. Lu, S. Li, Z. Guo, O. K. Farha, B. G. Hauser, X. Qi, Y. Wang, X. Wang, S. Han, X. Liu, J. S. DuChene, H. Zhang, Q. Zhang, X. Chen, J. Ma, S. C. J. Loo, W. D. Wei, Y. Yang, J. T. Hupp and F. Huo, *Nat. Chem.,* **2012**, *4*, 310.
118 N. Toshima and T. Yonezawa, *New J. Chem.,* **1998**, *22*, 1179.
119 R. G. Chaudhuri and S. Paria, Gold-Based Core/Shell and Hollow Nanoparticles in *Kirk-Othmer Encyclopedia of Chemical Technology*, John Wiley & Sons, Inc., **2013**.
120 A. Roucoux, J. Schulz and H. Patin, *Chem. Rev.,* **2002**, *102*, 3757.
121 G. Viau, F. Fiévet-Vincent and F. Fiévet, *Solid State Ionics,* **1996**, *84*, 259.
122 J. Li, Q.-L. Zhu and Q. Xu, *Catal. Sci. Technol.,* **2015**, *5*, 525.
123 Y.-C. Lu, Z. Xu, H. A. Gasteiger, S. Chen, K. Hamad-Schifferli and Y. Shao-Horn, *J. Am. Chem. Soc.,* **2010**, *132*, 12170.
124 V. Petkov, B. N. Wanjala, R. Loukrakpam, J. Luo, L. Yang, C.-J. Zhong and S. Shastri, *Nano Lett.,* **2012**, *12*, 4289.
125 P. Venkatesan and J. Santhanalakshmi, *Chin. J. Catal.,* **2012**, *33*, 1306.
126 H. Dai, N. Cao, L. Yang, J. Su, W. Luo and G. Cheng, *J. Mater. Chem. A,* **2014**, *2*, 11060.
127 C. Fasciani, M. J. Silvero, M. A. Anghel, G. A. Argüello, M. C. Becerra and J. C. Scaiano, *J. Am. Chem. Soc.,* **2014**, *136*, 17394.
128 M. S. Holden, K. E. Nick, M. Hall, J. R. Milligan, Q. Chen and C. C. Perry, *RSC Adv.,* **2014**, *4*, 52279.
129 X.-Y. Liu, Y. Zhang, M.-X. Gong, Y.-W. Tang, T.-H. Lu, Y. Chen and J.-M. Lee, *J. Mater. Chem. A,* **2014**, *2*, 13840.
130 Ş. Neaţu, J. A. Maciá-Agulló, P. Concepción and H. Garcia, *J. Am. Chem. Soc.,* **2014**, *136*, 15969.
131 Y. Zhao, C. Ye, W. Liu, R. Chen and X. Jiang, *Angew. Chem., Int. Ed.,* **2014**, *53*, 8127.
132 F. Tao, M. E. Grass, Y. Zhang, D. R. Butcher, J. R. Renzas, Z. Liu, J. Y. Chung, B. S. Mun, M. Salmeron and G. A. Somorjai, *Science,* **2008**, *322*, 932.
133 M. Chen, D. Kumar, C.-W. Yi and D. W. Goodman, *Science,* **2005**, *310*, 291.
134 W. Hou, N. A. Dehm and R. W. J. Scott, *J. Catal.,* **2008**, *253*, 22.
135 D. I. Enache, J. K. Edwards, P. Landon, B. Solsona-Espriu, A. F. Carley, A. A. Herzing, M. Watanabe, C. J. Kiely, D. W. Knight and G. J. Hutchings, *Science,* **2006**, *311*, 362.

136 L. Guczi, A. Beck, A. Horváth, Z. Koppány, G. Stefler, K. Frey, I. Sajó, O. Geszti, D. Bazin and J. Lynch, *J. Mol. Catal. A: Chem.,* **2003**, *204–205*, 545.
137 N. Dimitratos, J. Lopez-Sanchez, D. Lennon, F. Porta, L. Prati and A. Villa, *Catal. Lett.,* **2006**, *108*, 147.
138 N. Dimitratos, J. A. Lopez-Sanchez, J. M. Anthonykutty, G. Brett, A. F. Carley, R. C. Tiruvalam, A. A. Herzing, C. J. Kiely, D. W. Knight and G. J. Hutchings, *Phys. Chem. Chem. Phys.,* **2009**, *11*, 4952.
139 A. J. Frank, J. Rawski, K. E. Maly and V. Kitaev, *Green Chem.,* **2010**, *12*, 1615.
140 A. F. Lee, C. V. Ellis, K. Wilson and N. S. Hondow, *Catal. Today,* **2010**, *157*, 243.
141 X. Gu, Z.-H. Lu, H.-L. Jiang, T. Akita and Q. Xu, *J. Am. Chem. Soc.,* **2011**, *133*, 11822.
142 M. Bowker, R. D. Smith and R. A. Bennett, *Surf. Sci.,* **2001**, *478*, L309.
143 X. Y. Liu, A. Wang, T. Zhang and C.-Y. Mou, *Nano Today,* **2013**, *8*, 403.
144 M. Turner, V. B. Golovko, O. P. H. Vaughan, P. Abdulkin, A. Berenguer-Murcia, M. S. Tikhov, B. F. G. Johnson and R. M. Lambert, *Nature,* **2008**, *454*, 981.
145 M. Gao, A. Lyalin and T. Taketsugu, *Catalysts,* **2011**, *1*, 18.
146 K. Okazaki, S. Ichikawa, Y. Maeda, M. Haruta and M. Kohyama, *Appl. Catal., A,* **2005**, *291*, 45.
147 J. T. Miller, A. J. Kropf, Y. Zha, J. R. Regalbuto, L. Delannoy, C. Louis, E. Bus and J. A. van Bokhoven, *J. Catal.,* **2006**, *240*, 222.
148 R. Kumar, A. Ghosh, C. R. Patra, P. Mukherjee and M. Sastry, Gold Nanoparticles Formed within Ordered Mesoporous Silica and on Amorphous Silica in *Nanotechnology in Catalysis, Vol. 1* (Eds.: B. Zhou, S. Hermans, G. A. Somorjai), Kluwer Academic/Plenum Publishers, New York, **2004**.
149 Q. Fu, H. Saltsburg and M. Flytzani-Stephanopoulos, *Science,* **2003**, *301*, 935.
150 C. J. Karwacki, P. Ganesh, P. R. C. Kent, W. O. Gordon, G. W. Peterson, J. J. Niu and Y. Gogotsi, *J. Mater. Chem. A,* **2013**, *1*, 6051.
151 S. Wang, K. Yin, Y. Zhang and H. Liu, *ACS Catal.,* **2013**, *3*, 2112.
152 K. Sun, J. Liu, N. Nag and N. D. Browning, *Catal. Lett.,* **2002**, *84*, 193.
153 M. Morad, M. Sankar, E. Cao, E. Nowicka, T. E. Davies, P. J. Miedziak, D. J. Morgan, D. W. Knight, D. Bethell, A. Gavriilidis and G. J. Hutchings, *Catal. Sci. Technol.,* **2014**, *4*, 3120.
154 G. L. Brett, Q. He, C. Hammond, P. J. Miedziak, N. Dimitratos, M. Sankar, A. A. Herzing, M. Conte, J. A. Lopez-Sanchez, C. J. Kiely, D. W. Knight, S. H. Taylor and G. J. Hutchings, *Angew. Chem., Int. Ed.,* **2011**, *50*, 10136.
155 A. Corma, *J. Catal.,* **2003**, *216*, 298.
156 T. F. Degnan Jr, *J. Catal.,* **2003**, *216*, 32.
157 G. Q. Lu and X. S. Zhao, Nanoporous Materials - An Overview in *Nanoporous Materials: Science and Engineering*, Imperial College Press, London, UK, **2004**.
158 A. B. Laursen, K. T. Højholt, L. F. Lundegaard, S. B. Simonsen, S. Helveg, F. Schüth, M. Paul, J.-D. Grunwaldt, S. Kegnæs, C. H. Christensen and K. Egeblad, *Angew. Chem., Int. Ed.,* **2010**, *49*, 3504.
159 N. E. Bogdanchikova, V. P. Petranovskii, R. Machorro M, Y. Sugi, V. M. Soto G and S. Fuentes M, *Appl. Surf. Sci.,* **1999**, *150*, 58.
160 N. Bogdanchikova, V. Petranovskii, S. Fuentes, E. Paukshtis, Y. Sugi and A. Licea-Claverie, *Materials Science and Engineering: A,* **2000**, *276*, 236.

161 J. Talebi, R. Halladj and S. Askari, *J. Mater. Sci.,* **2010**, *45*, 3318.
162 J. Čejka and D. Kubička, Zeolites and Other Micro- and Mesoporous Molecular Sieves in *Kirk-Othmer Encyclopedia of Chemical Technology*, John Wiley & Sons, Inc., **2010**.
163 M. A. Camblor and S. B. Hong, Synthetic Silicate Zeolites: Diverse Materials Accessible Through Geoinspiration in *Porous Materials* (Eds.: D. W. Bruce, D. O'Hare, R. I. Walton), John Wiley & Sons, Ltd, Chichester, **2011**.
164 E. J. P. Feijen, J. A. Martens and P. A. Jacobs, Hydrothermal Zeolite Synthesis in *Preparation of Solid Catalysts* (Eds.: G. Ertl, H. Knözinger, J. Weitkamp), Wiley-VCH, Weinheim, **1999**, pp. 262.
165 W. Loewenstein, *Am. Mineral.,* **1954**, *39*, 92.
166 D. B. Akolekar and S. K. Bhargava, *J. Mol. Catal. A: Chem.,* **2005**, *236*, 77.
167 S. L. James, *Chem. Soc. Rev.,* **2003**, *32*, 276.
168 O. K. Farha and J. T. Hupp, *Acc. Chem. Res.,* **2010**, *43*, 1166.
169 N. Stock and S. Biswas, *Chem. Rev.,* **2011**, *112*, 933.
170 S. T. Meek, J. A. Greathouse and M. D. Allendorf, *Adv. Mater.,* **2011**, *23*, 249.
171 H. Furukawa, K. E. Cordova, M. O'Keeffe and O. M. Yaghi, *Science,* **2013**, *341*, 974.
172 S. M. Cohen, *Chem. Rev.,* **2011**, *112*, 970.
173 Z. Wang and S. M. Cohen, *Chem. Soc. Rev.,* **2009**, *38*, 1315.
174 J. L. C. Rowsell and O. M. Yaghi, *J. Am. Chem. Soc.,* **2006**, *128*, 1304.
175 M. P. Suh, H. J. Park, T. K. Prasad and D.-W. Lim, *Chem. Rev.,* **2011**, *112*, 782.
176 K. Sumida, D. L. Rogow, J. A. Mason, T. M. McDonald, E. D. Bloch, Z. R. Herm, T.-H. Bae and J. R. Long, *Chem. Rev.,* **2011**, *112*, 724.
177 J. A. Mason, M. Veenstra and J. R. Long, *Chem. Sci.,* **2014**, *5*, 32.
178 S. El-Hankari, J. Huo, A. Ahmed, H. Zhang and D. Bradshaw, *J. Mater. Chem. A,* **2014**, *2*, 13479.
179 A. Torres-Knoop, R. Krishna and D. Dubbeldam, *Angew. Chem., Int. Ed.,* **2014**, *53*, 7774.
180 H.-L. Jiang, Y. Tatsu, Z.-H. Lu and Q. Xu, *J. Am. Chem. Soc.,* **2010**, *132*, 5586.
181 J. Gascon, A. Corma, F. Kapteijn and F. X. Llabrés i Xamena, *ACS Catal.,* **2014**, *4*, 361.
182 P. Garcia-Garcia, M. Muller and A. Corma, *Chem. Sci.,* **2014**, *5*, 2979.
183 A. Dhakshinamoorthy and H. Garcia, *ChemSusChem,* **2014**, n/a.
184 H.-T. Zhang, J.-W. Zhang, G. Huang, Z.-Y. Du and H.-L. Jiang, *Chem. Commun.,* **2014**, *50*, 12069.
185 C. He, K. Lu and W. Lin, *J. Am. Chem. Soc.,* **2014**, *136*, 12253.
186 N. C. Jeong, B. Samanta, C. Y. Lee, O. K. Farha and J. T. Hupp, *J. Am. Chem. Soc.,* **2011**, *134*, 51.
187 M. Kim, J. F. Cahill, H. Fei, K. A. Prather and S. M. Cohen, *J. Am. Chem. Soc.,* **2012**, *134*, 18082.
188 D. Cunha, M. Ben Yahia, S. Hall, S. R. Miller, H. Chevreau, E. Elkaïm, G. Maurin, P. Horcajada and C. Serre, *Chem. Mater.,* **2013**, *25*, 2767.
189 P. Valvekens, F. Vermoortele and D. De Vos, *Catal. Sci. Technol.,* **2013**, *3*, 1435.
190 O. M. Yaghi, M. O'Keeffe, N. W. Ockwig, H. K. Chae, M. Eddaoudi and J. Kim, *Nature,* **2003**, *423*, 705.

191 N. W. Ockwig, O. Delgado-Friedrichs, M. O'Keeffe and O. M. Yaghi, *Acc. Chem. Res.,* **2005**, *38*, 176.
192 N. C. Burtch, H. Jasuja and K. S. Walton, *Chem. Rev.,* **2014**, *114*, 10575.
193 I. J. Kang, N. A. Khan, E. Haque and S. H. Jhung, *Chem. Eur. J.,* **2011**, *17*, 6437.
194 C. Serre, F. Millange, C. Thouvenot, M. Noguès, G. Marsolier, D. Louër and G. Férey, *J. Am. Chem. Soc.,* **2002**, *124*, 13519.
195 G. Ferey, C. Mellot-Draznieks, C. Serre, F. Millange, J. Dutour, S. Surble and I. Margiolaki, *Science,* **2005**, *309*, 2040.
196 J. H. Cavka, S. Jakobsen, U. Olsbye, N. Guillou, C. Lamberti, S. Bordiga and K. P. Lillerud, *J. Am. Chem. Soc.,* **2008**, *130*, 13850.
197 S. S.-Y. Chui, S. M.-F. Lo, J. P. H. Charmant, A. G. Orpen and I. D. Williams, *Science,* **1999**, *283*, 1148.
198 K. S. Park, Z. Ni, A. P. Côté, J. Y. Choi, R. Huang, F. J. Uribe-Romo, H. K. Chae, M. O'Keeffe and O. M. Yaghi, *Proc. Natl. Acad. Sci.,* **2006**, *103*, 10186.
199 M. Meilikhov, K. Yusenko, D. Esken, S. Turner, G. Van Tendeloo and R. A. Fischer, *Eur. J. Inorg. Chem.,* **2010**, *2010*, 3701.
200 M. E. Silvestre, M. Franzreb, P. G. Weidler, O. Shekhah and C. Wöll, *Adv. Funct. Mater.,* **2013**, *23*, 1210.
201 S. Proch, J. Herrmannsdörfer, R. Kempe, C. Kern, A. Jess, L. Seyfarth and J. Senker, *Chem. Eur. J.,* **2008**, *14*, 8204.
202 L. Chen, Y. Peng, H. Wang, Z. Gu and C. Duan, *Chem. Commun.,* **2014**, *50*, 8651.
203 T. Tsuruoka, H. Kawasaki, H. Nawafune and K. Akamatsu, *ACS Appl. Mater. Interfaces,* **2011**, *3*, 3788.
204 H.-L. Jiang, B. Liu, T. Akita, M. Haruta, H. Sakurai and Q. Xu, *J. Am. Chem. Soc.,* **2009**, *131*, 11302.
205 Z. Sun, G. Li, L. Liu and H.-o. Liu, *Catal. Commun.,* **2012**, *27*, 200.
206 Y. Luan, Y. Qi, H. Gao, N. Zheng and G. Wang, *J. Mater. Chem. A,* **2014**, *2*, 20588.
207 R. Wu, X. Qian, K. Zhou, H. Liu, B. Yadian, J. Wei, H. Zhu and Y. Huang, *J. Mater. Chem. A,* **2013**, *1*, 14294.
208 H.-j. Zhang, S.-d. Qi, X.-y. Niu, J. Hu, C.-l. Ren, H.-l. Chen and X.-g. Chen, *Catal. Sci. Technol.,* **2014**, *4*, 3013.
209 J. He, J. Wang, Y. Chen, J. Zhang, D. Duan, Y. Wang and Z. Yan, *Chem. Commun.,* **2014**, *50*, 7063.
210 Y. E. Cheon and M. P. Suh, *Angew. Chem., Int. Ed.,* **2009**, *48*, 2899.
211 L. B. Vilhelmsen and D. S. Sholl, *J. Phys. Chem. Lett.,* **2012**, *3*, 3702.
212 M. Zhao, K. Deng, L. He, Y. Liu, G. Li, H. Zhao and Z. Tang, *J. Am. Chem. Soc.,* **2014**, *136*, 1738.
213 Y. Huang, Z. Zheng, T. Liu, J. Lü, Z. Lin, H. Li and R. Cao, *Catal. Commun.,* **2011**, *14*, 27.
214 T. T. Dang, Y. Zhu, J. S. Y. Ngiam, S. C. Ghosh, A. Chen and A. M. Seayad, *ACS Catal.,* **2013**, *3*, 1406.
215 T. Thanh Dang, A. Chen and A. Majeed Seayad, *RSC Adv.,* **2014**, *4*, 30019.
216 L. Shen, W. Wu, R. Liang, R. Lin and L. Wu, *Nanoscale,* **2013**, *5*, 9374.
217 D. Zhang, F. Ye, Y. Guan, Y. Wang and E. J. M. Hensen, *RSC Adv.,* **2014**, *4*, 39558.
218 J. Long, H. Liu, S. Wu, S. Liao and Y. Li, *ACS Catal.,* **2013**, *3*, 647.
219 Q.-L. Zhu, J. Li and Q. Xu, *J. Am. Chem. Soc.,* **2013**, *135*, 10210.

220 R. Cao, Y. Huang, Y. Zhang, X. Chen, D. Wu and Z. Yi, *Chem. Commun.,* **2014**.
221 L. Song, J. Zhang, L. Sun, F. Xu, F. Li, H. Zhang, X. Si, C. Jiao, Z. Li, S. Liu, Y. Liu, H. Zhou, D. Sun, Y. Du, Z. Cao and Z. Gabelica, *Energy Environ. Sci.,* **2012**, *5*, 7508.
222 F. Kleitz, Ordered Microporous and Mesoporous Materials in *Nanoscale Materials in Chemistry*, 2nd ed. (Eds.: K. J. Klabunde, R. M. Richards), John Wiley & Sons, Inc., Hoboken, **2009**.
223 C. L. Chen and C. Y. Mou, Mesoporous Materials as Catalyst Supports in *Nanotechnology in Catalysis, Vol. 1* (Eds.: B. Zhou, S. Hermans, G. A. Somorjai), Kluwer Academic/Plenum Publishers, New York, **2004**.
224 W. Xuan, C. Zhu, Y. Liu and Y. Cui, *Chem. Soc. Rev.,* **2012**, *41*.
225 A. J. J. Koekkoek, H. Xin, Q. Yang, C. Li and E. J. M. Hensen, *Micro. Meso. Mater.,* **2011**, *145*, 172.
226 Z. Kónya, V. F. Puntes, I. Kiricsi, J. Zhu, J. W. Ager, M. K. Ko, H. Frei, P. Alivisatos and G. A. Somorjai, *Chem. Mater.,* **2003**, *15*, 1242.
227 C.-W. Chiang, A. Wang and C.-Y. Mou, *Catal. Today,* **2006**, *117*, 220.
228 K. Na, S. Alayoglu, R. Ye and G. A. Somorjai, *J. Am. Chem. Soc.,* **2014**, *136*, 17207.
229 C. M. A. Parlett, L. J. Durndell, A. Machado, G. Cibin, D. W. Bruce, N. S. Hondow, K. Wilson and A. F. Lee, *Catal. Today,* **2014**, *229*, 46.
230 M. Chatterjee, H. Kawanami, M. Sato, A. Chatterjee, T. Yokoyama and T. Suzuki, *Adv. Synth. Catal.,* **2009**, *351*, 1912.
231 A. Quintanilla, S. García-Rodríguez, C. M. Domínguez, S. Blasco, J. A. Casas and J. J. Rodriguez, *Appl. Catal., B,* **2012**, *111–112*, 81.
232 A. Abad, A. Corma and H. García, *Chem. Eur. J.,* **2008**, *14*, 212.
233 H. Liu, Y. Liu, Y. Li, Z. Tang and H. Jiang, *J. Phys. Chem. C.,* **2010**, *114*, 13362.
234 A. Quintanilla, V. C. L. Butselaar-Orthlieb, C. Kwakernaak, W. G. Sloof, M. T. Kreutzer and F. Kapteijn, *J. Catal.,* **2010**, *271*, 104.
235 J. A. Lopez-Sanchez, N. Dimitratos, C. Hammond, G. L. Brett, L. Kesavan, S. White, P. Miedziak, R. Tiruvalam, R. L. Jenkins, A. F. Carley, D. Knight, C. J. Kiely and G. J. Hutchings, *Nat. Chem.,* **2011**, *3*, 551.
236 H. H. Kung, M. C. Kung and C. K. Costello, *J. Catal.,* **2003**, *216*, 425.
237 M. Haruta, T. Kobayashi, H. Sano and N. Yamada, *Chem. Lett.,* **1987**, *16*, 405.
238 J. Gong and C. B. Mullins, *Acc. Chem. Res.,* **2009**, *42*, 1063.
239 D. Widmann and R. J. Behm, *Acc. Chem. Res.,* **2014**, *47*, 740.
240 H. Wu, G. Pantaleo, A. Venezia and L. Liotta, *Catalysts,* **2013**, *3*, 774.
241 A. A. Herzing, C. J. Kiely, A. F. Carley, P. Landon and G. J. Hutchings, *Science,* **2008**, *321*, 1331.
242 L. Qi, C. Tang, L. Zhang, X. Yao, Y. Cao, L. Liu, F. Gao, L. Dong and Y. Chen, *Appl. Catal., B,* **2012**, *127*, 234.
243 J. Lu, C. Aydin, N. D. Browning and B. C. Gates, *Angew. Chem., Int. Ed.,* **2012**, *51*, 5842.
244 A. Aijaz, A. Karkamkar, Y. J. Choi, N. Tsumori, E. Rönnebro, T. Autrey, H. Shioyama and Q. Xu, *J. Am. Chem. Soc.,* **2012**, *134*, 13926.
245 Y. Zhou, Z. Xiang, D. Cao and C.-j. Liu, *Ind. Eng. Chem. Res.,* **2014**, *53*, 1359.
246 X. Zhang, X. Ke and H. Zhu, *Chem. Eur. J.,* **2012**, *18*, 8048.
247 G. Zhan, Y. Hong, F. Lu, A.-R. Ibrahim, M. Du, D. Sun, J. Huang, Q. Li and J. Li, *J. Mol. Catal. A: Chem.,* **2013**, *366*, 215.
248 C. Xu, Z. Wang, X. Huangfu and H. Wang, *RSC Adv.,* **2014**, *4*, 27337.

249 J. Zhu, J. L. Figueiredo and J. L. Faria, *Catal. Commun.,* **2008**, *9*, 2395.
250 V. R. Choudhary, D. K. Dumbre and S. K. Bhargava, *Ind. Eng. Chem. Res.,* **2009**, *48*, 9471.
251 J. Ni, W.-J. Yu, L. He, H. Sun, Y. Cao, H.-Y. He and K.-N. Fan, *Green Chem.,* **2009**, *11*, 756.
252 V. Peneau, Q. He, G. Shaw, S. A. Kondrat, T. E. Davies, P. Miedziak, M. Forde, N. Dimitratos, C. J. Kiely and G. J. Hutchings, *Phys. Chem. Chem. Phys.,* **2013**, *15*, 10636.
253 J. Pritchard, M. Piccinini, R. Tiruvalam, Q. He, N. Dimitratos, J. A. Lopez-Sanchez, D. J. Morgan, A. F. Carley, J. K. Edwards, C. J. Kiely and G. J. Hutchings, *Catal. Sci. Technol.,* **2013**, *3*, 308.
254 J. Pritchard, L. Kesavan, M. Piccinini, Q. He, R. Tiruvalam, N. Dimitratos, J. A. Lopez-Sanchez, A. F. Carley, J. K. Edwards, C. J. Kiely and G. J. Hutchings, *Langmuir,* **2010**, *26*, 16568.
255 H. Wang, W. Kong, W. Zhu, L. Wang, S. Yang and F. Liu, *Catal. Commun.,* **2014**, *50*, 87.
256 A. L. Tarasov, L. M. Kustov, V. I. Isaeva, A. N. Kalenchuk, I. V. Mishin, G. I. Kapustin and V. I. Bogdan, *Kinetics and Catalysis,* **2011**, *52*, 273.
257 A. L. Tarasov, L. M. Kustov, A. A. Bogolyubov, A. S. Kiselyov and V. V. Semenov, *Appl. Catal., A,* **2009**, *366*, 227.
258 Rhodia Chimie, P. Metivier, **2001,** *Method for preparing a 4-hydroxybenzaldehyde and derivatives,* US Patent 6,184,421.
259 A. Maclennan, A. Banerjee, Y. Hu, J. T. Miller and R. W. J. Scott, *ACS Catal.,* **2013**, *3*, 1411.
260 A. Maclennan, A. Banerjee and R. W. J. Scott, *Catal. Today,* **2013**, *207*, 170.
261 T. Balcha, J. R. Strobl, C. Fowler, P. Dash and R. W. J. Scott, *ACS Catal.,* **2011**, *1*, 425.
262 L. J. Durndell, C. M. A. Parlett, N. S. Hondow, K. Wilson and A. F. Lee, *Nanoscale,* **2013**, *5*, 5412.
263 B. N. Zope, D. D. Hibbitts, M. Neurock and R. J. Davis, *Science,* **2010**, *330*, 74.
264 K. Zhu, J. Hu and R. Richards, *Catal. Lett.,* **2005**, *100*, 195.
265 F. Brühne and E. Wright, Benzaldehyde in *Ullmann's Encyclopedia of Industrial Chemistry, Vol. 5*, 7th ed., Wiley-VCH Verlag GmbH & Co. KGaA, **2011**, pp. 223.
266 J. L. Opgrande, E. Brown, M. Hesser and J. Andrews, Benzaldehyde in *Kirk-Othmer Encyclopedia of Chemical Technology*, John Wiley & Sons, Inc., **2003**.
267 J.-P. Vidal, Vanillin in *Kirk-Othmer Encyclopedia of Chemical Technology*, John Wiley & Sons, Inc., **2006**.
268 R. G. Eilerman, Cinnamic Acid, Cinnamaldehyde, and Cinnamyl Alcohol in *Kirk-Othmer Encyclopedia of Chemical Technology*, John Wiley & Sons, Inc., **2000**.
269 R. P. Schulz, J. Blumenstein and C. Kohlpaintner, Crotonaldehyde and Crotonic Acid in *Ullmann's Encyclopedia of Industrial Chemistry*, Wiley-VCH Verlag GmbH & Co. KGaA, **2000**.
270 Yissum Research Development Company of the Hebrew University of Jerusalem, A. Levitzki, A. Gazit, M. Chorev and C. Gilon, **1995,** *Pharmaceutical compositions comprising benzylidene-and cinnamylidene-malononitrile derivatives for the inhibition of proliferative processes in mammalian cells, certain such novelcompounds and their preparation,* Canada Patent CA 1,334,826.

271 M. T. Musser, Cyclohexanol and Cyclohexanone in *Ullmann's Encyclopedia of Industrial Chemistry*, Wiley-VCH Verlag GmbH & Co. KGaA, **2011**.
272 W. B. Fisher and J. F. VanPeppen, Cyclohexanol and Cyclohexanone in *Kirk-Othmer Encyclopedia of Chemical Technology*, John Wiley & Sons, Inc., **2000**.
273 M. I. bin Saiman, G. L. Brett, R. Tiruvalam, M. M. Forde, K. Sharples, A. Thetford, R. L. Jenkins, N. Dimitratos, J. A. Lopez-Sanchez, D. M. Murphy, D. Bethell, D. J. Willock, S. H. Taylor, D. W. Knight, C. J. Kiely and G. J. Hutchings, *Angew. Chem., Int. Ed.,* **2012**, *51*, 5981.
274 S. Ghosh, S. S. Acharyya, D. Tripathi and R. Bal, *J. Mater. Chem. A,* **2014**, *2*, 15726.
275 S. A. C. Carabineiro, L. M. D. R. S. Martins, M. Avalos-Borja, J. G. Buijnsters, A. J. L. Pombeiro and J. L. Figueiredo, *Appl. Catal., A,* **2013**, *467*, 279.
276 J. Liu, R. Liu, H. Li, W. Kong, H. Huang, Y. Liu and Z. Kang, *Dalton Trans.,* **2014**, *43*, 12982.
277 A. Alshammari, A. Koeckritz, V. N. Kalevaru, A. Bagabas and A. Martin, *ChemCatChem,* **2012**, *4*, 1330.
278 Y. Liu, H. Tsunoyama, T. Akita, S. Xie and T. Tsukuda, *ACS Catal.,* **2010**, *1*, 2.

Chapter 2: Experimental

This chapter will cover the fundamental theory and application of techniques used within this thesis for the synthesis of materials, catalytic application and thorough characterisation. Through these techniques, it will be possible to generate new nanoparticle-based materials and comprehend their chemical, physical and catalytic properties. Where applicable, general procedures will be included in order to describe the synthetic processes and preparation methods used for characterisation of materials. Detailed synthetic procedures, calculations and preparation methods will be presented in the respective results chapters. All supplementary data and raw data files are stored electronically and coded to the laboratory notebook codes of the corresponding experiments.

2.1 Synthetic Techniques

The following experimental techniques describe the theory and practice in the synthesis of solid materials for subsequent use as catalysts.

2.1.1 Hydrothermal Synthesis

The synthesis of nanoporous materials can be achieved through a variety of different synthetic techniques. Hydrothermal synthesis is one of the oldest methods and synonymous with zeolite synthesis.[1-2] As earlier described in *Section 1.2.5.1*, zeolites are formed naturally in geographical areas subject to volcanic activity where temperatures and pressures are elevated and there is a large presence of moisture. In fact, whilst many of the naturally occurring zeolites have been reproduced in the lab, there are some examples of novel artificial structures which aren't known to exist in nature. Hydrothermal synthesis is a laboratory technique that goes some way to reproducing these conditions in a controlled and scientific manner, where an aqueous sol or gel is heated above the boiling point of water in a sealed steel autoclave to reach high pressures and temperatures. Although this synthetic technique is useful for the synthesis of microporous materials, it can also be used for the facile generation of dense phase inorganic materials.

As well as zeolites, it is possible to synthesise zeotypes and other microporous materials through hydrothermal methods. The technique is most applicable to porous materials with purely inorganic secondary building units due to the facile solubility of precursors in aqueous solutions. As such, inorganic-organic hybrid materials are often not suitable for these methods due to the low solubility of organic substituents. Some exceptions can be found where the organic molecules are particularly polar, or if acidic/charged functional groups facilitate aqueous dissolution. Porosity is generally introduced into materials through the use of structure directing agents such as amines, quaternary ammonium salts or even metal cations.

In this work, hydrothermal methods were used solely for the synthesis of inorganic nanoporous materials. Steel autoclaves are of a custom design as per the schematic in Figure 2.1.

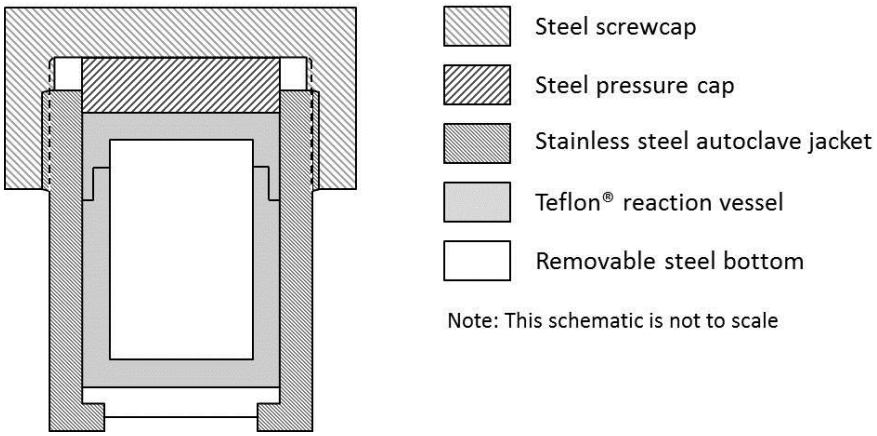

Figure 2.1 Schematic of custom-made hydrothermal autoclave with PTFE reaction liner (not to scale)

In a typical experiment, all precursors are weighed into the internal PTFE liner and the solvent or liquid precursors added to form a sol. The liners are sealed within a steel autoclave unit to maintain pressure upon heating, then placed in an oven at a set temperature for a designated amount of time. After the heating phase, the autoclave units are allowed to cool naturally to room temperature before the units are opened and the solid products collected by filtration. Crystalline materials are generally collected and analysed by X-ray diffraction as elaborated in *Section 2.3.1*.

2.1.2 Solvothermal Synthesis

Solvothermal synthesis is an extension of hydrothermal synthesis but with the use of an organic solvent rather than water. This is most suitable when using organometallic precursors or when organic moieties are being introduced into hybrid materials such as coordination polymers. The description of 'solvothermal synthesis' is more broadly used than hydrothermal synthesis and can, especially in the literature related to MOF synthesis, refer to the precipitation of self-assembled materials from solvents heated to temperatures above ambient RT. As with hydrothermal techniques that require heating above the boiling point of water to achieve high pressures, so also is the traditional definition for solvothermal methods;[3-4] however, for the sake of inclusivity of the literature, the broader semantics of the phrase shall be observed.

Solvothermal syntheses were used mainly in this work for the synthesis of MOFs below the boiling point of respective solvents, mostly DMF (BP 153 °C). As such, reactions could be carried out in glass reaction bottles with thermally stable plastic screw-top lids (≤ 140 °C). The bottle sizes were chosen so as not to fill more than 60 % of the volume with solvent so that any small internal build-up of pressure was negligible with respect to the strength of the bottle. Care was taken not to use any plastic fittings with defects or cracks by performing a visual inspection. It should be noted that solvothermal reactions heating close to or above the BP of the solvent should employ the use of mechanically stable steel autoclaves as outlined in the previous section.

2.1.3 Activation of MOFs

In the synthesis of highly porous MOFs, the pores are populated with solvent molecules. Where DMF is used as a solvent (and some others), the molecules can often be strongly coordinating to vacant sites on metal centres, as well as just pore-filling, and require thermal activation to remove the excess solvent to reveal the total internal surface areas that may be blocked without thorough evacuation. In some cases, simple heating of the MOF materials can remove coordinated solvents, although this can require a temperature close to or higher than the thermal stability of the framework. To minimise the detrimental effects on the MOF framework, heating can be performed in a vacuum; alternatively, pre-soaking in a solvent that can displace the DMF for

more labile coordinating molecules can allow for activation at much lower temperatures.

In this work, MOF materials are synthesised in DMF but washed thoroughly with methanol twice before drying in preparation for catalysis. Deposition of nanoparticles is also performed in methanol, which has the secondary function of acting as a further washing step to displace any fractions of DMF that may still be present. Performing thermogravimetric analysis (see *Section 2.3.6*) on samples can easily reveal temperatures at which different solvents are removed and the thermal stability of the frameworks.

2.1.4 Synthesis of Nanoparticle-Polymer Colloids

The merits of polymer stabilised colloids have been discussed in the previous chapter. The polarity and presence of heteroatoms in the polymers are useful, not just for the stabilisation of small metal nanoparticles, but also for forming interactions with a support surface. This technique was used in this work for preparing and depositing nanoparticles onto the surface of metal-organic frameworks, where the presence of functional organic groups from pendant organic linkers can enhance the interactions with the polymer stabilising agents.

Nanoparticle colloids are formed either in aqueous or methanolic solutions. A high dilution mixture is prepared by adding a small amount of an aqueous metal salt solution to a large amount of the water or methanol and stirred. An aqueous solution of PVP is also added at a designated metal:PVP ratio. A fresh batch of sodium borohydride ($NaBH_4$) solution (0.1 M) is prepared as a reducing agent and added dropwise to the vigorously stirred solution to generate the nanoparticle colloid. For platinum or palladium, solutions start off a pale red or brown colour respectively. After addition of the reducing agent, the colours intensify to give dark grey and dark grey-brown solutions. For the case of gold, a pale yellow solution turns to burgundy red upon reduction before turning very quickly to a cherry red at a point when the nanoparticles reach a size for effective LSPR to be observed from the solution. Solutions are left to stir to allow for complete reduction of salts and degradation of excess hydride salts, before direct addition of a MOF support to the solution. Overnight stirring is

usually sufficient for complete deposition of nanoparticles to the MOF particle surfaces, which are then collected and dried for use as a catalyst.

2.2 Catalytic Techniques

The following experimental techniques cover the theory and set-up of all equipment related to catalytic reactions and the analyses of associated samples.

2.2.1 Reactions in the Batch

Although there are many complex designs for reactors and reaction set-up to optimise the chemical engineering - with factors such as mass transfer and fluid dynamics in mind - this work will focus on reactions in simple batch reactors.[5] Reactions with a gaseous reactant such as O_2 require high pressure steel reactors, whereas reactions with simple liquid or soluble solid reactants require ambient pressure batch conditions in standard laboratory glassware. When carrying out high pressure or ambient pressure batch reactions, the ideal reactor should adhere to the following conditions:[6]

1. Reactants are quickly charged, mixed, and brought to temperature at the beginning of the reaction cycle.
2. Mixing and heat transfer are sufficient to assure that the batch remains completely uniform in temperature and composition throughout the reaction cycle.
3. The operating temperature is held constant.

A summary of batch reactions and conditions applicable to this work follows.

2.2.1.1 High Pressure Batch Reactions

Aerobic oxidation reactions require high pressure steel batch reactors in order to achieve good concentrations of O_2 in the reactor and encourage dissolution of the gas into the liquid phase. When a reactor contains both a liquid and gas phase, the composition of each phase can vary depending on the thermodynamic equilibriums at defined temperatures and pressures.[7] The concentration of an ambient gas phase reactant in solution increases proportionally to the pressure as defined by Henry's law (Equation 2.1) where

P_B is the partial pressure of gaseous reactant B, b_B is the molality (moles of B per kg of solvent) of reactant B in a given solvent and K_B is a constant associated with the solvent, pressure and temperature of the system.

$$P_B = b_B K_B \qquad \textbf{Equation 2.1}$$

As the active site is on a solid catalyst immersed in the liquid phase, it is imperative to push the equilibrium to high dissolution in the liquid phase to achieve the catalytic potential. This is achieved through the application of high pressures.

The batch reactor used was a custom design from Cambridge Reactor Design Ltd. (see Figure 2.2), with a 50 mL PTFE liner and total internal capacity of 75 mL. The reactor top was fitted with ports for an electronic thermostat, a sampling port with internal dip tube, a manometer for pressures up to 40 bar and a gas inlet/outlet for pressurising and depressurising the reactor. The reactor was stirred by magnetic stirring from an external stirrer plate beneath the reactor and heated through the same plate with a metal heating jacket covering the bottom section of the reactor.

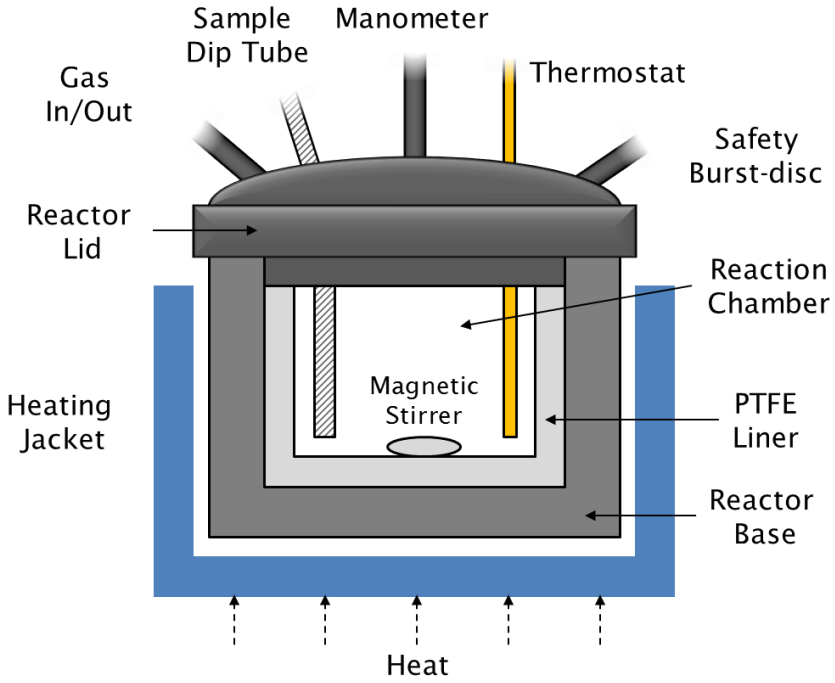

Figure 2.2 Schematic of high pressure batch reactor (not to scale)

A typical loading procedure involved measurement of all liquid and solid components to the PTFE liner with subsequent sealing of the reactor. Once all ports had been checked to be closed, the reactor was slowly pressurised to 20 bar with dry air (20 % O_2 by volume) and secured to a stand. The heater/stirrer plate and heating jacket was positioned in contact with the reactor and set to heat to a designated temperature. All reaction timings were commenced once the reactor has reached temperature. Reaction mixtures commonly consist of a solid powdered catalyst, solvent, reactant and internal standard for quantitative analysis.

2.2.1.2 Batch Reactions at Ambient Pressure

At ambient pressures, the thermodynamics of a reaction are much more easily controlled. Reactions are commonly carried out in glass round bottom flasks (RBF) with attached reflux condensers (even if not heated to reflux) and heated to temperatures in an oil bath or heating mantle. Due to good heat transfer from the heating source to the liquid-phase reaction mixture, an equilibrium at working reaction conditions can be achieved quickly at the initial stages of the reaction as per the requirements for an ideal batch reactor set out in *Section 2.2.1*. With oxidation reactions in mind, this set-up is suitable for liquid-phase oxidants such as TBHP and H_2O_2. The use of a thermostat can be useful for maintaining working temperatures although more rudimentary manual temperature regulation can be used as an alternative. A reaction mixture will commonly consist of a solid powdered catalyst, solvent, reactant, oxidant and internal standard for quantitative analysis by gas chromatography.

2.2.2 Gas Chromatography (GC)

Gas chromatography (GC)[8-10] is a technique used for analysing components of a mixture of chemicals by separating them in the gas phase. As with all chromatographic techniques, a stationary phase is employed in the form of a capillary column. This is contained within an oven for regulating the temperature and adjoined to an injector port at the inlet and a detector at the outlet (Figure 2.3 A).

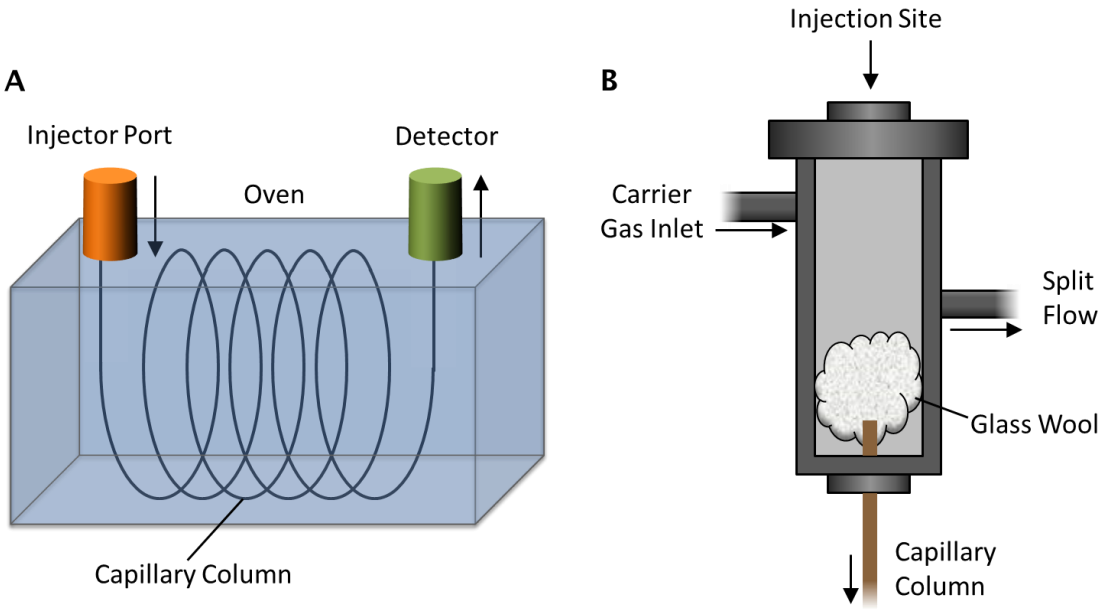

Figure 2.3 Schematic of gas chromatograph and the injector port

The injector port (Figure **2.3** B) usually consists of a septum on top to allow for facile injection of a liquid (or gas) sample into a heated chamber to volatilise the components (so should be heated to higher than the boiling point of the solvent and components). Glass or quartz wool is usually packed into the chamber to capture any heavy organic or particulate impurities, which would clog or pollute the column. A carrier gas inlet allows for flow of an inert gas such as helium or argon into the chamber to act as the mobile phase to carry the sample through the column. A split flow is a common feature on the injector port, although used in varying degrees depending on the type of sample being analysed. The function of the split flow is to reduce the concentration of sample entering the column by splitting the flow so that some of the sample gas is removed as exhaust gases; a split of 50:1 will split the flow volume by the same ratio with the smaller fraction entering the column

and the larger fraction leaving as exhaust waste. This can increase the lifetime of the column by reducing the exposure to sample chemicals.

Column properties can vary depending on the physical properties of the components that need to be separated. The most common columns employed contain a non-polar methylated silicone stationary phase functionalised with phenyl groups (1-5 %) that separate components largely on boiling point with some minor π-interactions between aromatic components and the column substituents.[11] It is also possible to gain specialist columns for separating chiral molecules by employing a chiral stationary phase, as well as other specially design columns, although a standard 5 % diphenyl silicone column (Elite-5; PerkinElmer) was sufficient for separations of components for analysis in this project.

There are a range of detectors that can be employed to analyse the outlet gas stream such as flame ionisation detectors (FID), mass-spectrometry detectors (MS) and thermal conductivity detectors (TCD). FIDs are widely applicable to most organic solutes with calorific value as the components are burnt upon reaching the detector, producing ions which are then detected by a metal probe with an applied voltage. The signal is detected by a change in current caused by the flow of ions to the probe, resulting in a peak on the chromatograph. The fluctuation in current is proportional to the rate of ionisation and hence the concentration of the component and its ionisation potential. Thus, for FIDs to be used quantitatively, calibrations need to be performed for each component to calculate their respective response factors (R_f).

Mass spectrometry detectors are also quite versatile and consist ultimately of a MS attached to the gas outlet of the GC. A quadrupolar MS instrument consists of four rods with opposing rf and dc fields on opposite rods. Ions pass down the chamber between each of the four rods as the voltages are sweeped to separate ions based on *m/z* values.[11-14] The outlet gas stream exits to the ion chamber *via* an ion source and is continually analysed with the output measured as a function of ion count or counts per second. As a component exits the column, a dramatic increase in ions is detected resulting in a peak with an associated mass spectrum. This gives the added benefit of having data to help identify the component and can be useful when a mixture contains some unknown compounds.

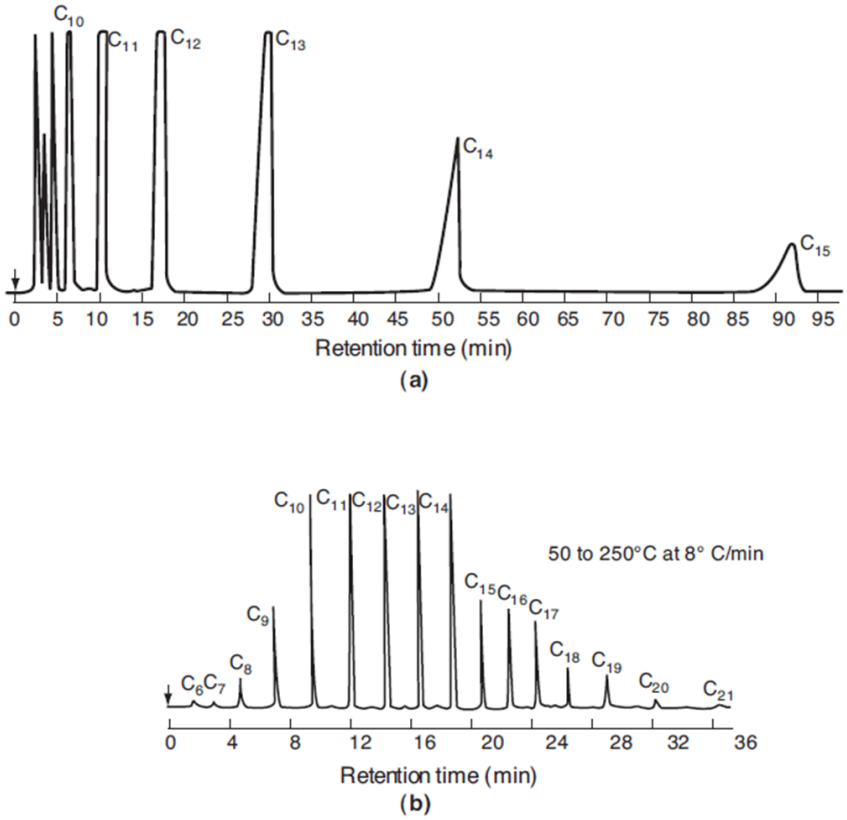

Figure 2.4 Example of a GC trace of hydrocarbon standards using an isothermal method (a) and a temperature programmed method (b)[9]

As much as the choice and setup of the hardware is important for the separation of components, the operating conditions are also key to achieving good quality resolution and component separation. The oven can be set to a single temperature for the duration of the experiment (isothermal) or initiated at a lower temperature and ramped at a specified rate to finish at a higher temperature (temperature-programmed) (Figure 2.4). This is ideal for attaining good resolution if there are multiple components with low boiling points.

2.2.2.1 Quantitative Analysis by GC

In this work, GC is used predominantly for analysing samples of catalysis reactions by monitoring conversions of starting materials and yields of products. Quantitative analysis is facilitated be performing calibrations with an internal standard to determine response factors (R_f) of each component in the system. A graph of peak area ratios against molar ratios as per Equation 2.2 gives a straight line where the gradient is the R_f.

$$\frac{peak\ area\ (A)}{peak\ area\ (IS)} = R_f \frac{moles\ (A)}{moles\ (IS)}$$ **Equation 2.2**

Figure 2.5 shows an example calibration plot of cinnamyl alcohol against an internal standard of chlorobenzene with a response factor of 1.4918. Molar quantities of components in real samples can then be calculated from the peak integrals directly by using Equation 2.3 once the R_f has been calculated.

$$moles\ (A) = \frac{moles\ (IS) \times peak\ area\ (A)}{R_f\ \times\ peak\ area\ (IS)}$$ **Equation 2.3**

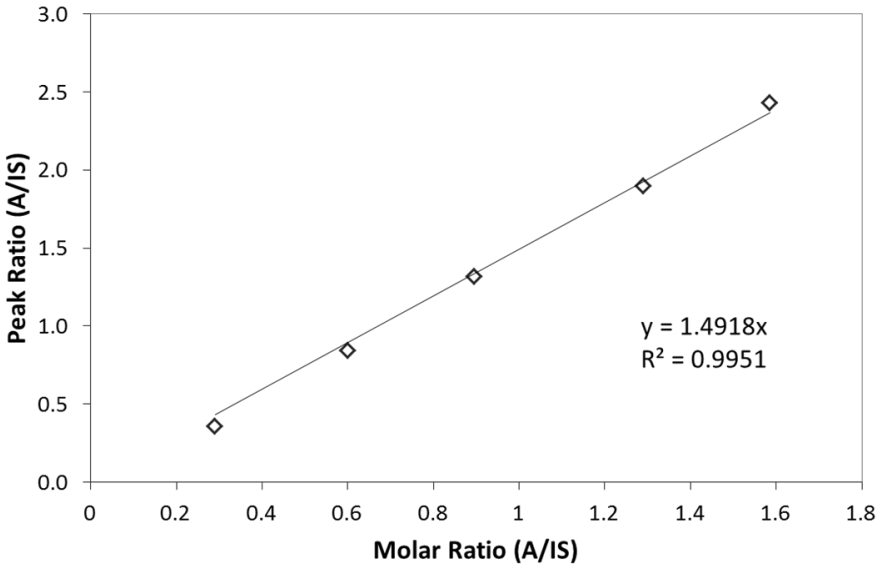

Figure 2.5 Example calibration of cinnamyl alcohol (A) against chlorobenzene (IS)

Conversions and selectivities are calculated according to Equation 2.4 and Equation 2.5 respectively where *i* and *f* subscripts refer to initial and final quantities. Mass balances compare the moles of known products to the initial moles of the reactant to determine if any undetectable products have formed, or if loss of reactant - other than the generation of products - has occurred.

$$Conversion\ (\%) = \frac{Reactant_i\ (mol) - Reactant_f\ (mol)}{Reactant_i\ (mol)} \times 100 \quad \textbf{Equation 2.4}$$

$$Selectivity\ (\%) = \frac{Product\ (mol)}{Reactant_i\ (mol) - \ Reactant_f\ (mol)} \times 100 \quad \textbf{Equation 2.5}$$

$$Mass\ Balance\ (\%) = \frac{\sum Products\ (mol)}{Reactant_i\ (mol)} \quad \textbf{Equation 2.6}$$

Once conversions and selectivities have been determined, individual yields of products, in terms of mol %, can then be calculated simply by multiplying conversion by selectivity as in Equation 2.7 assuming a quantitative mass balance is achieved.

$$Yield\ (mol\ \%) = Conversion\ (\%) \times Selectivity\ (\%) \quad \textbf{Equation 2.7}$$

2.3 Characterisation Techniques

The following experimental techniques cover a range of methods for characterising the physical, structural and chemical properties of all synthesised materials. As such, conclusions can be drawn as to the stability and integrity of synthesised materials as well as paving the way for drawing structure-property relationships from results obtained from application in catalytic processes.

2.3.1 Powder X-Ray Diffraction

X-Ray diffraction of powders (PXRD) is a powerful tool for characterising and identifying crystalline phases, phase purity and relative crystallinity of a

sample.[15-16] A monochromatic source of X-Rays is used to irradiate a sample and a detector is used to analyse any diffracted X-Rays. Signals are only detected when the diffracted beam is in-phase, thus leading to constructive interference. When the beam is out-of-phase, destructive interference occurs and no signal is detected. The source and detector are rotated about the sample and signals are recorded as a function of θ, with patterns plotting 2θ against signal intensity. This can be described mathematically by Bragg's law who first described this phenomenon in relation to the crystal structure and lattice planes.

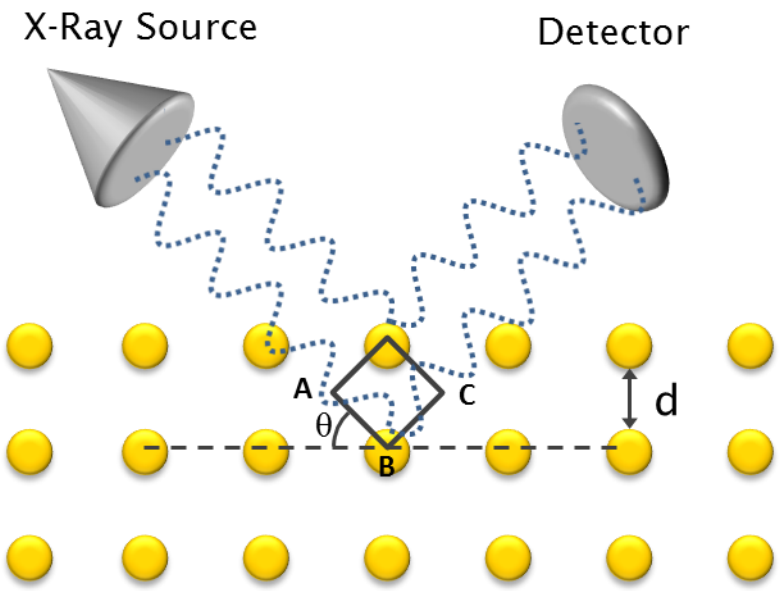

Figure 2.6 Schematic representation of X-Ray Diffraction

As per Figure 2.6, Bragg determined that for the diffracted X-Rays to be in phase, the extra distance travelled by rays diffracting off of sequential lattice planes must be equal to an integer value of the wavelength. This can be described as such:

$$n\lambda = AB + BC \qquad \textbf{Equation 2.8}$$

Since we know that $AB = CD$, then

$$n\lambda = 2AB \qquad \textbf{Equation 2.9}$$

And as

$$\sin\theta = \frac{AB}{d} \qquad \textbf{Equation 2.10}$$

Then

$$n\lambda = 2d\sin\theta \qquad \textbf{Equation 2.11}$$

Diffraction patterns were collected for all crystalline materials synthesised and referenced against reported literature data where possible. Patterns were indexed using CelRef to calculate lattice parameters and assign Miller indices (*hkl* values) to each peak. Miller indices are a way of assigning an orientation of a lattice plane with respect to the unit cell. Unit cells, the smallest irreducible 3D unit that can be continuously repeated to give an extended representation of the crystal structure, are given parameters *abc* corresponding loosely to the *xyz* Cartesian axes but specific to the lattice angles and unit cell dimensions. There are 14 distinct unit cell lattices known as Bravais lattices that crystals can adopt with the values of *abc* varying depending on the complexity of the structure.[15] The values of *hkl* are a measure of what fraction the planes dissect the corresponding *abc* lattice parameters. For example, an *hkl* value of 123 is a plane dissecting the unit cell at 1x *a*, 1/2 x *b* and 1/3 x *c*.

Crystal structures with high degrees of symmetry will have simple diffraction patterns as a lot of lattice planes will be crystallographically identical, for example in a cubic structure where *a=b=c* and all angles are 90°, planes with *hkl* values of 100, 010 and 001 are all identical and will appear as one peak in the diffraction pattern. In contrast, for a triclinic structure a≠b≠c and all angles are different, these values are not identical and so would appear as separate peaks on the pattern. The intensity of a diffraction peak is proportional to the ability of a lattice plane to diffract incident X-Rays. This can be attributed to a few factors, most notably the number of atoms within the plane or the electron

density of individual atoms within the plane; heavier atoms with more electrons have a better propensity for diffracting X-Rays.

2.3.2 Electron Microscopy

Electron microscopy is a powerful tool for imaging materials at extremely high resolution in the micro and nano regimes. With heterogeneous nanoparticle catalysts, understanding the physical properties of the surfaces and locations of nanoparticles is paramount to characterising and understanding the chemical/catalytic properties of the material. In optical microscopy, the resolution is proportional to the wavelength and thus finds its limitations when imaging of features requires resolution smaller than the wavelength of light (approximately 400-700 nm). Other factors also contribute to the resolution such as the refractive index of the imaging medium (often air) and in absolutely ideal conditions, the fundamental maximum resolution with green light is around 150 nm.[17] When imaging samples with features smaller than this, an alternative has to be used – the electron microscope. The resolution of electron microscopy is, in theory, limited by the wavelength of the electron, also known as the de Broglie wavelength, which is a function of the energy or momentum of the particle. In reality, other factors come in to play that limit the resolution of the electron microscope. The sampling volume - which is dependent on the spot size and therefore the probe size - is the ultimate limiting factor, but the probe has to be of sufficient size to generate a current significant enough for detection. As such, the absolute resolution of an electron microscope has been defined as "the smallest probe which can provide an adequate signal from the specimen."[17] The two most commonly used forms of electron microscopy are scanning electron microscopy (SEM) and transmission electron microscopy (TEM).

2.3.2.1 Scanning Electron Microscopy (SEM)

Scanning electron microscopy is useful for imaging and analysing the surfaces of bulk materials. A sample is subjected to a primary electron beam which interacts with the surface in a variety of different modes. This range of interactions is probed by analysing the electrons or X-rays that are ejected from the surface (Figure 2.7).

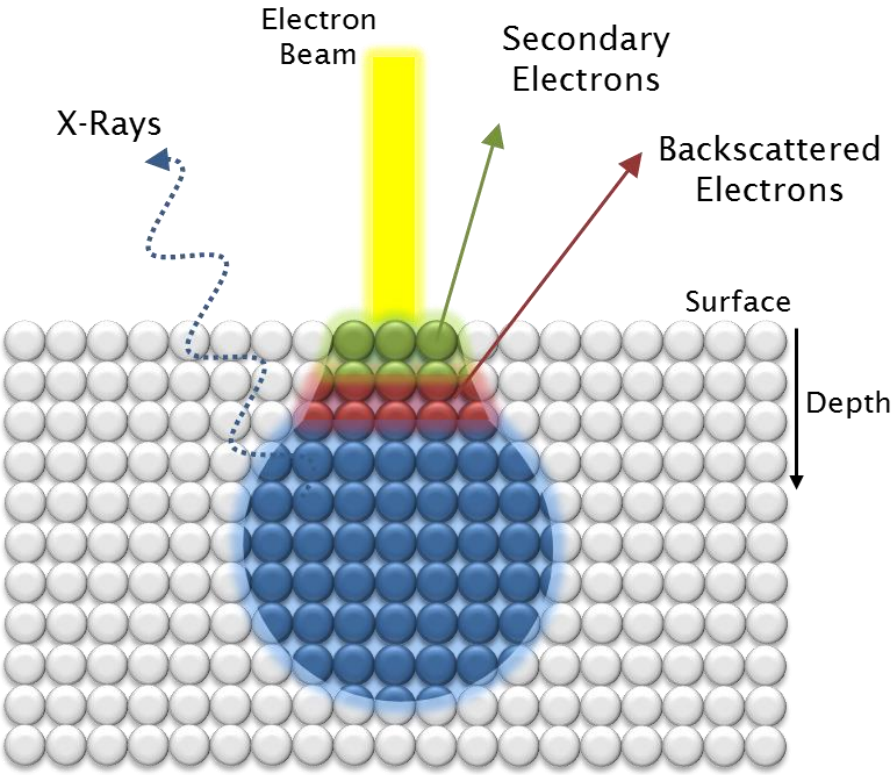

Figure 2.7 Bulk sample penetration depth of an electron beam at which secondary electrons, backscattered electrons and X-Rays may be detected.

Elastic scattering leads to generation of backscattered primary electrons in SEM (Figure 2.8 A), although the intensity is low due to the low probability of electrons being elastically scattered at high angles. Inelastic scattering is more significant for imaging; secondary electrons are emitted due to the displacement of inner-shell electrons by the high energy incident primary electrons that results in a transfer of energy (Figure 2.8 B). This has the additional effect of producing X-rays as a valence electron drops in energy to fill the hole left by the emitted secondary electron. These X-rays are useful for elemental analysis in a technique called energy dispersive X-ray spectroscopy described in *Section 2.3.2.3*. Figure 2.7 highlights the depth of penetration at which these different types of electrons and X-rays can escape the surface to be detected, also known as the sampling volume. Secondary electrons are emitted only from a very thin layer of the surface approximately 10-20 nm thick, backscattered electrons from a slightly thicker layer at approximately 1 µm and X-rays can be emitted from up to 5 µm into the sample.

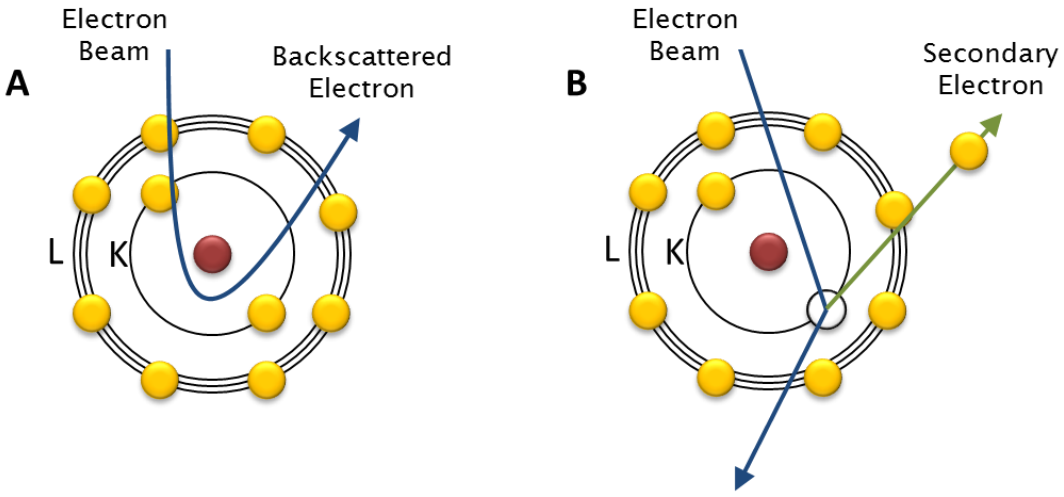

Figure 2.8 Elastic scattering to produce backscattered electrons (A) and inelastic scattering to generate secondary electrons (B)

To generate a topographical image - the most common use of SEM - a detector is used to detect the quantity of secondary electrons emitted from a sample. As the orientation of a surface changes with respect to the electron beam, the distinct shape of the electron penetration volume (Figure 2.7) also changes resulting in a shift in the quantity of secondary electrons that are able to escape the surface. This quantity, also called the secondary electron coefficient, is at a minimum when the surface is perpendicular to the electron beam and increases as the sample is tilted. The change in the secondary electron coefficient across a sample is mapped as contrast in a black and white image to generate the classical micrograph associated with SEM.

For high quality images, a sample must be conducting to allow for effective interaction of the beam with a sample surface and reduce the build-up of charge that can distort the image. To aid conductivity, powdered samples are mounted on carbon tape and sputter-coated in a thin layer of gold prior to loading into the SEM chamber. Collected micrograph images are used for analysis of crystallite sizes, shapes and surface morphologies, connected with other characterisation techniques, to contribute to determination of the structural nature of the catalyst and the roles played in catalysis.

2.3.2.2 Transmission Electron Microscopy (TEM)

Transmission electron microscopy (TEM) works on a similar basis to SEM, except that the transmitted beam of electrons is analysed as opposed to those emitted back from the sample. As such, a sample specimen must be thin enough to allow for transmission of the electron beam. This is compositionally dependent, with lighter elements allowing for a higher degree of electron transmission than heavier elements, but the specimen should be in the region of a few hundred nanometres or less. This is known as the mass-contrast effect. For samples containing high concentrations of heavy elements, such as 4d and 5d transition metals, less than 100 nm is ideal.

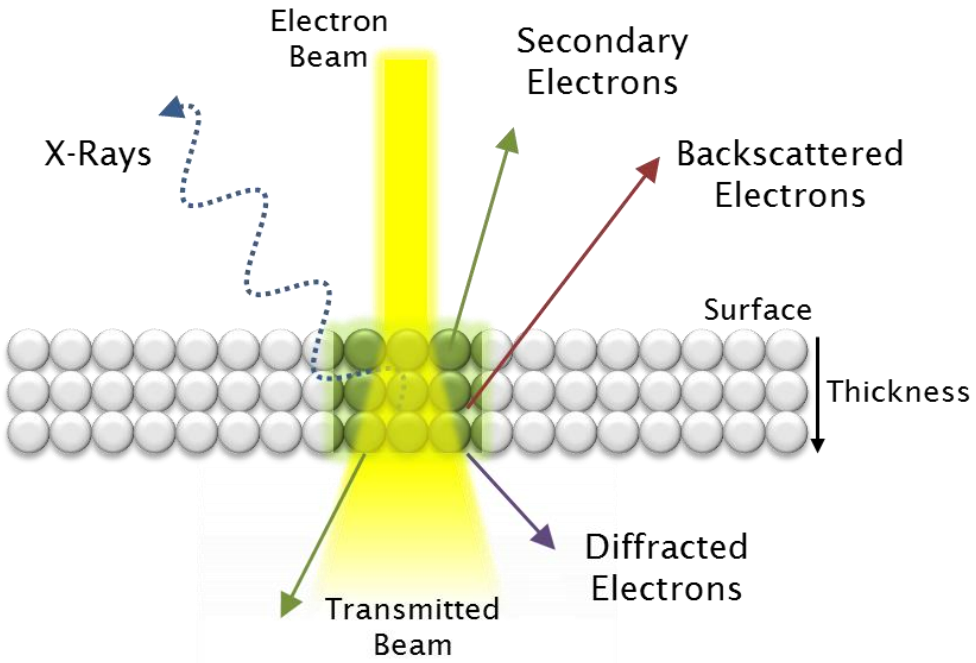

Figure 2.9 Transmission of an electron beam through a thin sample showing generation of secondary, backscattered and diffracted electrons and X-rays.

To form an image from the transmitted electron beam, high energy primary electrons that are scattered in either an inelastic or elastic fashion by a small degree are collected. After passing through the objective lens and objective aperture below the sample to filter out any highly scattered electrons, an image is formed where areas of low scattering (and therefore low mass/thickness) appear bright as the intensity of electrons collected is high,

and areas of high scattering (and so high mass/thickness) appear dark as few electrons are collected. This type of imaging is known as bright field imaging.

It is also possible to image a sample through high angle annular dark field (HAADF) imaging. In this technique, the detector is positioned at a high angle with respect to the transmitted electron beam and thus detects electrons scattered at high angles rather than low angles. As such, areas of high mass/thickness appear bright and *vice versa* for areas of low mass/thickness in contrast to bright field imaging.

In this work, bright field imaging was the main imaging technique used for imaging nanoparticles on the surface of supports for structural and positional characterisation. Typical sample preparation involves creating a suspension of the powdered sample in ethanol and loading onto a carbon film, lacey carbon or holey carbon coated copper mesh TEM grid. After solvent evaporation, the grid was loaded into the vacuum chamber of a TEM for analysis. This technique was used for high resolution imaging of nanoparticles. Size distributions of generated nanoparticles were generated by analysis of 100-200 particles by Image J, an image analysis software. As introduced in Chapter 1, the size and morphology of nanoparticles can play a significant role in the catalytic activity with respect to oxidation reactions. As such, this technique can aid in structural characterisation to link in with catalytic properties to determine any size-related effects.

2.3.2.3 Energy Dispersive X-Ray Spectroscopy (EDX)

The ability to probe elemental composition of a sample in an electron beam is a particularly useful tool that can be performed simultaneously to imaging in an electron microscope. This technique is termed energy dispersive X-ray spectroscopy (EDX) and relies on the emission of X-rays generated when inner-shell electrons are ejected as secondary electrons.

Figure 2.10 gives a more detailed representation of how X-rays are emitted. When an incident electron beam knocks out an inner electron to form an excited-state atom, at some point the atom will relax back into a ground state. The vacant inner state is occupied by a higher energy electron in an outer state with the excess energy being emitted as an Auger electron with kinetic energy, or as an X-Ray with a characteristic wavelength as in Equation 2.12, where ΔE is

the energy difference between the state of the higher energy electron and the vacant inner state.

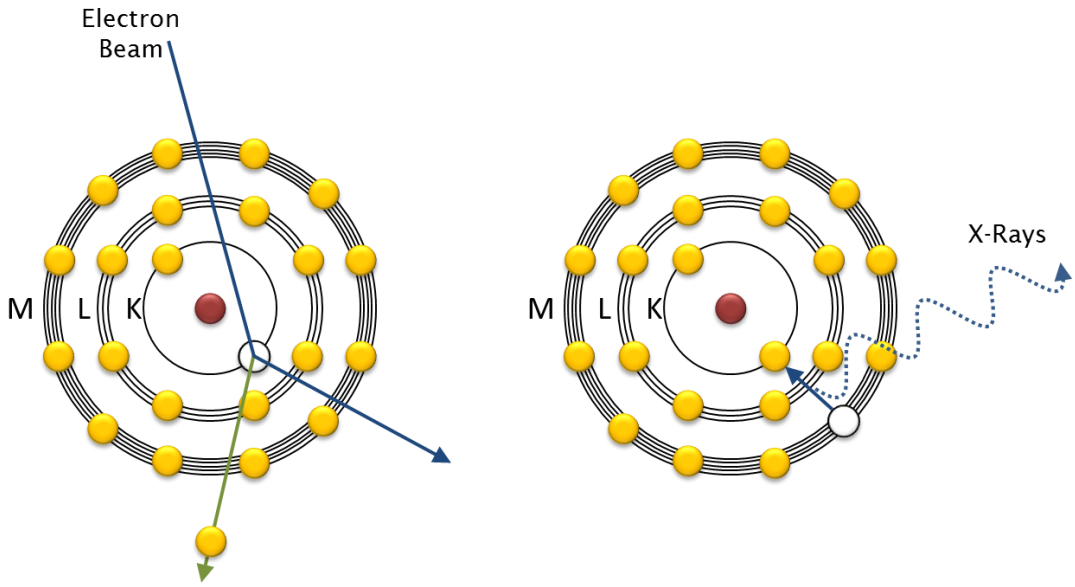

Figure 2.10 Generation of X-rays from relaxing of excited atoms after generation of secondary electrons

$$\lambda = \frac{hc}{\Delta E} \qquad \textbf{Equation 2.12}$$

For example, if an electron from the M shell drops to fill a vacant site in the K shell as in Figure 2.10, a characteristic X-ray will be emitted with an energy, $\mathrm{E} = (\mathrm{E}_M - \mathrm{E}_L)$. The values of the electron shells are well defined for each element and as such, this characteristic energy can be referenced back to identify what element that X-ray was emitted from. In this work, EDX was mainly used for qualitative identification purposes of material elemental compositions. Quantitative analysis is possible through this technique, however precise calibrations are needed and errors can be high due to the abundance of secondary effects that can occur in the dissipation of energy at the sample surface. Therefore, other techniques were used in qualitative assessment of samples.

2.3.3 X-Ray Photoelectron Spectroscopy (XPS)

As shown in the previous section, X-rays can be particularly useful for identifying the elemental composition of a material. This is also possible through the use of X-ray photoelectron spectroscopy (XPS)[18] which can also provide some information on the chemical nature of elemental components, including oxidation states. It is a form of surface analysis, probing the very top layer of a surface to a depth of ~10 nm.

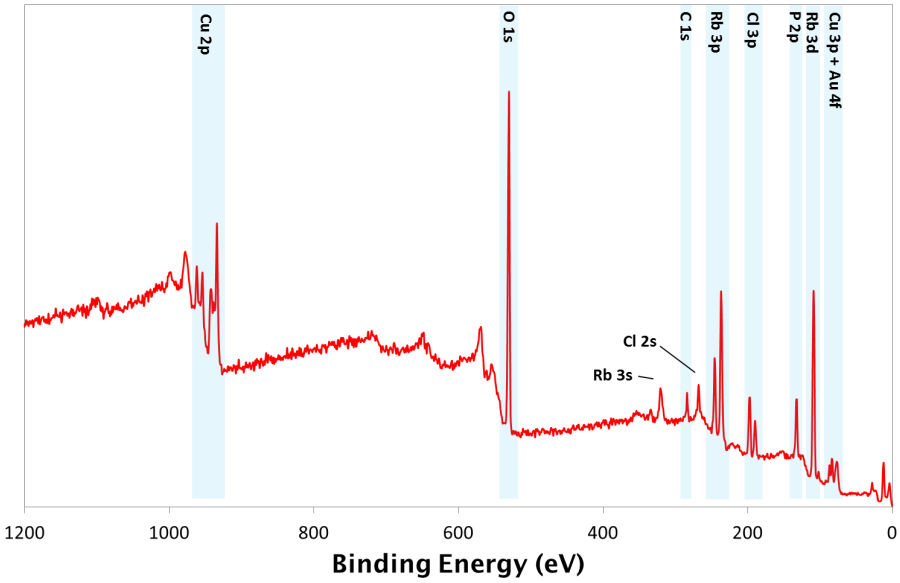

Figure 2.11 Example XPS survey spectra of a material containing Cu, O, Rb, Cl, P and Au

In this technique, a sample is irradiated with X-rays of a specific wavelength that results in the emission of photoelectrons – electrons emitted by excitation from a photon. As a photon is a massless packet of energy, complete energy transfer occurs with the resultant annihilation of the photon. If the energy is ample, the electron will be ejected with a degree of kinetic energy (KE) which is the quantity measured by the instrument. The overall KE of an ejected electron will be equal to the photon energy minus the binding energy (BE). Hence, any factors that affect the binding energy of an electron, such as oxidation state and chemical environment, can be probed. XPS spectra are plotted as a function of KE *versus* intensity to provide a plot with distinctive shape, however the BE values are often more useful and as the BE is inversely proportional to the KE, it is commonplace to plot the spectra with the BE on the x-axis in

reverse order tending towards 0 at the right-hand side. Survey spectra are low resolution scans that probe the entire spectrum between the minimum and maximum potential KEs of a photoelectron based on the incident X-ray beam energy, as can be seen from Figure 2.11.

High resolution scans of small BE windows can be acquired to gain detailed information about a peak of study. In XPS, peaks are assigned spectroscopic labelling based on the respective quantum numbers related to the electron emission, and are thus related to orbital splitting. The spectroscopic notation of a peak is denoted in the form nl_j where n is the principal quantum number, l is the angular momentum quantum number (a value for l of 0 = s, 1 = p, 2 = d etc.) and j is the spin-orbit coupling defined as $l + s$ with s being the spin angular momentum with values of ± ½.

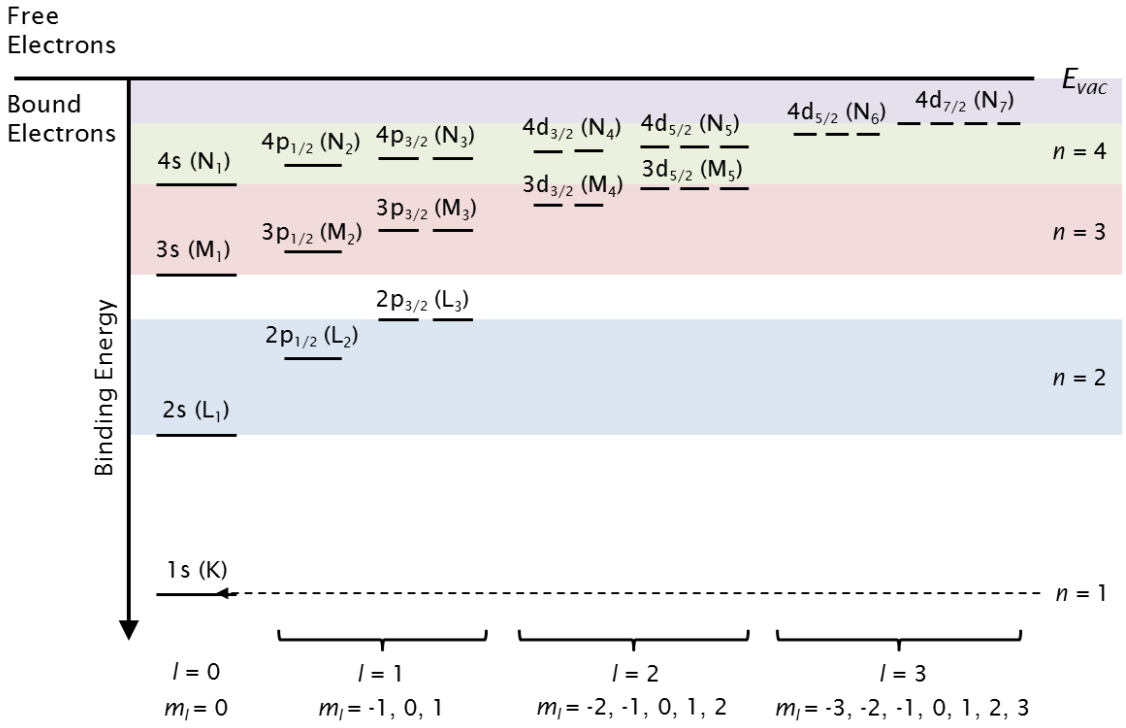

Figure 2.12 Simplified representation of energy levels with spectroscopic and X-ray notation (in brackets) showing quantum numbers of electrons present in these states

Photoelectrons generated from energy levels with non-zero values of l display doublet peaks in the spectra due to the spin-orbit coupling. These doublets have characteristic ratios in relation to the degeneracy of those states. For example, photoelectrons ejected from 3d energy levels will have a ratio of 2:3

for the 3/2 and 5/2 *j* states respectively as displayed graphically in Figure 2.12.

XPS is used in this work primarily for identifying the oxidation state of components within a material. When an atom is ionised, it loses a valence electron. The ionisation energy of the atom increases due to the size constriction of the orbitals and the subsequent increase in attractive forces between the nucleus and remaining electrons. Consequently, the binding energy is increased by a few eV and this can be detected by XPS. Samples are mounted onto carbon tape before loading into the XPS chamber for analysis.

2.3.4 X-ray Absorption Spectroscopy (XAS)

X-ray absorption spectroscopy is a method that works complimentary to XPS in identifying the chemical and structural environment of elements within a sample. Whereas XPS is a surface sensitive technique which analyses the emitted photoelectrons, XAS monitors an X-ray beam transmitted through a sample (and is thus a bulk analysis technique) detecting changes in the absorption of the sample with respect to the energy of the incident X-rays.[19] An incident X-ray beam is scanned through an energy range, where absorption events that lead to the generation of secondary electrons and photoelectrons contribute to a reduction in intensity of the transmitted beam at discrete energy values.

The intensity of a transmitted X-ray beam (I_t) through a sample is a function of the intensity of the incident beam (I_0), the thickness of a sample (x) and the absorption coefficient of the sample (μ) in the relationship shown in Equation 2.13.

$$I_t = I_0 e^{-\mu x} \qquad \textbf{Equation 2.13}$$

The absorption coefficient is dictated by the composition of the sample as each element has differing absorption potentials with heavier elements generally absorbing more X-rays than lighter elements. As such, the absorption coefficient can be more generally described as “the probability for an X-ray to

be absorbed by a sample",[19] with data being plotted as this value against the energy of the incident beam.

An example X-ray absorption spectrum is shown in Figure 2.13 with the two analysis regions, XANES (X-ray absorption near-edge spectroscopy) and EXAFS (Extended X-ray absorption fine structure spectroscopy), identified which will be discussed further in the proceeding sections. The spectrum shown is an example of what would be detected for an absorption edge of a single element component in a sample, in an energy range of approximately 1200 eV around a single electronic transition.

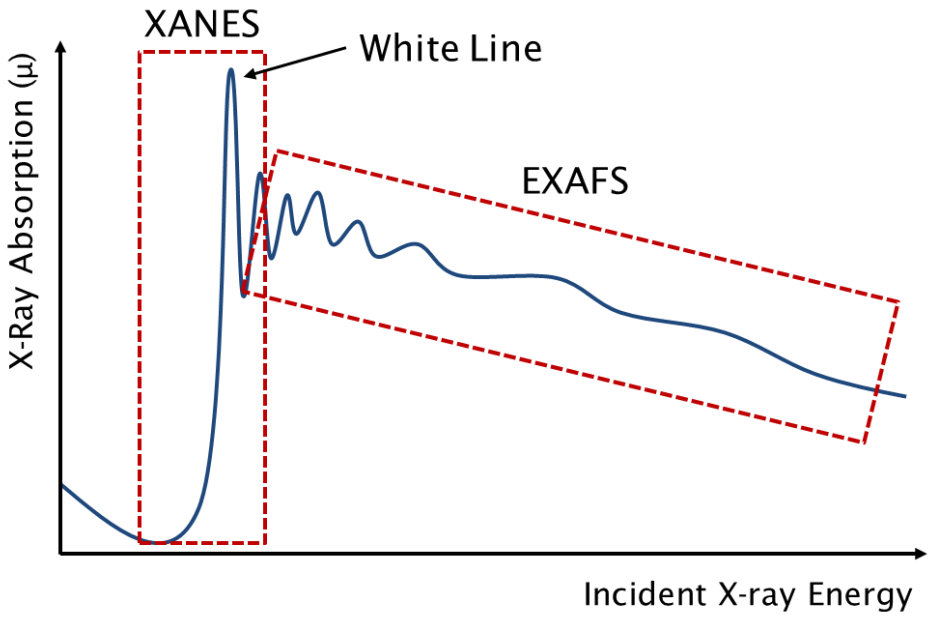

Figure 2.13 X-ray absorption spectrum with XANES region, EXAFS region and White Line identified

2.3.4.1 Extended X-Ray Absorption Fine Structure Spectroscopy (EXAFS)

The EXAFS region of the XAS spectrum occurs after the initial absorption edge of an elemental electronic transition in a sample. It is characteristic of an oscillatory appearance and can extend up to 1000 eV above the absorption edge. The oscillatory features contain information about the local environment around the atoms within the sample, revealing the types and numbers of neighbouring atoms that surround the absorbing atoms and information about the bonding.

When a sample is irradiated with a monochromatic X-ray beam with energy sufficient to eject a photoelectron possessing KE equal to the difference between the incident energy and BE, the photoelectrons propagate from the atom as spherical waves and are scattered from neighbouring atoms. The phase of the scattering can positively or negatively influence the absorbing capabilities of the sample. If the scattered waves are in-phase with the original waves - the interatomic distances are equal to an integer value of the photoelectron wavelength (Figure 2.14 B) – then consequently, a maxima will be observed for μ in the oscillatory EXAFS region of the spectrum at a specific energy value. If the waves are out-of-phase (Figure 2.14 C), then a minima is observed at that energy.

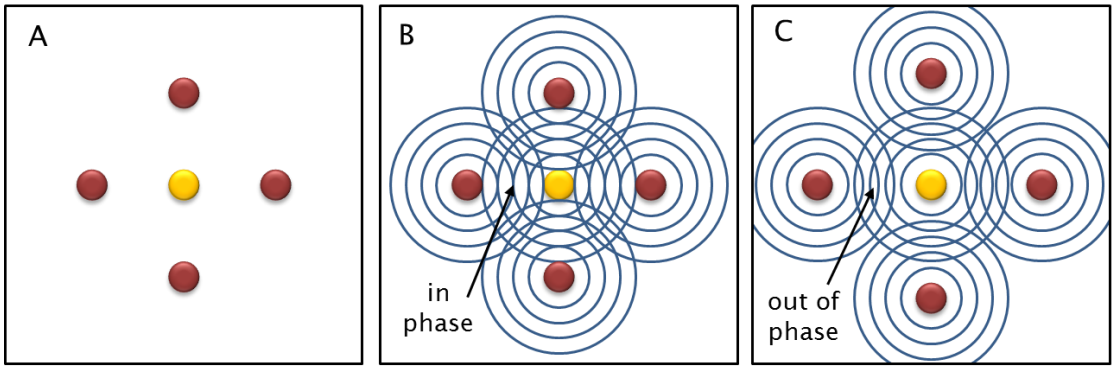

Figure 2.14 X-ray absorption processes showing (A) no absorption, (B) in-phase scattering of photoelectrons and (C) out-of-phase scattering.

Neighbouring atoms equidistant from the absorbing atom will all contribute to the same signal in the EXAFS plot and are thus considered part of the same *shell*. A system may have multiple shells, especially in bulk materials, with the number of atoms in each shell referred to as the coordination number (CN). It is important to note that signals generated for a specific element will be an average of the local chemistry and structure across the bulk of the sample. Transmitted X-rays are detected using ionisation detectors consisting of gas chambers with an ionisable gas. As the gas molecules are ionised by the X-rays, a current is observed that is proportional to the intensity of the beam.

In this work, EXAFS was used to determine the transition of the local environment for metals being reduced from chlorometallate anions to metallic

nanoparticles through transmission mode experiments. The nature of metal bonding was probed to detect the contribution of M-Cl bonds and M-M (1st shell) bonds to determine the degree of reduction across the bulk of a catalyst sample, and where possible, the geometry of the species through analysis of CNs. In addition, it has been possible to estimate the sizes of NPs across the bulk through a technique that compares measured CNs with particles sizes for particles below 3 nm.[20] XAS samples were prepared by grinding the catalyst materials with cellulose as a binder and pressed into pellets. The concentration ratio of catalyst to cellulose was determined by calculating the ideal absorption values where the total of all elements within the sample was less than 2.5 absorption lengths ($\mu x = 2.5$) with the partial absorption of the element of study to be as close to 1 absorption length ($\mu x = 1$) as possible. This was to maximise the X-ray absorption of the element of study to get a good signal whilst still allowing a reasonable amount of transmitted X-rays through the sample for detection. Data is analysed by fitting a proposed model to the raw data to achieve the best fit possible.

2.3.4.2 X-Ray Absorption Near-Edge Spectroscopy (XANES)

Other important data that can be acquired from an XAS spectrum are those within the XANES region close to the absorption edge (approximately -50 eV to +200 eV) of an elemental component of the sample material. The main absorption edge is characteristic of the absorption of the incident X-rays for excitation of a photoelectron into the continuum. Features at the absorption edge include the *white line* (a strong peak at the edge as labelled in Figure 2.13), shoulders and isolated small peaks in the *pre-edge* (the region just before the edge step) that are related to the density of unoccupied orbitals that an electron can be excited to, at slightly lower energies than required for complete excitation and ejection from the atom. A change in oxidation state of an element within a system can result in a shift of the edge to higher energies due to the increase in binding energy (as described in more detail in *Section 2.3.3*). As such, the chemical environment can be probed as a bulk technique, complimentary to XPS that can acquire similar data with specificity toward the surface of a sample.

XANES was used primarily in this work for comparison of samples with standards; to monitor the change in the average oxidation state of elements within catalyst materials across different activation methods.

2.3.5 Inductively Coupled Plasma – Optical Emission Spectroscopy (ICP-OES)

For many catalysts, it is useful to be able to quantify the amount of a specific element related to the active centre of a catalyst for effective calculations of catalytic efficiency. Inductively coupled plasma (ICP) spectrometry[21-22] provides a sensitive and precise way to acquire this information. Samples studied by ICP must be in the solution or gas phase, thus solid samples must be digested by strong acids (H_2SO_4, HNO_3 and sometimes HF) to liberate all components into the solution phase for effective analysis. The solution sample is then injected as an aerosol through the use of a nebuliser and propelled into a channel containing plasma generated from argon, reaching up to 10,000 K at its core and instantly vaporising the sample. Components of the sample exist as free atoms in the gas phase, with the extreme thermal environment and high quantities of atomic collisions leading to the promotion of sample atoms to excited states. Relaxation of the excited states results in the emission of photons with quantised energy values characteristic of the emitting element. These photons can be detected as a function of wavelength, with the intensity of the emissions proportional to the concentration of the element. This detection is known as optical emission spectroscopy (OES) or synonymously as atomic emission spectroscopy (AES).

ICP-OES was used for quantitative analysis of noble metals in supported NP catalysts for calculation of concentrations in terms of weight % or mole %. These values were necessary for accurate determination of TONs and TOFs. This method was also used for analysis of catalytic reaction mixtures after separation from a used catalyst to determine the extent, if any, of NP leaching from the catalyst into solution.

2.3.6 Thermogravimetric Analysis (TGA)

Thermogravimetric Analysis (TGA) is a particularly effective tool for probing the thermal properties of materials with respect to mass changes.[23] Typical TGA equipment will consist of a small balance to hold a sample with a surrounding furnace and gas inlet/outlet to control the atmospheric composition during an analysis. Samples of about 5-10 mg are loaded onto the balance in a small ceramic crucible and the mass monitored as the temperature is changed as per the experiment required. Common experiments probe the thermal stabilities of materials and as such will ramp the temperature at a steady rate from ambient conditions to a maximum chosen to decompose the sample. Atmospheric conditions can be inert or in the presence of oxygen depending on the information that is required. For example, when organic molecules are present in the material, an inert atmosphere will leave carbon residues upon thermal decomposition, however in the presence of O_2, carbon compounds will be fully combusted to CO_2 and thus all carbon will be removed from the system. Each method will change the final mass of the material after the thermal analysis.

In this work, TGA was mostly used in the characterisation of MOF materials to determine the thermal stability of the framework. Features observed in a TGA plot include the removal of solvent from the pores that results in a loss in mass, and eventual decomposition of the framework. Experiments were carried out in the presence of O_2 for complete combustion of organic moieties to leave thermodynamically favourable dense phase metal-oxide powders as the decomposition products.

2.3.7 Gas Adsorption Surface Analysis Studies

Gas adsorption is a powerful technique for probing the surface areas of materials, as well as determining pore volumes and pore sizes of nanoporous materials amongst other applications.[24] Adsorption is generally seen as interactions between a surface and surrounding molecules that result in a temporary increase in concentration of a component at the interface.[25] Molecules can adsorb to a surface through two main routes; physisorption and chemisorption. Physisorption is a general mechanism by which the concentration molecule can build up on a surface through weak, but favourable interactions without forming a chemical bond. Chemisorption involves the

formation of a formal chemical bond between an adsorbate and the surface and is a much stronger interaction than physisorption.

Two main models are proposed for the adsorption of molecules to a surface; the Langmuir model and the Brunauer-Emmett-Teller model (BET) as shown in Figure 2.15. The Langmuir model proposed that adsorption of the first monolayer of an adsorbate required the most energy, and so at low pressures, the number of available adsorption sites was limited to those directly on the surface, with multilayer adsorption only coming into effect at ambient pressures ($p/p^{\circ} \approx 1$). The BET model is an extension of the Langmuir model but takes into account the fact that non-uniform multilayer adsorption at low pressures is closer to reality, often producing Type II isotherms (according to the IUPAC classification). The isotherm is concave to the p/p° axis before levelling out and then becoming convex to the p/p° axis at values close to 1. This is indicative of an adsorbed layer that increases in thickness with increasing pressure. Both models have made non-realistic assumptions including that there are no adsorbate-adsorbate interactions and that layers beyond the first monolayer act like liquids, however the BET model provides a closer description to an ideal situation as is extensively used in the literature for measuring surface areas. As such, the BET model has been applied to all gas adsorption isotherms collected in this work.

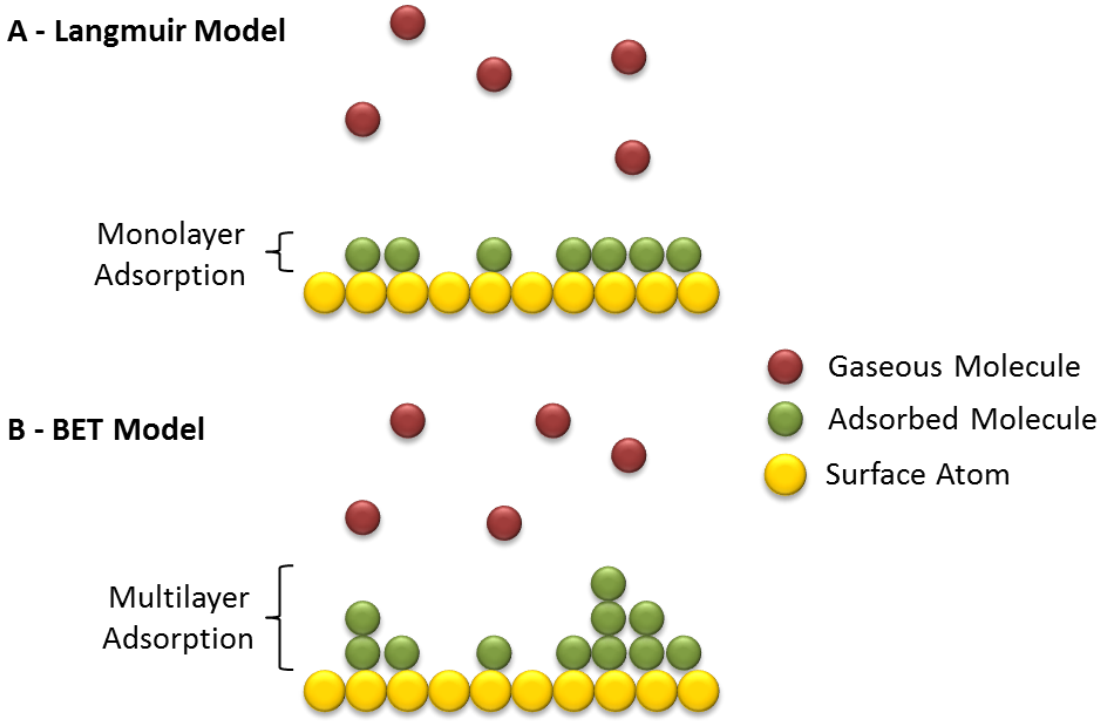

Figure 2.15 Gas adsorption theories by Langmuir (A) and BET (B) models

Typical isotherms for surface area studies are collected using small inert gas probe molecules such as Ar or N_2 for accurate measurement of surface areas where small features or pores are present, the latter which is used for collected isotherms in this work. Samples are first prepared by outgassing (or degassing) to remove any adsorbed molecules such as coordinating solvents, H_2O or CO_2. To outgas, a sample is first purged by evacuating the containing vessel to low pressures then refilled with dry N_2 to displace any weakly bound adsorbates left in small concentrations. The process is repeated then heated to an elevated temperature under vacuum for a duration of time to remove any more strongly bound or chemisorbed species. The isotherm is then collected by evacuating the vessel and increasing the pressure step-wise to pre-programmed values up to $p/p^o = 1$ to measure an adsorption isotherm, and then decreasing the pressure in the same way to achieve a desorption isotherm.

The surface area is then calculated by a two-step approach. Firstly, the monolayer capacity (n_m) must be determined and then the specific surface area calculated from this value. To determine n_m, a BET plot must be constructed from the BET equation which is written in Equation 2.14 where *n* is the total adsorbed quantity of N_2 and C is a constant with positive quantity and

interpreted by Brunauer as 'the average heat of adsorption on the less active part of the adsorbing layer'.[25]

$$\frac{p/p^o}{n(1-p/p^o)} = \frac{1}{n_m C} + \frac{C-1}{n_m C}(p/p^o) \qquad \textbf{Equation 2.14}$$

The BET plot of $(p/p^o)/(n(1-p/p^o))$ against (p/p^o) gives a straight line graph of gradient $g = (C-1)/n_m C)$ and intercept $i = 1/n_m C$. Thus the monolayer capacity can be calculated from the following relationship:

$$n_m = \frac{1}{(g+i)} \qquad \textbf{Equation 2.15}$$

BET plots are normally linear in the range p/p^o = 0.05-0.30 and thus these values are used. Once the monolayer capacity is known, the BET specific area can be calculated from the following relationship:

$$a(BET) = n_m L \sigma \qquad \textbf{Equation 2.16}$$

Where L is Avogadro's constant and σ is the average area occupied by each molecule. For nitrogen molecules, 0.162 nm^2 is commonly used as the value for σ.

2.4 References

1 E. J. P. Feijen, J. A. Martens and P. A. Jacobs, Hydrothermal Zeolite Synthesis in *Preparation of Solid Catalysts* (Eds.: G. Ertl, H. Knözinger, J. Weitkamp), Wiley-VCH, Weinheim, **1999**, pp. 262.

2 J. Čejka and D. Kubička, Zeolites and Other Micro- and Mesoporous Molecular Sieves in *Kirk-Othmer Encyclopedia of Chemical Technology*, John Wiley & Sons, Inc., **2010**.

3 S. Iwamoto and M. Inoue, *J. Jpn. Pet. Inst.,* **2008**, *51*, 143.

4 G. Demazeau, *J. Mater. Sci.,* **2008**, *43*, 2104.

5 K.-D. Henkel, Reactor Types and Their Industrial Applications in *Ullmann's Encyclopedia of Industrial Chemistry*, Wiley-VCH Verlag GmbH & Co. KGaA, **2000**.

6 E. B. Nauman, *Chemical Reactor Design, Optimisation, and Scaleup*, 2nd ed., John Wiley & Sons, Inc., Hoboken, **2008**.

7 I. Kikic and T. W. D. Loos, Thermodynamic Properties at High Pressure in *High Pressure Process Technology: Fundamentals and Applications* (Eds.: A. Bertucco, G. Vetter), Elsevier Science B. V., Amsterdam, **2001**.

8 P. J. F. Sandra, Gas Chromatography in *Ullmann's Encyclopedia of Industrial Chemistry*, Wiley-VCH Verlag GmbH & Co. KGaA, **2001**.

9 N. H. Snow and G. C. Slack, Chromatography, Gas in *Kirk-Othmer Encyclopedia of Chemical Technology*, John Wiley & Sons, Inc., **2011**.

10 G. Guiochon and O. Trapp, Basic Principles of Chromatography in *Ullmann's Encyclopedia of Industrial Chemistry*, Wiley-VCH Verlag GmbH & Co. KGaA, **2012**.

11 F. G. Kitson, B. S. Larsen and C. N. McEwan, *Gas Chromatography and Mass Spectrometry: A Practical Guide*, Academic Press, Ltd., London, **1996**.

12 K. Downard, *Mass Spectrometry: A Foundation Course*, The Royal Society of Chemistry, Cambridge, **2004**.

13 E. de Hoffmann, Mass Spectrometry in *Kirk-Othmer Encyclopedia of Chemical Technology*, John Wiley & Sons, Inc., **2005**.

14 M. Linscheid, Mass Spectrometry in *Ullmann's Encyclopedia of Industrial Chemistry*, Wiley-VCH Verlag GmbH & Co. KGaA, **2001**.

15 C. Hammond, *The Basics of Crystallography and Diffraction*, 2nd ed., Oxford University Press, Oxford, **2008**.

16 K. Tsuji, X-Ray Technology in *Kirk-Othmer Encyclopedia of Chemical Technology*, John Wiley & Sons, Inc., **2007**.

17 P. J. Goodhew, F. J. Humphreys and R. Beanland, *Electron Microscopy and Analysis*, 3rd ed., Taylor & Francis, London, **2001**.

18 P. v. d. Heide, *X-Ray Photoelectron Spectroscopy: An Introduction to Principles and Practices*, John Wiley & Sons, Inc., Hoboken, **2012**.

19 S. D. Kelly, D. Hesterberg and B. Ravel, Analysis of Soils and Minerals Using X-Ray Absorption Spectroscopy in *Methods of Soil Analysis Part 5: Mineralogical Methods*, Soil Science Society of America, Madison, **2008**.

20 A. M. Beale and B. M. Weckhuysen, *Phys. Chem. Chem. Phys.,* **2010**, *12*, 5562.

21 X. Hou and B. T. Jones, Inductively Coupled Plasma/Optical Emission Spectroscopy in *Encyclopedia of Analytical Chemistry* (Ed.: R. A. Meyers), John Wiley & Sons Ltd, Chichester, **2000**.

22 J. R. Dean, Inductively Coupled Plasma Spectrometry in *Kirk-Othmer Encyclopedia of Chemical Technology*, John Wiley & Sons, Inc., **2007**.

23 M. E. Brown, *Introduction to Thermal Analysis: Techniques and Applications*, 2nd ed., Kluwer Academic Publishers, Dordrecht, **2001**.
24 K. S. Walton and R. Q. Snurr, *J. Am. Chem. Soc.,* **2007**, *129*, 8552.
25 F. Rouquerol, J. Rouquerol and K. Sing, *Adsorption by Powders and Porous Solids: Principles, Methodology and Applicationd*, Academic Press, London, **1999**.

Chapter 3: Synthesis of Nanoparticles by *in-situ* Extrusion from Nanoporous Frameworks

Special Acknowledgements

The following special acknowledgements recognise the contributed work of colleagues and collaborators to the presented content of this chapter.

Sivan Van Aswegen: An undergraduate project student who contributed to the preparation of catalyst batches and sampling of catalytic reactions. (University of Southampton, UK)

Dr Gillian Collins: For helpful discussions and collection of images related to the TEM analysis of materials presented in this chapter. (University College Cork, Ireland)

"There are more things in heaven and earth, Horatio,
Than are dreamt of in your philosophy."

Hamlet (Act 1, Scene 5, 167-8)

3.1 Introduction

3.1.1 Porous Metal Phosphates in Catalysis

Microporous phosphate materials have been synthetically produced for a few decades, with aluminophosphates (AlPO) being some of the most well-known of these materials. Pioneered by Wilson and Flanigen *et al.*[1-2] in the 1980's, the effort was to discover new zeolite-like topologies with different compositions and new catalytic properties. As the phosphate groups are also tetrahedral in shape, it was possible to synthesise materials with equivalent topologies to zeolites and hence the association of the term *zeotypes*. Examples of new topologies unique to aluminophosphate materials were also discovered, for example AFI (AlPO-5) and AEI (AlPO-18). Contrary to zeolites however, AlPOs have a neutral framework owing to the charge on the phosphate groups being equal and opposite to those on the aluminate groups. Isomorphous substitution of a small amount of a redox active metal, or metal with lower oxidation state than the phosphorous can provide isolated redox activity or Brønsted acidity that has been utilised for a variety of catalytic applications.[1, 3-8]

Efforts have also been dedicated toward the synthesis of microporous transition metal phosphate materials, with abundant and cheap transition metals being a target for potential redox catalysis. Whilst there are a lot of examples of iron phosphates used for catalysis,[9-15] they seem notoriously elusive from a synthetic point of view, often requiring inert atmospheres for synthetic preparation and only remaining stable for short periods of time. Just a handful of examples of open-framework cobalt phosphates exist with few catalytic studies.[16-22] To date, no examples of open-framework manganese phosphates used in catalysis exist to date. In fact, only a small number of references could be found for open-framework manganese phosphates in their entirety.[23-24] The implications being that the complexity of these open frameworks, potentially originating from the diverse chemistry available to transition metals in terms of stable oxidation states and coordination geometries, could well have a detrimental effect on structural stability, favouring the formation of dense-phases instead.

On the contrary, recent research on the introduction of high quantities of fluorine or chlorine into the synthesis of transition metal phosphates can in fact have a positive role in promoting the formation of low density, open-framework topologies. This is exemplified in the work by Cheetham, Férey and co-workers,[25-26] who successfully incorporated fluorine into microporous phosphate frameworks amongst others, and Armstrong *et al.*[27] who further drew on the hypothesis that halogens could induce the formation of microporous frameworks, reporting more than 50 new structures. The authors rationalise this by their observation that the high concentration of chloride or fluoride ions in the system induce the formation of more terminated polyhedra, by substituting in positions where oxygen may otherwise be present and lead to oxygen-bridging. This has opened up a whole new field and broadened the scope for exploring the role of these materials in the field of catalysis; either by direct use as a catalyst or by formation of hybrid materials that combines unique properties in novel catalytic applications.

3.1.2 Copper Chlorophosphates with CU-2 Topology

A particular framework that has sparked some interest recently for its intriguing properties is a copper chlorophosphate. Possessing CU-2 topology, this framework was first reported in 1999[28] and synthesised by molten salt templating methods at temperatures between 500-800 °C. The framework was one of a series reported where the cationic alkali metal counter-ions within the framework could be varied (K, Rb, Cs) and the phosphates could also be replaced with arsenates. A general formula can be written as $A_2Cu_3(X_2O_7)_2Cl_y$.(salt) (A= K, Rb, Cs; X= P, As).

Figure 3.1 shows a topological view of the CU-2 topology with 2 types of parallel 1D channels running through the material having channel diameters of 5.3 and 12.7 Å respectively. Using terminology commonly associated with zeolites and similar materials, the channels can also be considered as 8-ring and 16-ring channels where 8 or 16 Cu/(P,As) units are linked by bridging oxygen atoms. The copper species are distorted square planar in shape and act as walls between 2 large channels or a large and small channel with an overall net negative charge and composition $Cu_3(P_2O_7)_2^{2-}$. Both channels are occupied by alkali metal salts with alternation of -A-Cl-A-Cl- (A = K, Rb, Cs) in the smaller

channel and a salt-like lattice within the larger channels, where Cl atoms loosely coordinate to the axial positions of the CuO_4 units in the framework skeleton. The material can crystallise in two space groups depending on the amount of chlorine present in the smaller channels. Where chlorine is present at every available site (-A-Cl-A-Cl-) the material has a space group of *I*4*/mcm*, however when vacant sites are left (-A-□-A-Cl-), the material has a space group of *P*4*/nbm*. Viewing the structure from a perpendicular axis (a-axis) as in Figure 3.2 shows individual pyrophosphate units within the structure where two adjacent phosphate units share a bridging oxygen atom along the direction of the channels (c-axis).

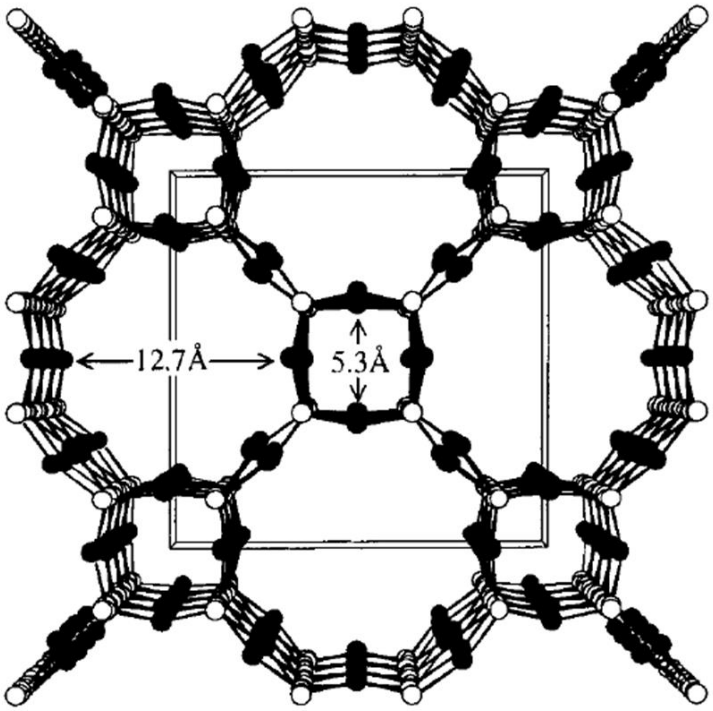

Figure 3.1 Microporous Framework topology of CU-2 based materials (black spheres - Cu; white spheres - P,As; O and Cl omitted for clarity). Reprinted with permission from Q. Huang, M. Ulutagay, P. A. Michener and S.-J. Hwu, *J. Am. Chem. Soc.*, **1999**, 121, 10323. Copyright 1999 American Chemical Society.

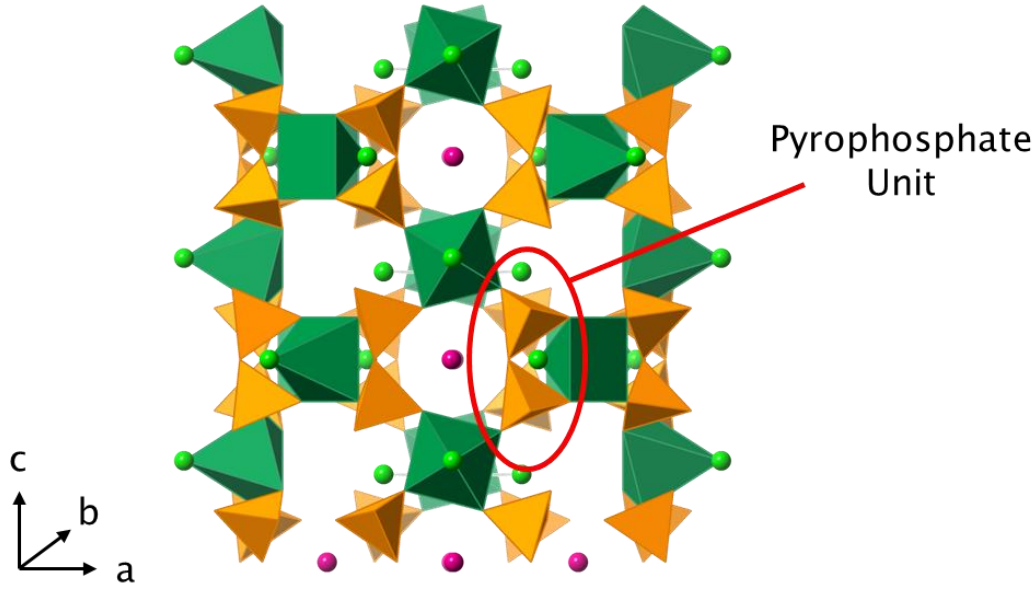

Figure 3.2 Crystallographic representation of CU-2 topology showing pyrophosphate units along the c-axis (Cl – green spheres, Rb – pink spheres, Cu – green polyhedra, P – orange polyhedra; oxygen omitted for clarity)

In a recent study by Williams *et al.*,[29] the analogous copper phosphate with CU-2 topology was synthesised for the first time using hydrothermal methods, and thus greatly reduced the temperature at which these materials could be synthesised from over 500 °C to just 175 °C. The method was demonstrated to be successful in synthesising K, Rb and Cs analogues as before, however they also demonstrated that complex anions such as $[CuCl_4]^{2-}$, $[PO_4H_n]^{n-3}$, $[AuCl_4]^{-}$, $[PtCl_4]^{2-}$, $[PdCl_4]^{2-}$ and $[PtBr_4]^{2-}$ could also be incorporated into the larger channel of the CU-2 topological framework *in-situ*. Figure 3.3 shows a crystallographic representation of one of these materials with square planar $[PtCl_4]^{2-}$ stacked down the larger channels and also containing Rb counter-ions to the negatively charged framework and the supported complex anions. Note that the channel Cl ions are shown to be coordinating to the square planar copper sites, with the smaller channel Cl ions in a μ_4-bridging configuration to the four Cu species within the pore walls.

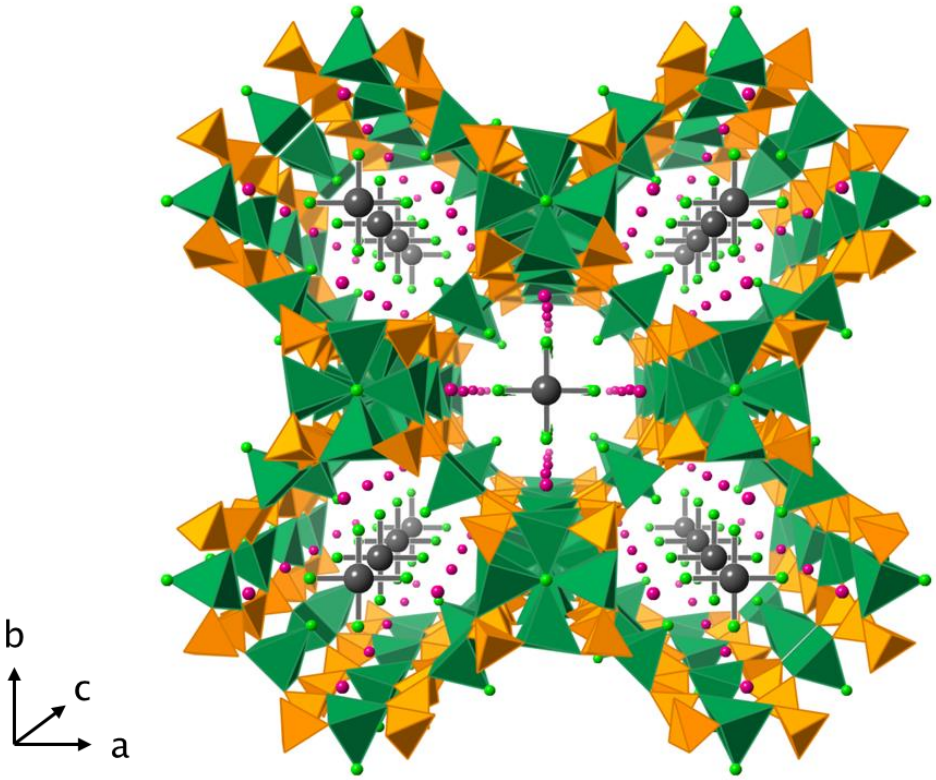

Figure 3.3 Representative crystal structure of the $[PtCl_4]^{2-}$ supported $Rb_9Cu_6(P_2O_7)_4Cl_2$ framework (Pt – grey spheres, Cl – green spheres, Rb – pink spheres, Cu – green polyhedra, P – orange polyhedra; oxygen omitted for clarity)

Incorporation of the complex anions was achieved by the facile addition of a source of the anion to the mixture of components before hydrothermal treatment (e.g. $HAuCl_4$, K_2PtCl_4). It is speculated that these complex anions along with the presence of the large quantity of alkali metal salts can act as structure directing agents (SDAs) to enhance the formation of the microporous framework.

3.1.3 Ion Exchange in Copper Chlorophosphates

Alluded to by both Huang[28, 30] and developed further by Williams,[29] these materials have shown a propensity towards facile anion and cation exchange. By soaking the material in a concentrated solution containing a different metal salt, it is possible, for example, to exchange Cs^+ and $[PO_4H_n]^{n-3}$ ions within the porous framework for K^+ and Cl^- ions. This can be monitored visually by a clear colour change from blue to green, characteristic of absorption from Cu-Cl

bonding interactions. Whilst in this example both cation and anion are exchanged simultaneously, it is also possible to perform cation and anion exchange individually, a relatively unique property for a microporous ion exchange material.

With the array of various anions that can be supported in this copper chlorophosphate by direct synthesis, as well as their ability to perform facile ion exchange processes, this led on naturally to explore the potential for utilising these unique properties for the preparation of new hybrid materials. These materials have shown to support complex noble metal chlorides and thus exploration into using these materials for preparation of highly active noble metal catalysts was a logical step. From here on in, the copper chlorophosphate framework material will be abbreviated to CuClP. Other potential applications highlighted include anion recognition, separation and conduction devices.[29]

3.1.4 Aims and Objectives

In this chapter, synthesis of the $[AuCl_4]^-$, $[PtCl_4]^{2-}$ and $[PdCl_4]^{2-}$ will refined to obtain phase pure and homogeneous materials. Thermal extrusion of the chlorometallate anions will be explored through an oxidative calcination to form active metallic species. The use of a variety of characterisation techniques will be used to evaluate structure-property relationships for the aerobic oxidation of benzyl alcohol, with kinetic studies to determine activation energies of the respective calcined catalysts.

3.2 Synthesis, Structural Characterisation and Catalytic Activity in Aerobic Oxidations

3.2.1 Synthetic Variables

Hydrothermal synthesis of materials can be very sensitive, and commonly have only a narrow range of variables (temperature, reactant quantities, pH, time etc.) suitable for phase-pure products. Prior work[29, 31] has established a method for synthesising a phase-pure batch of Au/CuClP and thus synthesis conditions were replicated for use with the gold, platinum and palladium analogues, each producing phase-pure samples as a result. Due to the quantities of catalyst required to run realistic catalytic reactions with the reactor setup, the synthesis prep was scaled up by 2 times with little effect on the resulting products and crystallinities obtained. When the synthesis was scaled up further (4-6 times the original reported conditions), significant quantities of an amorphous blue phase was observed, reducing the phase-purity of the materials and making them unsuitable for use in a catalytic reaction. When prepared, the mixture has a very low concentration of water in the system, so effective mixing and diffusion could be an issue in the scaled up syntheses. As such, the lower quantity scale-up of 2 times the original quantities was used for the preparation of catalysts in this chapter as described in the preceding experimental section.

It was also shown in these studies that thermal treatment of the Au supported material yielded the presence of metallic gold as determined by temperature-programmed PXRD.[29] Further studies showed that calcination at 500 °C in a flow of dry air for 16 hours was sufficient to reproduce these structural observations, with preliminary catalytic data showing promise for the aerobic oxidation of benzyl alcohol.[31] This triggered interest in exploring further the relationship between these active noble metal species and the resulting active catalytic properties.

3.2.2 Elucidation of Structural Properties

To understand the structural properties of the catalyst material and associated activity toward activation of O_2 and aerobic oxidation reactions, a variety of

techniques were employed to elucidate and rationalise the structural properties of the material. A simulated PXRD pattern was generated from the original CIF file[29] of single crystal data from the $[CuCl_4]^{2-}$ supported CuClP framework. The material was synthesised without the presence of a noble metal chloride to show that hydrothermal synthesis conditions employed were sufficient to replicate a phase-pure sample of the framework. As shown in Figure 3.4, there is a good correlation between the simulated and real patterns of the synthesised 'blank' framework.

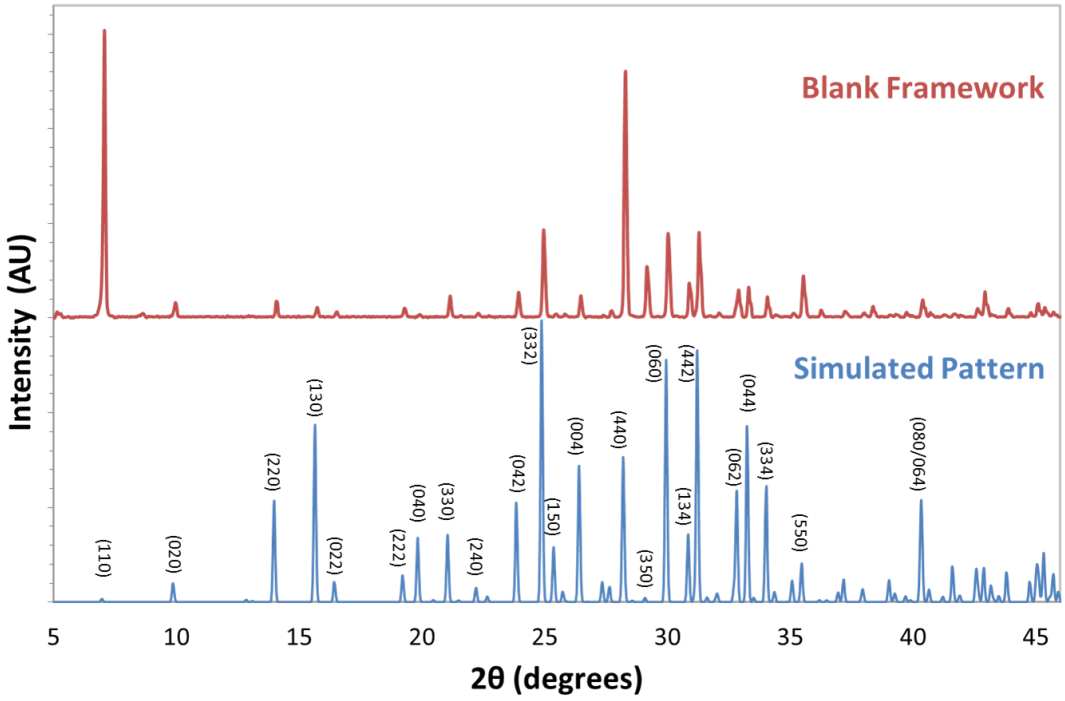

Figure 3.4 PXRD of blank framework synthesised without any noble metal source (red line) and associated simulated pattern (blue line) (Major peaks are labelled with associated *hkl* values)

PXRD patterns were also collected for the calcined materials containing $[AuCl_4]^-$, $[PtCl_4]^{2-}$ and $[PdCl_4]^{2-}$. As can be seen from Figure 3.5, there is also a good correlation and preserved crystallinity with that of the blank and simulated frameworks, with only a few differences observed. For the Au/CuClP and Pt/CuClP calcined materials, the appearance of peaks at 2θ values of 38.2° and 39.8° respectively are indicative of the presence of crystalline metallic phases of the present noble metals, giving rise to the implication that a degree of reduction has occurred.

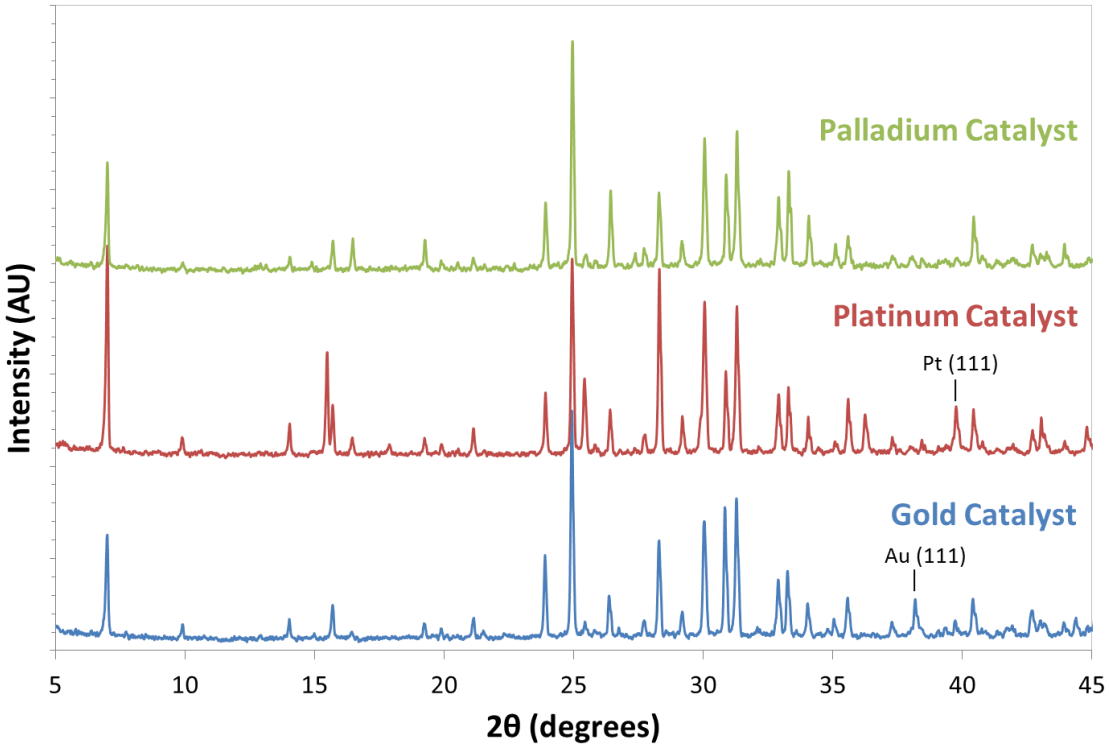

Figure 3.5 PXRD patterns of calcined $[AuCl_4]^-$ (blue line), $[PtCl_4]^{2-}$ (red line) and $[PdCl_4]^{2-}$ (green line) loaded $Rb_9Cu_6(P_2O_7)_4Cl_n$ catalyst materials.

To confirm the noble metal content of the framework material and accurately calculate turn-over numbers, ICP analysis was performed on the active calcined catalyst materials (Table 3.1, Table 3.2 and Table 3.3). The noble metal content is referenced against Rb and Cu, both of which are part of the parent host framework.

Table 3.1 Elemental composition of Au, Rb and Cu in a calcined Au/CuClP catalyst as determined by ICP-OES

Element	Weight %	Atomic %
Au	6.43	3.26
Rb	29.49	34.50
Cu	17.77	27.95

Table 3.2 Elemental composition of Pt, Rb and Cu in a calcined Pt/CuClP catalyst as determined by ICP-OES

Element	Weight %	Atomic %
Pt	2.72	1.39
Rb	31.90	37.32
Cu	18.32	28.83

Table 3.3 Elemental composition of Pd, Rb and Cu in a calcined Pd/CuClP catalyst as determined by ICP-OES

Element	Weight %	Atomic %
Pd	3.34	3.14
Rb	31.32	36.64
Cu	18.51	28.83

Interestingly, despite equivalent molar quantities of the noble metal chloride precursors being used in the hydrothermal synthesis of the materials, the atomic % varies slightly with the platinum material displaying lower values and implying that less of the precursor had been incorporated to the channels of the framework. It is possible that a small amount of the K_2PtCl_4 remained and was washed away at the aqueous washing stage post-synthesis. Composition values for the rubidium and copper content between samples, representative of the framework components, remain fairly consistent as would be expected.

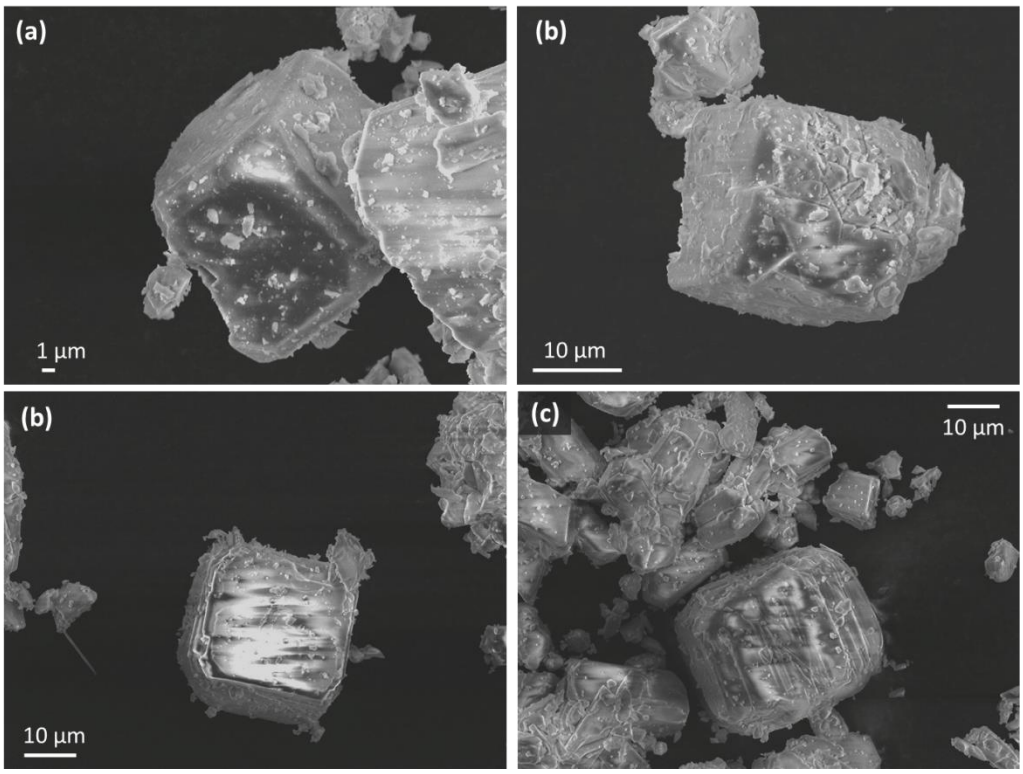

Figure 3.6 SEM micrographs of as-synthesised $[AuCl_4]^-$ supported materials (a-b) and equivalent calcined materials (c-d)

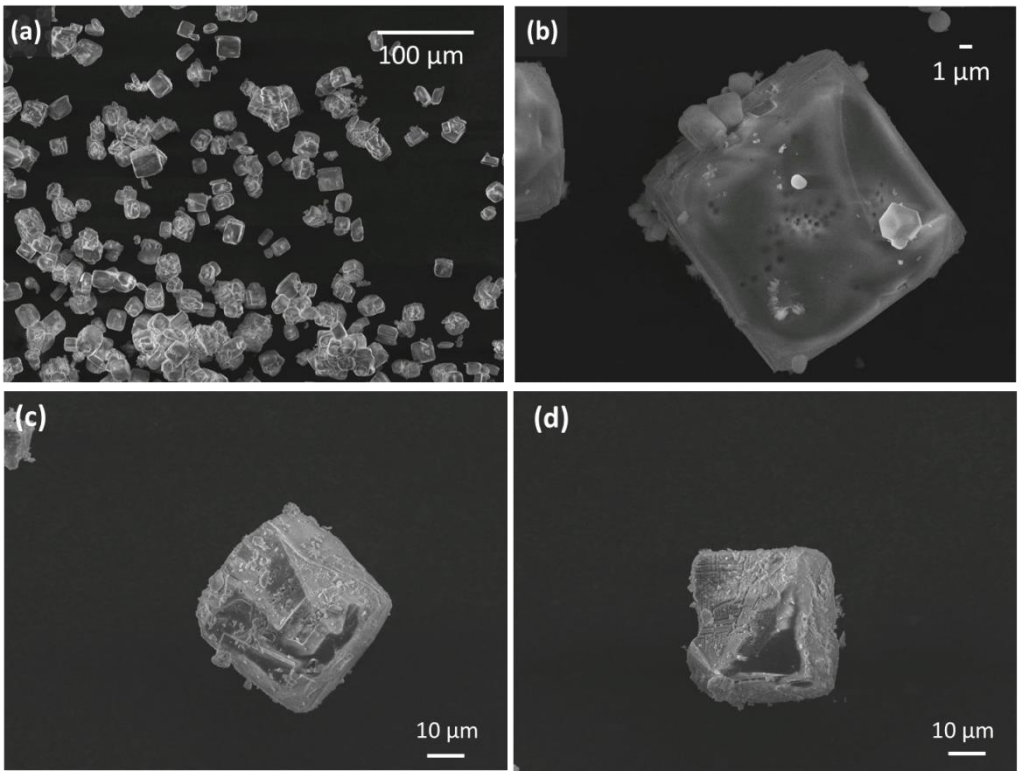

Figure 3.7 SEM micrographs of as-synthesised $[PtCl_4]^{2-}$ supported materials (a-b) and equivalent calcined materials (c-d)

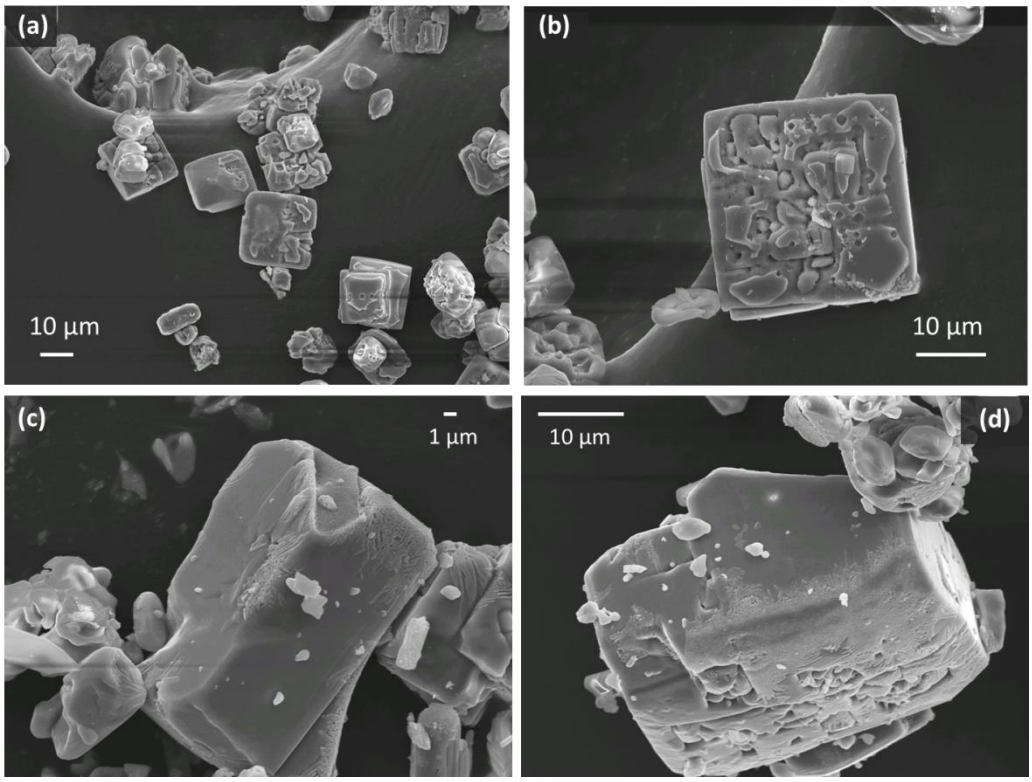

Figure 3.8 SEM micrographs of as-synthesised $[PdCl_4]^{2-}$ supported materials (a-b) and equivalent calcined materials (c-d)

For high resolution imaging of the framework crystals, a field emission scanning electron microscope (FESEM) was utilised so as to document not just the morphology of the framework crystals, but also any significant surface features. SEM micrographs of the Au/CuClP material have been reported previously,[29] but images were collected to confirm the crystal shape and distribution of samples prepared in this work (Figure 3.6 (a-b)). The morphology of the $[PtCl_4]^{2-}$ and $[PdCl_4]^{2-}$ supported phases have also been shown to have a homogenous distribution of cubic crystals across the synthesised material (Figure 3.7 (a-b) and Figure 3.8 (a-b)) with mean average crystal sizes in the region of 25-30 µm. Higher magnification images of the single-crystals have revealed that the surfaces on the Pd analogue appear roughened with clear features, whereas the Pt crystal faces are relatively smooth. As the noble metal chlorides are added to achieve similar wt % loadings, it is possible that elevated concentrations of Pd (owing to its lower atomic mass), or even chlorine content in the synthesis procedure, could influence the growth and surface topography of crystals in the hydrothermal

process. It is well known that high concentrations of chloride ions can have corrosive properties towards metals and other materials.[32]

SEM micrographs were also collected for each of the calcined materials (all (c-d) images in Figure 3.6, Figure 3.7 and Figure 3.8). Single-crystals are broken due to the grinding of the material in preparation for calcination and use as a catalyst, however there is clear evidence of fragmented single-crystals with retained cubic crystal morphology. Coupled with PXRD analysis, it is clear that the crystalline nature of the framework is unchanged through the calcination process.

Although some smaller fragments of the CuClP framework material can be seen in the SEM images, there was no clear evidence of large particles or crystals of metallic species in the as-synthesised Au, Pt and Pd/CuClP materials. The Au analogue did occasionally contain a large flake of crystalline gold that could be observed by eye in the filtered and washed batch of as-synthesised catalyst, but similar to the other two materials, no significant micron-sized metallic crystals were observed by SEM. It is hypothesised that due to the facile thermal reduction potential of $HAuCl_4$, reduction of a small fraction of the precursor gold salt occurred in the hydrothermal vessel before the formation of the $[AuCl_4]^-$ supported porous framework. Accurate loadings of noble metals were calculated by ICP-OES as discussed earlier and used for quantitative analysis of catalyst activity.

Table 3.4 EDX Spectra of as-synthesised and calcined Pt and Pd/CuClP materials

Catalyst Material	EDX Spectra
Pt/CuClP	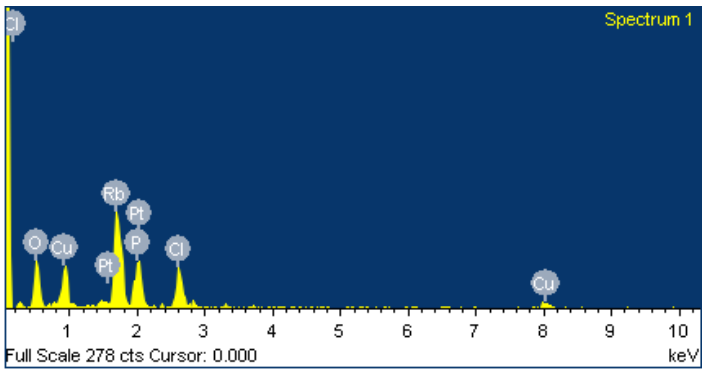

Catalyst Material	EDX Spectra
Pt/CuClP (calcined)	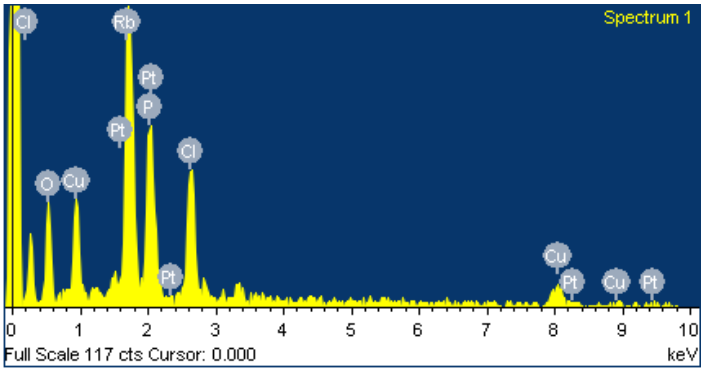
Pd/CuClP	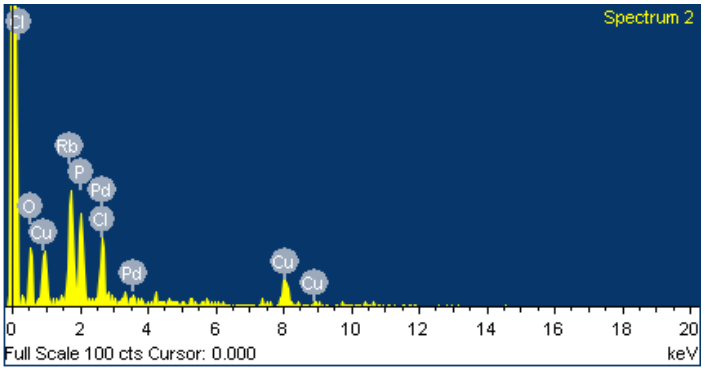
Pd/CuClP (calcined)	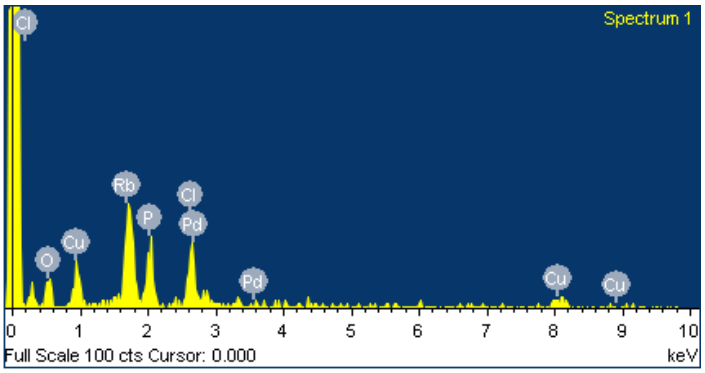

EDX analysis was also used for a qualitative study on probing the presence of noble metals across the material. Table 3.4 shows some representative spectra from each of the as-synthesised and calcined Pt and Pd/CuClP materials (EDX spectra of the Au/CuClP materials are reported elsewhere).[29, 31] Spectra were collected across 3-4 independent sites on the sample and are in good agreement. Due to the low loadings, the quantitative measurements had high associated errors so data was used from ICP measurements alone, however clear evidence of the presence of noble metals can be seen. One of the limitations of EDX is that it doesn't reveal any information on the nature of the noble metals, but as the probe depth of X-rays detected by the technique is

quite large at a few microns (see *Section 2.3.2.3*), it does provide representative information about the bulk of the material.

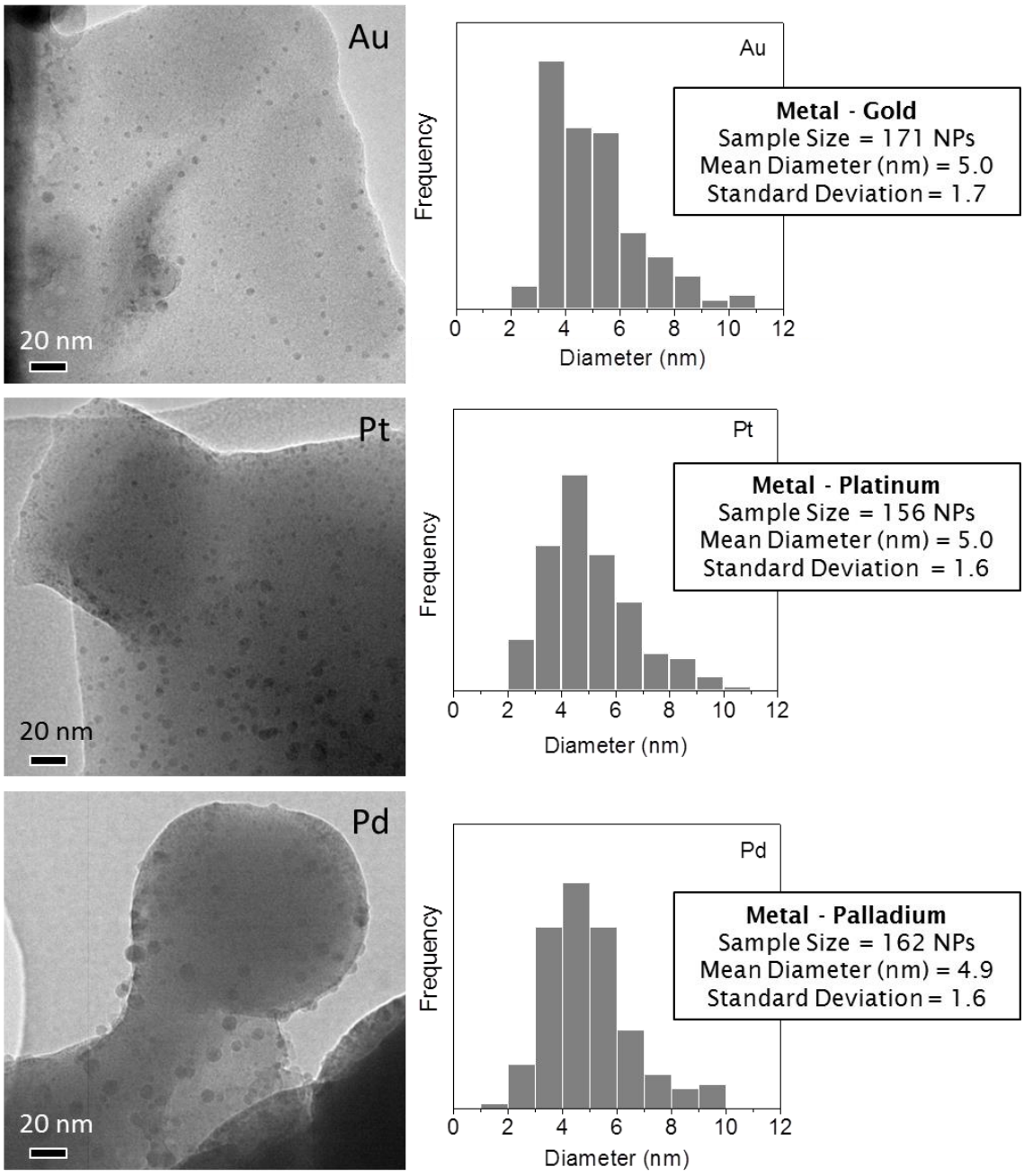

Figure 3.9 TEM images of calcined framework materials showing nanoparticles and respective particle size distributions

To deduce the nature of noble metal species clearly identified by PXRD and EDX analysis, TEM analysis of the calcined Au, Pt and Pd/CuClP catalyst materials was performed (Figure 3.9) to characterise the structural properties of the material surface in the nano-size regime. These images clearly reveal the

presence of well-defined, small metallic nanoparticles that are uniformly distributed across the chlorophosphate framework. As a result, the TEM images give clear evidence for the nature of the metallic species that were detected in the PXRD patterns. The majority of the nanoparticles display a spherical morphology with diameters ranging from 2-10 nm, but with average diameters of 5 nm for each of the materials. Particle size distribution histograms give a perspective on the particle sizes; whilst the average particle sizes are similar, it is noted that the distribution of gold nanoparticles shows the most asymmetry with modal preference of smaller particles between 3–4 nm. In conjunction with previous studies highlighted in the introduction, it would be expected that noble metal nanoparticles of these sizes and distributions should be active toward activating O_2 in select aerobic oxidation catalysis reactions.

3.2.3 Aerobic Oxidation of Benzyl Alcohol

The production of benzaldehyde is industrially significant as discussed in *Section 1.2.6.2*, and thus provides us with a relevant probe reaction for testing the aerobic oxidation capabilities of these materials. There is also a range of literature using NP catalysts for this reaction, as discussed in the same section, which gives us a benchmark for comparing these calcined NP catalysts with NP catalysts prepared by more traditional methods.

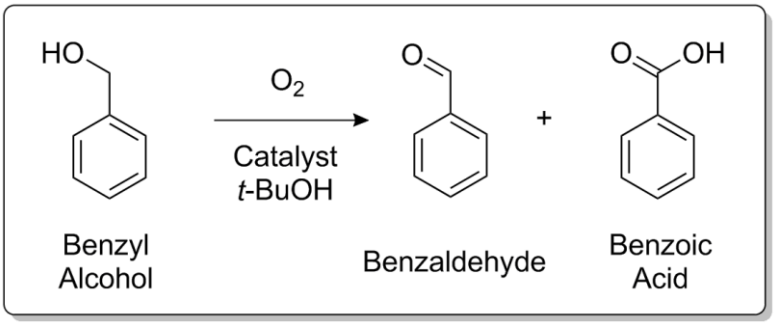

Scheme 3.1 Aerobic oxidation of benzyl alcohol to benzaldehyde and benzoic acid

Scheme 3.1 highlights the reaction and conditions that will be used for the aerobic oxidation of benzyl alcohol, with two main products; benzaldehyde, the desired product, and benzoic acid, a common over-oxidation by-product. Other literature has reported the formation of benzyl ethers as by-products,

however these tend to be more abundant in the oxidation of toluene or with peroxide-based oxidants.[33]

3.2.3.1 Establishing Working Catalytic Parameters

A few variables were taken into consideration when determining the working conditions for the selective aerobic oxidation of benzyl alcohol to benzaldehyde using NP/CuClP catalysts.

Benzyl Alcohol to Catalyst Ratio

As the catalyst was synthesised in relatively small batches, it was decided that 50 mg of catalyst with metal NP loadings of around 3-7 wt % was a reasonable amount to use per catalytic run. As such, 1g of benzyl alcohol was also determined to be a reasonable amount of substrate, providing a substrate to metal molar ratio of approximately 900:1 (based on 4 wt % Au loading) but dependent on the specific metal and metal loadings. Previous studies have also used similar ratios.[31]

Choice of Solvent

Due to the requirement to sample the reaction mixture over time, a solvent was necessary in the reactor setup. For all reactions, *tert*-butanol is used as a solvent for a variety of reasons. As *t*-butanol is a tertiary alcohol, it is itself resistant to facile oxidation compared with other isomers of butanol as there is no hydrogen atom on the α-carbon to facilitate any dehydrogenative oxidation mechanisms. It is a convenient solvent as it is able to solubilise a wide array of different organic compounds and is miscible in water,[34] preventing any competing hydrophobic/hydrophilic properties that could prevent effective diffusion at the catalyst surface. Consequently, this solvent is widely used in industrial processes.

Calculation of Oxygen (O_2) Concentrations

The molar quantity of oxygen present in the reactor for an oxidation reaction can be calculated by using the ideal gas law. The total volume of the reactor, including the volume of spaces within the head of the reactor, was calculated to be 75 mL. Typical reactions charged the reactor vessel with 30 mL of solvent, thus 45 mL of headspace is left after sealing the reactor.

The ideal gas law is written as in Equation 3.1.

$$PV = nRT \qquad \textbf{Equation 3.1}$$

Where *P* is the pressure, *V* is the volume occupied by the gas, *n* is the moles of gas, *R* is the ideal gas constant and *T* is the temperature. To calculate the moles, the equation can be rearranged for *n* as in Equation 3.2.

$$n = \frac{PV}{RT} \qquad \textbf{Equation 3.2}$$

Dry air is used as the source of O_2 with a percentage concentration of 21 %. As such, the partial pressure of O_2 will be substituted for total pressure in the equation to calculate the specific mole quantity. As the reactor is pressurised to 20 bar, this equates to a partial pressure of 4.2 bar for molecular oxygen.

$$n = \frac{4.2\ bar\ \times 45\ mL}{8.314\ Jmol^{-1}K^{-1}\ \times 298\ K} \qquad \textbf{Equation 3.3}$$

$$n = \frac{4.2\ \times 10^{5} kgm^{-1}s^{-2}\ \times 4.5\ \times 10^{-5} m^{3}}{8.314\ Jmol^{-1}K^{-1}\ \times 298\ K} \qquad \textbf{Equation 3.4}$$

$$= 7.629\ \times 10^{-3}\ mol$$

Converting to standard SI units gives the values as shown in Equation 3.4 which can be solved to give the moles of oxygen present in the reactor at 7.6 x 10^{-3} mol.

3.2.3.2 Comparison of Kinetics between Analogous Au, Pt and Pd Systems

Probing Catalytic Activity and Selectivity Properties

Reactions were carried out in a range of temperatures between 100 °C and 140 °C. Temperatures lower than this range produced negligible conversions, and higher temperatures sacrificed on the selective properties of the catalyst, yielding high levels of the undesirable benzoic acid. It was decided that identical reactions would be carried out at 130 °C as a compromise between activity and selectivity, and to compare the properties of different catalyst calcined under identical conditions.

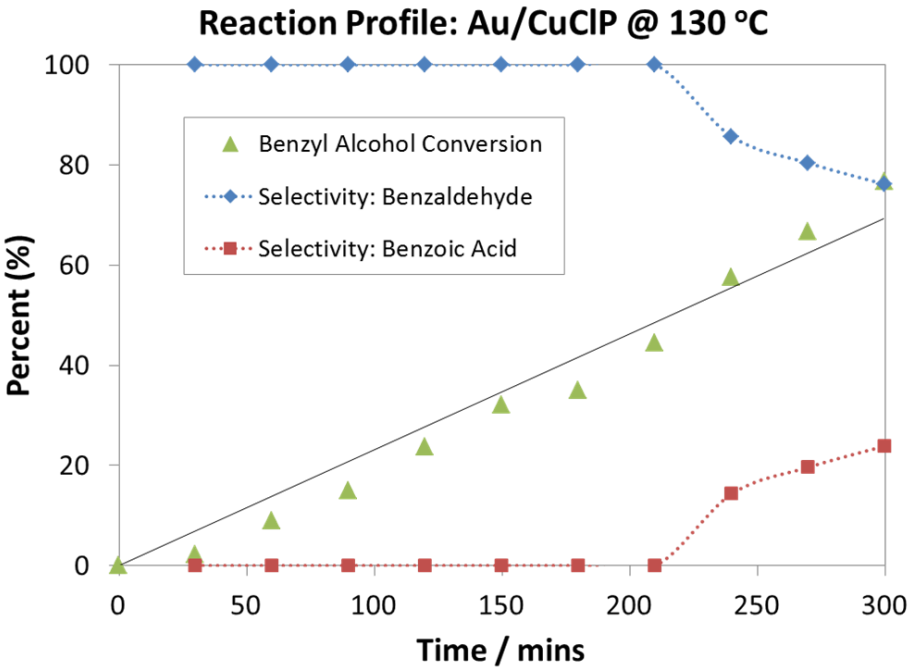

Figure 3.10 Reaction profile of aerobic oxidation of benzyl alcohol using calcined Au/CuClP catalyst. Benzyl alcohol (1.00g), catalyst (50 mg), diglyme (0.85 g), *tert*-butanol (30 mL), air (20 bar)

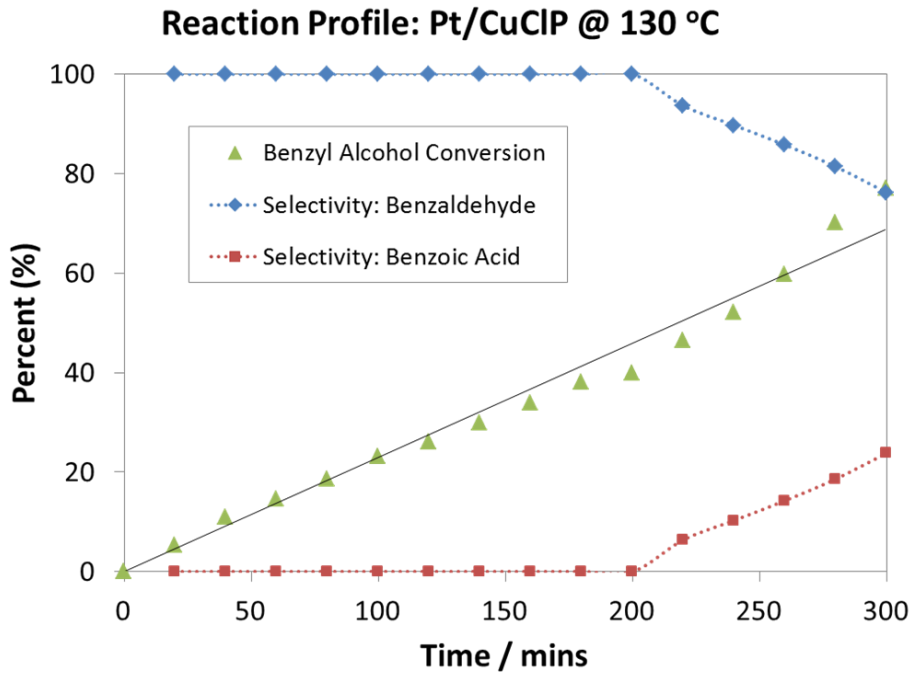

Figure 3.11 Reaction profile of aerobic oxidation of benzyl alcohol using calcined Pt/CuClP catalyst. Benzyl alcohol (1.00g), catalyst (50 mg), diglyme (0.85 g), *tert*-butanol (30 mL), air (20 bar)

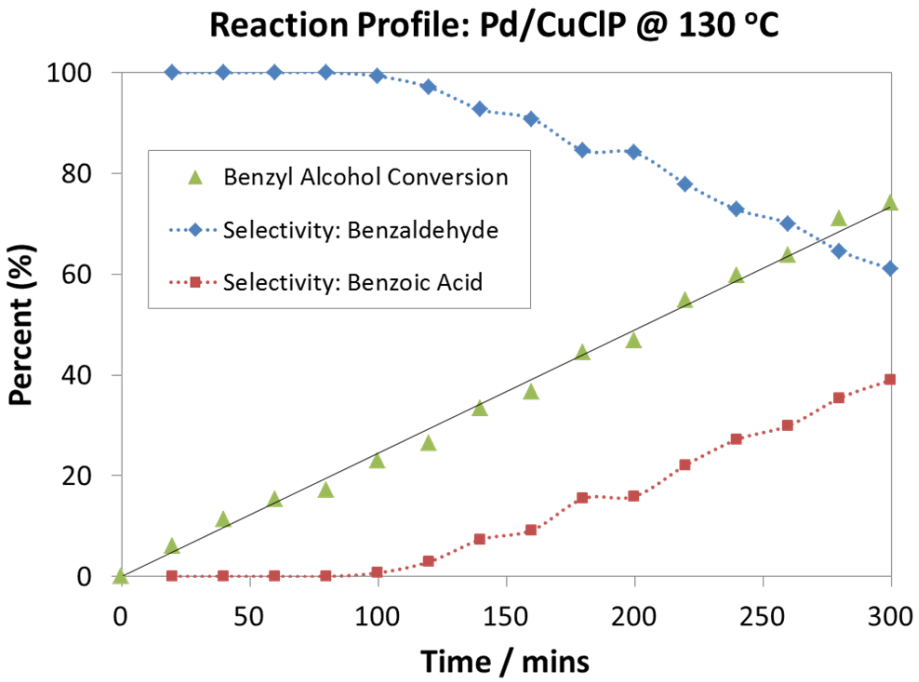

Figure 3.12 Reaction profile of aerobic oxidation of benzyl alcohol using calcined Pd/CuClP catalyst. Benzyl alcohol (1.00g), catalyst (50 mg), diglyme (0.85 g), *tert*-butanol (30 mL), air (20 bar)

In the preceding figures, the conversions of benzyl alcohol are normalised against the concentration of molecular oxygen in the system. As calculated in the previous section the quantity of oxygen (7.629×10^{-3} mol) is less than the quantity of benzyl alcohol (9.259×10^{-3} mol) representing a relative quantity of 82.4 mol% of oxidant. As 1 mol of oxygen is required to convert 1 mol of benzyl alcohol to benzaldehyde, this equates to a maximum benzyl alcohol conversion of 82.4 %. As such, conversions are normalised against this value, with a normalised conversion of 100 % equal to an absolute conversion of 82.4 %.

It is interesting to note that each of the noble metal catalysts (subjected to identical calcination conditions) demonstrate varying catalytic properties. The rates of conversion of benzyl alcohol are similar, with each achieving similar degrees of normalised conversion after 300 minutes of reaction, with the major differences observed in the selectivity profiles. Both the gold and platinum calcined catalysts maintain quantitative selectivities up to 200 minutes of reaction (approximately 50% normalised conversion) before the detection of benzoic acid as a by-product. At this point, benzoic acid is

produced in larger quantities with the gold catalyst compared with the platinum. In contrast, the palladium catalyst appears more unselective in its oxidation products, with benzoic acid being detected after just 100 minutes of reaction (~20 % normalised conversion).

Table 3.5 Comparison of catalytic data comparing conversion of benzyl alcohol with Au, Pt and Pd/CuClP calcined catalysts after 240 mins

CuClP Catalyst	Normalised Conversion (%)	Selectivity (%)	
		Benzaldehyde	Benzoic Acid
Blank	6.0	≥ 99.9	≤ 0.1
Au	57.5	85.6	14.4
Pt	52.1	89.7	10.3
Pd	59.7	72.8	27.2

Table 3.6 Comparison of catalytic data at isoconversion of benzyl alcohol with Au, Pt and Pd/CuClP calcined catalysts (estimated from plots)

CuClP Catalyst	Normalised Conversion (%)	Reaction Time (mins)	Selectivity (%)	
			Benzaldehyde	Benzoic Acid
Au	54	234	88	12
Pt	54	235	91	9
Pd	54	221	78	22

It is easy to observe from Table 3.5 showing the catalytic data for each of the catalysts after 240 mins of reaction, in conjunction with the reaction profile plots, that these catalysts do indeed have very different properties with the platinum catalyst maintaining superior selectivity over the other catalyst analogues. In fact, Table 3.6 shows even more compelling data that at an isoconversion of 54 % when benzoic acid was observed in all reaction samples, the selectivity properties for each catalyst are still different, eliminating the

possibility that each catalyst is operating with identical properties at different rates. These data also confirm that the calcined platinum catalyst has superior selectivity towards the aldehyde in comparison with the calcined gold and palladium catalysts. Oxidant efficiencies were calculated for the three catalysts based on conversion of benzyl alcohol. Under these conditions, the efficiencies are similar (Table 3.7), however follow trends similar to that observed for comparative conversions due to the identical conditions and quantities of O_2 employed.

Table 3.7 Oxidant efficiencies and catalytic activity measured by TON and TOF numbers of calcined Au, Pt and Pd/CuClP catalysts (TONs after 5 hours of reaction @ 130 °C)

CuClP Catalyst	Oxidant Efficiency (%)	TON	TOF (h^{-1})
Au	54.6	358	72
Pt	56.9	798	160
Pd	60.5	354	71

Putting these catalytic results more into context, Table 3.7 shows the TONs and TOFs of each of the catalysts based on the mole conversion of benzyl alcohol and the mole quantity of the noble metal present on the catalyst. As was seen in the reaction profiles and associated data, similar levels of conversion were observed for each of the calcined catalysts; however the platinum catalyst had a lower weight % loading as determined by ICP analyses. As such, the conversion per mole of metal (TON) is much higher, indicating that the calcined platinum catalyst is much more active. As a result of the oxidation reaction studies, it is clear to see that the calcined platinum catalyst is the most active and selective for the aerobic oxidation of benzyl alcohol to benzaldehyde.

Reaction profiles for each catalyst performed at 120 °C are shown in Figure 3.13 which highlight that these materials follow the same trends, in terms of relative conversion and selectivity, at lower temperatures. The calcined palladium material is still the least selective, and the platinum and gold materials maintain good selectivity and similar activity as before. The main difference is reduced rates compared with the 130 °C plots which

corresponds with the temperature dependence of the reaction and discussed in more depth later in the section.

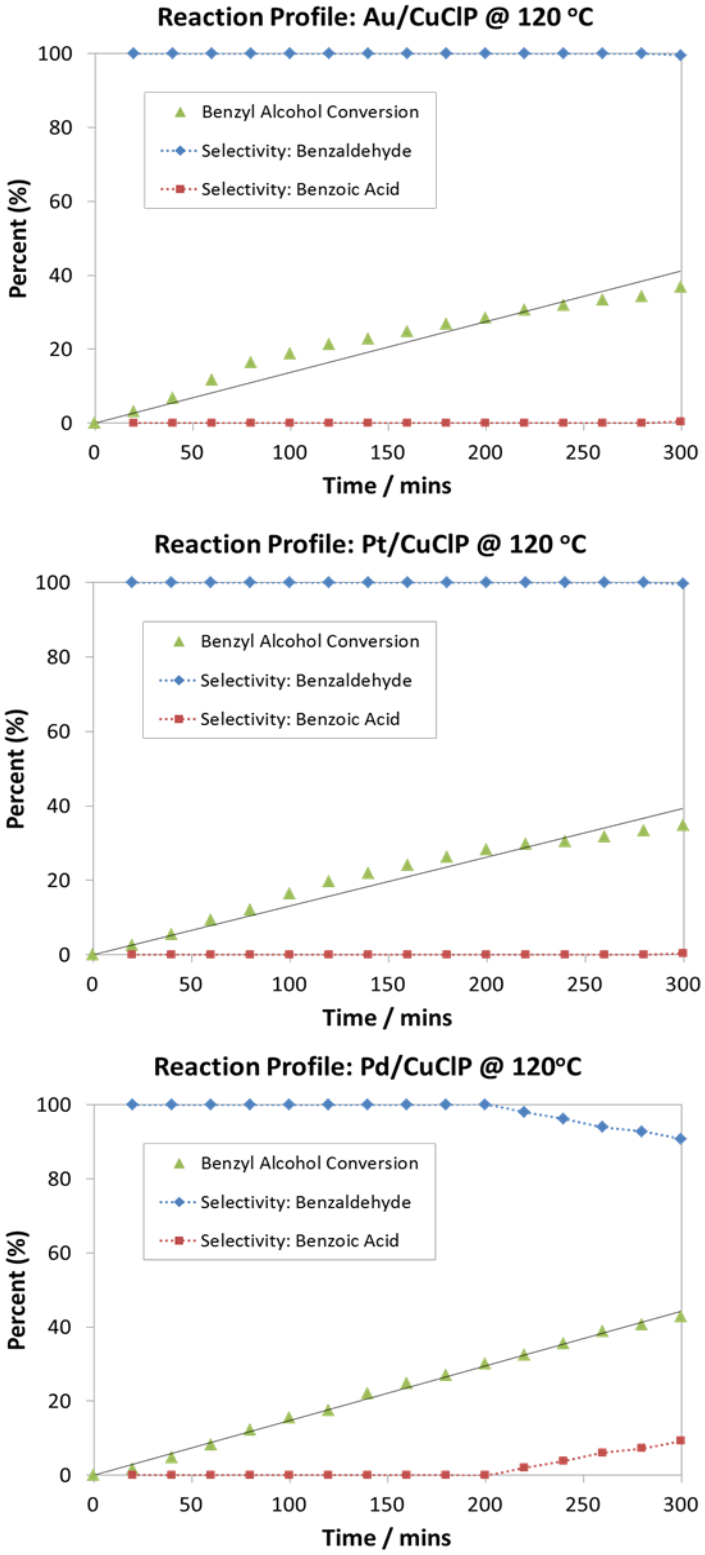

Figure 3.13 Reaction profiles of calcined gold, platinum and palladium NP materials at 120 °C. Benzyl alcohol (1.00g), catalyst (50 mg), diglyme (0.85 g), *tert*-butanol (30 mL), air (20 bar)

Kinetic Studies on Au, Pt and Pd/CuClP

Further kinetic studies were performed on each of the calcined Au, Pt and Pd/CuClP catalysts in an effort to determine the activation parameters for the reaction. To calculate activation energies (E_a), Arrhenius plots must be generated by conducting the reaction under identical conditions at three temperatures, sampling the reactions at least 10 times over the course of the reaction to quantitatively measure the development of absolute substrate conversions with time.

The following plots (Figure 3.14, Figure 3.15 and Figure 3.16) summarise the kinetic data collected for the three calcined catalysts at three temperatures in the pre-determined range. Linear trendlines are fitted to the data (forced through the origin) which show a good correlation to the data and thus indicate a zero-order rate of reaction with respect to the concentration of the substrate.

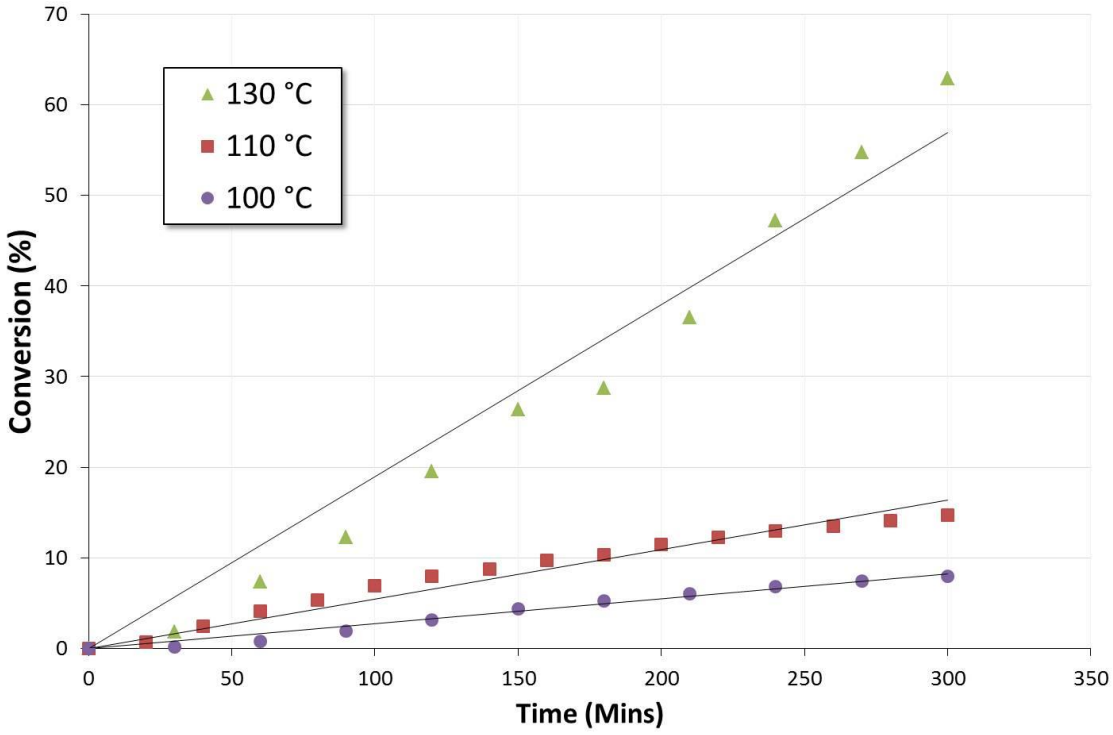

Figure 3.14 Kinetic plots of benzyl alcohol oxidation (absolute conversion) over time at different temperatures using Au/CuClP catalyst

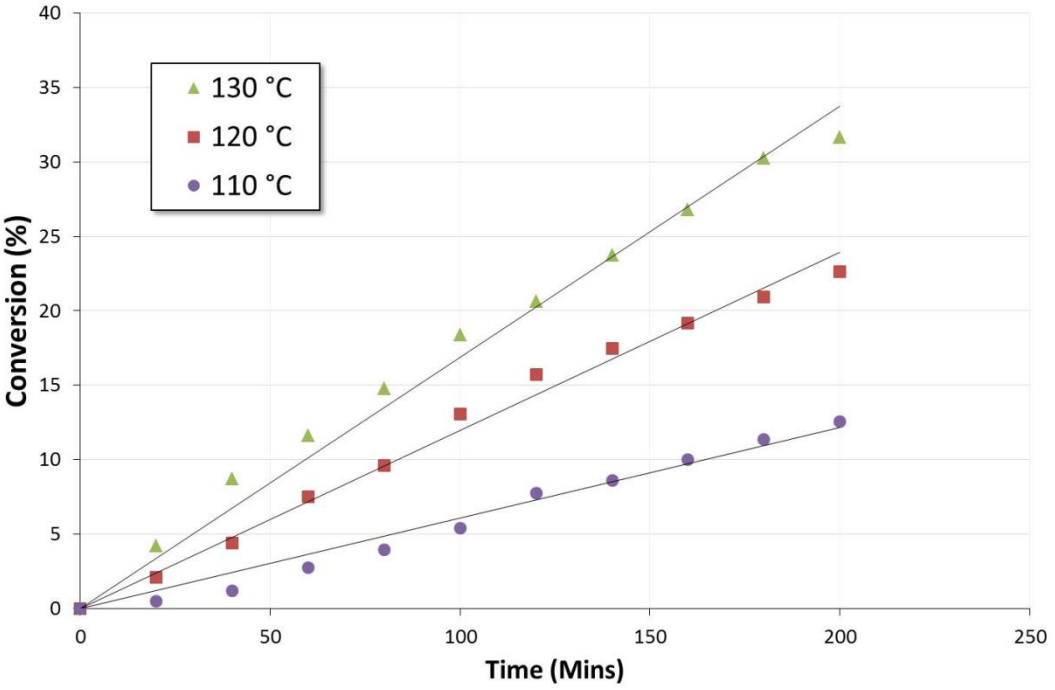

Figure 3.15 Kinetic plots of benzyl alcohol oxidation (absolute conversion) over time at different temperatures using Pt/CuClP catalyst

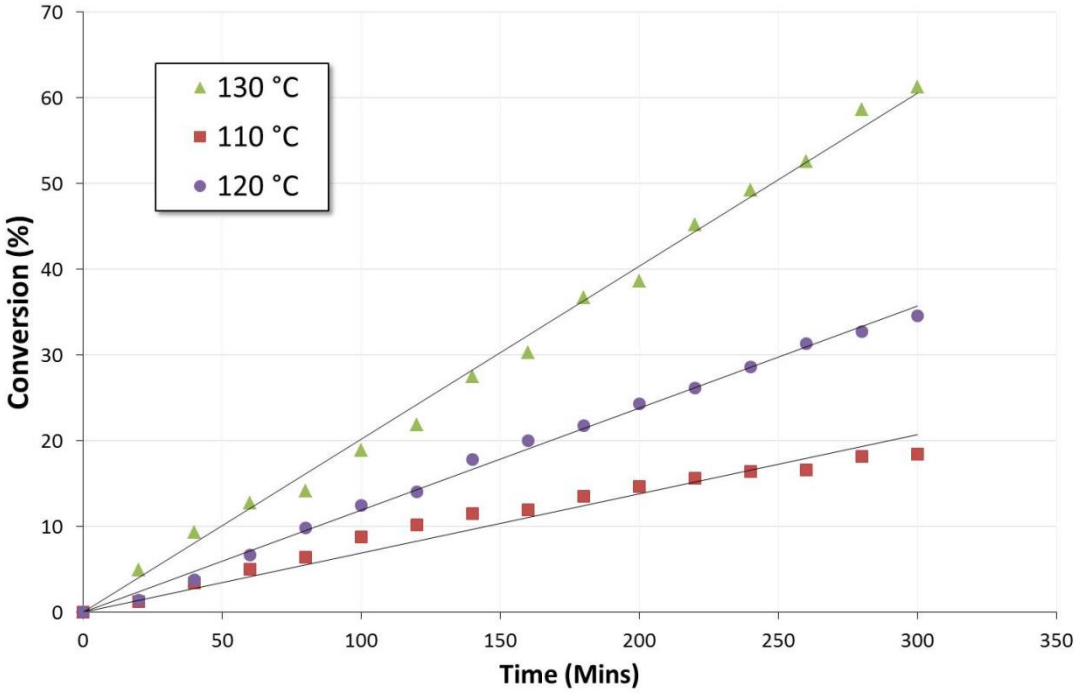

Figure 3.16 Kinetic plots of benzyl alcohol oxidation (absolute conversion) over time at different temperatures using Pd/CuClP catalyst

The quality of fit is reduced slightly for the higher temperature kinetic studies (measured by the R factors) and are likely due to experimental and equipment errors. The batch reactor is fitted with a feedback response hotplate and thermocouple to regulate the temperature. Where the thickness of the steel walls induced a lag-time between the response of the heating plate and a detectable rise in temperature, a small fluctuation in temperature about the set-point was noted over the course of the reaction. It was also observed that this fluctuation error was more pronounced at higher temperatures (in terms of absolute temperature) and could well have contributed to these minor discrepancies.

By applying the linear Arrhenius equation as described in Equation 1.4 in the introduction, it is possible to plot the natural log of the rate against 1/T to produce a linear graph with an gradient equal to $-E_a/R$ and an intercept of ln(A) (where E_a is the activation energy, R is the gas constant and A is the pre-exponential factor). Values for each of the kinetic plots have been plotted as shown in Figure 3.17 with the associated trendline equations and r-factors. Activation energies are calculated from these equations and displayed in the table inset within Figure 3.17.

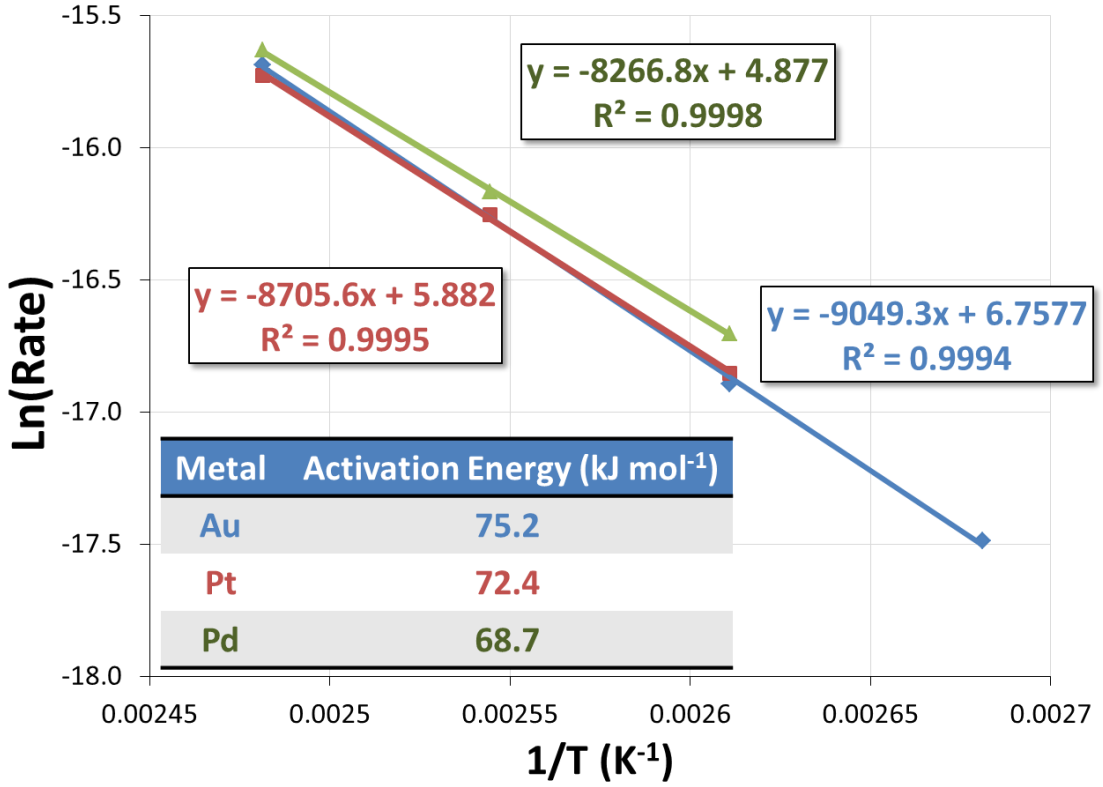

Figure 3.17 Arrhenius plot showing trendlines for calculation of activation energies

The calculated activation energies are in agreement with the previously reported literature for noble metal nanoparticle catalysts in the aerobic oxidation of benzyl alcohol;[35-37] whilst proving to be lower than those reported for the homogenous nitric acid oxidation of benzyl alcohol (95 kJ/mol)[38] and other heterogeneous catalysts based on molybdenum and tungsten at 84 and 96 kJ/mol respectively.[39-40]

This kinetic study is focused on the oxidation of benzyl alcohol to benzaldehyde and the respective activation energies; however one of the main limitations to this kinetic study is the observation of the formation of benzoic acid in the system, adding a level of complexity to the system that could influence the kinetic calculations. However, the kinetic parameters are determined on the basis of the conversion of the alcohol. Mechanistically, in the oxidation of benzyl alcohol on noble metal nanoparticle catalysts, it is generally accepted that the formation of the acid occurs solely from oxidation of the aldehyde product and not from direct oxidation of the alcohol.[33, 41] As a

result, it can be concluded that the formation of benzoic acid doesn't have a significant effect on the benzyl alcohol conversion directly.

On the other hand, where the production of benzoic acid could have an influence on the kinetics is in the depletion of oxygen from the system that is used in the over-oxidation of the aldehyde. Additionally, the formation of benzoic acid could also occur on the surface of the nanoparticles and thus compete with benzyl alcohol in surface adsorption. Nevertheless, a linear relationship is observed for the oxidation reactions both before and after the formation of benzoic acid is observed, with little effect on the rate of reaction for the conversion of benzyl alcohol to benzaldehyde. As a result, it can be concluded that the kinetic study is accurate in this case, despite the formation of benzoic acid as a by-product.

Recycling of Catalysts

Table 3.8 Recycle data for aerobic oxidation of benzyl alcohol showing conversion and benzaldehyde selectivity for the calcined Pt/CuClP catalyst at 130 °C after 5 hours.

Catalytic Data	1st Cycle	3rd Cycle
Conversion (%)	76.6	67.0
Selectivity (%)	76.2	82.1

Recycle tests for the best catalyst – the calcined Pt/CuClP material – shows that the materials can be effectively used for at least 3 cycles with a noted drop in activity of 9 %. Taking into account that some catalyst can be lost through sampling and the presence of a degree of error in the GC analysis, it is possible to conclude that the reduction in activity is negligible over 3 cycles, and thus proves to be a recoverable and recyclable catalyst.

3.2.3.3 Structural Characterisation Post-Catalysis

To test whether these catalysts are acting in a "true" heterogeneous fashion, it is necessary to determine that the reactions are occurring on NPs that are adhered to the surface of the framework host. ICP-OES data were collected for the reaction mixtures to accurately test for leaching of NPs into solution.

Table 3.9 Metal leaching studies conducted by ICP analyses on used reaction solutions

Metal	Maximum Concentration (ppm)	Concentration (ppm)	Metal Leaching (%)
Gold	137	0.1	< 0.1
Platinum	58	2.0	3.4
Palladium	71	< 0.1	< 0.1

ICP analyses were carried out by MEDAC Ltd. on the reaction solutions extracted post-catalysis. The maximum ppm values that would be observed if all the supported metal had leached was calculated and shown in Table 3.9, based on the relative quantities of catalyst used for the reaction mixture. As can be seen, low to negligible amounts of Au or Pd were detected, exemplifying the sufficient adhesion of the nanoparticles to the surface of the host framework material. Although a notable, but small fraction of Pt was detected in the reaction solution, this would not prevent the catalyst from being reused and plausibly a result of the much higher TONs noted for the Pt/CuClP catalyst. Given the lower Pt content compared with the Au and Pd catalysts, the loading could potentially be increased to maximise yields and efficiencies. Under these reaction conditions, the implications are that the catalyst is stable and suitable for multiple catalytic cycles (discussed later).

It is also necessary to probe the integrity of the material after use in a catalytic reaction to eliminate the possibility of decomposition products affecting the catalytic results. Powder X-ray diffraction was performed on the used catalysts to probe the crystallinity and integrity of the CuClP framework, as well as to test for the detection of crystalline metallic noble metal phases post-catalysis as seen in the patterns of the fresh calcined materials. As can be seen from previous characterisation[31] and in the following patterns (Figure 3.18, Figure 3.19 and Figure 3.20), there is a qualitative agreement in the reflections in the catalyst both before and after the catalytic process. Where relevant, the peaks corresponding to the metallic nanoparticle phases are also still visible. The intensity and sharpness of all peaks are relatively reduced in the used catalyst patterns; however this is likely due to a minor reduction in particle size

caused by grinding of the materials in the reactor from the magnetic stirring mechanism. Due to the small quantity of catalyst after a reaction, PXRDs were collected by depositing some of the material from an ethanolic suspension onto a flat surface to be inserted into the diffractometer for analysis.

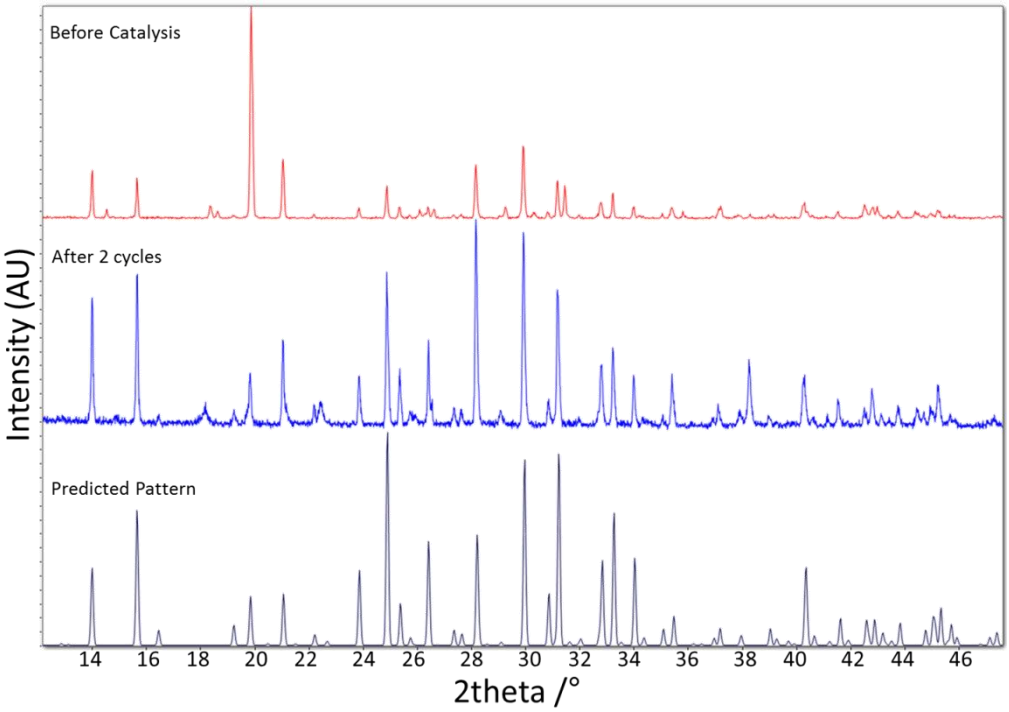

Figure 3.18 PXRD Patterns of fresh calcined Au NP material (red) and after 2 cycles in a catalytic reaction (blue)[31]

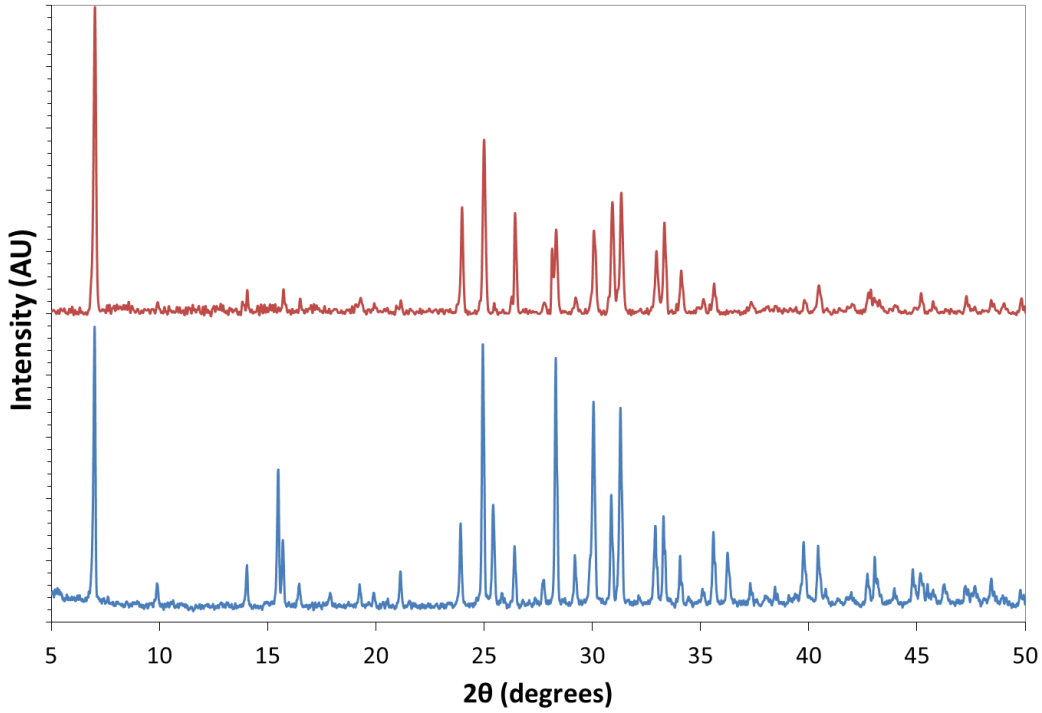

Figure 3.19 PXRD Patterns of fresh calcined Pt NP material (blue) and after use in a catalytic reaction (red)

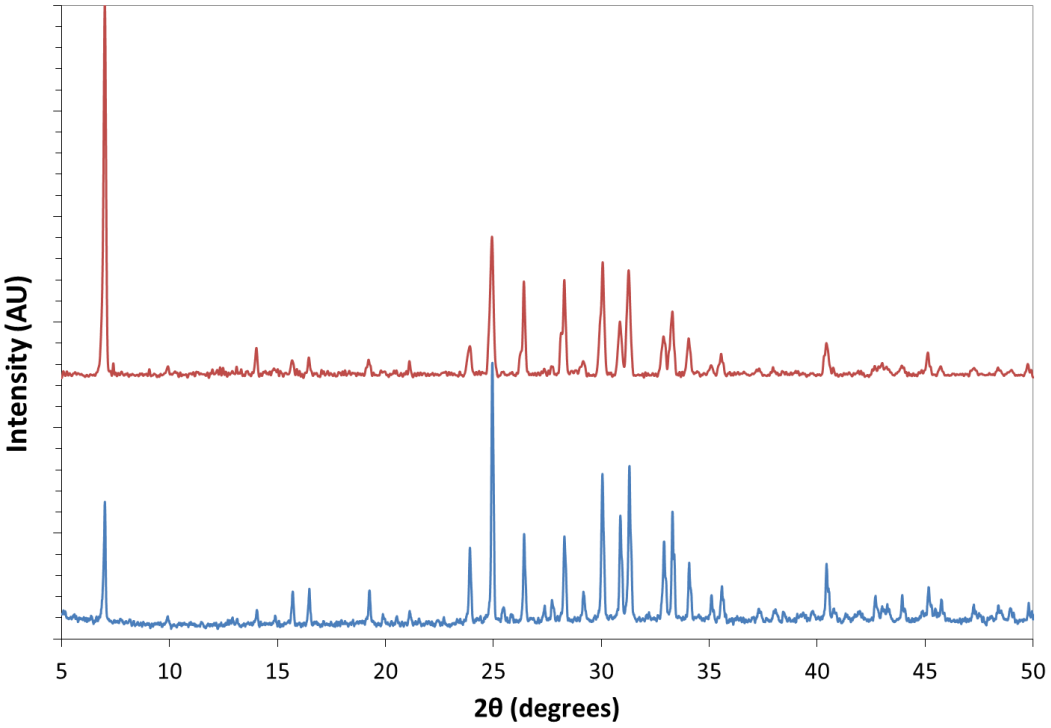

Figure 3.20 PXRD Patterns of fresh calcined Pd NP material (blue) and after use in a catalytic reaction (red)

Small discrepancies in the relative peak intensities are a result of sample preparation where preferred orientation can occur through flattening of the powdered sample into a sample holder. The reflection peaks in all samples are still well resolved with a high signal-to-noise ratio and at corresponding values of 2θ between patterns.

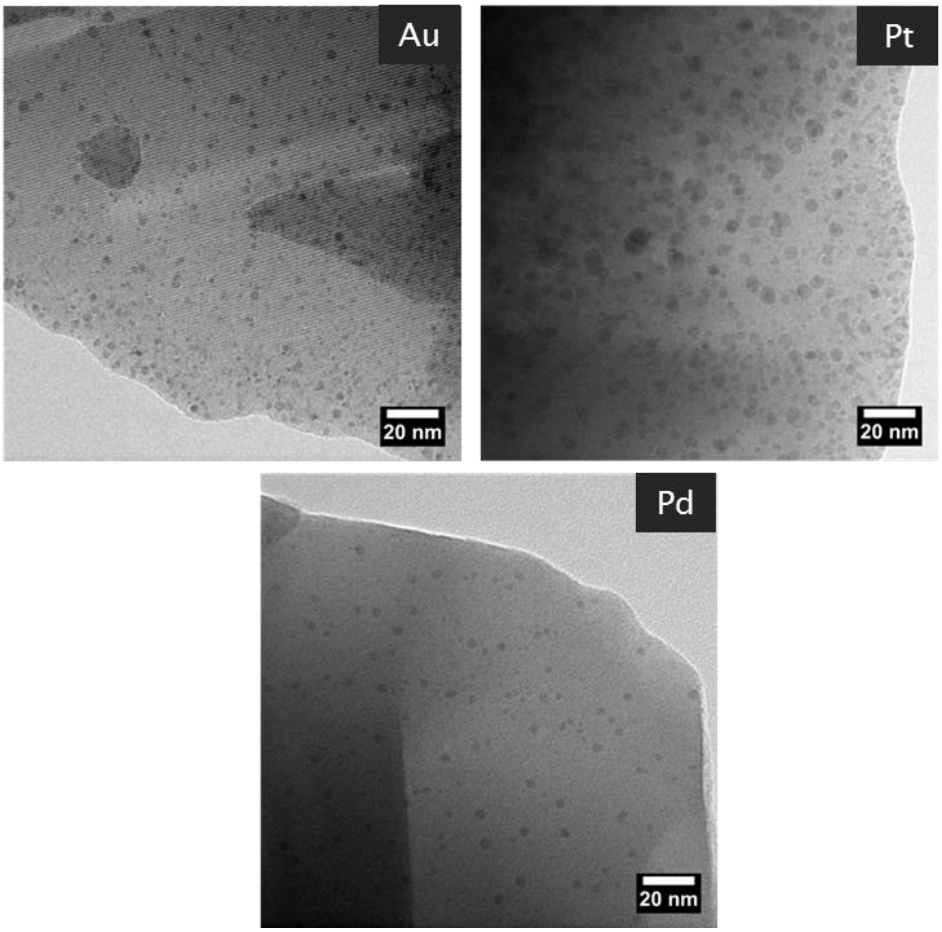

Figure 3.21 TEM images of NP materials after use in a catalytic process

Interestingly, TEM images of all three used catalysts (Figure 3.21) show that nanoparticles have maintained their monodispersity, site-isolation and adhesion to the surfaces of the CuClP framework. This was slightly unexpected due to the fact that reports of previous NP-based catalysts have been heavily dependent on stabilising or capping agents to prevent sintering and aggregation of NPs.[42-43] Capping agents were also required to maintain reasonable adhesion to the host surface and prevent leaching. What is observed in these materials is the opposite. This raises the question of why the integrity of the NP catalysts have remained unchanged, and could be indicative of superior interactions between the host framework surface and the *in situ*

generated NPs. Further, more detailed characterisation is required to be able to expose a justification for this unconventional observation.

3.2.3.4 Probing Activation Times

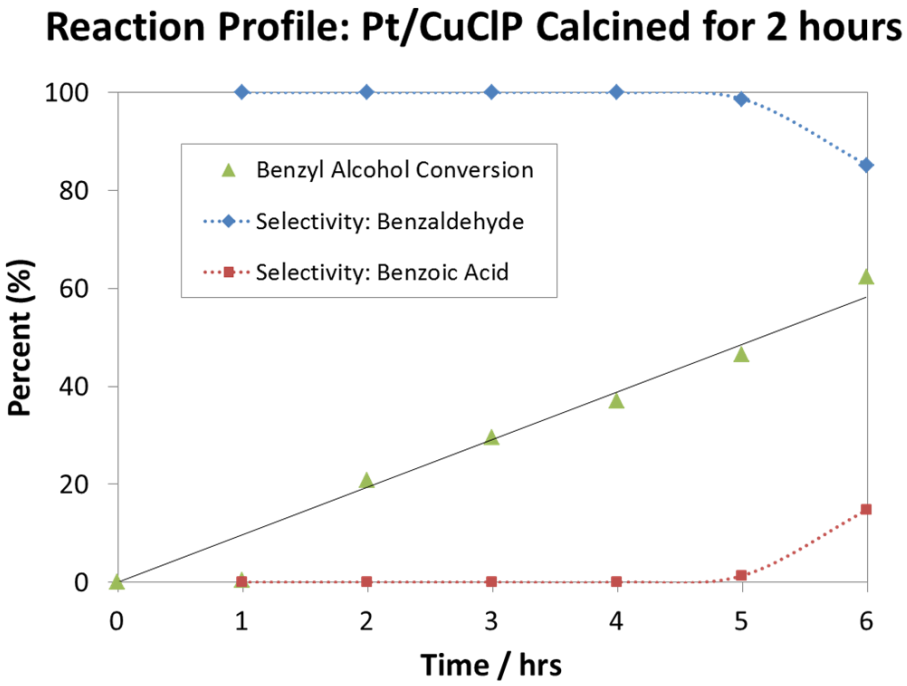

Figure 3.22 Reaction profile of aerobic oxidation of benzyl alcohol using Pt/CuClP catalyst calcined for 2 hours. Benzyl alcohol (1.00g), catalyst (50 mg), diglyme (0.85 g), *tert*-butanol (30 mL), air (20 bar), T = 130 °C.

Preliminary data was collected to identify catalytic differences between materials calcined at high temperatures for short and long periods. Due to the Pt/CuClP catalyst being the most active and selecitve to date, this material was studied for these effects. A sample of the Pt/CuClP catalyst, identified as the most promising catalyst from the kinetic studies, was calcined for 2 hours and used for the aerobic oxidation of benzyl alcohol akin to the previous studies where the materials were calcined for 16 hours. As can be seen in Figure 3.22, this material is also clearly active for this reaction, achieving significant conversions across the course of the 6 hour reaction. If these data is compared with the data collected for the 16 hour calcined material (Table 3.10; see also Figure 3.11), clear differences can be seen in the conversion rates and selectivity of products seen after 5 hours of reaction, with the 16 hour calcined material achieving better conversion but reduced selectivity. Interestingly, if

catalytic data at isoconversion are compared (Table 3.11), it appears that the materials show an almost identical profile in terms of selectivity, with the key differences related to the rates of conversions.

Table 3.10 Catalytic data for the aerobic oxidation of benzyl alcohol at 130 °C for 5 hours using Pt/CuClP calcined for 2 hours and 16 hours

Calcination Time (Hrs)	Normalised Conversion (%)	Selectivity (%)		*k* (M/s)
		Benzaldehyde	Benzoic Acid	
2	46.5	98.6	1.4	8.71×10^{-6}
16	52.1	89.7	10.3	1.09×10^{-5}

Note: Rate constant (*k*) calculated from zero-order integrated rate equation

Table 3.11 Catalytic data at isoconversion for the aerobic oxidation of benzyl alcohol at 130 °C using Pt/CuClP calcined for 2 hours and 16 hours

Calcination Time (hrs)	Normalised Conversion (%)	Reaction Time (mins)	Selectivity (%)	
			Benzaldehyde	Benzoic Acid
2	45	280	≥ 99	≤ 1
2	50	310	97	3
16	45	195	≥ 99	≤ 1
16	50	217	96	4

This reveals two key properties of the materials; firstly, the selectivity profiles of each catalyst are dependent on the type and nature of noble metal species rather than on the activation parameters. Secondly, the activity of the catalysts - and therefore the rates of conversion - are somewhat dependent on the parameters of activation, with time being a variable factor. The rate constants for each of the calcined platinum materials are shown in Table 3.10 and highlight the degree of difference between the two catalysts for the reaction. The rate constant for the 16 hour calcined material is only a factor of 1.25 larger than for the 2 hour calcined material. This is not a significant difference

given the large difference in catalyst activation time. What this does highlight is that the activation parameters do have an effect and should be probed further to establish a trending relationship between the two variables.

3.3 Conclusions

In light of the catalytic properties and structural characterisation performed on these materials, it is clear to see that active metal NPs have successfully been generated through thermal extrusion and reduction of noble metal chloride anions from the pores of a microporous copper chlorophosphate. Data also reveals that activated under these conditions, the platinum NP catalyst is both the most active and selective in the aerobic oxidation of benzyl alcohol to benzaldehyde. Each noble metal NP catalyst was shown to have differing selectivity profiles, highlighting that the catalytic properties are related to the physical and chemical properties of the active site. Interestingly, from calculations of activation energies for each material in relation to this reaction under the given conditions, the palladium NP catalyst has the greatest effect by providing a lower energy pathway; however this has led to the material being a relatively unselective catalyst. The catalysts also show significant conservation of integrity of both the host framework and the nanoparticles.

From the literature, it is clear that bare noble metal NPs easily aggregate over time with inevitable deactivation of the catalysts. As such, stabilising agents are required to maintain the structural integrity and isolated nature of the NPs over many cycles of a catalytic reaction, sacrificing the available surface sites for reaction.[42, 44] In this work, it has been shown that uncapped nanoparticles can be generated *in situ* by thermal extrusion of anions that leads to a highly stable NP supported catalyst that is active for the aerobic oxidation of benzyl alcohol. Structural characterisation of materials post-catalysis clearly identify that NPs remain isolated and adhered to the framework surface, thus overcoming this limitation.

Although compelling evidence has already been presented for the structural features and resulting catalytic properties of the NP/CuClP catalysts, further characterisation is necessary to probe the nature of the noble metal species across the bulk rather than at isolated sites of characterisation as for the electron microscope techniques already utilised.

These results illustrate that these materials are indeed catalytically active, however thorough optimisation of the catalytic processes are yet to be realised. As a result of performing these reactions using one high-pressure reactor, high-throughput screening is not feasible in a realistic time-frame. However, to reveal the full potential of these catalysts, studies on the concentrations of the solvent, substrate and catalyst would need to be performed to determine the ideal working conditions for optimal activity and selectivity. Nonetheless, preliminary kinetic studies have shown that activation energies for the oxidation of benzyl alcohol are in agreements with values reported elsewhere for metal NP catalysts, further emphasising the success of this new extrusion method for generating active NP catalysts that already possess comparable properties. Comparing the calcined NP/CuClP catalyst materials withy catalytic data tabulated in *Section 1.2.6.2,* although similar yields and activities can be achieved, it has not yet been possible to achieve quantitative yields of benzaldehyde by aerobic oxidation of benzyl alcohol. Through a more thorough analysis of the structural properties and catalytic parameters, the catalysts can be engineered and optimised further to achieve closer to quantitative yields for this reaction. It would be interesting to examine the propensity of the NP/CuClP materials to achieve selective oxidation of other benzylic alcohols, linear allylic alcohols and saturated alcohols to see if functionality and stability of the substrate is an important factor in achieving high selectivity of products.

With nanoparticles already being utilised for a diverse range of reactions and chemical transformations, there is a large scope for applying this novel synthetic method for generating superior catalysts with these other catalytic reactions in mind. Other reactions of interest include selective oxidations of other industrially significant substrates (activation of C-H bonds in aliphatic molecules), hydrogenations and cross-coupling reactions such as Heck and Suzuki couplings.

3.4 References

1 E. M. Flanigen, B. M. Lok, R. Lyle Patton and S. T. Wilson, *Pure Appl. Chem.,* **1986**, *58*, 1351.
2 S. T. Wilson, B. M. Lok, C. A. Messina, T. R. Cannan and E. M. Flanigen, *J. Am. Chem. Soc.,* **1982**, *104*, 1146.
3 M. Dugal, G. Sankar, R. Raja and J. M. Thomas, *Angew. Chem., Int. Ed.,* **2000**, *39*, 2310.
4 W. Fan, B. Fan, M. Song, T. Chen, R. Li, T. Dou, T. Tatsumi and B. M. Weckhuysen, *Micro. Meso. Mater.,* **2006**, *94*, 348.
5 L. Gomez-Hortiguela, F. Cora, G. Sankar, C. M. Zicovich-Wilson and C. R. A. Catlow, *Chem. Eur. J.,* **2010**, *16*, 13638.
6 R. M. Leithall, V. N. Shetti, S. Maurelli, M. Chiesa, E. Gianotti and R. Raja, *J. Am. Chem. Soc.,* **2013**, *135*, 2915.
7 M. E. Potter, D. Sun, E. Gianotti, M. Manzoli and R. Raja, *Phys. Chem. Chem. Phys.,* **2013**, *15*, 13288.
8 E. Gianotti, M. Manzoli, M. E. Potter, V. N. Shetti, D. Sun, J. Paterson, T. M. Mezza, A. Levy and R. Raja, *Chem. Sci.,* **2014**, *5*, 1810.
9 K. Abu-Shandi, H. Winkler, B. Wu and C. Janiak, *CrystEngComm,* **2003**, 180.
10 P. Bonnet, J. M. M. Millet, C. Leclercq and J. C. Vedrine, *J. Catal.,* **1996**, *158*, 128.
11 K. H. Lii, Y. F. Huang, V. Zima, C. Y. Huang, H. M. Lin, Y. C. Jiang, F. L. Liao and S. L. Wang, *Chem. Mater.,* **1998**, *10*, 2599.
12 J.-X. Mi, C.-X. Wang, N. Chen, R. Li and Y. Pan, *J. Solid State Chem.,* **2010**, *183*, 2763.
13 K.-H. Lii, *J. Chem. Soc., Dalton Trans.,* **1996**, 819.
14 M. Riou-Cavellec, D. Riou and G. Ferey, *Inorg. Chim. Acta,* **1999**, *291*, 317.
15 J. R. D. DeBord, W. M. Reiff, C. J. Warren, R. C. Haushalter and J. Zubieta, *Chem. Mater.,* **1997**, *9*, 1994.
16 P. Y. Feng, X. H. Bu and G. D. Stucky, *Nature,* **1997**, *388*, 735.
17 A. Oki, M. Zeller, A. Reynolds, X. D. Qiu and A. D. Hunter, *J. Coord. Chem.,* **2007**, *60*, 995.
18 R. K. Chiang, *Inorg. Chem.,* **2000**, *39*, 4985.
19 X. You and L. Zhu, *Indian Journal of Chemistry,* **2010**, *49(A)*, 1478.
20 R. P. Bontchev, M. N. Iliev, L. M. Dezaneti and A. J. Jacobson, *Solid State Sci.,* **2001**, *3*, 133.
21 A. Choudhury, S. Neeraj, S. Natarajan and C. N. R. Rao, *Angew. Chem., Int. Ed.,* **2000**, *39*, 3091.
22 S. Neeraj, C. N. R. Rao and A. K. Cheetham, *J. Mater. Chem.,* **2004**, *14*, 814.
23 S. Neeraj, M. L. Noy and A. K. Cheetham, *Solid State Sci.,* **2002**, *4*, 397.
24 N. Rajic, A. Ristic and V. Kaucic, *Zeolites,* **1996**, *17*, 304.
25 G. Ferey, *J. Fluorine Chem.,* **1995**, *72*, 187.
26 T. Loiseau and G. Férey, *J. Fluorine Chem.,* **2007**, *128*, 413.
27 J. A. Armstrong, E. R. Williams and M. T. Weller, *J. Am. Chem. Soc.,* **2011**, *133*, 8252.
28 Q. Huang, M. Ulutagay, P. A. Michener and S.-J. Hwu, *J. Am. Chem. Soc.,* **1999**, *121*, 10323.
29 E. R. Williams, R. M. Leithall, R. Raja and M. T. Weller, *Chem. Commun.,* **2013**, *49*, 249.

30 Q. Huang, S.-J. Hwu and X. Mo, *Angew. Chem., Int. Ed.,* **2001**, *40*, 1690.
31 R. Leithall, Ph.D. thesis, University of Southampton (UK), **2014**.
32 B. D. Craig and D. S. Anderson, Chlorides in *Handbook of Corrosion Data*, 2nd ed., ASM International, Cincinnati, **1995**.
33 L. Kesavan, R. Tiruvalam, M. H. A. Rahim, M. I. bin Saiman, D. I. Enache, R. L. Jenkins, N. Dimitratos, J. A. Lopez-Sanchez, S. H. Taylor, D. W. Knight, C. J. Kiely and G. J. Hutchings, *Science,* **2011**, *331*, 195.
34 D. Stoye and W. Freitag, *Paints, Coatings and Solvents*, 2nd ed., Wiley-VCH, Weinheim, **1998**.
35 J. Pritchard, L. Kesavan, M. Piccinini, Q. He, R. Tiruvalam, N. Dimitratos, J. A. Lopez-Sanchez, A. F. Carley, J. K. Edwards, C. J. Kiely and G. J. Hutchings, *Langmuir,* **2010**, *26*, 16568.
36 A. M. Henning, J. Watt, P. J. Miedziak, S. Cheong, M. Santonastaso, M. Song, Y. Takeda, A. I. Kirkland, S. H. Taylor and R. D. Tilley, *Angew. Chem., Int. Ed.,* **2013**, *52*, 1477.
37 D. I. Enache, J. K. Edwards, P. Landon, B. Solsona-Espriu, A. F. Carley, A. A. Herzing, M. Watanabe, C. J. Kiely, D. W. Knight and G. J. Hutchings, *Science,* **2006**, *311*, 362.
38 S. R. Joshi, K. L. Kataria, S. B. Sawant and J. B. Joshi, *Ind. Eng. Chem. Res.,* **2004**, *44*, 325.
39 Solvay Interox Limited, A. Johnstone, K. T. Rowbottom, W. R. Sanderson, M. Jeff and M. Service, **1995,** *Oxidation of Alkylaromatics,* US Patent 5,473,101.
40 M. P. Chaudhari and S. B. Sawant, *Chem. Eng. J.,* **2005**, *106*, 111.
41 G. J. Hutchings and C. J. Kiely, *Acc. Chem. Res.,* **2013**.
42 J. A. Lopez-Sanchez, N. Dimitratos, C. Hammond, G. L. Brett, L. Kesavan, S. White, P. Miedziak, R. Tiruvalam, R. L. Jenkins, A. F. Carley, D. Knight, C. J. Kiely and G. J. Hutchings, *Nat. Chem.,* **2011**, *3*, 551.
43 A. Quintanilla, V. C. L. Butselaar-Orthlieb, C. Kwakernaak, W. G. Sloof, M. T. Kreutzer and F. Kapteijn, *J. Catal.,* **2010**, *271*, 104.
44 M. Luo, Y. Hong, W. Yao, C. Huang, Q. Xu and Q. Wu, *J. Mater. Chem. A,* **2015**, *3*, 2770.

3.5 Appendix

3.5.1 Experimental Methods

All chemicals used for materials synthesis and catalytic reactions were purchased from Sigma-Aldrich, Acros Organics or Fisher Scientific and used without further purification.

3.5.1.1 Synthesis of $[MCl_x]^{n-}$ supported Frameworks

Synthesis of $Rb_9Cu_6(P_2O_7)_4Cl_3.[MCl_4]$ (M = Au, Pt or Pd): Copper(II) fluoride (0.1168 g, 1.150 mmol), 85 wt % orthophosphoric acid (0.2 mL, 2.922 mmol), 50 wt % RbOH (0.28 mL, 2.382 mmol), RbCl (0.28 g; 2.316 mmol) and a source of MCl_x; $HAuCl_4$ (0.0978 g, 0.288 mmol), K_2PtCl_4 (0.1196 g, 0.288 mmol) or K_2PdCl_4 (0.0940 g, 0.288 mmol) are mixed in a PTFE liner of a custom-made 23 mL hydrothermal vessel. Due to the lack of liquid components and low quantities of reactants, the mixture is allowed to age for up to 1 hour and occasionally physically mixed to encourage a degree of homogenisation before heating.

The hydrothermal vessel is sealed in a steel autoclave and heated to 448 K for 2 days. Products form as brilliant green cuboid crystals for both the Au and Pt material, and light brown crystals for the palladium material. The crystalline materials are washed with deionised water (3 x 20 mL) to remove any excess salts and water soluble impurities. Samples are then dried and ground in a pestle and mortar prior to activation.

3.5.1.2 Activation by Thermal Extrusion

All catalyst materials in this chapter were calcined under a steady flow of dry air (measured approximately through the use of a bubbler; 2-3 bubbles per second) at 500 °C for 16 hours in a tube furnace to generate the active catalysts. After calcination, the Pd material appears unchanged in colour, but a minor change in the Au materials to a lighter green and a significant change in the Pt material was observed, becoming a darker khaki-green (Figure 3.23). The materials at this stage required no further treatment before use as catalysts.

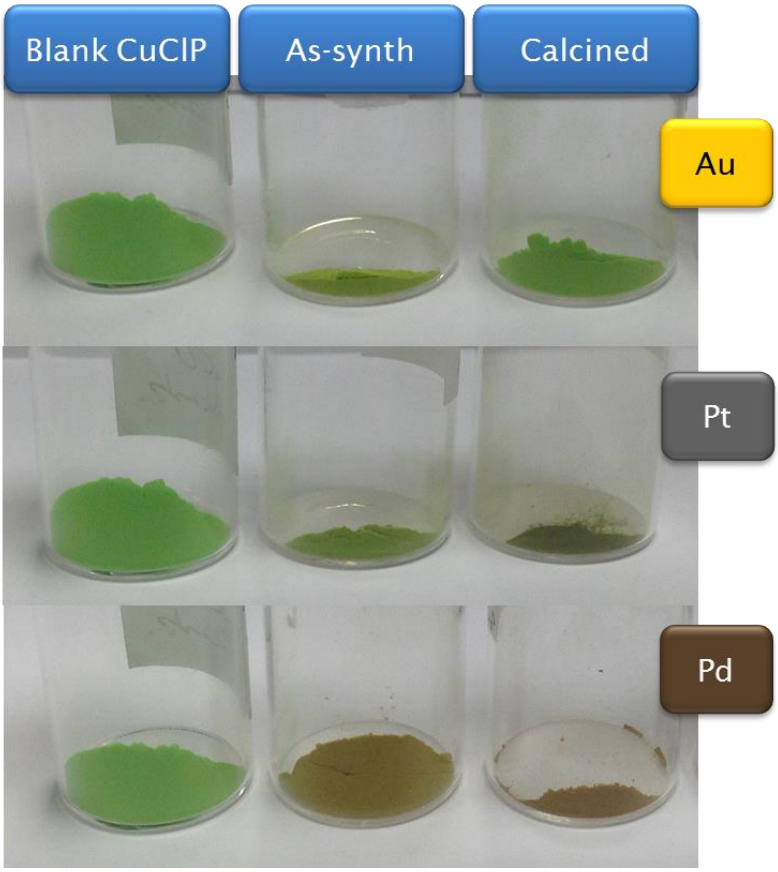

Figure 3.23 Photograph of the as-synthesised and calcined Au, Pt and Pd/CuClP materials compared with the blank framework

3.5.1.3 Aerobic Oxidation Reactions in High Pressure Batch Reactor

Heterogeneous oxidation catalysis was carried out in a 75 mL PTFE lined custom built batch reactor from Cambridge Reactor Design. The reactor was fitted with a pressure gauge, sampling port, thermostat with digital feedback to the heater/stirrer plate and a gas inlet port.

A typical catalytic reaction for the oxidation of benzyl alcohol is as follows; benzyl alcohol (1 g), diethylene glycol dimethyl ether (diglyme) as an internal standard (0.85 g) and *tert*-butanol as a solvent (30 mL) were weighed or measured into the 75 mL Teflon® liner. Subsequently, a catalyst material was weighed (0.05 g) and added to the mixture. A magnetic stirrer bar was added and the mixture stirred to achieve a homogenous distribution of reactants.

The liner was then sealed in the batch reactor and pressurised to 20 bar of air and heated to 130 °C using the thermocouple and digital temperature

regulator. An aliquot (0.5-1.5 mL) was removed into a 2 mL eppendorf vial once the mixture had reached temperature, and centrifuged to remove any suspended catalyst. The sample was then capped in a GC vial ready for analysis. Further samples were taken at designated time intervals by flushing the sampling port with a small amount of the reaction mixture into a waste vial to remove any residues from previous sampling, with an aliquot being collected in an eppendorf vial, centrifuged and capped in a GC vial as before. The reaction was left for the duration (e.g. 6 hours) before being cooled naturally or in a bucket of ice, depressurised and dismantled for cleaning.

Recycle experiments were conducted as follows: The reaction mixture was carefully decanted from the catalyst which was then washed with a small amount of warm *tert*-butanol and decanted again. Finally, addition of a fresh reaction mixture prepared the catalyst for a further reaction cycle.

Sample Analysis by GC-FID: Samples were analysed by GC (PerkinElmer, Clarus 480) using an Elite-5 column equipped with a flame ionisation detector (FID) and an autosampler with a 5μL capacity syringe. Products were identified against authenticated standards and quantified by calibration against the known internal standard.

The GC method employed was as follows: The autosampler was programmed to wash once with acetone before performing 4x sequential washes in the sample and ejected to the waste. A 1 μL aliquot of the sample was then injected into the injector port and the syringe washed a further 2x in acetone for cleaning.

The injector port and detector were heated to 220 °C and 250 °C respectively for effective volatilisation of injected components and detection of gaseous components. Helium was used as a carrier gas with a flow of 50 mL/min and a split of 20:1.

A variable temperature program was used for the oven; first, the oven was equilibrated at 80 °C and held for 2 min after injection of the sample. Next, the oven was ramped at 15 °C/min up to 200 °C, then at 20 °C/min to 220 °C and held for a further 2 minutes. The total run time for the method was 13 minutes.

Calibration of Standards: Commercial standards of each of the starting and product materials were purchased for calibration and subsequent quantitative

analysis by GC. A series of 5 samples of were prepared with graduating concentrations of benzyl alcohol, benzaldehyde and benzoic acid in *tert*-butanol up to a maximum concentration of 0.31 mol dm^{-3}. A constant quantity of diglyme as an internal standard was added to each sample (0.21 mol dm^{-3}). Components were measured accurately to 4 decimal places.

The standards were run on the GC 3 times and the peak integrations recorded and averaged across the 3 samples to minimise the GC equipment error. Peak ratios were calculated for each of the components against the internal standard and plotted against the respective mole ratios as demonstrated in *Section 2.2.2.1* to calculate the response factors of each component. R_f values under this method were calculated for benzyl alcohol (0.5681), benzaldehyde (0.6693) and benzoic acid (0.8182) against diglyme.

3.5.2 Characterisation Equipment

A variety of techniques have been used to characterise synthesised materials.

Powder X-ray diffraction (PXRD)

PXRD patterns were collected on a Siemens D5000 diffractometer or a Bruker D2 Phaser diffractometer using monochromatic Cu K_{α_1} (Siemens) or non-monochromatic Cu K_α (Bruker) radiation (λ = 1.5406 Å). Samples were prepared by grinding into a fine powder and mounted in a sample holder with a small well to hold the powder in place during analysis.

Scanning Electron Microscopy (SEM) and Energy Dispersive X-ray Spectroscopy (EDX)

SEM images and EDX analysis were collected using a JEOL JSM-6500F field emission electron microscope using an accelerating voltage between 5-15 kV for imaging and 15-20 kV for EDX. Samples were mounted on carbon tape and coated with gold by sputter coating for imaging or non-coated for EDX experiments.

Transmission Electron Microscope (TEM)

TEM images were collected on a JEOL JEM-2100 LaB_6 microscope at University College Cork, Ireland, with a 200 kV accelerating voltage; powder samples were prepared by suspending 1-2 mg in 1-2 mL ethanol and dropping on to

lacey carbon or carbon film copper mesh grids, allowing for evaporation of the solvent before loading into the microscope.

Inductively Coupled Plasma – Optical Emission Spectroscopy (ICP-OES)

ICP-OES analysis was performed by MEDAC Ltd. using a Varian Vista MPX ICP-OES system. Solid samples are prepared by digestion in HF before analysis, whereas reaction solutions are used directly for analysis.

Chapter 4: Understanding Activation of Extruded Metal Nanoparticles through Structure-Property Correlations

Special Acknowledgements

The following special acknowledgements recognise the contributed work of colleagues and collaborators to the presented content of this chapter.

Sivan Van Aswegen: An undergraduate project student who contributed to the preparation of catalyst batches and sampling of catalytic reactions. (University of Southampton, UK)

Davide Ansovini: For useful conversations regarding kinetics and reaction mechanisms, and help carrying out additional high pressure batch reactions. (University of Southampton, UK)

Dr Gillian Collins: For helpful discussions and collection of images related to the TEM analysis of materials presented in this chapter. (University College Cork, Ireland)

Dr Peter P. Wells: For help carrying out XAS experiments on B18 at Diamond Light Source in Harwell. In addition, for help fitting the XAS data to obtain local structure and bonding information. (UK Catalysis Hub, Research Complex at Harwell, UK)

Dr Naoko Sono: Collection of XPS data at EPSRC's XPS user's service at the University of Newcastle's NEXUS facility. Also, for helpful advice towards the fitting of XPS data in CasaXPS.

"In the beginning You laid the foundations of the earth,
and the heavens are the work of your hands."

Psalm 102:25

4.1 Introduction

4.1.1 Importance of Activation Parameters

The work from *Chapter 3* has shown insights into how nanoporous materials can be exploited to form metal nanoparticles *in situ,* by thermal extrusion and activation of chlorometallate anions from the internal pores of the framework. The catalytic studies showed that the resulting heterogeneous materials were indeed active as aerobic oxidation catalysts; however, the latter part of the work also highlighted that the conditions used to activate the material and generate the metal nanoparticles can have an effect on the resulting catalysis, with the activity related to the structural properties of the material.

In this chapter, the activation parameters will be probed further with a specific focus on the atmospheric conditions under which the activation is performed. The view to which is to draw more detailed structure-property correlations, that can reveal more about the materials and the origin of their activity and how they can be engineered further to improve their catalytic properties.

4.1.2 Reduction Methods for Synthesis of Nanoparticles

The transformation of the chlorometallate anions to the metallic nanoparticles through the extrusion method is a reduction process. In the activation step by calcination (heating to 500 °C) as used in *Chapter 3*, reduction by thermal degradation is exploited to extrude and generate the active nanoparticulate species. This is a less traditional route for the reduction of metal salts to metallic species, where chemical reductions using reducing agents, or thermal treatment in the presence of H_2 is more common. The exact choice of reduction method can be dependent on the stability and nature of the support, whether nanoparticles are prepared prior to addition on, or in the presence of the support, and of course whether the reduction is performed in the liquid phase or on a solid powder.

Chemical reduction to form nanoparticles on supports

Chemical reduction is often done using strong reducing agents[1] such as ($NaBH_4$)[2-5] or hydrazine,[5-6] especially when nanoparticles are prepared in solutions due to the compatibility of the reducing agent for the preparation of

a range of aqueous concentrations. Where DP methods are employed, urea can be employed as the precipitating agent[7] as described in full in *Section 1.2.4.2*. In the few examples where nanoparticles are prepared in organic solvents, mild and compatible reducing agents such as oleylamine (which can double as a stabilising agent) have been used.[8]

Reduction in the presence of H_2

When reduction of a metal precursor is done in the presence of a support, and where a support is more sensitive towards a strong chemical reducing agent, thermal reduction is often performed in the presence of H_2 to provide a reducing atmosphere.[9] Although it is known that gold(III) precursors can be reduced in oxidising atmospheres at relatively low temperatures,[9] it is more difficult to achieve reduction of platinum or palladium precursors under these conditions without heating to very high temperatures. As such, the presence of H_2 can provide enough of a reducing atmosphere at more moderate temperatures to afford more facile reduction procedures. This technique is common where impregnation methods have been used to form a dry material loaded with a metal precursor.[9-10] It is also well documented that synthesis of nanoparticles in the presence of H_2 can lead to smaller nanoparticles in comparison to calcination in air.[9, 11-12]

In a bimetallic system, a recent report studied the effect of H_2 reduction *versus* aerobic calcination of traditional wet impregnated TiO_2 materials on the particle size and composition of AuPd nanoparticles.[10] It was discovered that particle sizes with an average size of 4.7 nm (σ = 1.7) could be generated by calcination at 400 °C, but that a disparity was observed in the composition with smaller particles being Au-rich and larger particles being Pd-rich. In addition, it was noted that core-shell structures were favoured in gas-phase aerobic calcination, exhibiting an Au_{core}-Pd_{shell} nanostructure. In stark contrast, reduction of the impregnated materials in the presence of H_2 at the same temperature resulted in the formation of similar size particles with a complete alloy nanostructure determined by XPS and STEM. It is interesting to note little change in the particle sizes commonly observed in monometallic systems. Both materials were applied in the aerobic oxidation of benzyl alcohol, with the reduced materials achieving 76 % conversion and 85 % aldehyde selectivity in contrast with 14 % conversion and 80 % selectivity for the calcined catalysts.

The differences in catalytic activity in this case were attributed to the nanostructure of the particles.

Furthermore, catalysts were reduced at temperatures as low as 250 °C with little effect on the catalytic output with measured conversion and selectivity both at 80 % . Calcination was ineffective at lower temperatures for complete reduction of metal salts, with the authors concluding that both temperature and atmosphere are important for gas-phase activation of nanoparticle catalysts.[10]

4.1.3 Oxidation of Benzylic Alcohols: The Case of Vanillin

The oxidation of alcohols to aldehydes is of key industrial importance as has been highlighted in *Section 1.2.6.2*. Their distinct aromas have made them key ingredients as flavourings and fragrances in foods, cosmetics and perfumes amongst others.[13] Benzylic aldehydes are of no exception with benzaldehyde, vanillin, *o*-anisaldehyde responsible for having odours of almond, vanilla and aniseed/liquorice respectively. Noble metal nanoparticles have shown a proficiency toward the selective oxidation of alcohols, but with a specific focus on the oxidation of benzyl alcohol. To understand this, the mechanism of surface oxidation must be examined to identify any differences that may occur on the surfaces between linear alcohols and benzylic alcohols.

Mechanism of alcohol oxidation and aldehyde formation

A general mechanism toward the oxidation of alcohols on NP surfaces has been previously studied, with the conclusion that differing mechanisms can occur for the different noble metals.[14-15] In the case of gold, it has been determined that the adsorption of O_2 or a peroxide can form an activated superoxo-species adsorbed on the surface.[16] The subsequent adsorption of the alcohol to form an adsorbed surface-alcoholate species occurs. Abstraction of the β-hydride to the surface of the metal generates the desorbed aldehyde species, with the surface hydrides reacting with the activated surface peroxo-species to form water and regenerate sites for adsorption and further catalytic cycles (Figure 4.1).

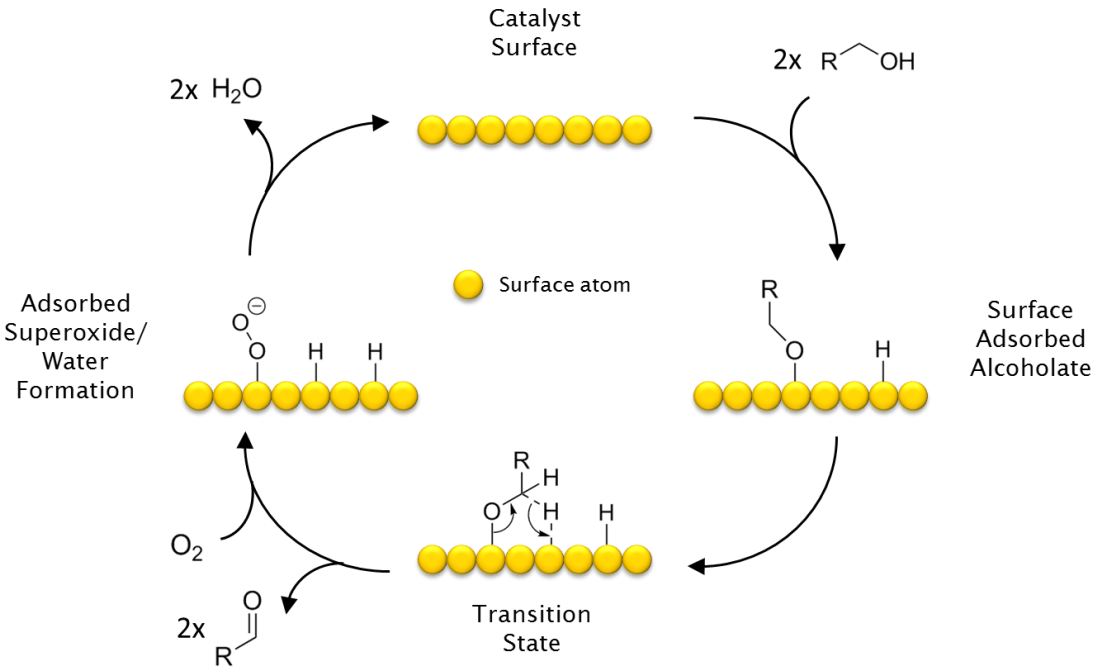

Figure 4.1 Proposed mechanism for alcohol oxidation on a metal NP surface with O_2 as an oxidant

Kinetic experiments on the oxidation of alcohols on gold surfaces showed that the presence of radical trapping compounds (such as TEMPO) had negligible effects on the rates and progression of the reaction, thus implying 2-electron transfer mechanisms.[16] In addition, it was shown by calculation of Hammett constants (a measure of electron donating or withdrawing effect of *para*-substituents on the rate of reaction) that the reaction must proceed *via* a carbocation-like intermediate, consistent with an adsorbed alcoholate species and confirmation of a non-radical mechanistic pathway.[16-17] The β-hydride abstraction has been confirmed through a separate isotopic labelling experiment using deuterium, with cleavage of the C-H(D) bond leaving a partial positive charge that facilitates the formation and concerted desorption of the aldehyde product.[17] Additional studies have also concluded that the cleavage of the benzyl C-H bond is also the rate-determining step[14, 17] in the case of the oxidation of benzyl alcohol to benzaldehyde.

Comparing gold against palladium in the aerobic oxidation of primary alcohols, the main difference observed is in the mechanism by which the oxidant is involved in the reaction. For gold, the oxidant is directly activated by adsorption to form the superoxo-species, however for palladium, proximal O_2 molecules abstract the surface bound hydride species to form H_2O_2.[14-15, 18]

Whilst some of the literature refers to this mechanism when discussing the oxidation of benzylic alcohols with metal nanoparticles, some literature has gone further to examine the role of the aromatic benzene ring in the interaction with the nanoparticle surfaces. It was shown through the use of temperature programmed desorption that benzyl alcohol has a strong interaction with the surface of gold with binding energies of 90 or 105 kJ/mol.[19] Studies using electron energy loss spectroscopy (EELS) show that it is common for aromatic molecules to have strong binding energies that result from geometrical alignment of the ring almost parallel to the metal surface - implying the presence of electronic interactions between the aromatic π-system and the metal surface.[19-20] Interestingly, a previous study of the aerobic oxidation of benzyl alcohol and octan-1-ol using the same gold catalysts showed much higher activity toward the oxidation of benzyl alcohol.[21] Whilst the study doesn't exclusively discuss the mechanistic pathways by which the reaction occurs, it is possible that the enhanced interaction of the aromatic reactant with the nanoparticle surface, thus bringing the alcohol group in close proximity to the metal surface, could be a contributing factor to lowering the activation energy of the reaction profile.

The case of vanillin

With these facts in mind, it prompted us to look at the application of these nanoparticle catalysts toward the oxidation of other industrially significant benzylic alcohols. The production of vanillin is interesting due to its high commercial value and importance as the most highly demanded and produced chemical for the flavours and fragrances industry,[22] and second only to aspartame amongst all food additives.[23] As well as a flavouring agent, it is also used in other industries, including as an intermediate towards pharmaceuticals such as L-3,4-dihydroxy-phenylalanine (L-DOPA), a key therapeutic agent used to combat Parkinson's disease.[22] Currently, vanillin is produced by one of three industrial synthetic pathways: (i) a method by which lignins are degraded into vanillin and other products, but which involves solvent intensive processes using multiple extraction and distillation steps, (ii) a synthetic route via the oxidation of guaiacol,[22, 24] but which utilises mineral acids or heavy-metal promotors such as lead, bismuth and/or cadmium sources, and (iii) a high-cost biosynthetic pathway employing microbial oxidation of a carbon source and subsequent enzyme-catalysed reduction to form vanillin.[23, 25]

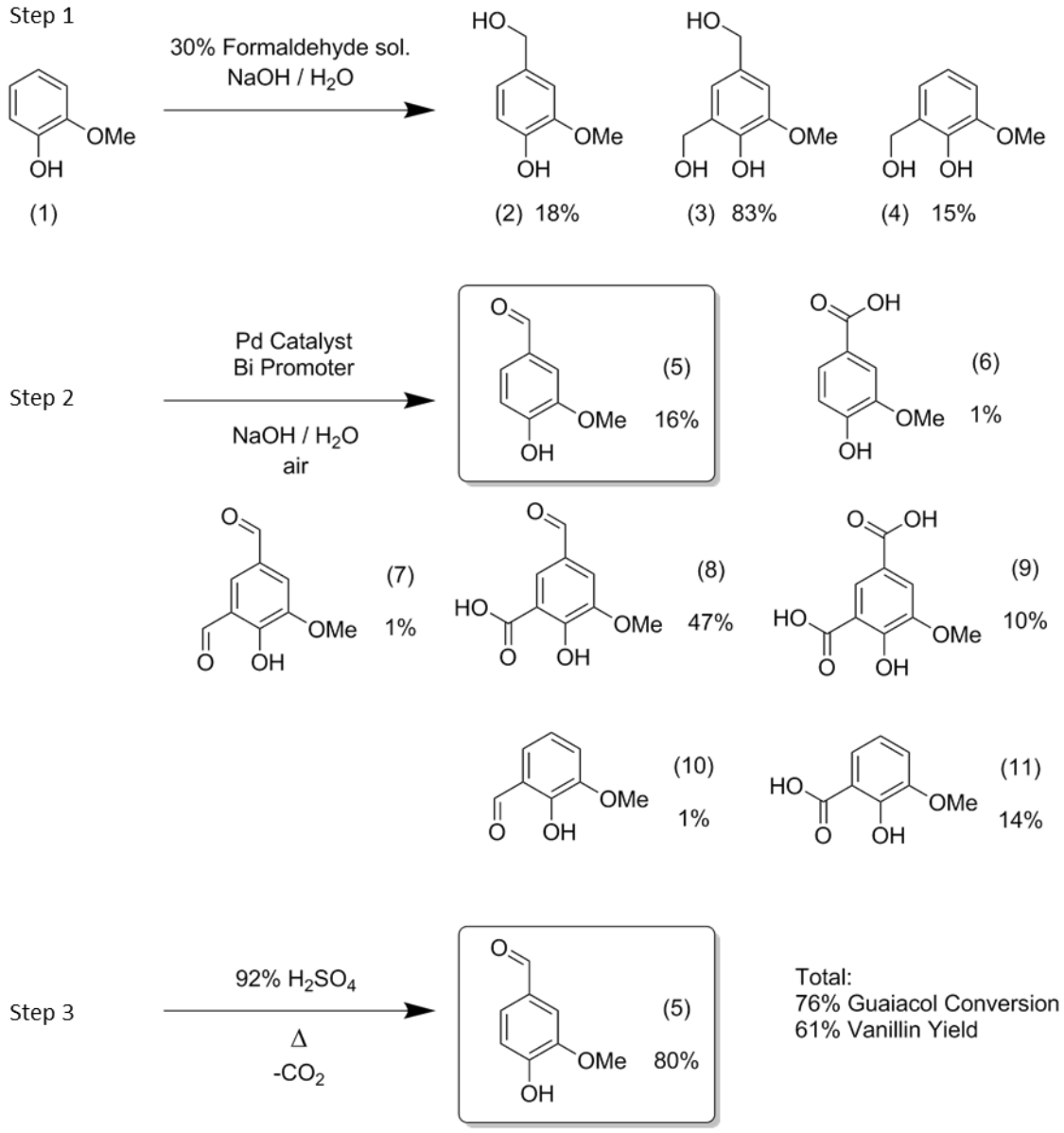

Figure 4.2 Industrial preparation of vanillin (5) from guaiacol (1) using formaldehyde

Key: (1) Guaiacol, (2) 4-(hydroxymethyl)-2-methoxyphenol (vanillyl alcohol), (3) 4,6-di(hydroxymethyl) guaiacol, (4) *p*-hydroxymethyl guaiacol, (5) 4-hydroxy-3-methoxybenzaldehyde (vanillin), (6) 4-hydroxy-3-methoxybenzoic acid (vanillic acid), (7) 4,6-(diformyl) guaiacol, (8) *o*-carboxyvanillin, (9) 4,6-(dicarboxy) guaiacol, (10) *o*-vanillin, (11) *o*-vanillic acid.

The routes largely employed by industry are those originating from guaiacol via the addition of formaldehyde or glyoxylic acid. The former route is highlighted in more detail in Figure 4.2, where it is easy to see that the procedure is not inherently selective, forming a multitude of oxidation

products. A final decarboxylation step succeeds in converting some of the by-products to vanillin, however a total yield of only 61 % can be achieved.

The addition of glyoxylic acid to guaiacol, oxidation and subsequent acid catalysed decarboxylation (Figure 4.3) is an alternative route to the formation of vanillin, however this route features much less in industry and is not particularly atom-efficient. The decarboxylation is a necessary step to achieve any yield of vanillin.

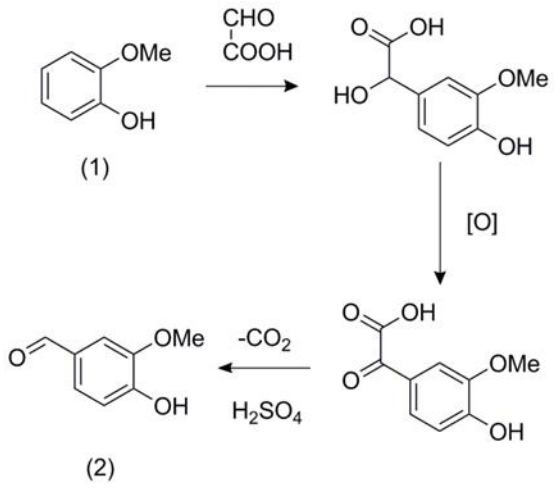

Figure 4.3 Alternative industrial route to vanillin (2) by addition of glyoxylic acid to guaiacol (1)

Both of these routes involve multi-step processes with modest yields, and which employ reasonably harsh or toxic conditions at some point in the synthesis. Nonetheless, they are still the best methods that are employed currently for commercial production of vanillin. As such, there is scope for the application of the extruded metal nanoparticle catalysts in the selective oxidation reactions to form vanillin in good yields, whilst removing the need for harsh conditions or toxic reagents in the process.

4.1.4 Aims and Objectives

In this chapter, thermal extrusion by reduction juxtaposed with calcination will be evaluated for the respective efficiencies towards quantitative nanoparticle formation. Bulk characterisation techniques including XAS and XPS will be used to identify the chemical nature of the isolated active sites, evaluating the

effects on the aerobic oxidation of vanillyl alcohol to the industrially significant product vanillin

4.2 Structure-Property Correlations of Reduced NP/CuClP Catalysts

4.2.1 Structural Characterisation Including X-ray Spectroscopic Techniques

4.2.1.1 Transmission Electron Microscopy

TEM analysis has already been performed on the calcined catalysts as shown in *Section 3.2.2*, which revealed the presence of small metal nanoparticles on the surface of the CuClP framework. Nanoparticles were observed on each of the calcined Au, Pt and Pd analogues. Similarly, TEM analysis was performed on the reduced materials to probe for the generation of nanoparticles under alternative reducing conditions. Figure 4.4 shows collected micrographs that establish the presence of metallic nanoparticles also on the reduced materials. The presence of crystalline embedded nanoparticles for the Au and Pt materials, with typical diameters of 2-6 nm, can be seen in Figure 4.4 (a) and (b). High-resolution TEM analysis on individual nanoparticles, shown in Figure 4.4 (e) and (f), reveal lattice fringe spacings which can be measured at 0.20 nm and 0.23 nm respectively. These fringe spacings can be attributed to Au(200) and Pt(111), confirming the composition of the identified nanoparticles.[26] There is evidence of Pd nanoparticle formation on the reduced $[PdCl_4]^{2-}$ supported material as well, as seen in Figure 4.4 (d) and (g), displaying lattice fringes of 0.22 nm, characteristic of Pd(111).[26] However, the morphology of the reduced Pd catalysts shows some differences compared to the Au and Pt catalysts, with the presence of larger particles (20-50 nm) embedded in a matrix, as shown in Figure 4.4 (c). The identification of larger Pd particles could be a result of the slightly harsher reducing conditions in the presence of H_2.

Due to sensitivity (dynamic changes in crystal orientation) of the sample under the electron beam,[27] the atomic resolution crystallinity of these particles could not be probed in greater detail. The nanoparticles are innately located at the edges of the composite material.

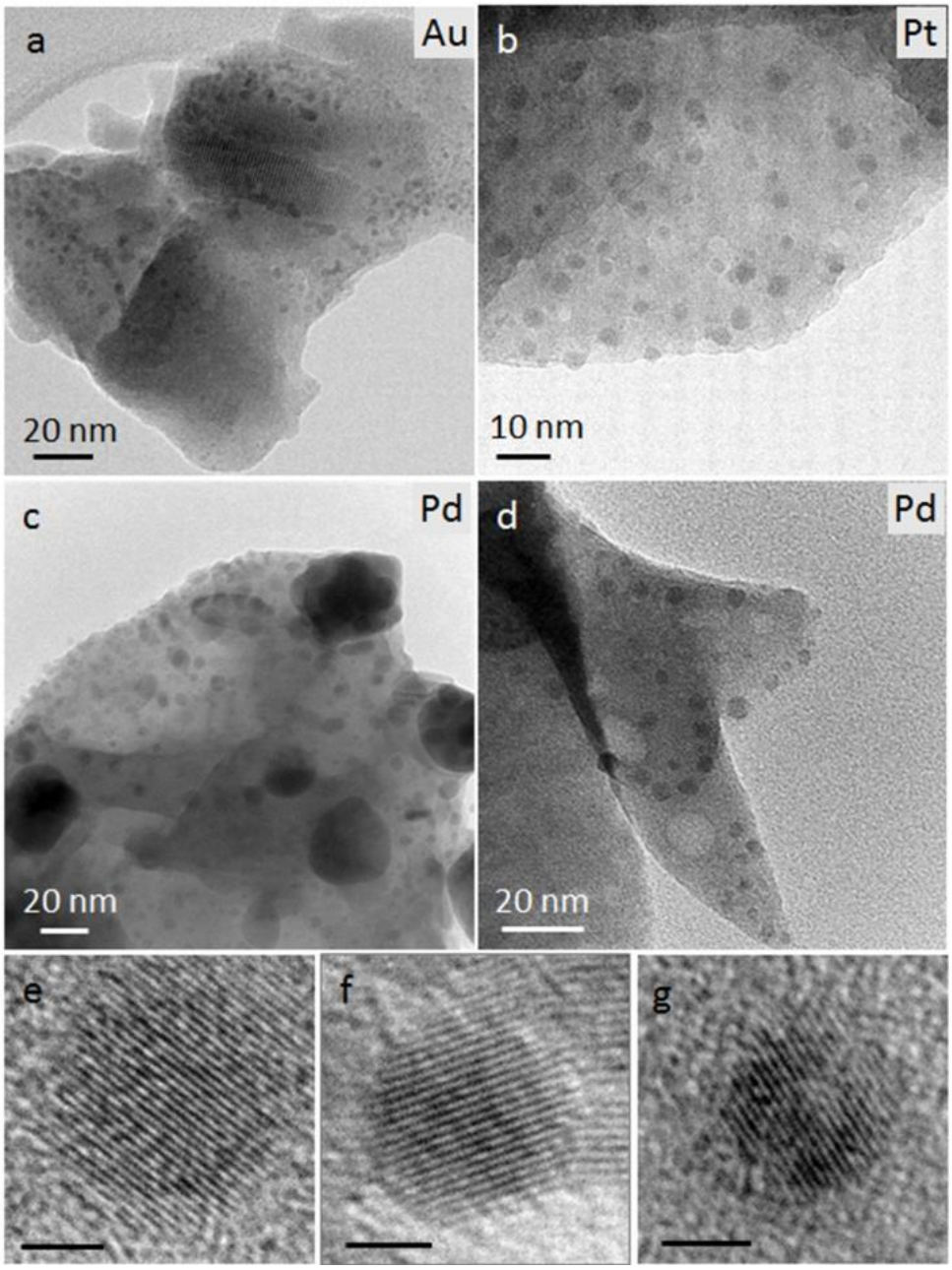

Figure 4.4 TEM images of reduced (a) Au, (b) Pt and (c)-(d) Pd catalysts, with magnified images of individual Au (e), Pt (f) and Pd (g) nanoparticles (scale bars in (e)-(g) are 2 nm).

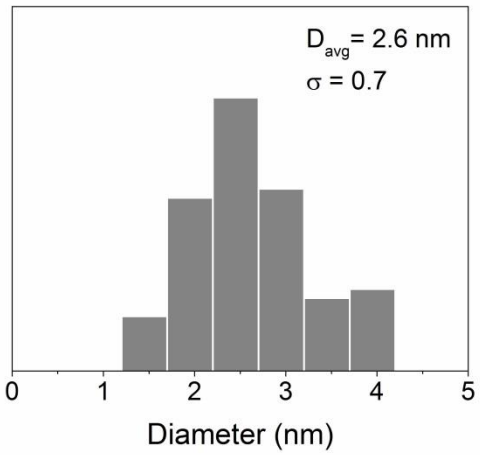

Figure 4.5 Particle size distribution histogram of the reduced Pt/CuClP catalyst calculated from TEM images (98 particles)

4.2.1.2 Powder X-ray Diffraction

PXRD patterns were collected for each of the reduced materials, with stark differences noted in comparison with the PXRD of the calcined materials (Figure 3.5) shown in *Section 3.2.2* in the previous chapter. Two obvious differences are noted; firstly, the appearance of a broad hump has appeared in the PXRD pattern of the Pt/CuClP as seen in Figure 4.6 (labelled (a)). This feature is present at the location that would be expected for the Pt(111) reflection, with the broad nature of the peak indicative of ultra-small particles – a relationship dictated by the Scherrer equation (Equation 4.1).[28]

$$\beta = \frac{K\lambda}{t\cos\theta} \qquad \textbf{Equation 4.1}$$

In this relationship, the broadening of a peak (β) is a function of the X-ray wavelength (λ), the shape correction factor (K), the thickness of the crystal sample (t) and the Bragg angle (θ). The theory stems from the concept that at minor deviations from the Bragg angle, the disparity between the phases of X-rays reflected from the first plane is negligible, resulting in only minor reduction in the intensity of the diffracted beam. At planes deeper into the crystallite, the disparity between the X-ray phases increases, eventually leading to complete destructive interference on a bulk crystal. In a situation where a crystallite has a finite thickness, there may not be enough planes present to

allow for complete destructive interference at minor deviations of θ, thus resulting in a broadening of the diffraction peak proportional to the particle size. The broadening of the peak (β) is quoted as a measure of the peak width at half the maximum peak intensity and is approximately equal to 2 $\delta\theta$, where $\delta\theta$ is the angular range at which the peak is broadened to.

To quantitatively apply this equation, a pattern must be collected using a monochromatic X-ray source. As this pattern was collected using a non-monochromatic source, the relationship can only be treated qualitatively with TEM used to accurately measure the nanoparticle sizes.

Another clear observation noted from these XRD patterns is the drop in crystallinity of the reduced Pd catalyst, noted from the reduced intensity of the diffraction peaks as well as the broadening of the peaks resulting in poorer resolution. Given that each of the materials were reduced under identical conditions, it is interesting to note the different behaviour. These results could also be indicative of the strength of interactions between the chlorometallate anions and the supporting framework. Clearly, the extrusion of the $[PdCl_4]^{2-}$ species is having a detrimental effect on the framework indicating more integral interactions between the $[PdCl_4]^{2-}$ and the parent framework toward the material stability in this analogue compared with the Au and Pt materials. The presence of the larger particles observed by TEM (Figure 4.4 (c)) could also be a result of the reduced framework stability and consequential degradation. Furthermore, as well as noting the lack of stability of the Pd/CuClP, this further enhances the observation that the Au and Pt/CuClP materials are particularly stable to the anion extrusion under reducing conditions.

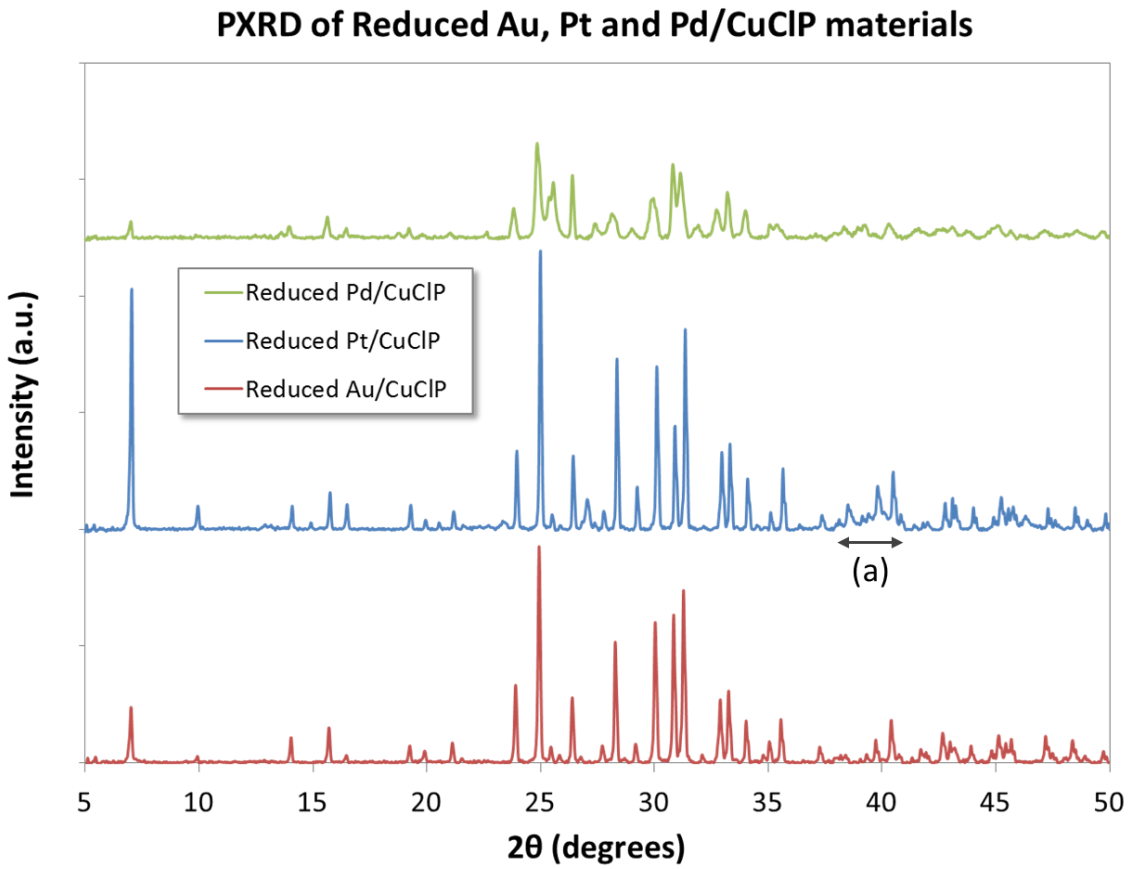

Figure 4.6 PXRD patterns of reduced Au, Pt and Pd/CuClP catalyst materials, with (a) highlighted Pt NP feature

4.2.1.3 X-ray Absorption Spectroscopy

With the exception of PXRD, the majority of characterisation techniques used thus far have analysed site-specific structural properties of the CuClP materials. To obtain more detailed information on the representative bulk structural properties of these materials, XAS studies were undertaken on both the calcined and reduced materials. XAS spectra were collected about the Au L_{III}, Pt L_{III} and Pd K X-ray absorption edges. Initially, the EXAFS data were first analysed and compared against reference data collected from a metallic source and the relevant starting precursors ($KAuCl_4$, K_2PtCl_4 and K_2PdCl_4).

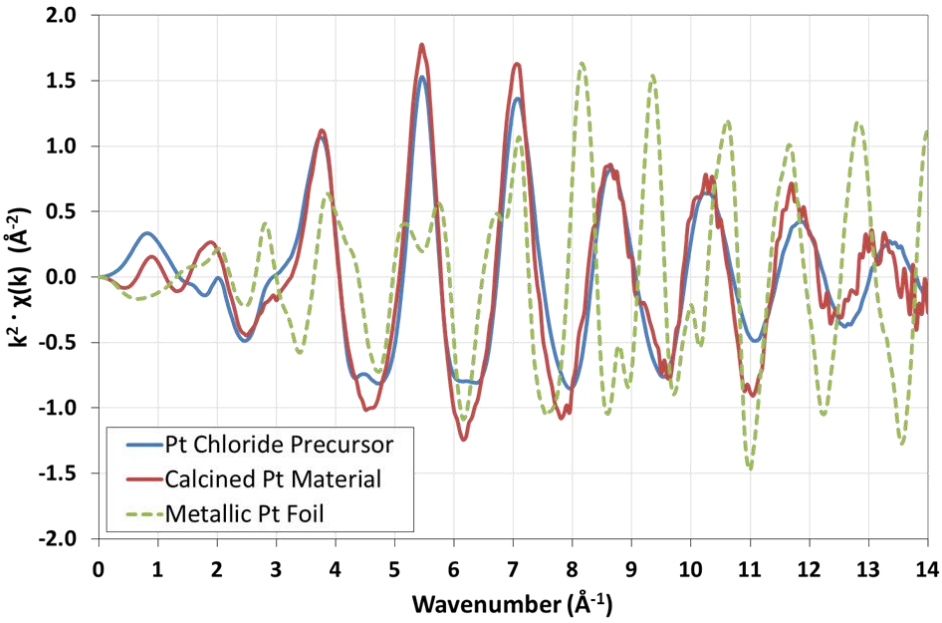

Figure 4.7 Non-fitted k^2 weighted k-plot EXAFS spectra of calcined Pt material (red line), metallic Pt standard (dotted green line) and K_2PtCl_4 standard (blue line)

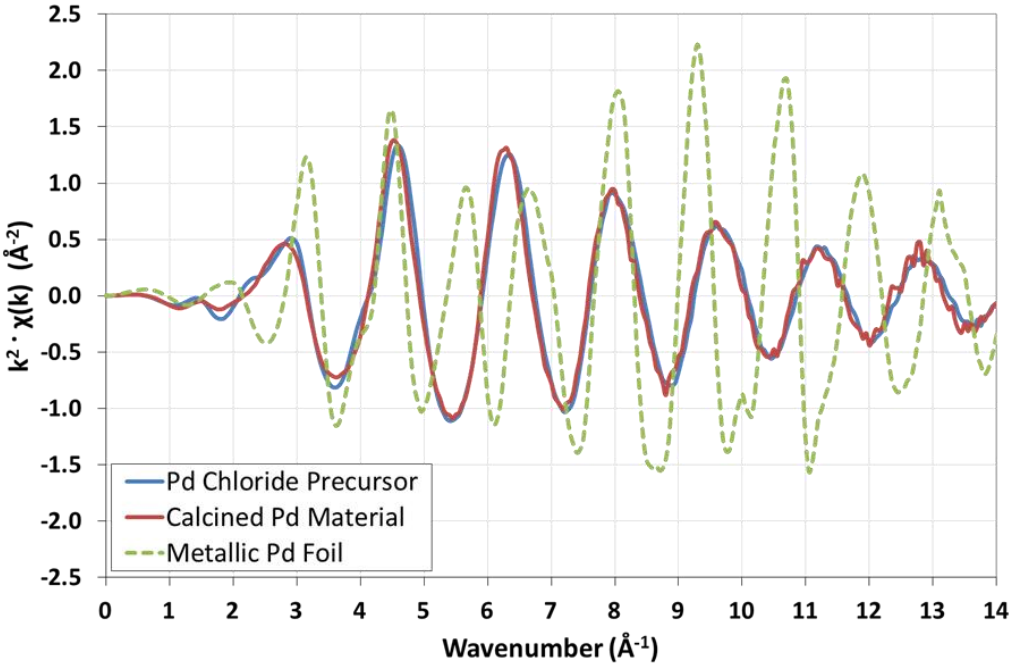

Figure 4.8 Non-fitted k^2 weighted k-plot EXAFS spectra of calcined Pd material (red line), metallic Pd standard (dotted green line) and K_2PdCl_4 standard (blue line).

A background was fitted to the XAS spectra and the EXAFS portion plotted as $\chi(k)$ against the photoelectron wavenumber (k). The wavenumber of the generated photoelectron is determined by the relationship in Equation 2.1, where m_e is the mass of an electron, E is the X-ray energy, E_0 is the energy of the absorption edge (and so E-E_0 is the kinetic energy of the photoelectron) and $\hbar$ is the reduced Planck's constant.

$$k = \sqrt{\frac{2m_e(E - E_0)}{\hbar^2}} \qquad \textbf{Equation 4.2}$$

As such, $\chi(k)$ is a measure of the absorption oscillations about the pre-determined background value as a function of k. A k-weighting of k^2 was applied to amplify the oscillations at high values of k for more effective analysis.

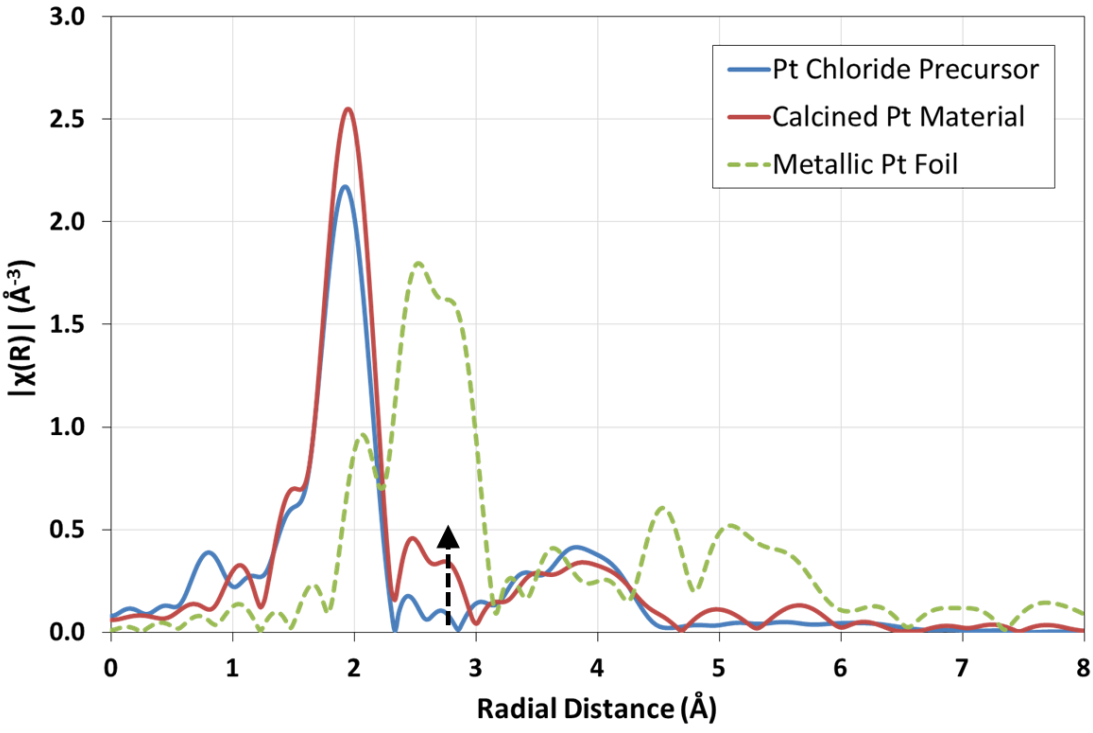

Figure 4.9 Non-fitted Fourier transform EXAFS spectra of calcined Pt material (red line), metallic Pt standard (dotted green line) and K2PtCl4 standard (blue line)

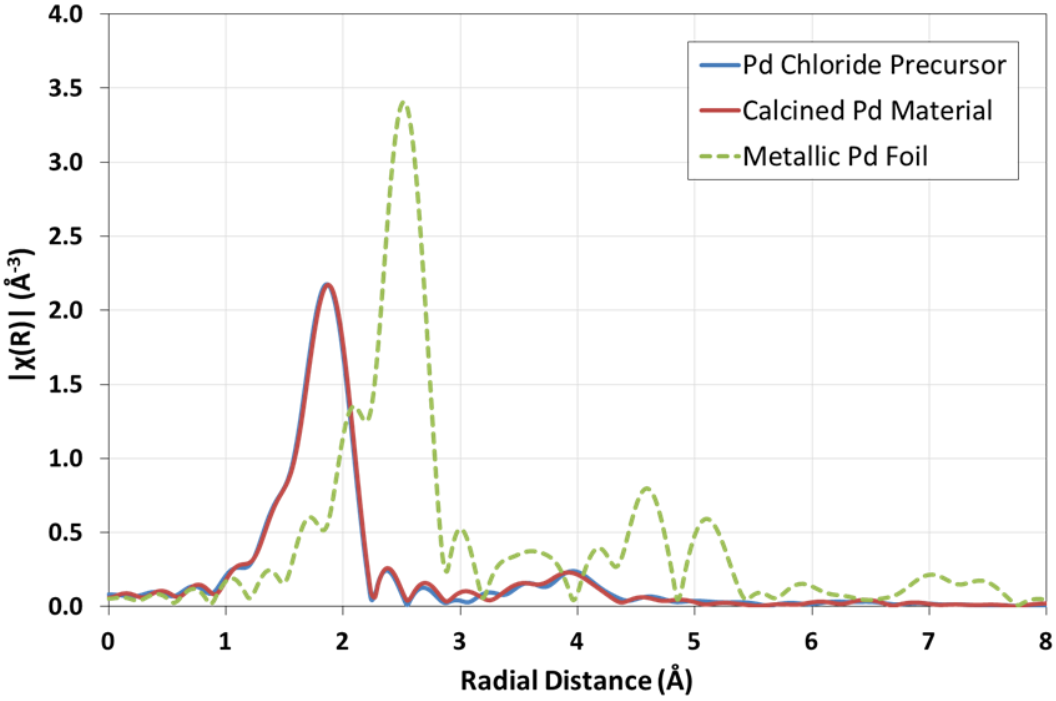

Figure 4.10 Non-fitted Fourier transform EXAFS spectra of calcined Pd material (red line), metallic Pt standard (dotted green line) and K_2PdCl_4 standard (blue line)

In Figure 4.7 and Figure 4.8, the EXAFS k-plots of the calcined Pt and Pd/CuClP materials have been compared against both metallic foils and the precursors. It is very clear to see that the materials match up very closely with the data collected for the precursor rather than the metallic foils. In contrast with data collected thus far, this reveals that from a bulk perspective, the majority of the Pt and Pd present in the calcined materials remain as chlorometallate anions in the material, not as metallic NPs as initially hypothesised. TEM data of the calcined materials along with XRD confirms the presence of some metallic NP species in all of the samples, however the EXAFS measurements indicate that these are present only as a small fraction of the total noble metal content of a given sample.

Radial distance plots of the raw data were also generated for the Pt and Pd materials, constructed by the Fourier Transform of the k-plots, that highlight the nearest neighbouring atoms in shells surrounding the absorbing atom at a distance, R (Å) (Figure 4.9 and Figure 4.10). Again, it is clear to see the data matching closely with the anionic precursor standards, with main signals around 1.8-1.9 Å, representative of the Pt-Cl and Pd-Cl bonding neighbours

respectively. Interestingly, the R-plot of the calcined Pt/CuClP material shows a slight disparity to the standard, with elevated signals around 2.4 and 2.7 Å related to the metallic Pt-Pt bonding as seen by the metallic Pt standard (highlighted in Figure 4.9). This could indicate a larger fraction of NP generation compared with the other analogues, and would account for the comparatively heightened activity and selectivity observed for the calcined Pt catalyst in *Chapter 3*.

Figure 4.11 shows the non-phase-corrected Fourier transform (both magnitude and imaginary component) of the k^3 weighted EXAFS data for each of the reduced Au, Pt and Pd catalyst materials, with the fitting parameters generated detailed in Table 4.1. Interestingly, there were some stark differences compared with the calcined materials, especially for the Pt/CuClP. The EXAFS data of the reduced Pt sample is consistent with that expected for Pt nanoparticles. The long-range structure in the radial distribution function is indicative of metallic particles and EXAFS data can be modelled by including the contribution from the nearest three Pt-Pt distances and a multiple scattering Pt-Pt path from the primary Pt coordination shell. The coordination numbers of the different scattering paths (8.4) as seen in Table 4.1 are smaller than that expected for a bulk Pt structure (12.0), indicating the nanoparticulate nature of the Pt.

The EXAFS data of the reduced Pd sample is similar to the initial Pd precursor used for the preparation of the materials, with the largest contribution in the Fourier transform resulting from the primary Pd-Cl coordination shell, not too dissimilar from the calcined material. The main difference however, is that the EXAFS data also suggests the presence of Pd nanoparticles as indicated by a second feature in the imaginary part of the Fourier transform, which is consistent with a Pd-Pd scattering distance. The weak Pd-Pd contribution is evidence that only a small fraction of Pd sites are present as metallic species, with the majority of Pd sites consistent with the initial catalyst precursor. These larger fractions of metallic Pd could also be a result of the framework degradation observed by PXRD that led to formation of slightly larger particles seen in the TEM analysis.

The radial distribution plot for the reduced Au sample is dominated by one component, which can be assigned to an Au-Cl scattering path. There is a good degree of correlation between the EXAFS data of the reduced Au sample and

the $KAuCl_4$ precursor, indicating that the significant component in this reduced sample is the $[AuCl_4]^-$ anion. Whilst there is no observable metallic contribution from the EXAFS data, some NP formation is clearly observed by TEM and is present at least in a minor fraction.

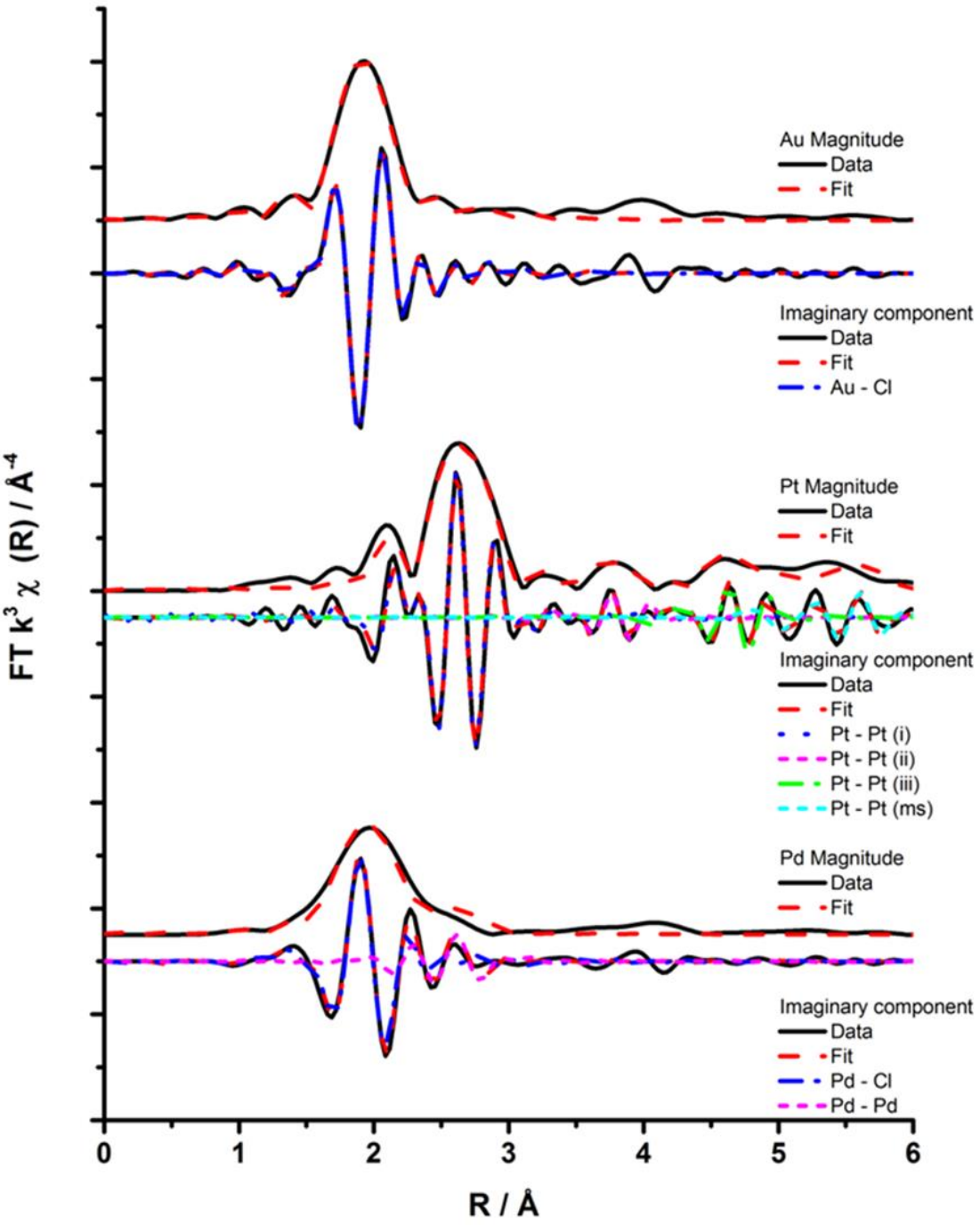

Figure 4.11 Magnitude and imaginary component of the k^3 weighted Fourier transform for the EXAFS data of the reduced Au (top), Pt (middle), and Pd (bottom) samples. Associated scattering paths are included for the imaginary component.

Table 4.1 EXAFS fitting parameters for the reduced Au, Pt and Pd/CuClP samples

Sample	Shell	CN	*R* / Å	$2\sigma^2$ / Å^2	E_f / eV	R_{factor}
Reduced Au sample	Au -Cl	3.7 (2)	2.29 (1)	0.002 (1)	10 (1)	0.005
Reduced Pd sample	Pd - Cl	3.3 (3)	2.35 (1)	0.003 (1)	10 (2)	0.004
	Pd - Pd	1.3 (5)	2.77 (2)	0.004 (2)		
Reduced Pt sample	Pt – Pt_1	8.4 (5)	2.76 (1)	0.005 (1)	7 (2)	0.007
	Pt – Pt_2	3 (1)	3.91 (2)	0.005 (1)		
	Pt – Pt_3	10 (3)	4.79 (2)	0.007 (1)		
	Pt – Pt (ms)	13 (3)	5.65 (2)	0.011 (2)		

Fitting parameters: (Au sample) $S_0^2 = 0.75$ as deduced by $KAuCl_4$ standard; Fit range 3.5<k<12.5, 1.1<R<3; # of independent points = 10; (Pd sample) $S_0^2 = 0.82$ as deduced by $PdCl_2$ standard; Fit range 3<k<11.5, 1<R<3; # of independent points = 11; (Pt sample) $S_0^2 = 0.91$ as deduced by Pt foil standard; Fit range 3.5<k<14, 1<R<6; # of independent points = 32

It is well known that Pd can easily oxidise to PdO_x species in the presence of O_2.[29] As such, a reference of a PdO standard was used to collect an XAS spectrum for comparison with both the calcined and reduced Pd/CuClP materials to investigate the possibility that particles of PdO were being formed. Figure 4.12 shows a distinctive k-plot and R-plot for PdO, showing two clear shells at 1.6 and 3.0 Å, the former of which is indicative of Pd-O neighbours.[30] Qualitative observation reveals that none of these features are visible in the data presented for the Pd/CuClP materials, with fitting of the reduced Pd/CuClP data (Table 4.1) clearly indicating the presence of Pd-Cl and Pd-Pd bonding alone with no contribution from Pd-O.

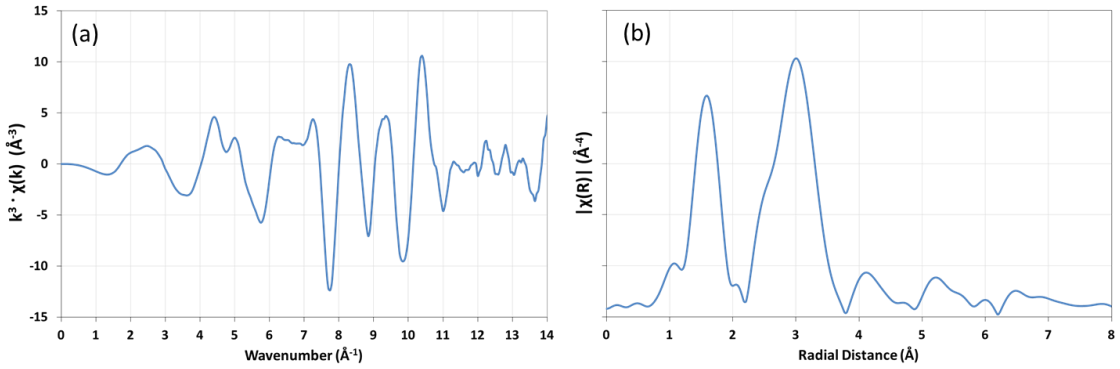

Figure 4.12 Non-fitted EXAFS spectra of PdO including k_3 weighted k-space plot (a) and fourier transform of EXAFS (b).

In conjunction with the EXAFS analysis, similar trends can also be observed in the XANES analysis of the XAS spectra at the absorption edge. The reduced Au/CuClP sample analysed shows a clear mismatch with the metallic standard (Figure 4.13), with the absorption edge occurring at slightly higher energy as expected for elements in higher oxidation states. This further corroborates the bulk presence of the $[AuCl_4]^-$ species as predominant over any metallic species.

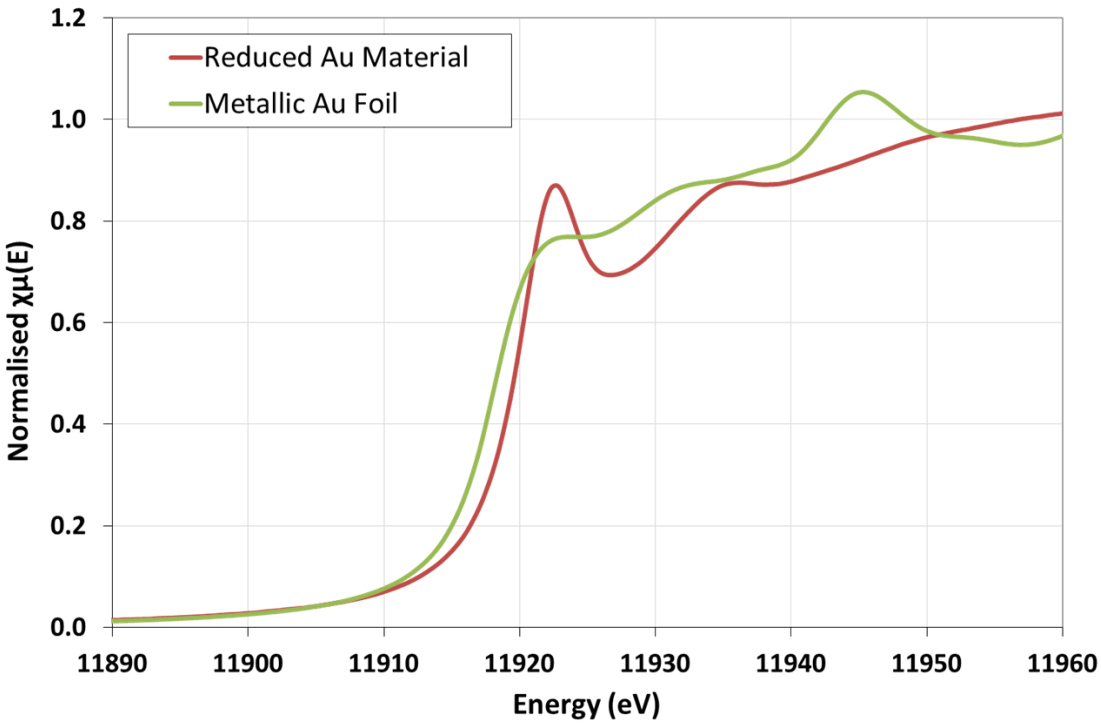

Figure 4.13 XANES spectra of reduced Au/CuClP material and a metallic Au foil standard

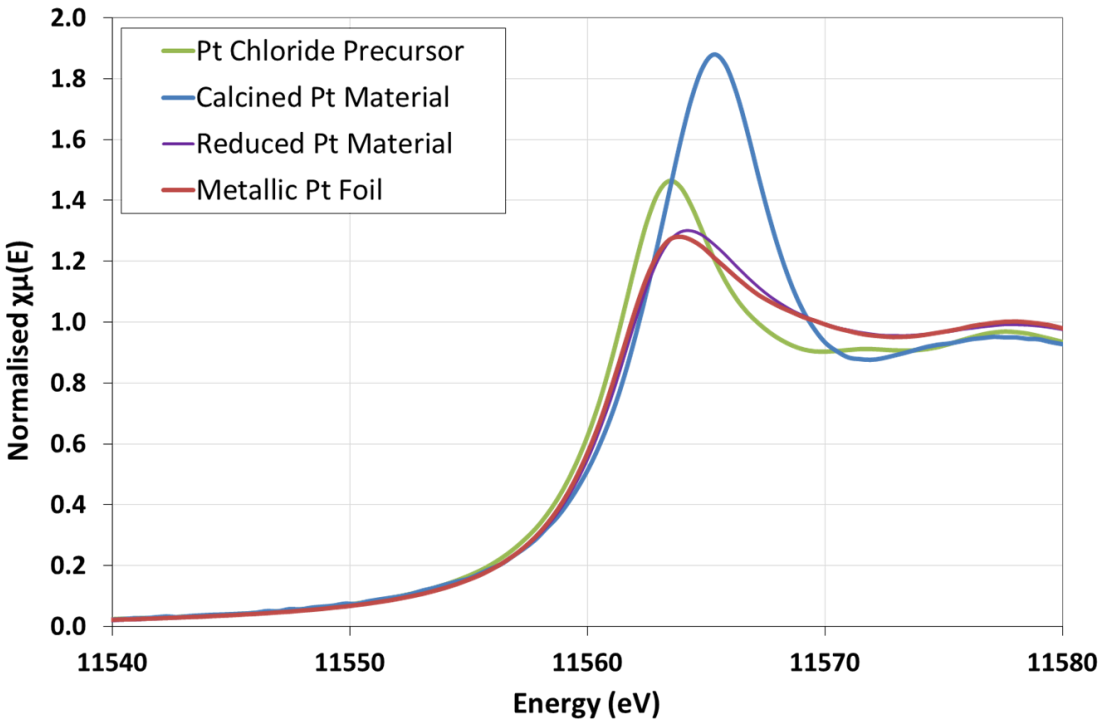

Figure 4.14 XANES spectra of calcined and reduced Pt/CuClP materials with the K_2PtCl_4 precursor and metallic Pt foil standards

The case of the Pt XANES is slightly more complex. The reduced material matches very closely with the metallic standard confirming complete reduction of the Pt species to metallic NPs. On the other hand, the spectrum of the calcined material is different from both the precursor and metallic standards. The shape and relative intensity of the white line is indicative of the precursor, however the increased intensity compared with the precursor and shift of the absorption edge to higher energy is unusual. A detectable fraction of metallic Pt was noted in the EXAFS data, even though relatively small, particularly in the R-plot. This XANES data of the calcined material could be revealing a snapshot of the early stages of extrusion and NP formation. In a recent XAS study on $[PtCl_4]^{x-}$ species,[31] an increase in the white line intensity was observed when $[PtCl_4]^{x-}$ was confined in the pores of a nanoporous silica. The authors attribute this phenomenon to a change in the geometry of the Pt species as it forms dimeric species of $[Pt_2(\mu\text{-}Cl_2)Cl_6]^{2-}$ confirmed by DFT calculations. The fitted EXAFS data confirm an increase in coordination number of the Pt-Cl shell from 4 to 5, coinciding with the geometry predicted by DFT. In light of these observations, it is possible that something similar could be happening in the calcined Pt system, where square planar $[PtCl_4]^{2-}$ anions supported in the

framework are forming dimeric species as precursors to cluster formation and eventual reduction to the NPs observed on the material surface.

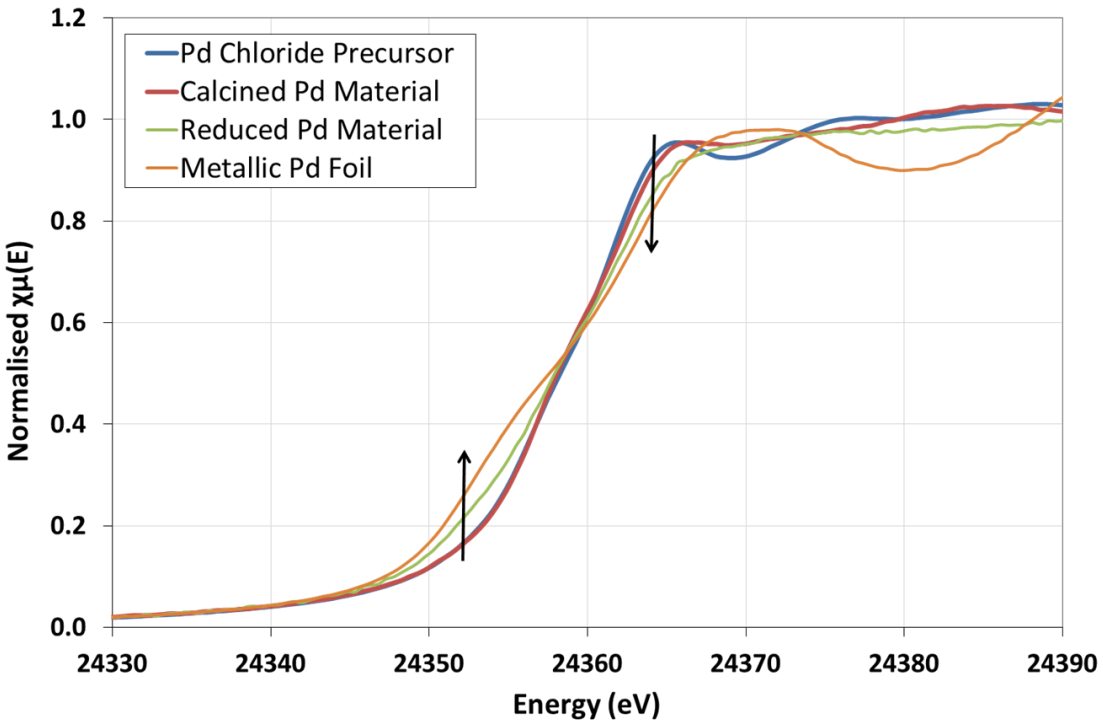

Figure 4.15 XANES spectra of calcined and reduced Pd/CuClP materials with the K_2PdCl_4 precursor and metallic Pd foil standards

The Pd XANES spectra are also in agreement with the aforementioned EXAFS trends. Pre-edge features are more common when analysing K-absorption edges that involve the transition of 1s elections. Typically, to obey the Laporte orbital selection rules[32] in an electronic transition, $\Delta l = \pm 1$ and thus a transition from an s-orbital to a p-orbital must occur in this circumstance. Due to degrees of p-d hybridisation, the forbidden transition from an s-orbital to a d-orbital can occur, resulting in low intensity absorptions that manifest as features in the pre-edge region.[33] The metallic standard displays a shoulder to the absorption edge around 24.345 keV and a lower intensity white line at 24.364 keV compared with the chlorometallate precursor. Whilst the calcined Pd/CuClP material shows a good agreement in the XANES pre-edge shape and absorption edge position, the reduced Pd/CuClP shows an intermediate spectrum with a slightly more pronounced pre-edge shoulder than the precursor, and a reduction in the intensity of the white line. This clearly shows a combination of both metallic and anionic precursor as discovered in the EXAFS data also.

Bulk analysis by XAS has revealed stark differences between each of the reduced Au, Pt and Pd/CuClP materials. Reduced under identical conditions, the Pt material has shown a propensity for complete extrusion and reduction of the associated anionic precursor to form NPs on the surface of the material. The XAS analysis of the reduced Au material has indicated negligible reduction of the precursor, with only minor fractions of NP identified by TEM analysis. Finally the Pd material has revealed a slightly larger fraction of extrusion and reduction, although in light of the TEM and PXRD results, the metallic fraction is distributed amongst some larger particles caused by some CuClP framework degradation. However, the major fraction still remains as the $[PdCl_4]^{2-}$ species.

4.2.1.4 X-Ray Photoelectron Spectroscopy

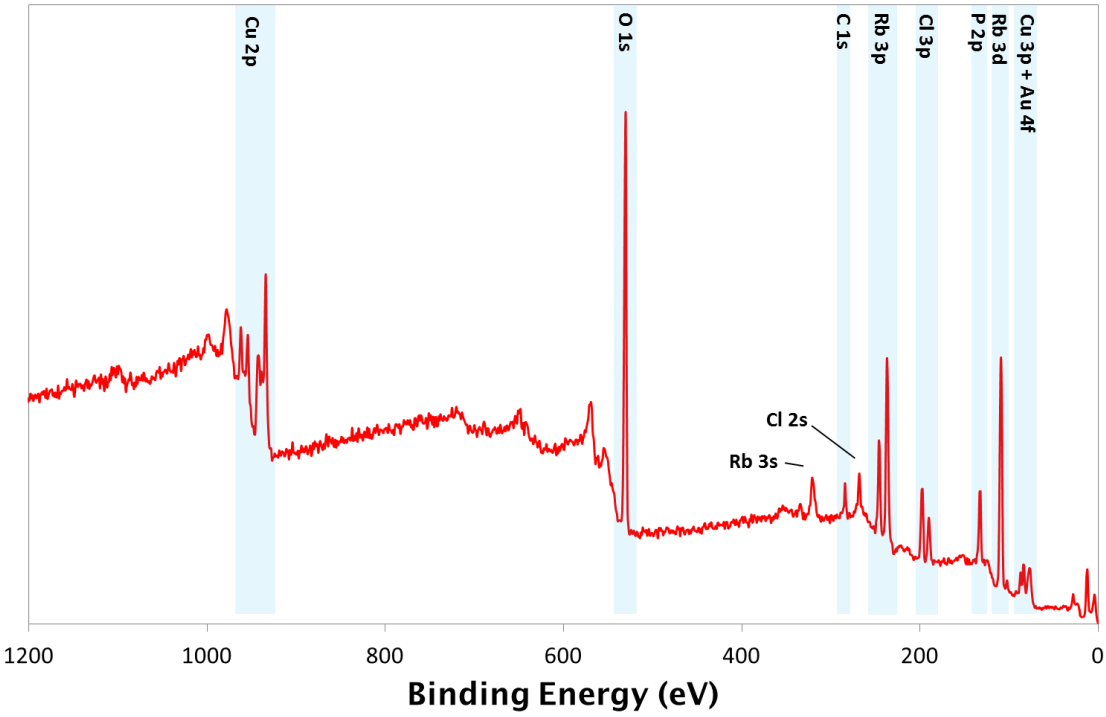

Figure 4.16 Example survey spectra of a reduced Au/CuClP catalyst

High resolution XPS data were also acquired in order to further probe the nature of the metallic species, and to contrast these findings with the XAS studies. Figure 4.16 shows an example of a survey spectra collected for a reduced Au/CuClP material. The regions related to photoelectrons ejected from various elements present in the sample, and their respective electronic shells, are highlighted and labelled. All other peaks are related to the detection of Auger electrons and are not analysed in this study.

As can be seen in the high resolution XPS spectra for the Au samples (Figure 4.17), a signal for Au(0) is present, not only in the reduced sample, but also in the calcined and as-synthesized materials. It is highly likely that these are generated from small amounts of larger crystalline gold impurities in the synthesis step, before the actual formation of the crystalline framework. This is apparent from the observation that the Au(0) $4f_{7/2}$ signal has a binding energy that is typical of bulk gold at 84.1 eV. It was further noted in the calcined sample that the presence of the Au(0) signal increases relative to that of the Au(III) $4f_{7/2}$ signal at 86.8 eV, but a slight shift to lower binding energy for the Au(0) $4f_{7/2}$ to 83.9 eV was observed. Furthermore, for the reduced sample, almost complete conversion of Au(III) to Au(0) was observed, with a greater shift in the Au(0) $4f_{7/2}$ peak to a lower binding energy of 83.6 eV. This shift to a lower binding energy for the Au(0) peaks has been observed, as a notable characteristic, for the formation of nanoparticulate gold.[34-35] Miller *et al.*[34] attribute this phenomenon to a change in the local electronic structure close to the Fermi level of the small nanoparticles, in comparison with bulk gold.

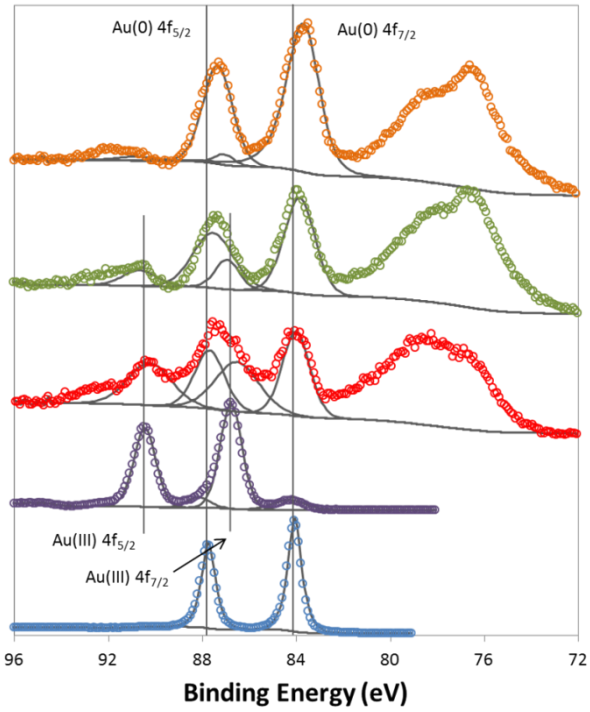

Figure 4.17 XPS spectra of as-synthesised (red), calcined (green) and reduced (orange) Au/CuClP materials against $KAuCl_4$ (purple) and metallic (blue) standards

In stark contrast with XAS, XPS is a surface sensitive technique and thus it is interesting to note the presence of metallic Au NPs in the XPS, even though a larger proportion of the Au present was shown to manifest as $[AuCl_4]^-$ from the EXAFS measurements (Figure 4.11). These results indicate that these materials are composed of isolated fractions of surface NPs, and hence represent distinct, discrete regions of Au species across a single-crystal of the framework.

The large peak adjacent to the Au 4f peaks at lower binding energy (76-78 eV) in the XPS spectra (Figure 4.17) is associated with a Cu 3p signal originating from the framework. Whilst this is clearly resolved from the Au peaks in the XPS spectra, there is some overlap with the Pt 4f peaks as can be seen in Figure 4.18. For the sake of clarity, only peaks from the Pt have been displayed in the high resolution spectra, however an example of peak fitting including the Cu 3p assignments can be seen in Figure 4.19. From the Pt XPS data, a similar trend to the Au materials is observed; namely, that calcination of the as-synthesized Pt sample results in the generation of a small quantities of Pt(0) that is apparent at 71.2 eV (compared with Pt(II) at 72.4 eV). However, the most striking observation was noted for the reduced sample (Figure 4.18), where complete reduction of the Pt(II) is apparent, and only peaks associated with the metallic Pt(0) dominate the spectra. These results, juxtaposed with observations from the EXAFS data (Figure 4.11 and Table 4.1), further corroborate the findings relating to the complete reduction of the $[PtCl_4]^{2-}$ species to metallic NPs.

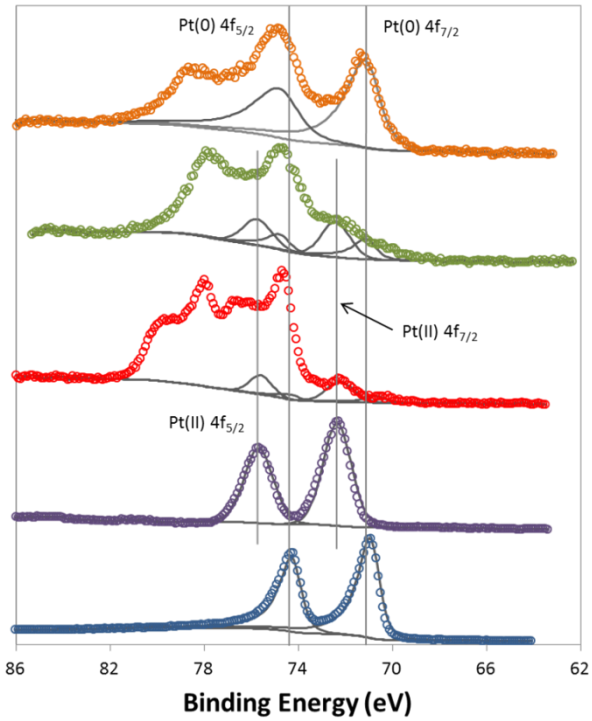

Figure 4.18 XPS spectra of as-synthesised (red), calcined (green) and reduced (orange) Pt/CuClP materials against K_2PtCl_4 (purple) and metallic (blue) standards

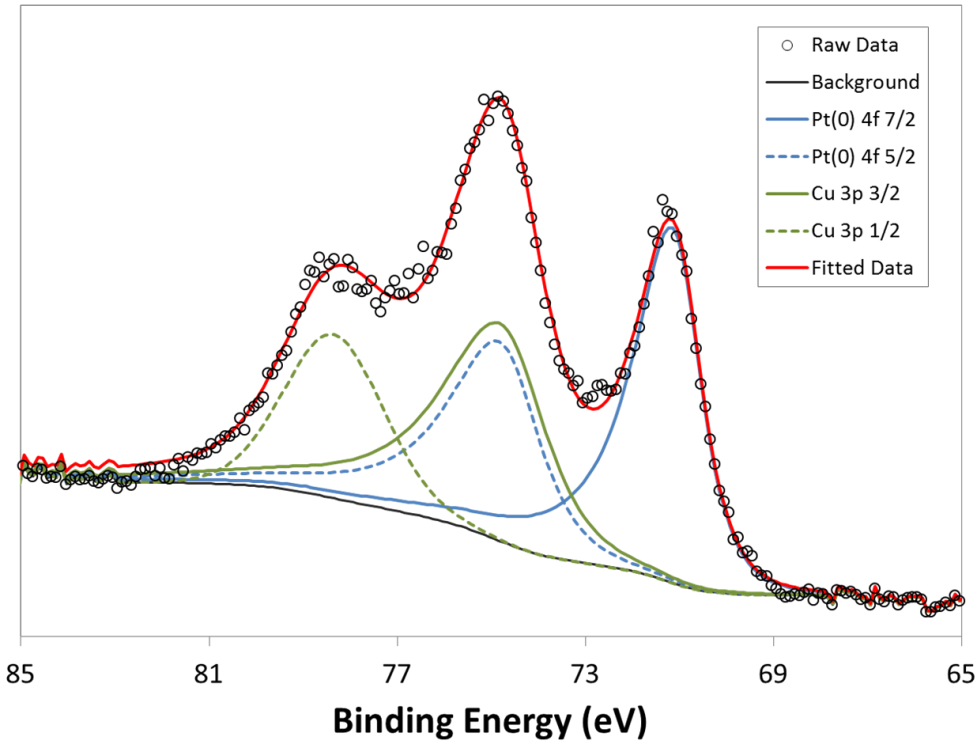

Figure 4.19 High Resolution XPS spectra of reduced Pt catalyst with example fitting including assignment of Cu 3p peaks.

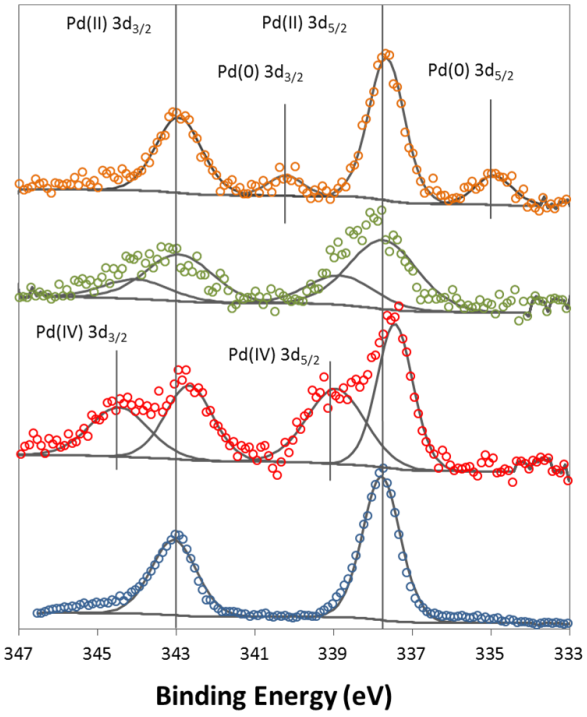

Figure 4.20 XPS spectra of as-synthesised (red), calcined (green) and reduced (orange) Pd/CuClP materials against a K_2PdCl_4 (blue) standard

XPS data from the Pd 3d region of the spectra (Figure 4.20) clearly show a transition from a mixture of Pd(IV) and Pd(II) species in the as-synthesized material (binding energies of 338.9 and 337.6 eV respectively), to predominantly Pd(II) in the calcined analogues, with some indications for the presence of Pd(0) (335.0 eV) in the reduced samples. This, in conjunction with the EXAFS data, clearly shows that, although the reduction process seems to be much better for extruding nanoparticles than calcination, the presence of metallic Pd(0) is still minor in comparison with Pd(II) species. It can also be concluded that the EXAFS data provide no evidence of any significant PdO_x phase, with the major contribution in the Fourier transform associated with the characteristic scattering of Pd-Cl (Figure 4.11 and Table 4.1). EXAFS data was also acquired for a PdO standard (Figure 4.12), which illustrates two distinct shells at 1.6 and 3.0 Å (Pd-O and Pd-Pd scattering paths) in the Fourier transform, that are not present in the data obtained for these Pd materials. This supports the assertion that Pd oxide particles are not produced during the synthesis procedure and that the Pd(II) species are predominantly associated with the abundant chlorometallate precursor anions, as in the as-synthesized materials.

It is interesting to note that, although identical conditions were used for thermally activating the analogous metal chloride supported frameworks, the Pt material appears much more readily amenable and susceptible to nanoparticle formation by extrusion, than the Au or Pd. This could be attributed to the differing strength of interactions between the discrete chlorometallate anions within the framework channels and the framework matrix.

4.2.2 Aerobic Oxidation of Vanillyl Alcohol and Activation Effects by Reduction

All three catalysts (calcined and reduced under identical conditions, as outlined in the experimental section) were probed for their catalytic potential, with a view to establishing some initial trends that could be rationalised, not only on the basis of the shape and size of the nanoparticles, but more importantly on their propensity to readily extrude from their crystalline microporous framework. The aerobic oxidation of vanillyl alcohol to vanillin, an intermediate step in the industrial process to form vanillin from guaiacol (Figure 4.2 and Figure 4.3), was used as a model probe reaction, given its importance from an industrial perspective.

The catalytic oxidation is composed of three main steps; namely i) the adsorption of the alcohol on the surface with the formation of a metal-alcoholate species, ii) the β-hydride elimination that results in the formation of the metal-hydride intermediate and the carbonyl compound, which subsequently desorbs, and iii) the oxidation of the metal hydride intermediate with concomitant formation of water and subsequent regeneration of the metallic active site, which is now available for further catalytic turnover.[16, 36-37] Interestingly, as reported in Figure 4.21, the calcined catalysts show only modest activity towards this oxidation reaction with little difference between them in terms of activity. Despite the small differences, similar trends are observed to the aerobic oxidation of benzyl alcohol as reported in Chapter 3, with the Pd material showing slightly higher conversions, and the Au analogue showing the lowest. Similarly, it can be observed from the selectivity profiles that at 8-10 hours of reaction, the Pt catalyst is also marginally more selective.

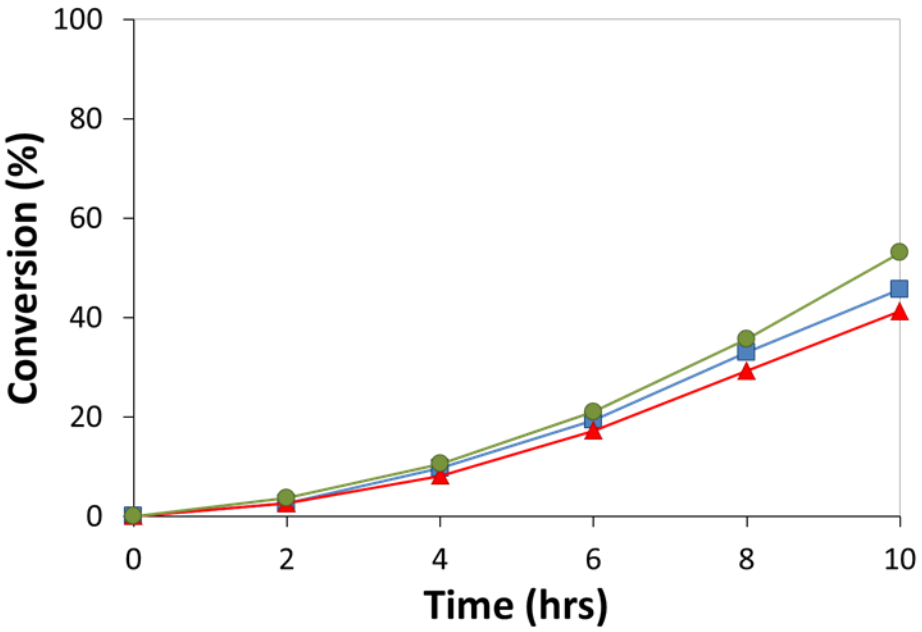

Figure 4.21 Reaction profile of calcined Au (red), Pt (blue) and Pd/CuClP (green) catalysts for aerobic oxidation of vanillyl alcohol

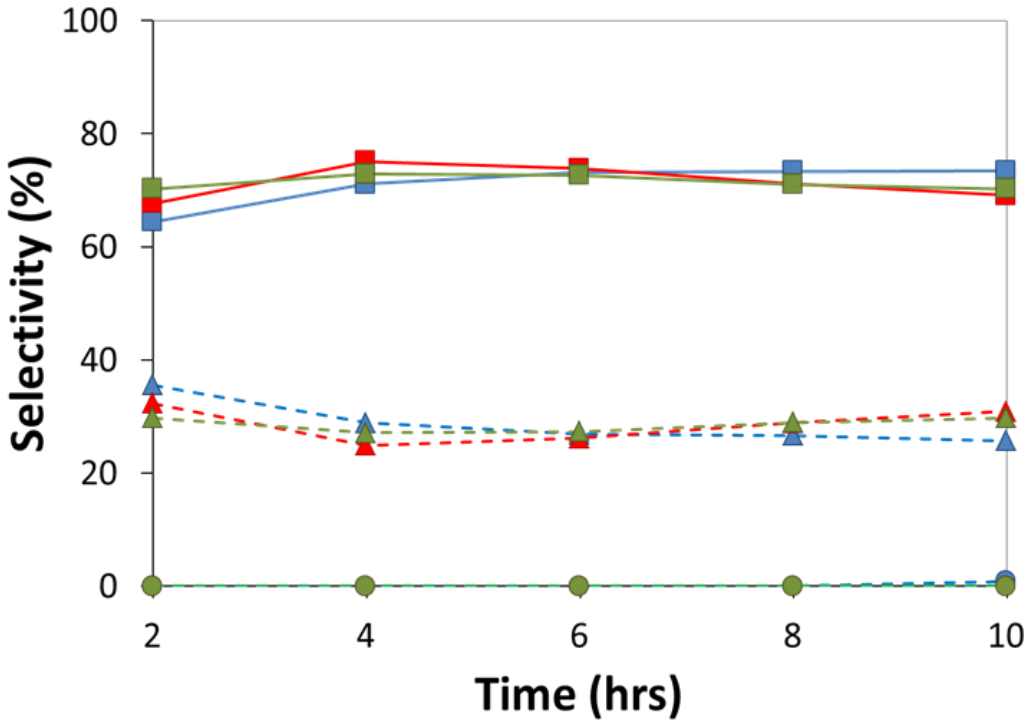

Figure 4.22 Selectivity profiles of calcined Au (red), Pt (blue) and Pd/CuClP (green) catalysts towards vanillin (squares), vanillic acid (circles) and vanillyl *tert*-butyl ether (triangles)

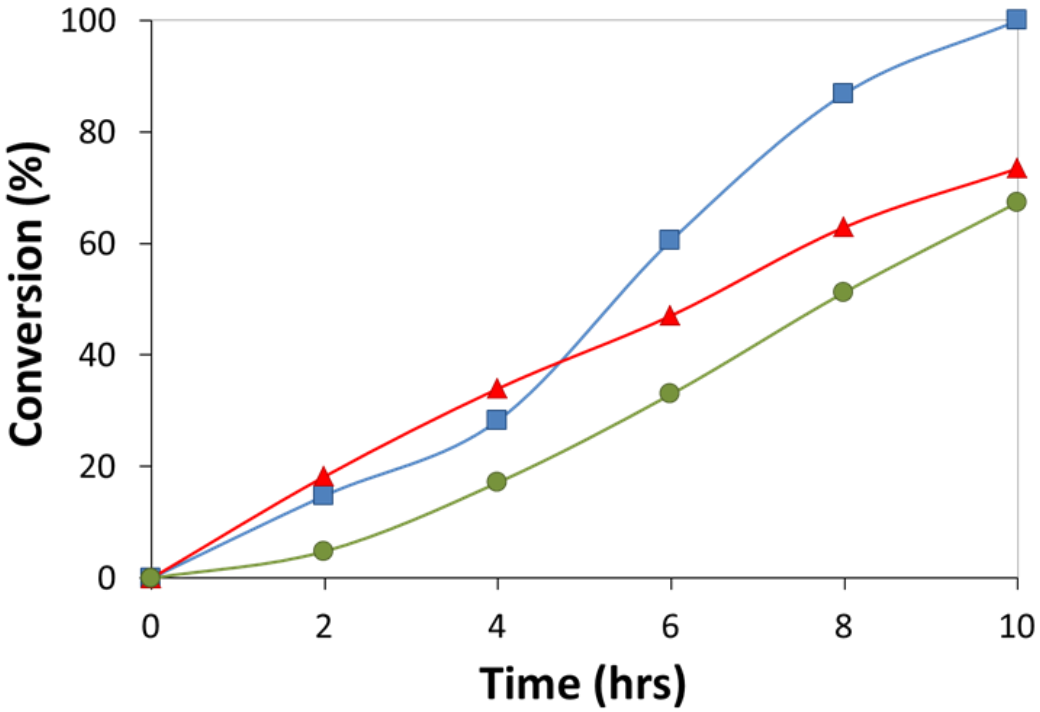

Figure 4.23 Reaction profile of reduced Au (red), Pt (blue) and Pd/CuClP (green) catalysts for aerobic oxidation of vanillyl alcohol

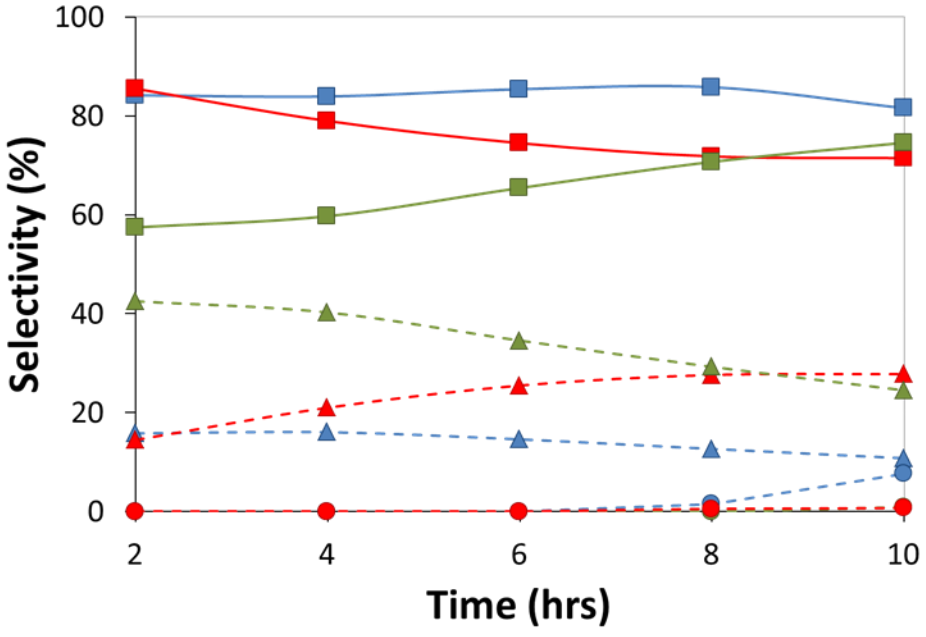

Figure 4.24 Selectivity profiles of reduced Au (red), Pt (blue) and Pd/CuClP (green) catalysts towards vanillin (squares), vanillic acid (circles) and vanillyl *tert*-butyl ether (triangles)

In contrast to the benzyl alcohol oxidation, the rate of reaction appears to increase over time for all three calcined catalysts, rather than having a linear zero-order rate of reaction. It is possible that this could be due to a prolonged period of activation or slightly different operating mechanisms; however more detailed kinetic studies would need to be undertaken to shed further light on the exact cause.

Comparatively, as shown by the reaction profiles in Figure 4.24, all three reduced catalysts were shown to have higher activities for this aerobic oxidation than the calcined catalysts, with the reduced Pt-analogue affording close to 100 % conversion and selectivities for vanillin in excess of 80%. These results show a significant increase in activity and efficiency for this one-step process that was devised, in contrast with the multi-step processes that are currently employed in industry.

It is also striking to note that the three reduced catalysts show more compelling differences in their activity when compared with the calcined catalysts. The reduced Au and Pd activities have increased by a fraction, even though they are surpassed by that of the Pt material. Errors involved in the data for samples make it difficult to determine trends in the development of the reaction rate over time with these data, although the Pt and Pd seem to indicate a lesser induction period with the rate increasing to a point half way through the reaction before reducing at high conversion levels for the Pt, or stabilising for the Pd/CuClP. The Au material shows a trend closer to a linear zero-order-type rate of reaction; however as before, more detailed kinetic studies would be necessary to draw unambiguous conclusions.

Contrasting the selectivity profiles, the selectivity of Pt towards vanillin increases slowly over time until vanillic acid is produced in small quantities at prolonged reaction times. The Pd/CuClP material also has a steady increase in selectivity over time, with the Au/CuClP material showing opposite properties with a steady drop in selectivity from the start of the reaction. More significantly, the main by-product in this reaction is not the over-oxidation product (the carboxylic acid) as with the benzyl alcohol oxidation, but an ether formed with the solvent *tert*-butanol molecules as identified by GC-MS. The origin of the 4-hydroxy-3-methoxybenzyl *tert*-butyl ether (vanillyl *tert*-butyl ether) can be potentially justified on the basis of the generation of a hydride species,[37-38] that induces local acidity in the nanoparticle, thus facilitating the

etherification between the stabilized vanillyl alcoholate and the adsorbed *tert*-butanol solvent molecules (Scheme 4.1). It is well-known that *p*-hydroxybenzylic alcohols can undergo an etherification reaction in presence of another alcohol under acidic or harsh oxidative conditions.[39]

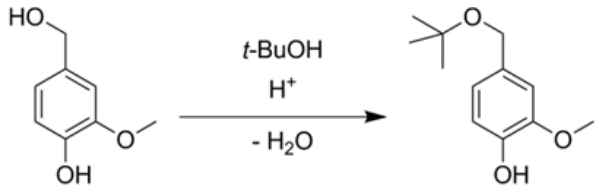

Scheme 4.1 Formation of ether by-product by reaction of vanillyl alcohol with *t*-butanol

The ether is not observed in the equivalent aerobic oxidation reaction with benzyl alcohol, however higher temperatures are required for this reaction which may well facilitate the formation of this by-product.

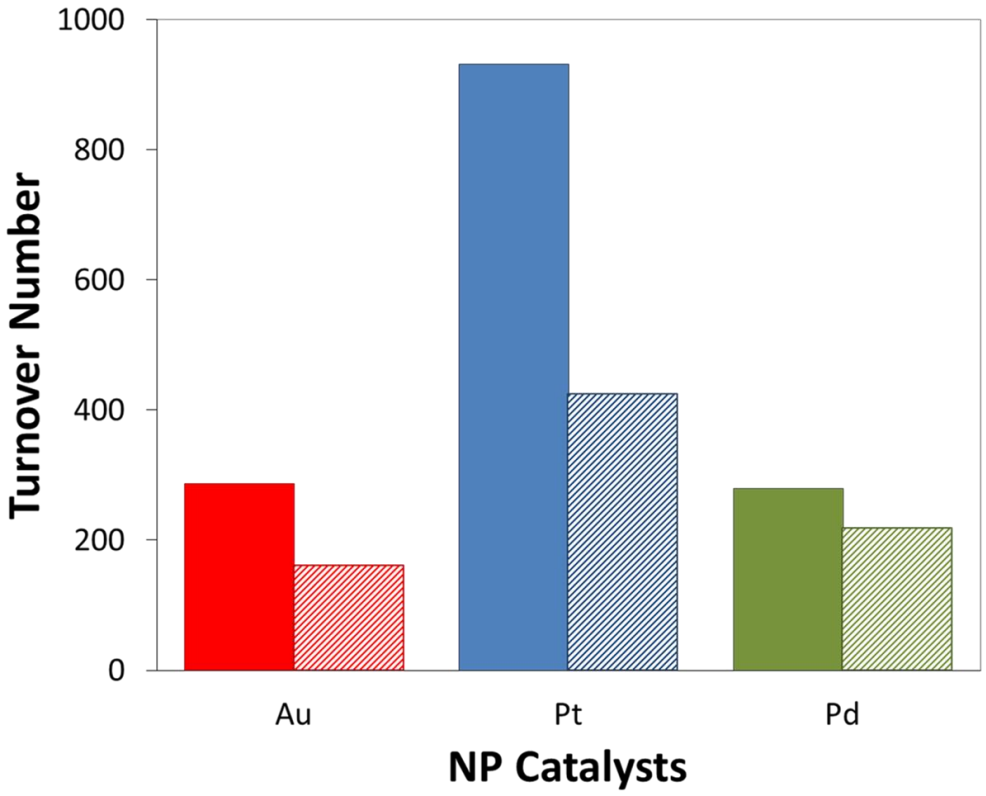

Figure 4.25 TONs of reduced (solid) and calcined (striped) Au, Pt and Pd/CuClP catalysts for the aerobic oxidation of vanillyl alcohol after 10 hours of reaction @ 170 °C

Given the challenging aspects of this aerobic oxidation, turnover numbers (TONs) obtained with the Au and Pd catalysts were modest. However, the performance of the corresponding Pt-analogue far exceeded that of its Au and Pd counterparts, with the reduced Pt catalyst, to the best of our knowledge, yielding unprecedented turnover values for this aerobic oxidation at moderate reaction conditions (Figure 4.25). This clearly highlights the superior role of the Pt NP catalyst, in this series of materials, for aerobic oxidation reactions. From the XPS and EXAFS data, the high activity of the Pt material can be attributed to the complete extrusion of the $[PtCl_4]^{2-}$ precursor, to yield stabilised discrete nanoparticles that are amenable for catalysis, in stark contrast with the Au and Pd materials. In light of these results, it is easy to conclude that the activation parameters can have significant effects on the extrusion process and the ability to generate nanoparticles by complete reduction.

4.3 Conclusions

Au, Pt and Pd/CuClP materials were successfully activated under reducing conditions, for structural and catalytic comparison of the activation parameters with the calcined materials from *Chapter 3*. Elucidation of the bulk and surface structural properties revealed unambiguous differences between each of the noble metal materials reduced under identical conditions. EXAFS and XANES of the calcined materials revealed that only minor fractions of the supported $[AuCl_4]^-$, $[PtCl_4]^{2-}$ and $[PdCl_4]^{2-}$ anions were extruded to generate the metallic NP species observed by TEM, with the bulk metals remaining predominantly in their precursor form. In contrast, reduction in the presence of H_2 allowed for the complete reduction of Pt anions to generate metallic NPs, however a small fraction of reduction was observed for the Au/CuClP, similar to the calcined analogue. The Pd/CuClP showed formation of metallic species in the EXAFS and XANES spectra, however TEM and PXRD studies revealed some degradation of the framework, contrary to the Pt and Au systems, that formed a fraction of small NP species as observed in the calcined material, but also larger particles at 20-50 nm in size.

Given the identical reduction conditions, these results show that the interactions between the complex anions and the supporting framework must

differ, either in the type of interactions or the strength of interactions. The framework itself is neutral with the charge of the anions countered by the presence of rubidium ions; however localised dipolar or electrostatic interactions could be occurring. Alternatively, the presence of copper chloride species in the pores, as observed in the 'blank' framework synthesised without the presence of a noble metal source, could form competing interactions within the pores of the framework given that the loadings of the noble metals are low.

Using the aerobic oxidation of vanillyl alcohol to vanillin, it was also determined that the reduced Pt/CuClP catalyst performs significantly better than the Au and Pd catalysts, highlighting the structural differences and also confirming that the NPs are the active site for this reaction, with the increase in activity showing a correlation with the degree of extrusion and NP formation. With complete extrusion of the Pt/CuClP system, it would be interesting to further probe the effects of pressure on the catalytic activity to identify whether the reaction follows an expected deviation from Henry's law as would be expected for higher concentrations of O_2, or whether other mechanistic effects have a greater handle on the rates of the reaction. It would also be further useful to establish the effects of catalyst and substrate concentrations in the oxidation of vanillyl alcohol to build up a better understanding of the mechanism and how it compares with the related non-functionalised benzyl alcohol.

To summarise, it is interesting to note the ease of extrusion of the Pt material over the analogues counterparts. Activation in the presence of H_2 has proved more effective than at higher temperature under an aerobic atmosphere in the extrusion processes, that has generated NP catalysts with higher activity than calcined catalysts for activation of O_2 toward oxidation reactions.

Whilst the reduced catalysts have shown interesting catalytic properties, a small by-product was observed in the ether formation of vanillyl alcohol with the solvent *t*-butanol molecules. The reactions were run as proof of concept and only a small degree of optimisation was performed. Even though the selected conditions outperformed the activity and yields observed for industrial catalysts, for more improved catalytic potential, screening of different solvents (in an effort to remove the ether by-product) and reactant concentrations could be performed.

It has been further established that the activation parameters play the most significant role in determining the catalytic activity, correlated closely with the extent of extrusion and reduction of the complex anions to NPs. This work focused mostly on the effect of atmospheric composition during activation, however it would be interesting to see the effects of reduction time (as identified in a preliminary study at the end of the last chapter) and activation temperature on the extrusion and reduction process. It is possible that higher temperature or longer activation times could favour more complete extrusion in the case of the Au material, or in contrast, lower temperatures may well be more conducive toward the extrusion of the Pd material to preserve the integrity of the host framework.

In addition, earlier work in chapter 3 indicated that the selectivity profiles of extruded catalysts were specific to the metal, with rates of reaction dependent on the extent of extrusion. Recent studies have shown interesting properties of bimetallic[40-44] and trimetallic[40, 45] NP compositions in oxidation reactions.[46-48] As such, this extrusion method could be applied in the generation of active and uncapped multimetallic NP catalysts, for highly selective oxidation reactions on a wide variety of alcohol substrates, not restricted only to benzylic alcohols. It has been shown that changing the temperature and atmosphere of activation in bimetallic systems can have a significant influence on the nanostructure of bimetallic systems, with alloyed particles being more active toward oxidation of alcohols.[10] It would be interesting to probe the nanostructure effects of this extrusion method, to see how the process might influence formation of alloy, cluster-in-cluster or core-shell type structures. Furthermore, given the recent reports of the activation of aliphatic molecules with NP catalysts, these materials could be applied in the more cumbersome and energy intensive oxidations. In addition to oxidation reactions, other organic transformations could be explored, as well as alternative applications such as antibacterial activity noted from AuPt bimetallic NPs.[49]

4.4 References

1 D. Seo and H. Song, Synthesis of Gold Nanoparticles in Liquid Phase in *Gold Nanoparticles for Physics, Chemistry and Biology* (Eds.: C. Louis, O. Pluchery), Imperial College Press, London, **2012**.
2 M. Zhao, K. Deng, L. He, Y. Liu, G. Li, H. Zhao and Z. Tang, *J. Am. Chem. Soc.,* **2014**, *136*, 1738.
3 Y. Luan, Y. Qi, H. Gao, N. Zheng and G. Wang, *J. Mater. Chem. A,* **2014**, *2*, 20588.
4 H. Dai, N. Cao, L. Yang, J. Su, W. Luo and G. Cheng, *J. Mater. Chem. A,* **2014**, *2*, 11060.
5 A. Aijaz and Q. Xu, *J. Phys. Chem. Lett.,* **2014**, 1400.
6 D. Zhang, F. Ye, Y. Guan, Y. Wang and E. J. M. Hensen, *RSC Adv.,* **2014**, *4*, 39558.
7 Z. Sun, G. Li, L. Liu and H.-o. Liu, *Catal. Commun.,* **2012**, *27*, 200.
8 R. Wu, X. Qian, K. Zhou, H. Liu, B. Yadian, J. Wei, H. Zhu and Y. Huang, *J. Mater. Chem. A,* **2013**, *1*, 14294.
9 C. Louis, Chemical Preparation of Gold Nanoparticles on Surfaces in *Gold Nanoparticles for Physics, Chemistry and Biology* (Eds.: C. Louis, O. Pluchery), Imperial College Press, London, **2012**.
10 M. Morad, M. Sankar, E. Cao, E. Nowicka, T. E. Davies, P. J. Miedziak, D. J. Morgan, D. W. Knight, D. Bethell, A. Gavriilidis and G. J. Hutchings, *Catal. Sci. Technol.,* **2014**, *4*, 3120.
11 H. S. Oh, J. H. Yang, C. K. Costello, Y. M. Wang, S. R. Bare, H. H. Kung and M. C. Kung, *J. Catal.,* **2002**, *210*, 375.
12 G. C. Bond, C. Louis and D. T. Thompson, *Catalysis by Gold, Vol. 6*, Imperial College Press, London, **2006**.
13 A. G. Abatjoglou and D. J. Miller, Aldehydes in *Kirk-Othmer Encyclopedia of Chemical Technology*, John Wiley & Sons, Inc., **2011**.
14 H. Tsunoyama, H. Sakurai, Y. Negishi and T. Tsukuda, *J. Am. Chem. Soc.,* **2005**, *127*, 9374.
15 J. Muzart, *Tetrahedron,* **2003**, *59*, 5789.
16 A. Abad, A. Corma and H. García, *Chem. Eur. J.,* **2008**, *14*, 212.
17 P. Fristrup, L. Johansen and C. Christensen, *Catal. Lett.,* **2008**, *120*, 184.
18 K. Mori, T. Hara, T. Mizugaki, K. Ebitani and K. Kaneda, *J. Am. Chem. Soc.,* **2004**, *126*, 10657.
19 J. C. F. Rodríguez-Reyes, C. M. Friend and R. J. Madix, *Surf. Sci.,* **2012**, *606*, 1129.
20 T. J. Rockey, M. Yang and H.-L. Dai, *J. Phys. Chem. B,* **2006**, *110*, 19973.
21 D. I. Enache, D. W. Knight and G. J. Hutchings, *Catal. Lett.,* **2005**, *103*, 43.
22 J.-P. Vidal, Vanillin in *Kirk-Othmer Encyclopedia of Chemical Technology*, John Wiley & Sons, Inc., **2006**.
23 Board of Directors operating Michigan State University, J. W. Frost, **2002,** *Synthesis of vanillin from a carbon source,* US Patent 6,372,461 B1.
24 Rhodia Chimie, P. Metivier, **2001,** *Method for preparing a 4-hydroxybenzaldehyde and derivatives,* US Patent 6,184,421.
25 J. Hansen, E. H. Hansen, H. P. Sompalli, J. M. Sheridan, J. R. Heal and W. D. O. Hamilton, **2013,** *Compositions and methods for the biosynthesis of vanillin or vanillin beta-d-glucoside,* WO Patent 2013022881 A1.
26 Y. Tan, X. Dai, Y. Li and D. Zhu, *J. Mater. Chem.,* **2003**, *13*, 1069.

27 C. Díaz, M. L. Valenzuela, D. Bravo, C. Dickinson and C. O'Dwyer, *J. Colloid Interface Sci.,* **2011**, *362*, 21.
28 C. Hammond, *The Basics of Crystallography and Diffraction*, 2nd ed., Oxford University Press, Oxford, **2008**.
29 C. M. A. Parlett, D. W. Bruce, N. S. Hondow, A. F. Lee and K. Wilson, *ACS Catal.,* **2011**, *1*, 636.
30 J. Keating, G. Sankar, T. I. Hyde, S. Kohara and K. Ohara, *Phys. Chem. Chem. Phys.,* **2013**, *15*, 8555.
31 C. Li, Y. Wang, X. Guo, Z. Jiang, F. Jiang, W. Zhang, W. Zhang, H. Fu, H. Xu and G. Wu, *J. Phys. Chem. C.,* **2014**, *118*, 3140.
32 P. Atkins, T. Overton, J. Rourke, M. Weller and F. Armstrong, *Inorganic Chemistry*, 5th ed., Oxford University Press, Oxford, **2010**.
33 M. Newville, Fundamentals of XAFS in *Spectroscopic Methods in Mineralogy and Materials Sciences* (Eds.: G. S. Henderson, D. R. Neuville, R. T. Downs), Mineralogical Society of America, **2014**.
34 J. T. Miller, A. J. Kropf, Y. Zha, J. R. Regalbuto, L. Delannoy, C. Louis, E. Bus and J. A. van Bokhoven, *J. Catal.,* **2006**, *240*, 222.
35 M. Turner, V. B. Golovko, O. P. H. Vaughan, P. Abdulkin, A. Berenguer-Murcia, M. S. Tikhov, B. F. G. Johnson and R. M. Lambert, *Nature,* **2008**, *454*, 981.
36 S. E. Davis, M. S. Ide and R. J. Davis, *Green Chem.,* **2013**, *15*, 17.
37 Y. H. Ng, S. Ikeda, Y. Morita, T. Harada, K. Ikeue and M. Matsumura, *J. Phys. Chem. C.,* **2009**, *113*, 12799.
38 X. Wang and L. Andrews, *Angew. Chem., Int. Ed.,* **2003**, *42*, 5201.
39 R. Ramu, N. Ravindra Nath, M. R. Reddy and B. Das, *Synth. Commun.,* **2004**, *34*, 3135.
40 H. Zhang and N. Toshima, *Catal. Sci. Technol.,* **2013**, *3*, 268.
41 J. K. Edwards, J. Pritchard, L. Lu, M. Piccinini, G. Shaw, A. F. Carley, D. J. Morgan, C. J. Kiely and G. J. Hutchings, *Angew. Chem., Int. Ed.,* **2014**, *53*, 2381.
42 V. Petkov, B. N. Wanjala, R. Loukrakpam, J. Luo, L. Yang, C.-J. Zhong and S. Shastri, *Nano Lett.,* **2012**, *12*, 4289.
43 X.-Y. Liu, Y. Zhang, M.-X. Gong, Y.-W. Tang, T.-H. Lu, Y. Chen and J.-M. Lee, *J. Mater. Chem. A,* **2014**, *2*, 13840.
44 N. Dimitratos, J. A. Lopez-Sanchez, J. M. Anthonykutty, G. Brett, A. F. Carley, R. C. Tiruvalam, A. A. Herzing, C. J. Kiely, D. W. Knight and G. J. Hutchings, *Phys. Chem. Chem. Phys.,* **2009**, *11*, 4952.
45 P. Qiao, S. Xu, D. Zhang, R. Li, S. Zou, J. Liu, W. Yi, J. Li and J. Fan, *Chem. Commun.,* **2014**, *50*, 11713.
46 L. Kesavan, R. Tiruvalam, M. H. A. Rahim, M. I. bin Saiman, D. I. Enache, R. L. Jenkins, N. Dimitratos, J. A. Lopez-Sanchez, S. H. Taylor, D. W. Knight, C. J. Kiely and G. J. Hutchings, *Science,* **2011**, *331*, 195.
47 T. Balcha, J. R. Strobl, C. Fowler, P. Dash and R. W. J. Scott, *ACS Catal.,* **2011**, *1*, 425.
48 G. L. Brett, Q. He, C. Hammond, P. J. Miedziak, N. Dimitratos, M. Sankar, A. A. Herzing, M. Conte, J. A. Lopez-Sanchez, C. J. Kiely, D. W. Knight, S. H. Taylor and G. J. Hutchings, *Angew. Chem., Int. Ed.,* **2011**, *50*, 10136.
49 Y. Zhao, C. Ye, W. Liu, R. Chen and X. Jiang, *Angew. Chem., Int. Ed.,* **2014**, *53*, 8127.

4.5 Appendix

4.5.1 Experimental Methods

4.5.1.1 Synthesis of $[MCl_x]^{n-}$ supported Frameworks

Synthesis of $Rb_9Cu_6(P_2O_7)_4Cl_3.[MCl_4]$ (M = Au, Pt or Pd): A slightly modified method was used from the previous chapter, reducing the levels of noble metal chlorides used in an effort to eliminate small quantities of larger bulk metal species being produced in the synthesis step.

Copper(II) fluoride (0.1168 g, 1.150 mmol), 85 wt % orthophosphoric acid (0.2 mL, 2.922 mmol), 50 wt % RbOH (0.24 mL, 2.037 mmol), RbCl (0.28 g; 2.316 mmol) and a source of MCl_x; $HAuCl_4$ (0.0489 g, 0.144 mmol), K_2PtCl_4 (0.0515 g, 0.124 mmol) or K_2PdCl_4 (0.0405 g, 0.124 mmol) are mixed in a PTFE liner of a custom-made 23 mL hydrothermal vessel. Due to the lack of liquid components and low quantities of reactants, the mixture is allowed to age for 30 mins to 1 hour and occasionally physically mixed to encourage a degree of homogenisation before heating.

The hydrothermal vessel is sealed in a steel autoclave and heated to 448 K for 2 days. Products form as brilliant green cuboid crystals for both the Au and Pt material, and light brown crystals for the palladium material. The crystalline materials are washed with deionised water (100 mL) to remove any excess salts and water soluble impurities. Samples are then dried and ground in a pestle and mortar prior to activation.

4.5.1.2 Activation by Reduction

In addition to thermal calcination conditions as described in the third chapter, materials were also prepared by a thermal reduction method. For reduction, materials were ground and loaded into a ceramic boat, inserted into a tube furnace and heated under a steady flow of 5 % H_2/N_2 (measured approximately through the use of a bubbler; 2-3 bubbles per second) at 200 °C for 2 hours to generate the active catalysts. After reduction, the Au material appears mostly unchanged in colour, the Pt material changes to a very dark khaki green – more so than the in the calcination process, and the Pd materials becomes black

(Figure 4.26). The materials at this stage require no further treatment before use as catalysts.

Where described further in this chapter, calcined materials refer to those thermally activated in air at 500 °C for 2 hours, and reduced materials refer to those thermally activated in 5 % H_2/N_2 at 200 °C for 2 hours.

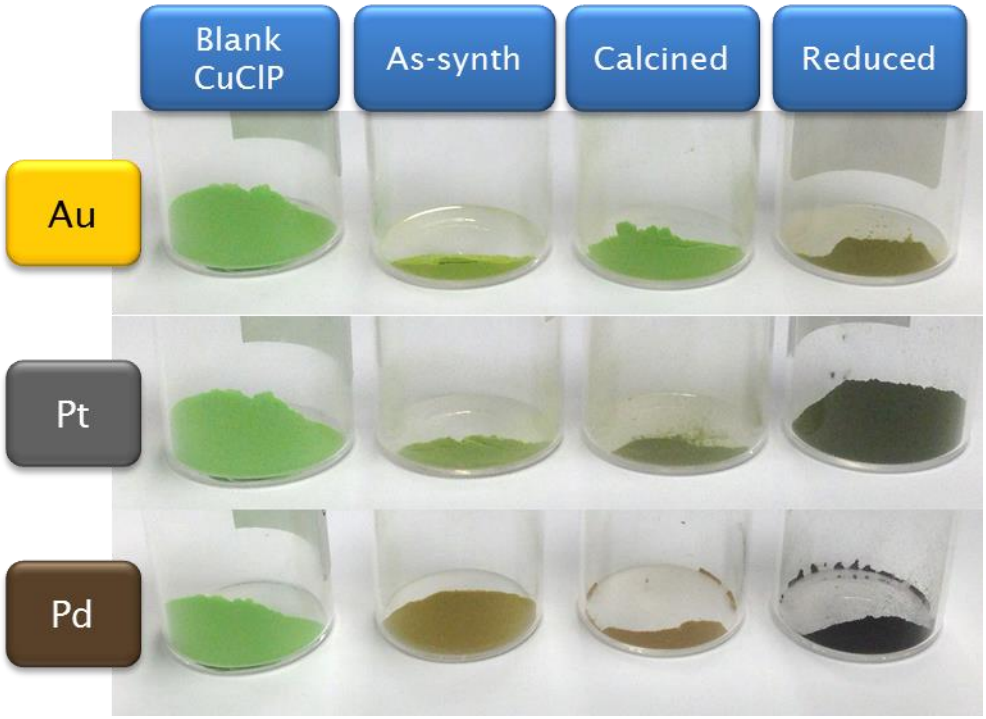

Figure 4.26 Photographs of blank framework along with each of the as-synthesised, calcined and reduced versions of the Au, Pt and Pd loaded catalysts

4.5.1.3 High Pressure Aerobic Oxidations of Vanillyl Alcohol

A typical catalytic reaction for the oxidation of vanillyl alcohol is as follows; vanillyl alcohol (1 g), diethylene glycol dimethyl ether (diglyme) as an internal standard (0.85 g) and *tert*-butanol as a solvent (30 mL) were weighed or measured into the 75 mL Teflon® liner. Subsequently, a catalyst material was weighed (0.05 g) and added to the mixture. A magnetic stirrer bar was added and the mixture stirred to achieve a homogenous distribution of reactants.

The liner was then sealed in the batch reactor and pressurised to 20 bar of air and heated to 170 °C using the thermocouple and digital temperature regulator. An aliquot (0.5-1.5 mL) was removed into a 2 mL eppendorf vial once the mixture had reached temperature, and centrifuged to remove any

suspended catalyst. The sample was then capped in a GC vial ready for analysis. Further samples were taken at designated time intervals by flushing the sampling port with a small amount of the reaction mixture into a waste vial to remove any residues from previous sampling, with an aliquot being collected in an eppendorf vial, centrifuged and capped in a GC vial as before. The reaction was left for the duration (e.g. 10 hours) before being cooled naturally or in a bucket of ice, depressurised and dismantled for cleaning.

Sample Analysis by GC-FID: Samples were analysed by GC (PerkinElmer, Clarus 480) using an Elite-5 column equipped with a flame ionisation detector (FID) and an autosampler with a 5μL capacity syringe. Products were identified against authenticated standards and quantified by calibration against the known internal standard.

The GC method employed was as follows: The autosampler was programmed to wash once with acetone before performing 2x sequential washes in the sample and ejected to the waste. A 2 μL aliquot of the sample was then injected into the injector port and the syringe washed a further 2x in acetone for cleaning.

The injector port and detector were heated to 320 °C and 300 °C for effective volatilisation of injected components and detection of gaseous components. Helium was used as a carrier gas with a flow of 50 mL/min and a split of 20:1.

A variable temperature program was used for the oven; first, the oven was equilibrated at 80 °C and held for 1.5 min after injection of the sample. Next, the oven was ramped at a rate of 40 °C/min up to 280 °C and held for a further 5 minutes. The total run time for the method was 11.5 minutes.

Calibration of Standards: Commercial standards of each of the starting and product materials were purchased for calibration and subsequent quantitative analysis by GC. A series of 5 samples were prepared with graduating concentrations of vanillyl alcohol, vanillin and vanillic acid in *tert*-butanol up to a maximum concentration of 0.22 mol dm^{-3}. A constant quantity of diglyme as an internal standard was added to each sample (0.21 mol dm^{-3}). Components were measured accurately to 4 decimal places.

The standards were run on the GC 3 times and the peak integrations recorded and averaged across the 3 samples to minimise the GC equipment error. Peak ratios were calculated for each of the components against the internal standard

and plotted against the respective mole ratios, as demonstrated in *Section 2.2.2.1*, to calculate the response factors of each component. R_f values under this method were calculated for vanillyl alcohol (2.7561), vanillin (1.3793) and vanillic acid (2.5564) against diglyme.

4.5.2 Characterisation Equipment

X-Ray Photoelectron Spectroscopy (XPS)

XPS analysis was performed using a Thermo-Scientific Theta Probe instrument equipped with monochromated Al K_α source in NEXUS facility, University of Newcastle. A flood gun was used for charge compensation. A pass energy of 200 eV and a step size of 1.0 eV was employed for all survey spectra while a pass energy of 40 eV and a step size of 0.1 eV was used for high-resolution spectra of the elements of interest. High-resolution spectra were collected for Au 4f transitions over a BE range of 72-96 eV, Pt 4f transitions between 62-86 eV and Pd 3d transitions between 333-347 eV. Where possible, samples were compared against commercial standards of the chlorometallate precursors ($KAuCl_4$, K_2PtCl_4 or K_2PdCl_4) or elemental metal (Note: $KAuCl_4$ was used as an alternative to $HAuCl_4$ due to the hygroscopic nature of the material and thus difficulty handling the material for analysis). All XPS spectra were calibrated against the carbon and/or oxygen 1s peaks, and high resolution spectra were fitted with Shirley backgrounds before peak analysis using the CasaXPS software.[1]

X-ray Absorption Spectroscopy (XAS)

Au, Pt and Pd XAS studies were carried out on the B18 beam-line at the Diamond Light Source, Didcot, UK. Measurements were performed using a QEXAFS set-up with a fast-scanning Si (111) or Si (311) double crystal monochromator. The normal time resolution of the spectra reported herein was 1 min/spectrum (k_{max} = 16); on average, six scans were acquired to improve the signal to noise level of the data. All samples were diluted with cellulose and pressed into pellets to optimize the effective edge-step of the XAFS data and measured in transmission mode using ion chamber detectors. All transmission XAFS spectra were acquired concurrently with the appropriate reference foil placed between I_t and I_{ref}. XAS data processing and EXAFS analysis were performed using IFEFFIT[2] with the Horae package[3] (Athena and Artemis).

The amplitude reduction factor, S_o^2, was derived from EXAFS data analysis of known compounds, and used as a fixed input parameter.

Transmission Electron Microscopy (TEM)

TEM images were collected on a JEOL JEM-2100 LaB_6 microscope with a 200 kV accelerating voltage; powder samples were prepared by suspending 1-2 mg in 1-2 mL ethanol and dropping on to lacey carbon or carbon film copper mesh grids, allowing for evaporation of the solvent before loading into the microscope.

Powder X-ray Diffraction (PXRD)

PXRD patterns were collected on a Siemens D5000 diffractometer or a Bruker D2 Phaser diffractometer using monochromatic Cu K_{α_1} radiation (λ = 1.5406 Å). Samples were prepared by grinding into a fine powder and mounted in a sample holder with a small well to hold the powder in place during analysis.

Chapter 5: Design of Nanoparticle/UiO-66 Hybrid Catalyst Materials for Oxidation and Tandem Applications

Special Acknowledgements

The following special acknowledgements recognise the contributed work of colleagues and collaborators to the presented content of this chapter.

William Webb: For help conducting some Knoevenagel condensation reactions and tandem reactions using amino-functionalised MOF materials (University of Southampton, UK)

Benny Chew: For useful discussions and collection of additional data via GC-MS (National University of Singapore and Institute of Materials Research and Engineering, Singapore)

Hui Ru Tan: For collection of TEM images of nano-MOF and nanoparticle/MOF materials (Institute of Materials Research and Engineering, Singapore)

"Look up at the stars and not down at your feet.
Try to make sense of what you see,
and wonder about what makes the universe exist.
Be curious."
Stephen Hawking

5.1 Hybrid NP/MOF Materials and Applications

Given the rise in applied research with metal-organic frameworks (MOFs), it is not unsurprising to note the increase in reports of NP/MOF materials in the field of catalysis.[4-5] MOFs possess a unique combination of properties that have given them scope for application in a multitude of areas; high porosity, large internal surface areas, low density, ease of synthetic modification and selective adsorption to name but a few.[6-8] Comprised of metal or metal oxide cluster nodes and linking organic struts, a wide array of MOFs can be synthesised from the vast number of metal and organic ligand combinations.

In terms of catalysis, MOFs can be used directly with vacant sites on metal centres acting as active sites,[9-13] or functionality within the organic linkers exploited.[9-10, 14-15] In addition MOFs can be used as hosts for other active moieties added to the structure, such as organometallic species coordinated to the framework ligands[16-18] or active nanoparticle species.[19-22] As this project has been investigating the properties of nanoparticle hybrid materials, the use of MOFs as supports for NPs has been of particular interest, a summary of which can be found in *Section 1.2.5.2*. Of course, despite the many thousands of reported MOF structures in the literature, not all are suitable as supports for catalytic applications. Many MOFs are sensitive to changes in temperature and chemical environment,[23-25] and would lose structural integrity over the course of a catalytic reaction and are thus not be suitable for a process requiring reproducibility and recyclability. As such, widely reported applications and further development of MOF materials and devices have been limited, more so, to the structures with good stability, both thermal and chemical. One particular MOF of recent interest is UiO-66 and the associated isoreticular family of MOFs. Reported first in 2008 by J. Cavka *et al.*,[26] there are now more than 100 papers reporting detailed structural characterisation and applications of these materials, with some of these discussed further in the following sections.

5.1.1 UiO-66: Family, Properties and Stability

5.1.1.1 The Structure of UiO-66 and Isoreticular Analogues

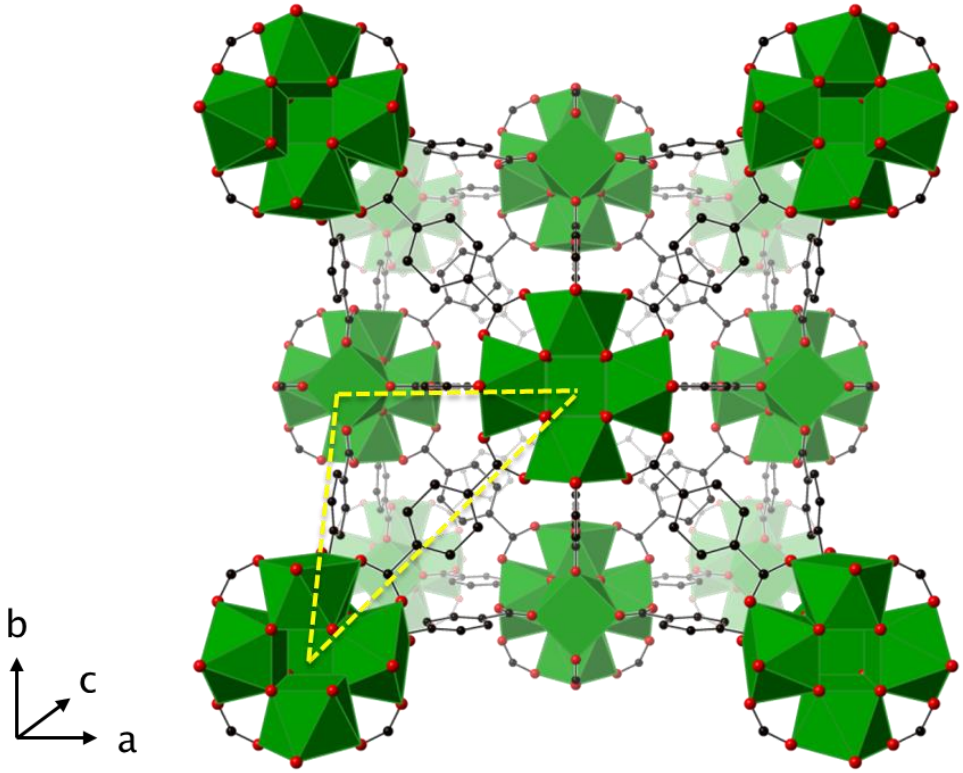

Figure 5.1 Representative crystal structure of UiO-66 with triangular pore window highlighted (Zr – green polyhedra; C – black spheres; O – red spheres; H omitted for clarity)

UiO-66 is a zirconium terephthalate MOF, where the node consists of a zirconium oxide based cluster with a general formula $Zr_6O_4(OH)_4(CO_2)_{12}$ that are linked together by linear and rigid, bidentate terephthalate molecules. Figure 5.1 shows a representative crystal structure, where the nodes can clearly be seen with green polyhedra representing the location of the Zr atoms. The nodes are oriented in a face-centred cubic (or cubic close packed) arrangement throughout the structure, with each node coordinated to 12 other nodes via the linkers – the highest coordination of nodes in any reported MOF structure – and equivalent to the expanded structure often observed in pure metals.[26] Due to the 'fcc' nature of the framework, the orientation of the terephthalate linkers are alternated by 90° if viewed down the a, b or c axes.

The node can be visualised as having two main features – the inner core and outer coordination sphere. The inner core consists of a Zr_6O_6 octahedron with 8-coordinate Zr atoms linked by alternating μ_3-O and μ_3-OH groups. The outer coordination sphere consists of the coordinating $-CO_2$ groups from the organic ligands that complete the coordination of the Zr atoms in the inner core, and the cluster as a whole.

Triangular pore-windows with accessible diameters of 6Å,[26] as highlighted in Figure 5.1, allow access to the internal structure of the UiO-66 framework with two main cage structures; an octahedral cage with a diameter of 11Å and a tetrahedral cage of 8Å.[27] All cages are linked by the triangular windows, and thus access is limited to molecules smaller than the accessible diameter of the window.

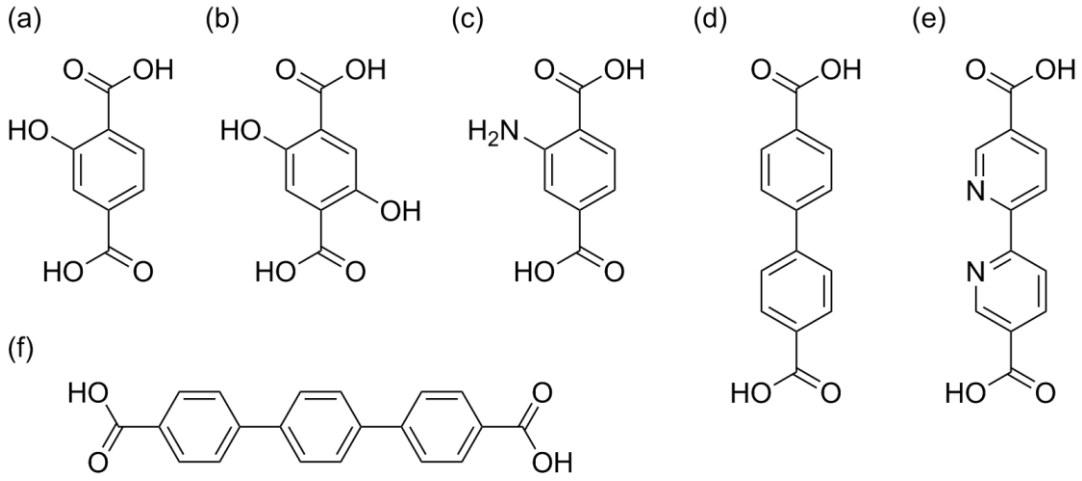

Figure 5.2 Alternative organic linkers in isoreticular UiO-type MOFs. (a) 2-hydroxyterephthalic acid, (b) 2,5-dihydroxyterephthalic acid, (c) 2-aminoterephthalic acid, (d) 1,4'-biphenyldicarboxylic acid, (e) 2,2'-bipyridyl-5,5'-dicarboxylic acid and (f) 4,4"-terphenyldicarboxylic acid

With a strong and rigid base structure, an isoreticular (same net) series of MOFs can be synthesised by using slightly modified or extended organic ligands. The term 'isoreticular' refers to the fact that with these new ligands, the structure and bonding of the framework remains unchanged, however the internal porosity and window/cage sizes are altered. Reticular synthesis and the comparison of basic net-like structures was first proposed by O'Keefe *et al.*[28-29] in an attempt to categorise MOFs based on their basic connectivity

between nodes and ligands. Additional groups can be added to the terephthalate linker such as hydroxyl groups and amine groups (Figure 5.2 (a-c)) which invariably lead to a small reduction in porosity. The length of the linkers can be extended by adding additional phenyl groups as in Figure 5.2 (d) and (f), also reported in the original paper with UiO-66 and formally named UiO-67 and UiO-68 respectively, and increase the sizes of the windows and cavities, as well as the total surface area within the structure (Table 5.1). The phenyl groups can also be replaced by pyrdiyl groups as in Figure 5.2 (e) to provide coordinating environments for extra-framework metal centres. This was first utilised in the incorporation of Ir, Re and Ru complexes within the modified UiO-67 parent framework for application in catalytic water oxidation, and photocatalytic CO_2 reduction and aza-Henry reactions.[16] Many other ligands have also been synthesised containing halogens, sulphur containing groups and bulkier ligands,[30] however this list in Figure 5.2 provides a flavour for the versatility that can be achieved within the isoreticular family of zirconium based UiO-type MOFs.

Table 5.1 Change in porosity for isoreticular UiO-type MOFs

MOF	Organic Linker	Window Size (Å)	BET Surface Area (m^2/g)
UiO-66	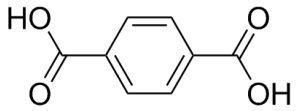	6	1187
UiO-67	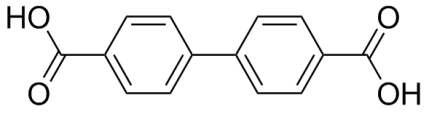	8	3000
UiO-68	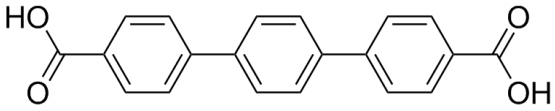	10	4170

5.1.1.2 Thermal and Chemical Stability

Both UiO-66 and UiO-67 were first reported to have very high thermal stabilities for MOFs, with decomposition temperatures around 540 °C, rivalled only by MIL-53 (an aluminium terephthalate) and some ZIFs.[26] The group 4 metals – titanium, zirconium and hafnium – are known to be oxophilic,[31-32] and

form very strong bonds with the carboxylate coordinating groups of the organic linkers. To corroborate this, TG-MS experiments were conducted on UiO-66 which showed a significant quantity of benzene within the waste stream, indicating that the C-C bonds in the linker between the aromatic rings and the carboxylate groups are the weakest, and so the first to break, compared with the strength of the coordinating bonds between the linker and the zirconium-based nodes.[26] It is hypothesised by the original authors that the strength of the inorganic building unit is the key to the structural integrity of the material.[26]

In addition to the superior thermal stability, one very fascinating property of UiO-66 is the noteworthy stability in the presence of water. Many MOFs are sensitive to hydrolysis, where reaction of a MOF with water generates free protonated ligands and hydroxylated metal complexes ($M(OH)_x$).[33] Insertion of water between the metal-oxygen bonds of the ligands can lead to ligand displacement and generation of metal-aqua complexes ($M(OH_2)_x$) and free ligand.[33] Even well-known and heavily utilised MOFs such as HKUST-1, a copper trimesate MOF, is subject to degradation in the presence of water and thus suitable for dry/low water concentration applications. Both of these degradation mechanisms are a result of water molecules interfering with the $M—O_{ligand}$ bonds of the framework. As already established, UiO-66 possesses strong ligand-metal bonding which in turn provides significant stability, even in the presence of water, with a resistance to hydrolysis. Water adsorption isotherms of UiO-66 and NH_2-UiO-66 show that at high levels of relative humidity, the frameworks can absorb high loadings of water in a fully reversible manner, with a small hysteresis observed due to rehydroxylation of the previously activated and dehydroxylated material.[34-35] The water stability of these frameworks are of significant importance when being considered for application in oxidation catalysis. Water is a common by-product of oxidation reactions, even when the simple oxidant, molecular O_2, is employed. In addition, simple, green peroxides such as H_2O_2 or TBHP (*tert*-butyl hydroperoxide) are often supplied as a fraction in an aqueous solution for stability. As such, water stability is a key property when considering supports for NPs to be used in oxidation processes.

On the contrary, the larger pore isoreticular structures of UiO-67 and UiO-68 were shown to have a much lower resistance to degradation in water, with

decomposition of the frameworks and complete loss of porosity after exposure to high humidity environments at 25 °C.[36] This implies that the lengthening of the organic linker has a detrimental effect on the strength of the coordination bonding with the metal oxide nodes. In addition, another study[37] showed that for the larger pore analogues capillary-force driven channel collapse was also a significant factor in the framework degradation.

A study on the stability of UiO-66 and related structures also tested for the resilience to acidic and basic environments.[36] UiO-66 and NH_2-UiO-66 were subjected to 24 hours soaking in 0.1M HCl or NaOH solutions at room temperature. Probed by PXRD, it was interesting to note that both frameworks were stable within the acidic environments, but complete loss of crystallinity was observed in the basic solution. Similar to the juxtaposition of framework stability in water, the larger pore frameworks were also more susceptible to degradation even in the mild acidic and basic environments.

To date, very little attention has been paid to the mechanical stability of UiO-type frameworks. The first report of the UiO-66 structure highlighted briefly that the framework was stable under significant pressures up to 10,000 kg/cm^2. A more thorough study by Zhou *et al.*[38] has further probed the mechanical properties of UiO-66, revealing that the minimal shear modulus (G_{min}) is an order of magnitude higher than for other MOFs of similar porosity such as MOF-5, HKUST-1 and ZIF-8, and encroaching on values expected for zeolites. The authors attribute this phenomenon to the comparatively high connectivity of the UiO-66 framework with other MOFs, which provides extra stability to shear forces in all directions. An additional study[39] on the incorporation of acidic modulators to the UiO-66 synthesis has shown that modulating can increase stability of the framework, by increasing the time required for complete collapse under ball-milling cycles. The effect is rationalised by the electron withdrawing effects of the acid modulators that increase the effective positive charge on the Zr^{4+} ions and thus resulting in stronger ionic bonding with the carboxylate ligands.

From a general stability standpoint, UiO-66 is clearly a leader in thermal, chemical and mechanical stability when compared with many reported MOF materials. As a result, UiO-66 is presented as a good potential host for NPs with a view to catalytic and multifunctional applications.

5.1.1.3 General Applications

Gas adsorption has been a key study and application for MOF based materials, and UiO-66 is of no exception, but with only moderate results. A study evaluating the dehydroxylated UiO-66 for gas-based applications[35] showed minimal adsorption of CO at RT, but at 77 K, adsorption of CO giving rise to an IR signal at 2155 cm^{-1} attributed to weak Brønsted acidity that could influence gas adsorption properties. Although moderate adsorption of CO_2 and CH_4 were established at pressures below atmospheric pressure, the absorption capacity at intermediate pressures between 1-10 bar superseded that of MIL-100, MIL-101 and MOF-177. It was found that functionalising the linker with pendant non-coordinated carboxylic acid groups could dramatically increase the CO_2 adsorption and selectivity over N_2.[40] In addition, the amino-functionalised UiO-66 has found promise in the adsorption of toxic gases such as NH_3 and CNCl, limited only by mass-transfer kinetics afforded by the lack of hierarchical structure to the porosity.[41] The moderate gas adsorption properties are likely due to the inert and stable nature of the parent framework, with likely applications mostly with functionalised frameworks in niche areas.

UiO-66 has also been applied toward molecular separations, where the intrinsic microporosity lends itself more closely to application in this area. A variety of studies have been undertaken on the separations of small, linear and cyclic hydrocarbons such as n-hexane and cyclohexane,[42] as well as substituted benzenes in normal-phase and reverse-phase HPLC with UiO-66 as the stationary phase.[43] UiO-66 was effective for complete separation of the notoriously difficult isomeric *ortho*-, *meta*- and *para*-xylene mixtures in mixed methanol/water mobile phases.

In addition to more typical chemical applications, the biocompatibility of UiO-66 has been evaluated. To investigate the drug encapsulation and release properties of a series of MOFs, loading of caffeine to UiO-66 was achieved with good topical release properties over a 24 hour period.[44] It was also demonstrated that encapsulation of fluorescein isothiocyanate within NH_2-UiO-66 generated an fluorescent pH sensor for detection of physiological and pathological processes within living cells.[45]

Applications in catalysis of the UiO-66 framework directly have been few, however recent literature has indicated the framework to be active toward

some photocatalytic processes.[46] None-the-less, most examples of the use of UiO-type materials in catalysis have relied on the functionalisation of the framework by pendant groups on the ligand or addition of active moieties through other means. So much so that one group of researchers have described the non-functionalised UiO-66 as inert.[47] Some examples of ligand functionalisation include addition of $-SO_3H$ groups[14] for enhanced acetalisation and benzimidazole formation,[48] use of $-NH_2$ groups for Knoevenagel condensation reactions,[49-50] esterification of levulinic acid,[51] acetalisation of benzaldehyde,[52] and addition of squaramide functionality for Friedel-Crafts reactions.[53] Bipyridyl ligands have also been used to incorporate Ir, Ru and Re for organic aza-Henry reactions and water oxidation,[16] Mo for epoxidation reactions[54] and Pd for cross-coupling reactions.[55] Catecholate type ligands were used to incorporate Fe and Cr centres for oxidation reactions.[56] As can be seen, a diverse range of functionality can be incorporated into the robust UiO-type family of MOFs.

5.1.2 NP/UiO-66 Materials and Current Uses

There exist a few examples whereby nanoparticles have been loaded on to UiO-66 for catalytic applications. The support of Pd on UiO-66 has been the most studied thus far, with one early study evaluating the propensity for the cages within UiO-66 to template the formation of Pd clusters.[57] By evaluating the thermodynamics of pore-filling, the authors concluded that although Pd clusters (and by extension, other metal clusters) could be formed within UiO-66, the concentration must be kept sufficiently low to prevent aggregation of particles in adjacent cages through the adequately sized pore-windows. This is in contrast to earlier work in Chapters 3-4 employing copper chlorophosphates as NP hosts that could achieve loadings in excess of 6 wt %. It was later confirmed that Pt nanoclusters could also be encapsulated within the amino-functionalised UiO-66 to afford a selective hydrogenation catalyst, reducing aldehydes to alcohols whilst preserving allylic groups.[58] A method for encapsulation of Au NPs was reported in an organic phase utilising oleylamine as a stabilising agent as well as a mild reducing agent at elevated temperatures.[59] Although this method was successful in generating an active CO oxidation catalyst, the method is difficult to apply to other metal chloride salts due to their insolubility in organic media.

A few reports have highlighted the structural encapsulation of NPs in UiO-66. One of the major issues with the synthesis of encapsulated NP@MOF materials is, firstly, confirming the positioning of NPs within the framework structure. The most common of NP characterisation techniques is TEM which only produces 2D images of the material. For more conclusive evidence of encapsulation, tomographic studies should be attempted, however this is not often reported in the literature. Some studies have also used BET gas adsorption analysis to note the reduction of surface areas, although blocking of pores can also be achieved through surface adhered nanoparticles that could produce similar results. Even if encapsulation of some NPs is achieved, it is thus far difficult to synthesise a material without the presence of some surface supported NPs. As a result, this brings in to question whether surface supported NPs, encapsulated NPs, or a mixture of the two are the major active sites in catalytic reactions.

The majority of NP/UiO-66 materials reported thus far have exploited the use of the MOF purely as a support or to template NPs by restricting the growth after nucleation of precursors. An Au@UiO-66 catalyst prepared by impregnation of $HAuCl_4$ and reduction by multiple methods was recently shown to be an active catalyst for the aerobic oxidation of benzyl alcohol.[60] The catalyst only achieved low TOFs, likely due to the formation of NP sizes in the region of 7-8 nm and congruent broad particle size distribution, with standard deviations as large as 4 nm and particles in excess of 15 nm observed. Other examples of hybrid UiO-66 based materials used in oxidation reactions include CdS decorated NH_2-UiO-66 for selective oxidation of *p*-substituted benzylic alcohols,[61] epoxidation of olefins by Mo(II) loaded PSM modified NH_2-UiO-66[17, 54] and photocatalytic oxidation of benzyl alcohol with mixed F- and NH_2-functionalised ligands in UiO-66.[62]

Given the potential catalytic properties of UiO-66 type frameworks as highlighted in *Section 5.1.1.3* , there is a vast opportunity for applying both supported NPs and the framework in multifunctional catalytic processes such as tandem/cascade reactions. Although there are a few reports of NP/MOFs for tandem reactions on other MOFs,[63-64] there are even fewer reports of NP/UiO-66 materials used in tandem reactions, but which as a proof-of-concept, confirm the potential scope for these materials in this field. As an example, a Pd@NH_2-UiO-66 material was used for sequential oxidation of benzyl alcohol to

benzaldehyde and acetalisation with ethylene glycol, although activities remained modest.[65] A blank NH_2-UiO-66 framework was used for a photo-induced oxidation and condensation reaction of benzyl alcohol,[66] although it is speculated that the photo-oxidation would only be applicable to low energy oxidation reactions.

5.1.3 Aims and Objectives

In this chapter, UiO-66 based nano-MOFs will be utilised as a host material for colloidal deposition of gold nanoparticles with a view to application in a tandem catalytic process. The gold nanoparticles will be used as active sites for activation of TBHP for selective oxidation of cinnamyl alcohol, with the addition of amine groups to the organic linkers in UiO-66 (NH_2-UiO-66) exploited as active sites to facilitate the Knoevenagel condensation of cinnamaldehyde with malononitrile.

5.2 Structural Properties of UiO-66 and Related NP Materials

Initially, two routes to the synthesis of NP/UiO-66 materials were explored; deposition and encapsulation. For NP deposition, synthesis of the framework material is performed in the first instance, whereas for encapsulation either the NPs can be pre-formed and the MOF grown around them, or NPs generated within the pores of a pre-formed MOF as further described in *Section 1.2.4.4*. Before the formation of the composite materials, the route to the framework synthesis was established. The original synthesis procedure for UiO-66[26] was reported to form a polycrystalline material with undefined morphology, and thus structural characterisation was performed from Rietveld refinement on powder diffraction data. A follow up procedure[68] detailed the use of monocarboxylic acids as modulators to produce single crystals of sizes up to the micron scale. To provide a consistent and reproducible surface area for nanoparticle deposition, as well as favourable mass transfer properties in catalytic reactions, a modulated synthesis was determined to be the most suitable from an application perspective. Benzoic acid was reported to be the best modulator for producing highly crystalline, homogeneous UiO-66 materials, and a ratio of 10:1 benzoic acid to $ZrCl_4$ was selected to produce single crystals with sizes in the region of 100-120 nm.

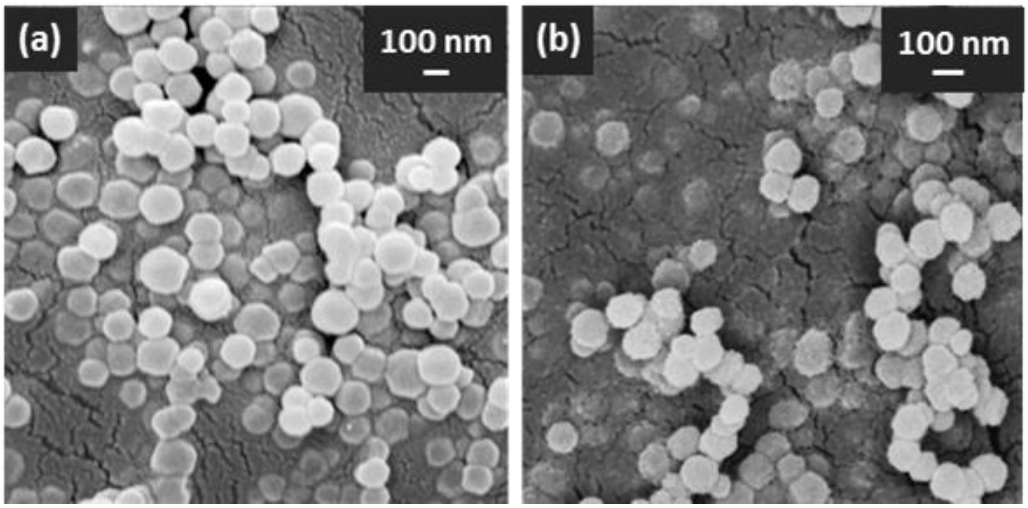

Figure 5.3 SEM micrographs of benzoic acid modulated (a) UiO-66 and (b) NH_2-UiO-66 nanocrystals

As can be seen from the SEM micrographs of both UiO-66 and NH_2-UiO-66 in Figure 5.3, the synthesis methods produced evenly distributed spherical nanocrystals of the respective materials, with a homogeneous size distribution. Both the blank and amino-functionalised frameworks could be prepared easily on the gram scale for sequential NP loading and eventual application as catalysts.

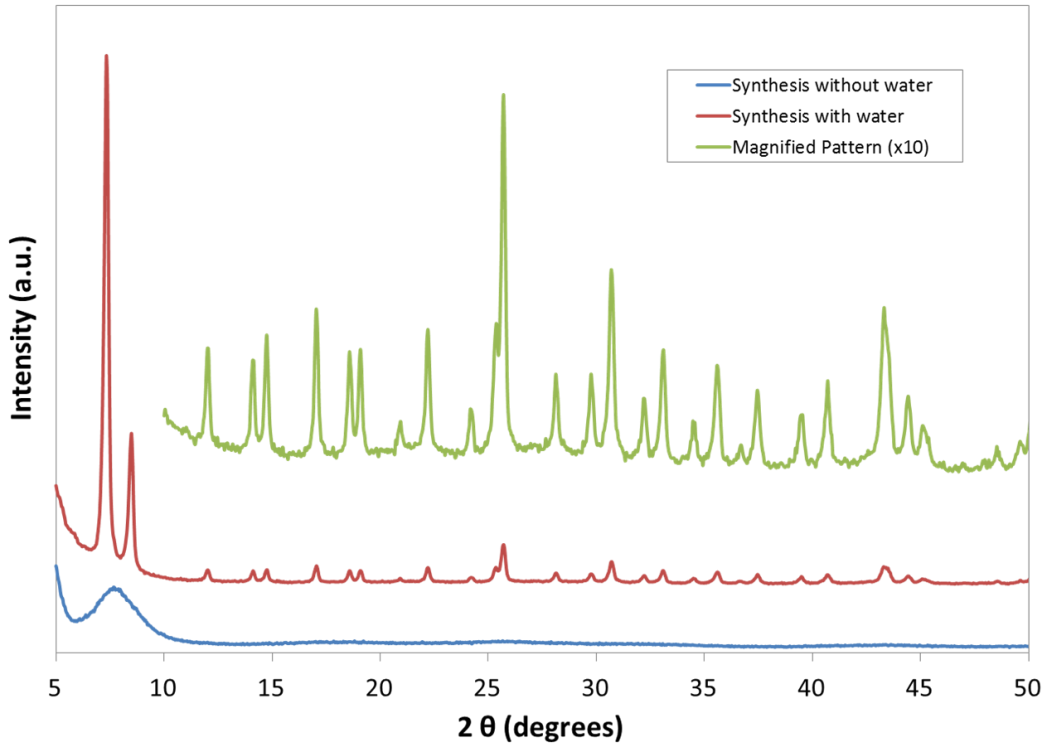

Figure 5.4 PXRD patterns of NH_2-UiO-66 synthesised without water (blue), with 6.7 equiv. of water to $ZrCl_4$ (red) and associated magnified region between 10-50 degrees (green). See Figure **5.7** for hkl assignment.

Interestingly, NH_2-UiO-66 required the addition of small amounts of water (less than 0.2 vol % in DMF or 6.7 equiv. to $ZrCl_4$) for the crystalline framework to form (See PXRD patterns in Figure 5.4). Some literature reports stipulate the addition of water[41, 68-69] whereas others do not.[20, 70-71] Given the low concentrations required, the presence of small amounts of water in solvents open to humidity from ambient conditions could be sufficient to drive the formation of the framework. In this study, in the absence of additional water, only an amorphous powder was produced. Although the addition of water has been identified as necessary by some groups, owing to the hydroxylated

nature of the Zr-based node, it is not fully understood why this is necessary for the synthesis of NH_2-UiO-66 but not for the parent UiO-66.

5.2.1 Deposition of Colloidal NPs

A variety of NP loading techniques have been outlined in *Section 1.2.4*, however for surface deposition of NPs, colloidal deposition by polymer-stabilisation provides both a narrow size distribution and simple procedure for preparation of NPs. A colloidal methanolic sol of Au NPs was prepared by creating a dilute solution of $HAuCl_4$ in methanol in the presence of PVP, the polymer stabilising agent, and subsequent chemical reduction by dropwise addition of $NaBH_4$.

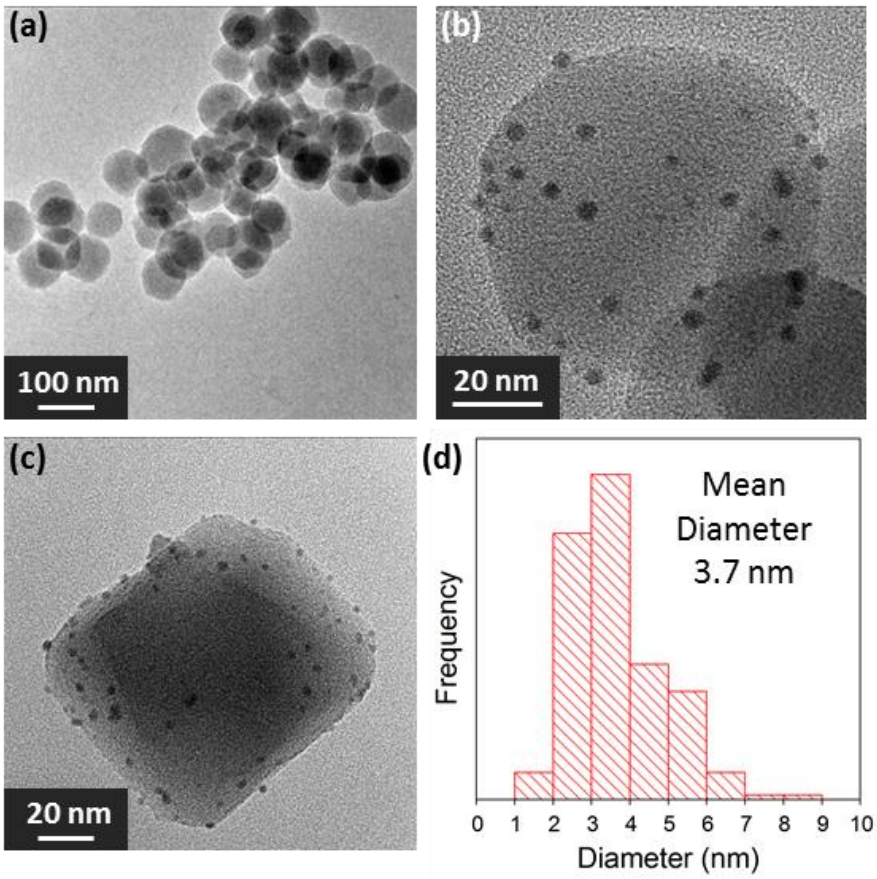

Figure 5.5 TEM micrographs of (a) UiO-66 nanocrystals, (b) Au/UiO-66, (c) Au/NH_2-UiO-66 and (d) NP size distribution of Au/NH_2-UiO-66 (Calculated from measurement of 200 particles)

Although similar principles have been demonstrated for other MOF supports,[72-73] this has not yet been demonstrated for UiO-66 materials. Figure 5.5 shows

TEM images collected on samples prepared by this method, with (a) showing bare UiO-66 nanocrystals, and (b) and (c) showing successful deposition of small, uniform NPs on UiO-66 and NH_2-UiO-66 respectively. Analysis of NP size distributions showed average mean diameters of 3.7 nm from a selection of 200 particles, with a reasonable size distribution and only a small fraction above 6 nm in size. In comparison with earlier methods reported in Chapters 3-4, this method has been successful in producing smaller nanoparticles of similar morphology to the extrusion activated NP/CuClP materials.

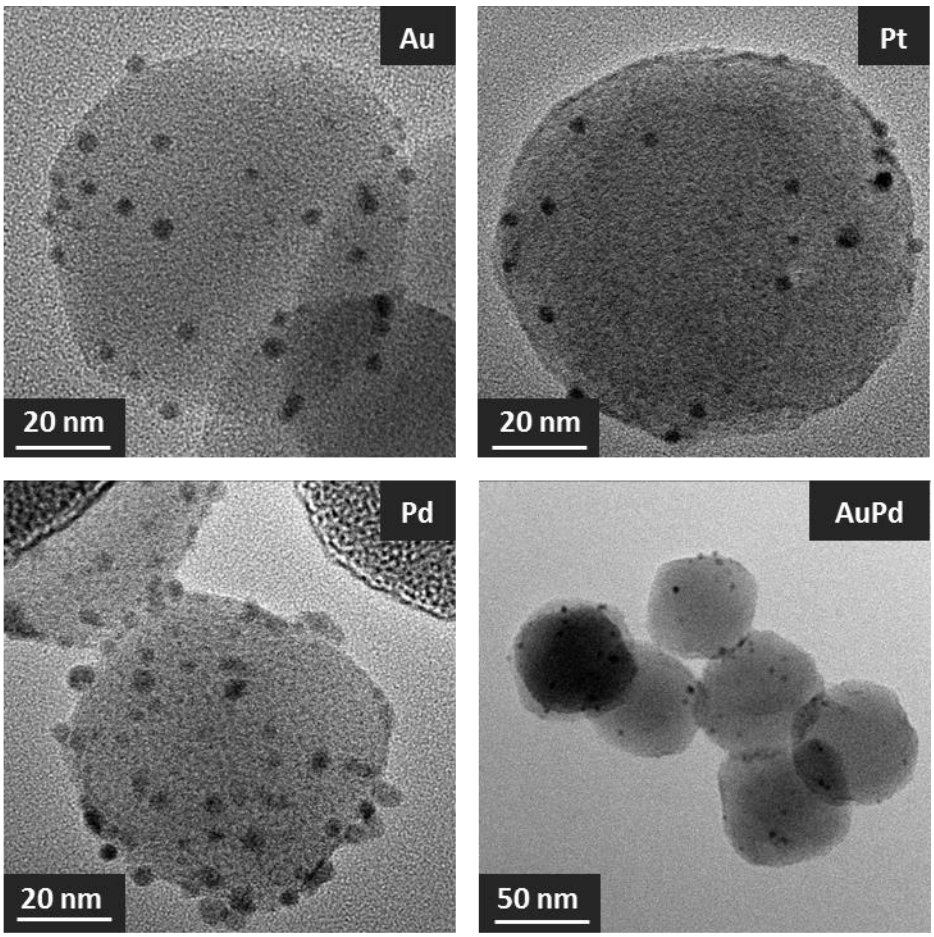

Figure 5.6 TEM Micrographs of Au/UiO-66, Pt/UiO-66, Pd/UiO-66 and AuPd/UiO-66 demonstrating the versatility of colloidal NP deposition method on UiO-66 nanocrystals.

To show the versatility and wide application of this facile deposition method, it was also successfully applied to the formation of Pt, Pd and bimetallic alloy AuPd nanoparticles as seen by the TEM micrographs in Figure 5.6. In all cases, NPs are homogeneously distributed across UiO-66 nanocrystals, with no observed aggregation providing isolated sites ideal for catalytic reactions.

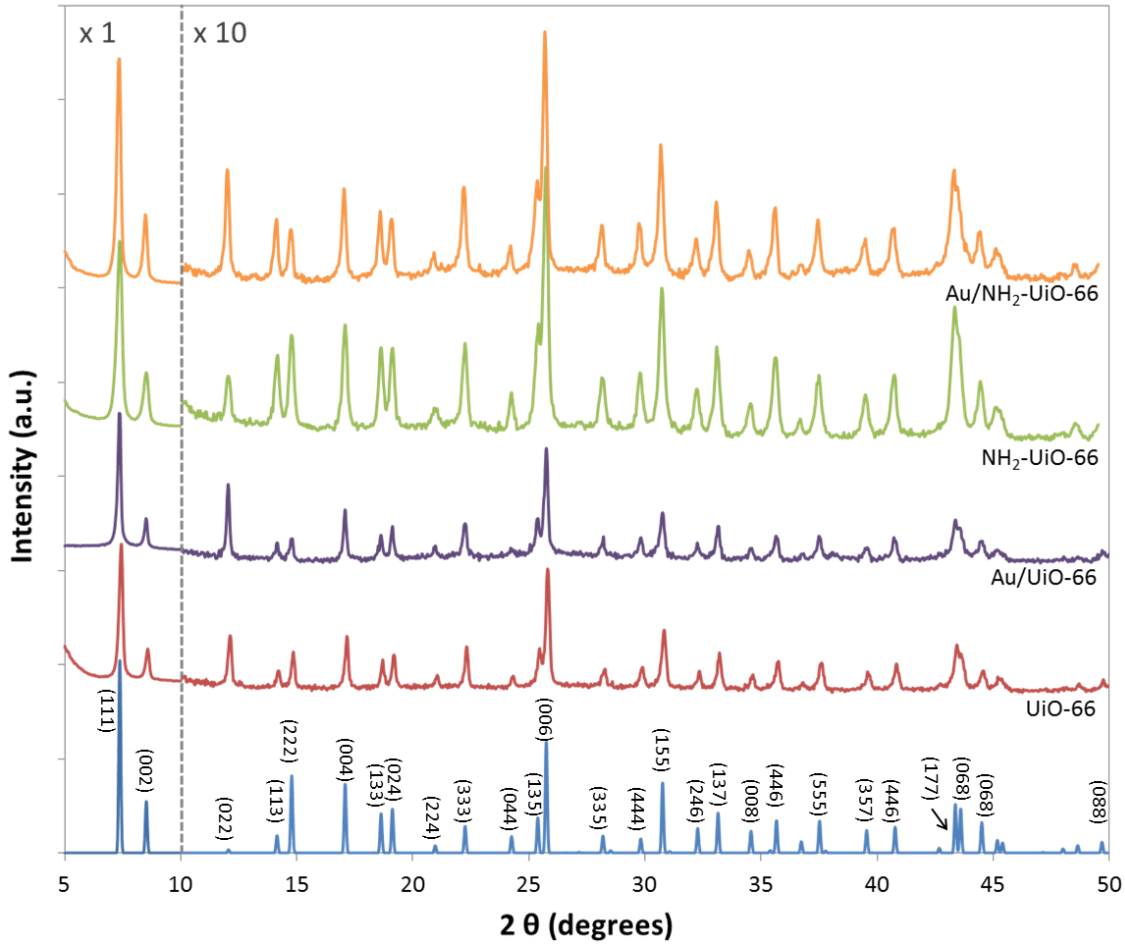

Figure 5.7 PXRD patterns of simulated UiO-66 (blue), UiO-66, NH_2-UiO-66 and Au deposited materials. (2θ region between 10-50 degrees magnified by 10x for clarity)

To probe the integrity of the deposited NP composite materials further, PXRD analysis was used to analyse the crystallinity of the preformed and deposited materials. As determined by patterns displayed in Figure 5.7, the framework is unaffected by deposition of NPs on either the blank or -NH_2 materials. Due to the high relative intensity of the 111 and 002 reflections, the 2θ region between 10-50 degrees is magnified by 10x for clarity and to highlight the similarity between the patterns of the different materials in this region.

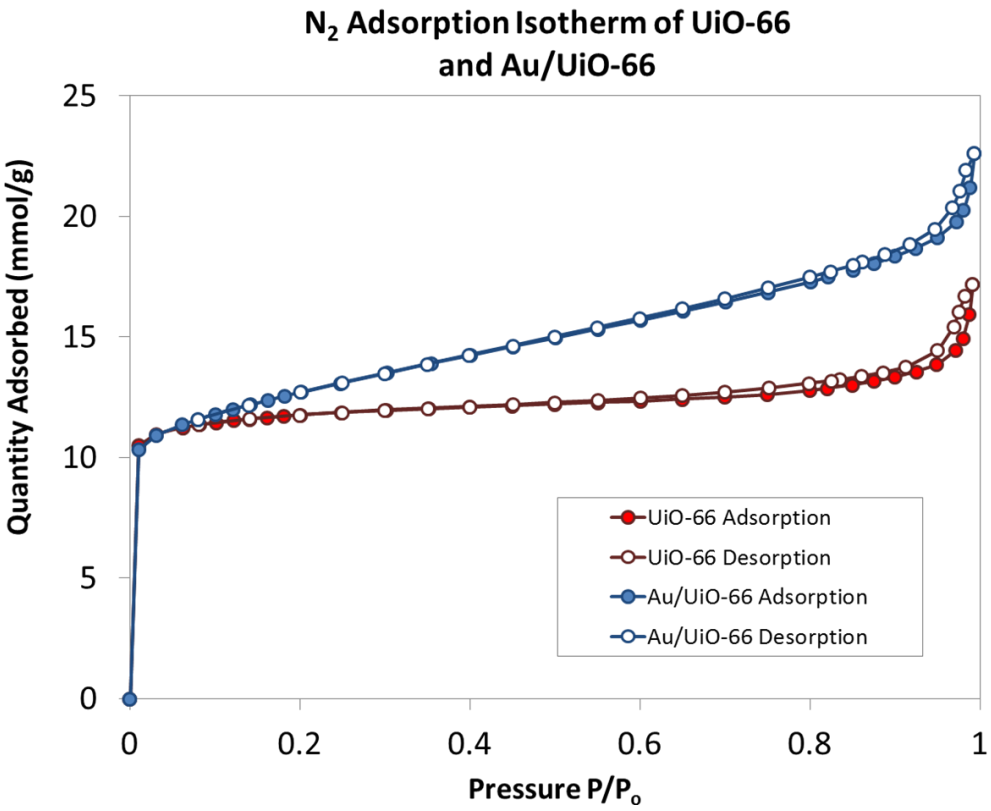

Figure 5.8 N_2 Adsorption isotherms of UiO-66 and Au/UiO-66 nanocrystals at 77 K

Nitrogen absorption isotherms were also collected to determine the porosity of the benzoic acid modulated framework materials and NP composites. The isotherm of the blank UiO-66 framework in Figure 5.8 depicts a Type II shape, and is in good agreement with those reported in the literature.[74] Only a minor hysteresis is observed in the desorption isotherm at p/p_o values close to 1, showing the complete reversibility of N_2 adsorption. These results indicate little effect of the NP deposition on the porosity of the MOF. Interestingly, the Au/UiO-66 material shows a much steeper increase in absorption capacity in the region of 0.2-0.7 p/p_0, normally associated with higher external surface areas[75] (as would be expected for the nanocrystalline particles). The almost plateau-like nature of the UiO-66 isotherm in this region could be a feature of compaction at some stage in the sample preparation, however the external surface area is clearly liberated again in the Au deposited sample.

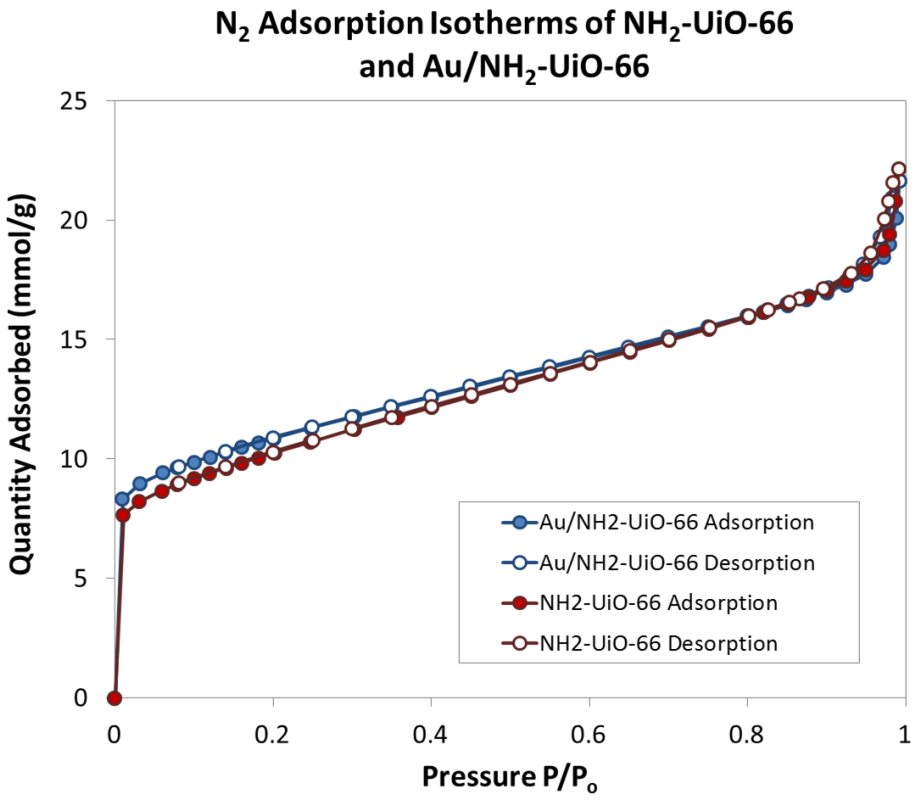

Figure 5.9 N_2 Adsorption isotherms of NH_2-UiO-66 and Au/NH_2-UiO-66 nanocrystals at 77 K

The N_2 adsorption isotherms for the NH_2-UiO-66 and Au/NH_2-UiO-66 materials also show reproducible Type II isotherms as for the UiO-66 frameworks. The steeper region in the p/p_0 range of 0.2-0.7 is also observed, clearly indicating the large external surface areas associated with the bulk nanocrystalline morphology of the material.

BET surface areas were calculated from the N_2 adsorption isotherms. As can be seen from the values in Table 5.2, both the UiO-66 and NH_2-UiO-66 materials modulated with 10 equivalents of benzoic acid have reasonable surface areas of 801 and 768 m^2/g. This is slightly larger than the value reported for materials modulated with 30 equivalents of benzoic acid at 600 m^2/g,[68] although lower than reported for the unmodulated synthesis of UiO-66 at 1187 m^2/g.[26] The drop in total surface area is likely due to the increased ratio of external to internal surface area from 8.6 % to 23.3 % (calculated from t-plot analysis) after modulation.

Table 5.2 BET Surface areas of UiO-type materials before and after Au NP deposition

Material	Micropore Volume (cm^3/g)	BET Surface Area (m^2/g)
	-	1160[a]
UiO-66	-	600[b]
	0.60	801
Au/UiO-66	0.78	914
NH_2-UiO-66	0.77	768
Au/NH_2-UiO-66	0.75	801

[a] Unmodulated synthesis of UiO-66. [b] Synthesised with 30 equiv. benzoic acid; SA calculated from Ar adsorption.[68]

What is more striking is the increase in surface area observed after NP deposition for both materials. The NP deposition involves stirring the material in methanol for up to 24 hours, and it is possible that this step is acting as an auxiliary washing step. The materials are synthesised in DMF and washed in methanol, but it is likely that some strongly bound DMF is not displaced in this step, and further not removed in degassing prior to BET analysis. The extended methanol wash could help to displace the final small fraction of DMF that is present, liberating the full accessible surface area after subsequent degassing at elevated temperatures. Another plausible explanation could be the removal of unreacted linker molecules as hypothesised in a recent study.[60]

TGA analysis was used to probe the thermal stability of the NP loaded materials. The thermal decomposition of UiO-66 follows initial solvent loss at low temperatures up to 100 °C (adsorbed solvent molecules and water from ambient conditions), a dehydroxylation transition around 200 °C with final collapse and decomposition of the framework. TGA experiments were carried out in air to allow for complete combustion of organic moieties to CO_2, leaving ZrO_2 as the final decomposition product. The thermal decomposition of UiO-66 and Au/UiO-66 at 493 °C and 479 °C respectively show high thermal stability for MOF materials, approaching the thermal stability of inorganic porous materials such as zeolites.[76]

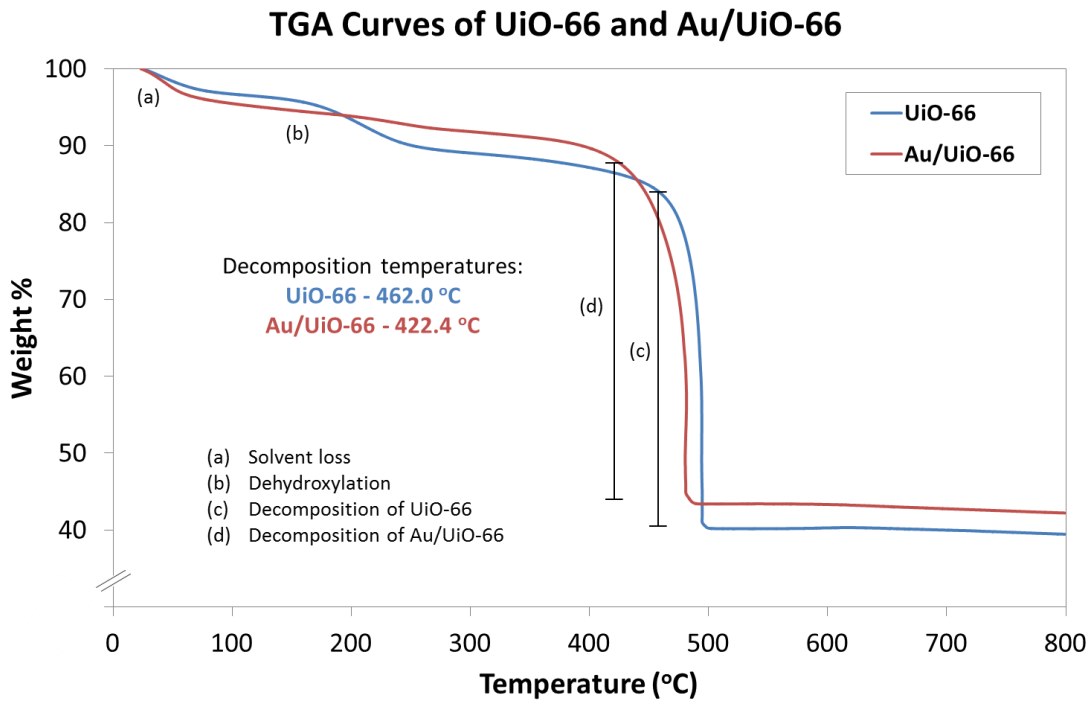

Figure 5.10 TGA Curves of UiO-66 and Au/UiO-66 in air (20 - 800 °C)

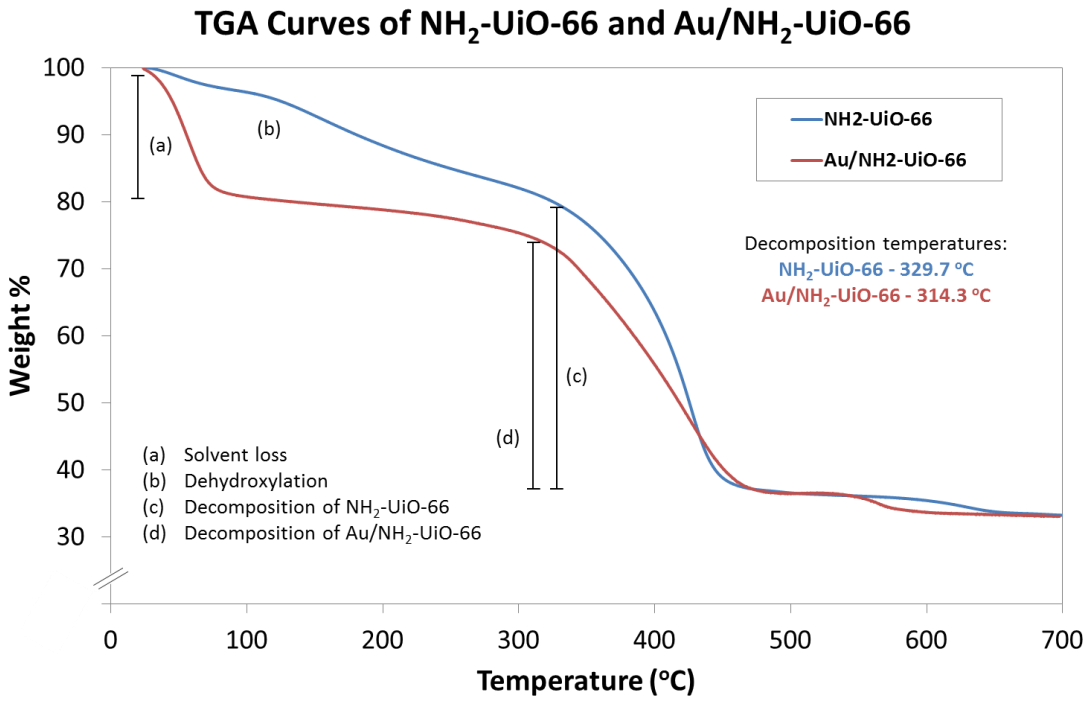

Figure 5.11 TGA Curves of NH_2-UiO-66 and Au/NH_2-UiO-66 in air (20 - 700 °C)

Juxtaposed with the UiO-66 TGA curves, it is possible to note that the NH_2-UiO-66 follows similar events of structural transition, leading to eventual decomposition. The amine MOF is slightly less stable, with decomposition

commencing around 320 °C and continuing gradually over a 100 °C increase, unlike the UiO-66 with sharp decomposition at higher temperatures. Nonetheless, thermal stability in excess of 300 °C is sufficient for most liquid-phase catalytic applications. It is possible to conclude that the deposition of colloidal Au NPs on both MOFs can be achieved with minimal effect on the thermal stability of the materials. The small drop in decomposition temperature (~15 °C) could be related to the removal of residual DMF molecules from the materials in the NP deposition as hypothesised by the noted increase in porosity from surface area analysis. The small transitions around 600 °C for all materials are representative of a phase change from tetragonal zirconia to monoclinic zirconia.[36]

Table 5.3 Weight loss of UiO-66 based materials as measured from TGA

Material	Weight Loss (%)
UiO-66 (Calculated)	53.7
UiO-66	52.0
Au/UiO-66	50.7
NH_2-UiO-66 (Calculated)	56.2
NH_2-UiO-66	53.3
Au/NH_2-UiO-66	51.0

The TGA data was further analysed and compared with calculated values of expected weight losses for full combustion of the organic moieties. From the formulas of each of the dehydroxylated UiO frameworks (UiO-66 – $Zr_6O_6(C_8H_4O_4)_6$; NH_2-UiO-66 ($Zr_6O_6(C_8H_5O_4N)_6$),[77] the mass contribution of the organics can be calculated at 53.7 wt % and 56.2 wt % for UiO-66 and NH_2-UiO-66 respectively. Table 5.3 shows the experimental data for the materials before and after Au NP deposition. The values are slightly lower than expected calculated values, however this is potentially due to the estimations of decomposition temperatures. As the decomposition is gradual, some error is involved in determining the point at which the framework material is intact. With this in mind, with the data treated identically, it is still possible to see a slightly higher weight loss by 1.3 % of the amino-functionalised MOF owing to

the presence of additional atoms to the linker. It is also possible to see lower weight losses for both Au loaded materials, accounting for the presence of the additional Au that will still be present on the decomposed product.

Accurate loadings of Au on UiO-66 and NH_2-UiO-66 were determined by ICP-OSE analysis performed by MEDAC Ltd. Although a target of 1 wt % was used in the deposition of NPs on the MOF materials, detailed analysis shows real loadings to be just short of this value, as can be seen in Table 5.4, with 0.64 wt % for Au/UiO-66 and 0.52 wt % for Au/NH_2-UiO-66. These values will be used to calculate TONs and TOFs where applicable in catalytic data.

Table 5.4 Au loadings as determined by ICP-OES analysis

Material	Au Loading (wt %)
Au/UiO-66	0.64
Au/NH_2-UiO-66	0.52

Given the analysis performed by TEM, BET, PXRD and TGA, it can be concluded that the colloidal NP deposition method has successfully yielded composite materials in Au/UiO-66 and Au/NH_2-UiO-66. The integrity and structural properties of both the nanoparticles and the MOF hosts are preserved and suitable for application in a catalytic oxidation and potential tandem processes.

5.2.2 Attempted Encapsulation of NPs

In addition to deposition of NPs, three methods were attempted for the encapsulation of NPs in UiO-66; a direct method whereby the MOF is grown in the presence of NPs, an oleylamine stabilised method[59] and wet impregnation.

Direct Method

In the direct encapsulation method, NPs were synthesised first by preparing a colloidal dispersion in methanol using PVP as a stabilising polymer. The methanol was then removed by evaporation and the NPs re-dispersed by sonication in the necessary volume of DMF required for the MOF synthesis with a predetermined loading. The benzoic acid modulated UiO-66 synthesis was then performed as normal using the NP/DMF sol. This method was tested for monometallic and bimetallic AuPd NP systems. After synthesis, TEM analysis

was used to characterise the nature of the NPs within the material, however very few small NPs were observed in the analysed samples.

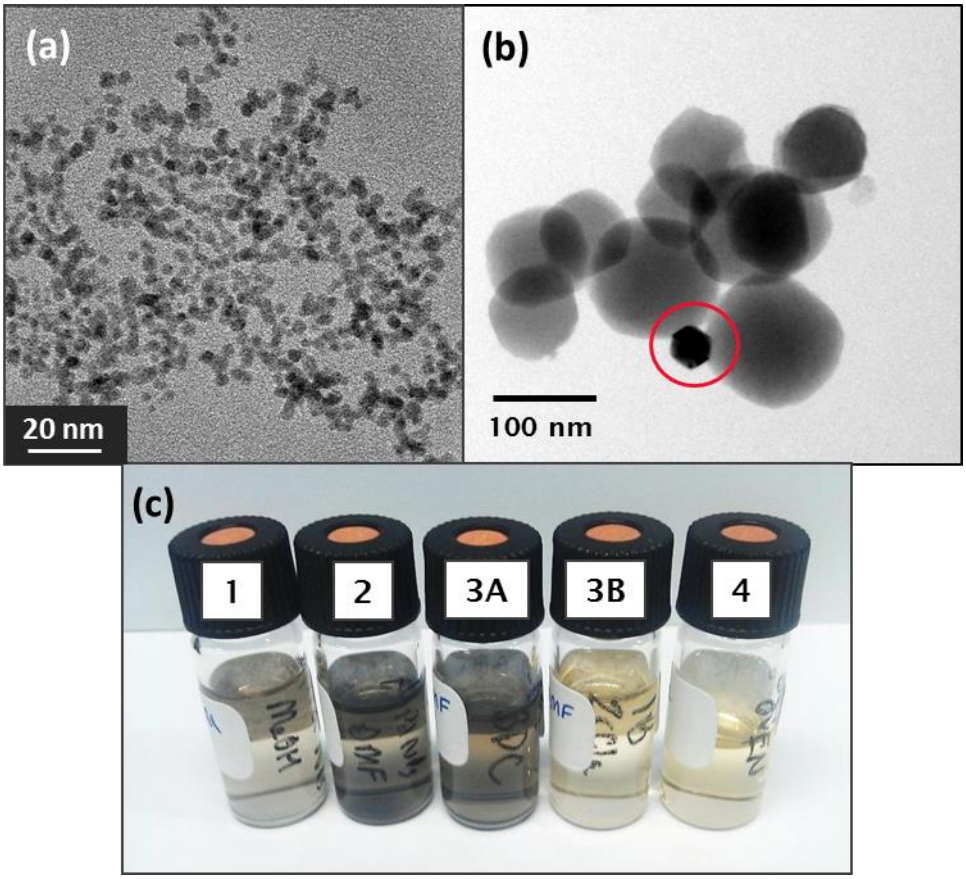

Figure 5.12 TEM micrographs of (a) AuPd NPs dispersed in DMF and (b) AuPd nanocrystals after UiO-66 synthesis. (c) Photograph of NP solutions: [1] NP synthesised in methanol, [2] redispersion in DMF, [3A] after addition of terephthalic acid, [3B] separate addition of $ZrCl_4$ and [4] combined 3A and 3B prior to synthesis.

The only observed metallic species were larger nanocrystals of 40-50 nm diameter with hexagonal morphology when viewed in 2D (likely a 2D projection of a dodecahedron), as highlighted in Figure 5.12 (b) for a bimetallic AuPd example. This was highly unexpected, so further investigation was needed. The synthesis procedure was repeated with samples of the NP sols removed for TEM analysis at each stage. The methanolic NP sol and dispersion in DMF showed discrete, uniform NPs (Figure 5.12 (a)) of sizes 3-5 nm as would be expected from the colloidal synthesis method. To the NP/DMF sols were added the MOF precursors separately, $ZrCl_4$ and terephthalic acid. It was quickly established that in the presence of $ZrCl_4$, the NPs were completely destroyed

and dissolved back into solution. This was further exemplified by the noticeable change in colour of the solutions as seen in Figure 5.12 (c). The NP solution in DMF (2) is a dark grey colour which is unchanged upon addition of terephthalic acid (3A). The dark grey colour is lost upon addition of $ZrCl_4$ to a very light brown (3B) – similar to that observed for solutions K_2PdCl_4 used to prepare the NPs in the first instance. It is known that high levels of chloride can be corrosive to metals[78] which in turn has led to the dissolution of the NPs. When combined with the NP/DMF/terephthalic acid mixture, the light brown colour is maintained (4). As the MOF precursor solution clearly had no NPs left and the noble metals now in solution, this has led to the formation of the larger nanocrystals observed in the TEM of the final products after MOF formation.

Direct encapsulation methods, therefore, cannot be applicable to UiO-66 synthesis methods were $ZrCl_4$ is used as a precursor. One study[79] reports the formation of the oxo-zirconium clusters with monodentate methacrylate and subsequent ligand exchange with terephthalic acid to form the UiO-66 framework, however it would be difficult to modulate the synthesis in this method and it is not clear whether the ligand exchange would favour nucleation around the NPs with the zirconium SBUs already formed. The integrity of the UiO-66 is also compromised with reduced crystallinity and porosity. Another report[80] has tried to improve on this by removing the chlorine from the synthesis by using a Zr(^{n}OPr) starting material. Although they achieve good crystallinity, porosity and thermal stability, significant control over the MOF crystal size and morphology is lost. When encapsulation of Au NPs was attempted, NPs were aggregated with sizes changing from a modal average of 3 nm to 15 nm with some particles as large as 28 nm. As of yet, encapsulation of NPs by direct methods has not been achieved with good precision and maintenance of both NP and MOF integrity. This proves a continued challenge due to the incompatibility of the common $ZrCl_4$ precursor with pre-synthesised NPs.

Oleylamine Method

A recent report[59] discussed the merits of using an organic medium and oleylamine as a stabilising ligand and mild reducing agent for encapsulation of NPs in UiO-66. The authors synthesised UiO-66 by an unmodulated method to form a polycrystalline product. The UiO-66 was subsequently immersed in

oleylamine and heated to 60 °C under a flow of nitrogen. A separate solution of $HAuCl_4$ in 1:4 solution of oleylamine in 1-octadecene was prepared and rapidly injected to the UiO-66 suspension with heating at 90 °C to reduce the gold salt and generate the Au/UiO-66 material.

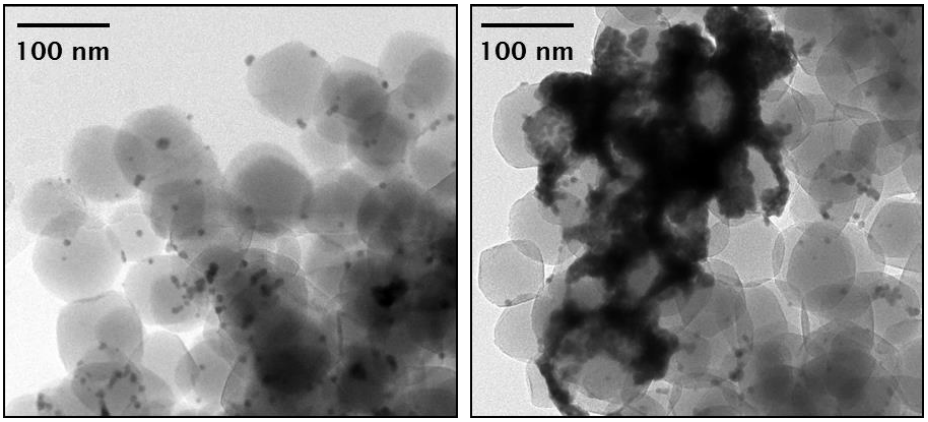

Figure 5.13 TEM micrographs of NPs and aggregates formed by oleylamine synthesis of Au/UiO-66

This method was applied using the benzoic acid modulated UiO-66, however, even after several attempts, high degrees of NP aggregation was observed as seen in Figure 5.13. Only small fractions of the Au NPs formed were well dispersed on the UiO-66 nanocrystals. Despite being able to achieve high loadings of Au, this method proved irreproducible. In addition, this method was used to attempt the synthesis of Pt@UiO-66 and Pd@UiO-66, however due to the insolubility of the chloride precursors (K_2PtCl_4 and K_2PdCl_4 respectively) in the oleylamine/1-octadecene mixture, this method could not be applied. This method was not used further due to the difficulties reproducing the results, however it might be theoretically possible to adopt organometallic Pt and Pd precursors to encourage solubility.

Impregnation Method

A more classical method of wet impregnation was also investigated as a potential route for NP encapsulation in UiO-66 nanocrystals. As is well documented,[81] and discussed in more detail in *Section 1.2.4.1,* NPs can be formed in the internal pores of a framework by impregnating porous materials with an aqueous solution of metal salts, dried and reduced at temperature in the presence of H_2. This method was applied to the nano-UiO-66 materials with mixed results.

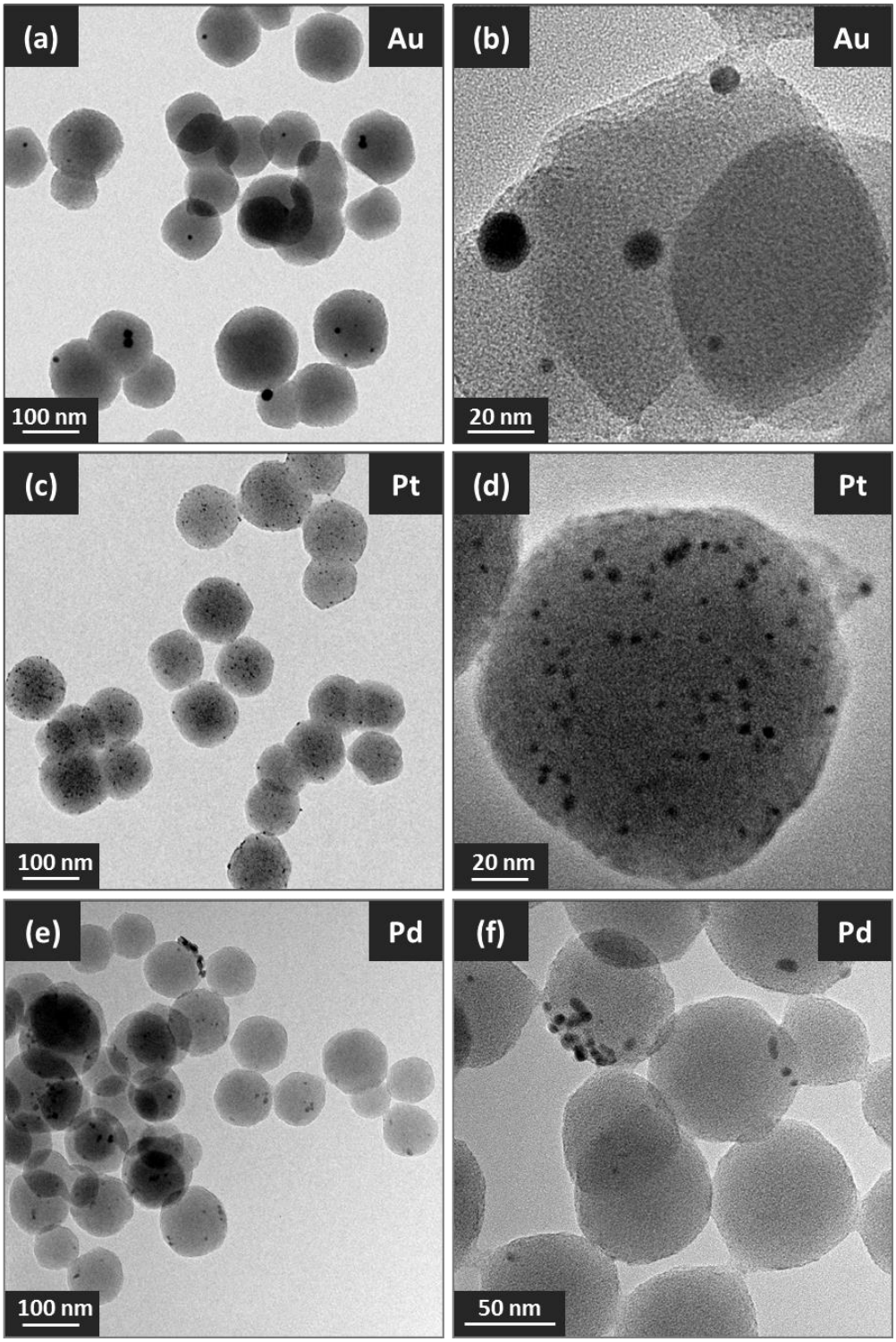

Figure 5.14 TEM of Au, Pt and Pd NPs impregnated to UiO-66 nanocrystals

As can be seen in Figure 5.14 (a-b), impregnation and reduction of $HAuCl_4$ yielded a broad size distribution of NPs with some in excess of 20 nm. As established earlier, the target is to achieve NPs less than 10 nm and ideally less than 5 nm is size. Due to the presence of a significant quantity of large

particles, the distribution is sparse. On the other hand, the impregnation and reduction of K_2PtCl_4 on UiO-66 nanocrystals was significantly more successful, as can be seen from TEM images in Figure 5.14 (c-d), in achieving smaller nanoparticles of platinum with average diameters between 3-4 nm. The NPs are well dispersed with no aggregation observed. Difficulty focusing on some of the NPs could indicate encapsulation of some Pt NPs, although tomographic imaging would need to be carried out to identify the exact location of the NPs. What is clear, however, is at least a small fraction of NPs present on the surface of the nanocrystals. Even if there is some encapsulation of nanoparticles within the pores of the framework, the impregnation method is unselective toward the location of nanoparticles. If eventually applied in a catalytic process, it would be difficult to determine whether encapsulated NPs, surface NPs or a mixture of both were active sites for the studied reactions. The method would need to be adapted or improved further to attain selective encapsulation of NPs. Similar to the Au NPs, synthesis of Pd NPs under these impregnation conditions yielded larger particles with some variable sizes and shapes (Figure 5.14 (e-f)). Some tubular morphology to particles was observed although it is not clear if particles are synthesised in this morphology or whether it is a result of aggregation and sintering. As such, it can be concluded that this method is only suitable for the formation of uniform, well distributed and site-isolated Pt NPs.

Three methods were investigated for the encapsulation of monometallic or bimetallic noble metal nanoparticles within UiO-66 nanocrystals. The direct method suffered from destruction of NPs prior to MOF synthesis, the oleylamine method from difficulties reproducing results and NP aggregation, and wet impregnation from large NP formation or unselective positioning of NPs with some observed on the surface. For the ease of reproducibility as well as the monodisperse nature of NPs and minimal effects on the integrity of the UiO-66 nanocrystal hosts, the deposited method for preparing NP/NH_2-UiO-66 composite materials will be tested for its activity in oxidation and tandem reactions.

5.3 Tandem Oxidation-Condensation Catalysis

It has already been shown in this work as well as others, that noble metal nanoparticles have a propensity for the activation of environmentally benign oxidants for selective oxidation catalysis. The choice of support can have a significant effect on the integrity of the catalyst, as well the activity and selectivity properties. Chapters 3 and 4 focused on the use of a porous copper chlorophosphate as a novel NP support, exploiting the anion exchange properties to generate NPs *in situ* without a capping agent. In this instance, the support was providing a convenient way to form an active NP catalyst with strong adhesion of NPs to the surface of the framework crystals. MOFs are interesting supports for their porosity to potentially encapsulate and stabilise NP formation, but more importantly from a catalytic perspective, for the ability to functionalise the frameworks for additional active properties. As such, the NP/UiO-66 can be functionalised with amine groups as basic sites to catalyse a reaction in addition to the oxidation reaction that can occur on the metal NP.

A selective oxidation reaction can generate aldehyde molecules with little over-oxidation to acids or esters, which in turn are active reactants for a variety of C-C bond forming condensation reactions. Some examples include aldol condensations, Knoevenagel condensations, Claisen condensations, Henry reactions and Friedländer condensations;[82-83] some of which are often catalysed by bases. A few recent articles[49-50, 84-85] have highlighted the use of amine-MOFs as catalysts for coupling via Knoevenagel condensation of aldehydes with activated methylene compounds such as malononitrile.

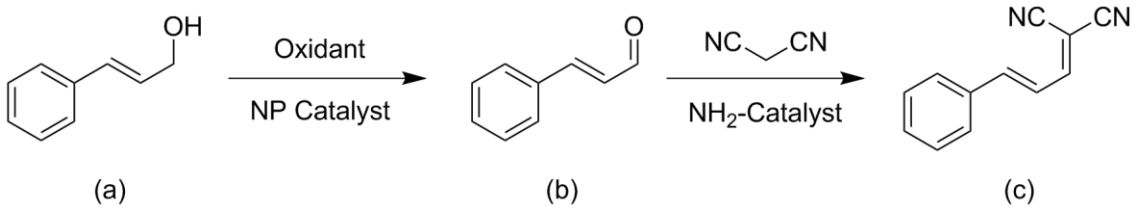

Scheme 5.1 Example of a 2-step oxidation and Knoevenagel condensation. (a) cinnamyl alcohol, (b) cinnamaldehyde and (c) cinnamylidene malononitrile

An example reaction of an oxidation followed by a Knoevenagel condensation can be seen in Scheme 5.5. This reaction involves the selective catalytic

oxidation of cinnamyl alcohol to cinnamaldehyde using a noble metal NP catalyst and a suitable oxidant. The second step is a Knoevenagel condensation of the aldehyde with malononitrile, catalysed by the basic amine groups on NH_2-UiO-66. By using a composite material of Au/NH_2-UiO-66, it should be possible to achieve this two-step reaction in tandem using the two active sites on the same catalyst in one pot. The aldehyde product is in itself produced as a flavouring agent with the sweet and spicy aroma of cinnamon,[86] but the final cinnamylidene malononitrile product has been shown to have anti-cancer properties and used in pharmaceutical formulations.[87] The challenge in this process is to selectively oxidise the alcohol without forming over-oxidation products, whilst also preserving the allylic group between the alcohol and aromatic ring. The aldehyde would need to be formed in high enough yield to allow for the second coupling step to occur.

5.3.1 Oxidation of Cinnamyl Alcohol with TBHP

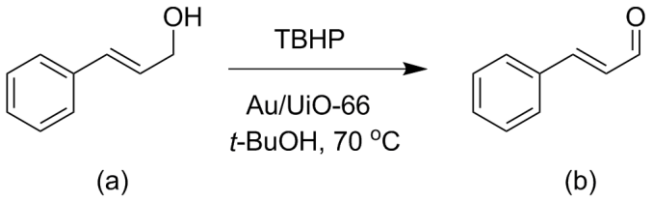

Scheme 5.2 TBHP oxidation of cinnamyl alcohol using Au/UiO-66. (a) cinnamyl alcohol and (b) cinnamaldehyde

To effect the tandem reactions, each step was initially conducted separately to gain a better understanding of the conditions required for each step. For the oxidation reaction, the single active site catalyst of deposited Au/UiO-66 was used to probe the activity of the Au NPs on the MOF support. The oxidant/solvent combination used for the reaction is *tert*-butyl hydroperoxide (TBHP) in *tert*-butanol. TBHP is a simple peroxide and can fully dissolve in *t*-butanol so not to limit the reaction with solubility problems. The consumption of TBHP during an oxidation process liberates *t*-butanol as a side product which is also the solvent for the reaction. From an economic standpoint, the *t*-butanol can be recycled as a solvent and so minimal waste is actually produced with the oxidant by-product being recycled into the system in a sustainable manner. It has already been demonstrated that *t*-butanol is a compatible

solvent for oxidation reactions earlier in this work, and is miscible with water (a by-product of the reaction and present in the TBHP reactant which comes as 70 % in H_2O) and so should prevent phase separation which could complicate the mechanism and kinetics of the reaction. Scheme 5.2 summarises the basic conditions used for this process.

As with mechanistic discussions associated with the oxidation of benzylic alcohols in *Section 4.1.3*, dissociation of the O-H bond in cinnamyl alcohol should form adsorbed alcoholate species on the surface of the gold nanoparticle. Contributions of π-interactions from the conjugated system in cinnamyl alcohol with the metal surface should aid in stabilising the surface adsorbed species, before abstraction of the β-hydrogen to liberate cinnamaldehyde. Simultaneous formation of activated surface *t*-butyl peroxide species will help to oxidise surface hydrides to generate water, *t*-butanol and free surface sites for further catalytic cycles. The difference in this system compared with the NP/CuClP catalysts is the presence of the stabilising PVP ligand. This in turn could block adsorption sites and reduce the catalytic potential of the catalyst.

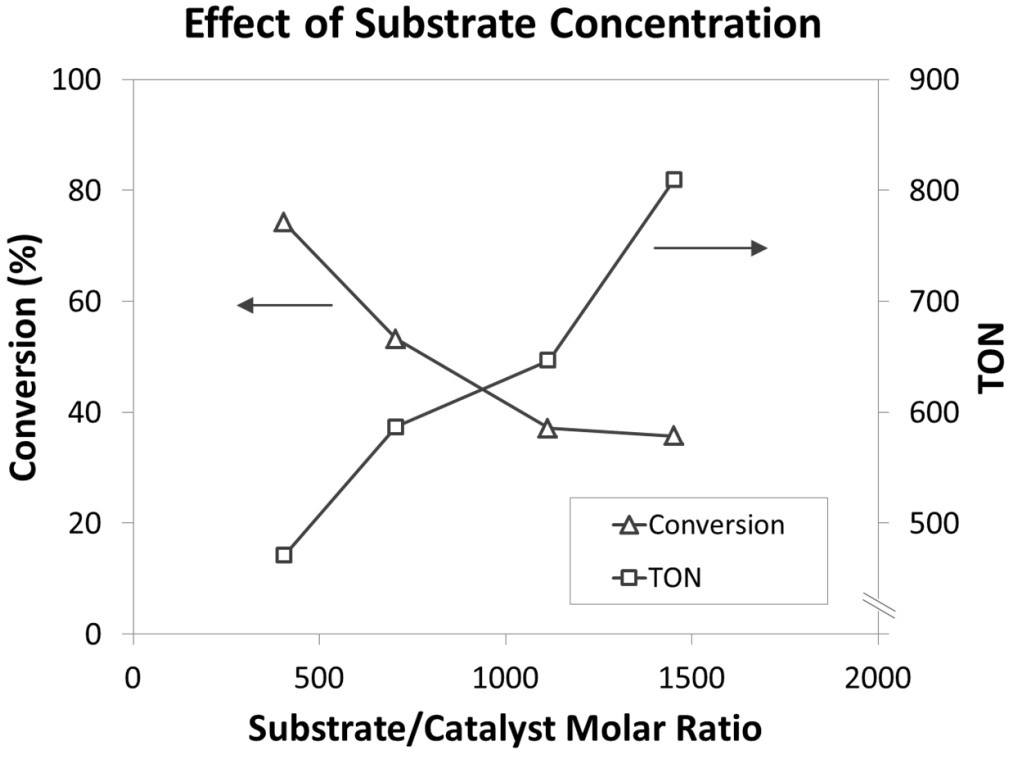

Figure 5.15 Effect of substrate concentration on the TBHP oxidation of cinnamyl alcohol. (Reaction conditions: Catalyst (10 mg;

0.64 wt % metal), chlorobenzene as internal standard (80 mg), TBHP (70 wt % in H_2O; 0.245 mL), t-butanol (7 mL), stirred for 5 hours at 70 °C)

To gain a better understanding of the oxidation process and the activity of the catalyst for the TBHP oxidation of cinnamyl alcohol, a series of reactions were run at 70 °C with different concentrations of cinnamyl alcohol. The catalytic properties are plotted in Figure 5.15 against the substrate/catalyst ratio.

It is clear to see that the substrate concentration has a significant effect on the progression of the reaction. Although the overall conversion percent of the reaction drops with high concentrations of the substrate, this equates to higher mole conversions as highlighted in the dramatic increase in the TON for the reaction over 5 hours. Although the catalyst can clearly reach a higher output, for the tandem reaction, it is important to bring the reaction as close to 100 % conversion as possible to reduce the possibility of additional by-products forming in the second step of the reaction. A compromise must be made between yields and selectivity over the two-step process. The data is further represented in Table 5.5 to show that over 5 hours of reaction, all reactions maintained maximum selectivity. It was noted that if reactions were left for longer times ~24 hours, a small presence of benzaldehyde was noted, likely due to decomposition of the cinnamyl alcohol or aldehyde product.

Table 5.5 Catalytic data showing effect of substrate concentration on the TBHP oxidation of cinnamyl alcohol (See Figure 5.15 for conditions)

No.	Sub/Cat Mol Ratio	Conversion (%)	Selectivity (%)	TON	TOF (h^{-1})
1	406.15	74.22	> 99	471	94
2	705.79	53.2	> 99	587	117
3	1115.78	37.1	> 99	647	129
4	1452.75	35.69	> 99	810	162

The effect of oxidant concentration was also tested at high substrate/catalyst ratios to investigate the effect on activity measured by TONs. As can be seen

from Figure 5.16, the increased concentrations of TBHP in the reaction led to higher conversions of cinnamyl alcohol. TONs in excess of 800 over 5 hours could be achieved with 3 equivalents of TBHP, although given the high concentration of cinnamyl alcohol, this equated to only 35 % conversion. The increase in conversion was also not linear with respect to TBHP concentration, with a decrease in benefit with higher concentrations of the oxidant. This can be further exemplified by analysing the oxidant efficiency of these reactions as plotted in Figure 5.17. Despite the higher TONs observed, the oxidant efficiency drops from 30 % at 0.5 equivalents to just over 10 % at 3 equivalents. This is particularly wasteful, with the maximum oxidant efficiency being only 33 % if the reaction were to reach 100 % conversion. This highlights that, as with the concentration of the substrate with respect to the catalyst, a compromise needs to be made to achieve high levels of substrate conversion at slightly reduced activity of the catalyst material.

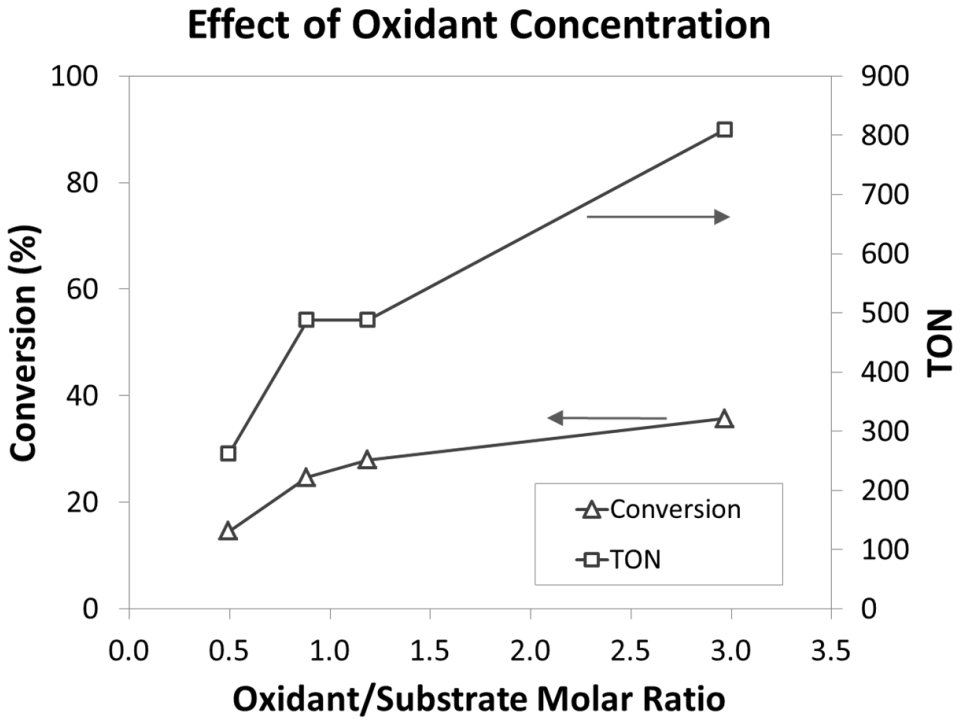

Figure 5.16 Effect of oxidant concentration on the TBHP oxidation of cinnamyl alcohol. (Reaction Conditions: Catalyst (10 mg; 0.64 wt % metal), cinnamyl alcohol (80 mg), chlorobenzene as internal standard (80 mg), TBHP (70 wt % in H_2O), *t*-butanol (7 mL), stirred for 5 hours at 70 °C)

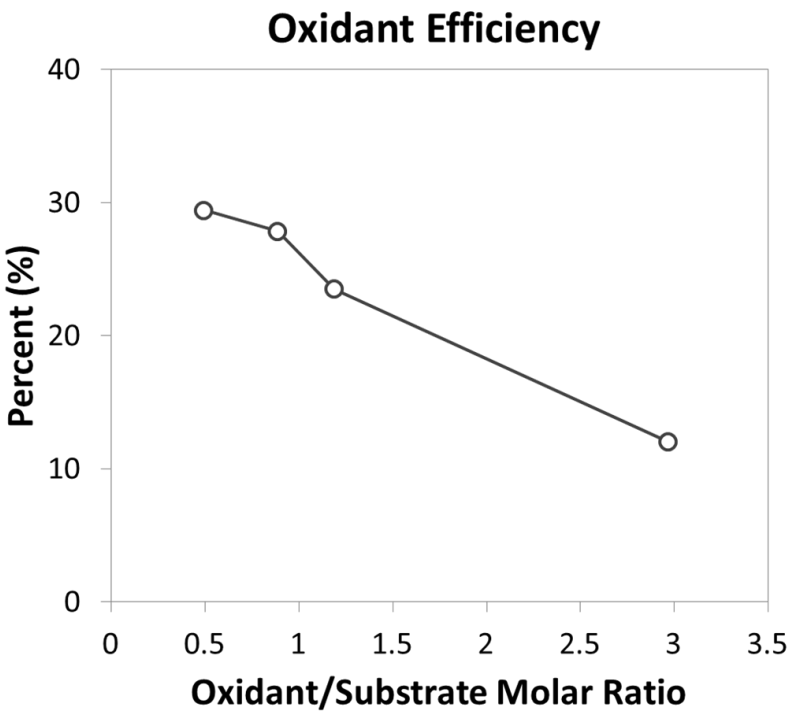

Figure 5.17 Oxidant efficiency (See Figure 5.16 for conditions)

Given the information obtained through the substrate and oxidant concentration effects, it is possible to begin making some proposals on the kinetic processes involved in the Au NP catalysed reactions. As the TONs increase with substrate concentration, it can be assumed that the surface of the Au NPs are not saturated with substrate molecules and thus that the reaction rate is not limited by the surface reaction, but rather by diffusion or adsorption of molecules to the NP surface. This is not surprising given that the reaction occurs in significant quantity of solvent. A solvent free reaction could reduce this limitation, however the substrate has a melting point of 33 °C and high viscosity that could pose a challenge for preparation of the reaction.

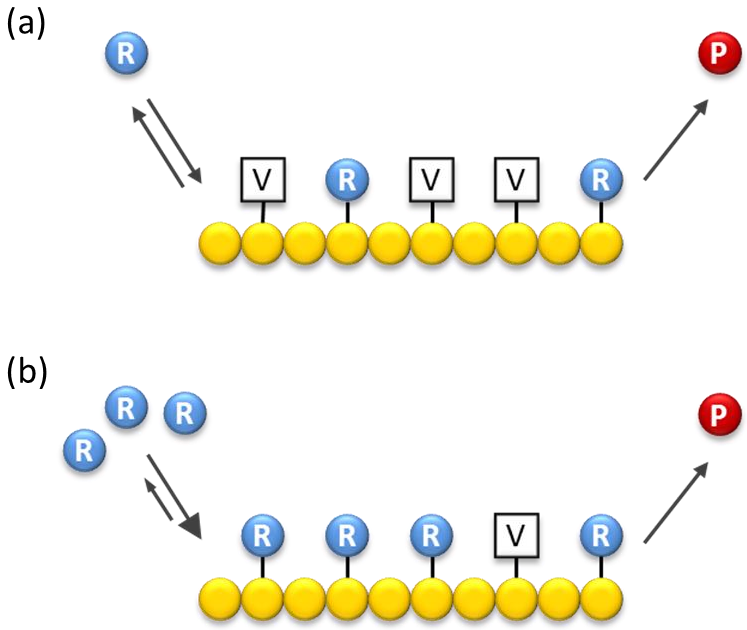

Figure 5.18 Effect of substrate concentrations on surface adsorption in diffusion limited processes

Figure 5.18 shows a representation of how diffusion or adsorption limited processes can shift the equilibrium in favour of surface bound species when the concentration of a reactant (R) is increased. In reality, this is a simplified representation of a unimolecular gas-phase reaction. This system is a bimolecular reaction with two reactants (cinnamyl alcohol and TBHP) in solution, adding an additional level of complexity, but similar principles can be applied. Two major mechanisms for bimolecular reactions on surfaces are Langmuir-Hinshelwood or Eley-Rideal as described in more detail in *Section 1.1.1.4*. It is likely that this reaction is more closely aligned with the former mechanism, given the evidence shown for the adsorption of alcohol species to the surface of Au NPs[88-90] and for formation of activated superoxide species on the Au NP surface from the oxidant.[91] There are only a few examples for Pd NPs whereby oxidations can occur by the close proximity of O_2 (as opposed to surface bound molecular oxygen) that would follow an Eley-Rideal type mechanism more closely.[88, 92] Further investigations would be required to confirm the exact mechanism of this particular system. What is clear from this catalytic data is that the selectivity toward cinnamaldehyde by the deposited Au/UiO-66 catalyst is very high, showing the ability of the catalyst to target the alcohol group, and resist oxidation of the allylic group

between the alcohol and benzene ring at high levels of conversion under these conditions.

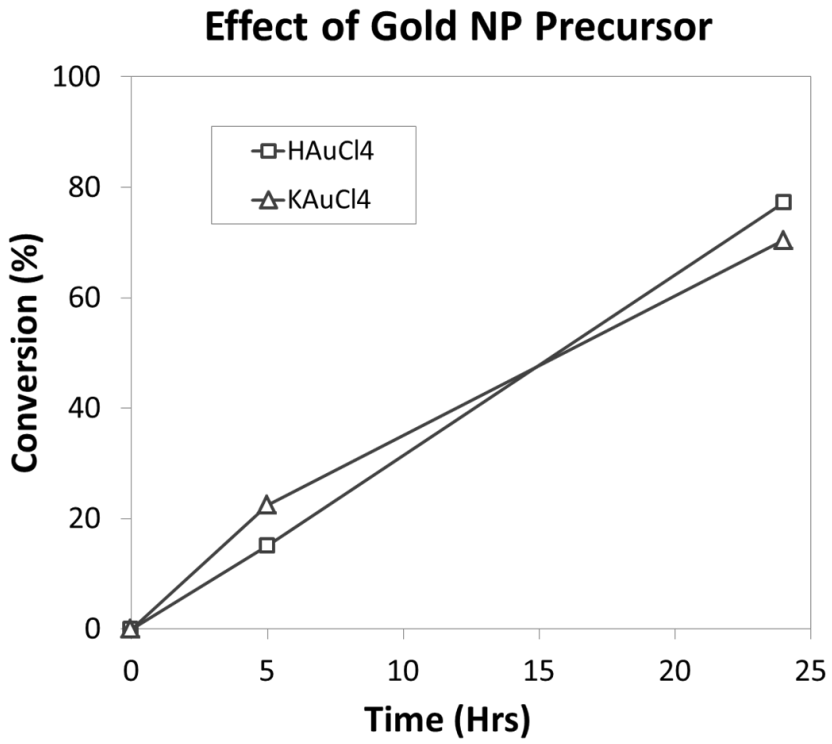

Figure 5.19 Comparison of catalytic properties of Au/UiO-66 prepared with different $HAuCl_4$ or $KAuCl_4$ precursors. (Conditions: Catalyst (10 mg; 0.64 wt % metal), cinnamyl alcohol (80 mg) chlorobenzene as internal standard (80 mg), TBHP (0.1 mL; 70 wt % in H_2O), *t*-butanol (7 mL), stirred at 70 °C)

In addition, an Au/UiO-66 material was prepared using $KAuCl_4$ as a precursor salt to NP formation and deposition on UiO-66 nanocrystals. TEM revealed little difference in the morphology, size and distribution of Au NPs across the sample. The pH of the methanolic Au solutions were analysed, both of which were quite acidic at pH values of 1 and 2 respectively, although this seemed to have little effect on NP preparation. To confirm, the materials were used for the aerobic oxidation of cinnamyl alcohol as before and the results plotted in Figure 5.19 . As can be seen, there was little effect on the resulting activity, with both catalysts achieving 75-77 % conversion over the course of 24 hours.

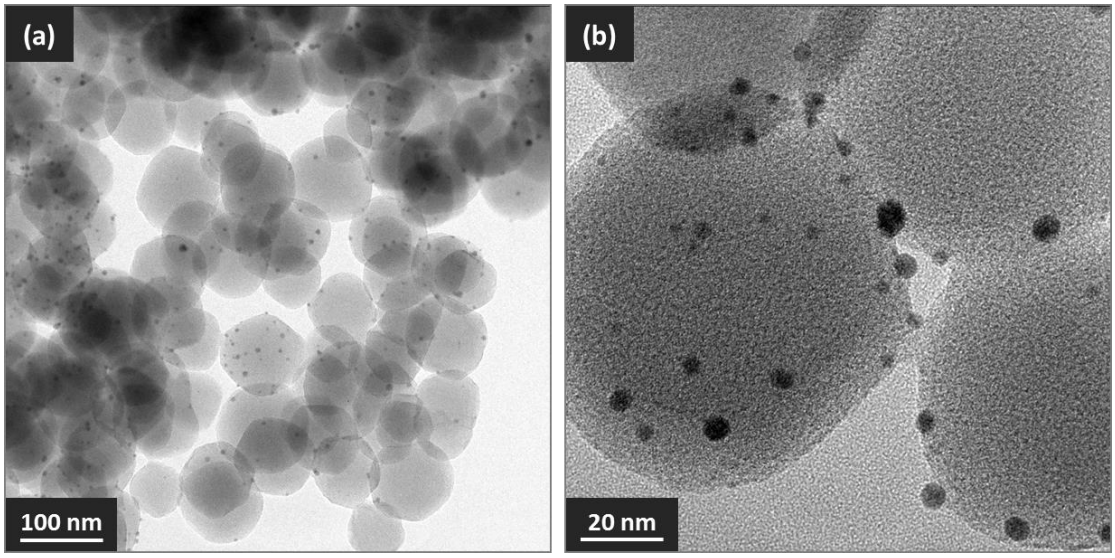

Figure 5.20 TEM micrographs of used Au/UiO-66 catalyst

TEM analysis was performed on the used Au/UiO-66 catalyst to investigate any effects that the catalytic reaction may have had on the morphology and size of the Au NPs. The images in Figure 5.20 clearly show that the NP morphology and sizes are kept intact and unchanged from the fresh catalyst. This would be important for the longevity of the catalyst material in for further catalytic cycles.

5.3.2 Knoevenagel Condensation with Malononitrile

With a more in-depth knowledge of the oxidation reaction, the second step of the tandem was also probed to gain a similar understanding so as to combine the stages into a one-pot method. Scheme 5.3 shows a representation of the reaction and the conditions required for implementation.

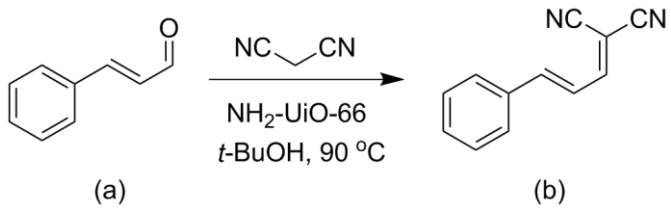

Scheme 5.3 Knoevenagel condensation of cinnamaldehyde with malononitrile using NH_2-UiO-66. (a) cinnamaldehyde and (b) cinnamylidene malononitrile

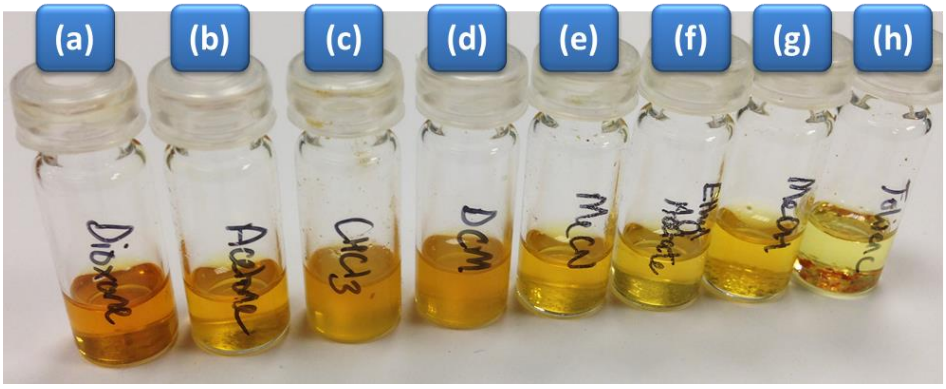

Figure 5.21 Cinnamylidene malononitrile solubility study. (a) 1,4-dioxane, (b) acetone, (c) chloroform, (d) dichloromethane, (e) acetonitrile, (f) ethyl acetate, (g) methanol, (h) toluene.

It quickly became apparent that the condensation product was soluble in *t*-butanol at reaction temperatures, but was reduced at RT, resulting in precipitation of the product at concentrations close to 50 % expect yields and above. This made analysis of reaction samples difficult without being able to keep the samples warm enough for complete solubility prior to injection.

A solubility test was performed on cinnamylidene malononitrile in a variety of solvents to find a solvent that could aid the solubility within reaction samples. The product (10 mg), prepared by an organocatalysed reaction with imidazole,[67] was weighed into small vials and a range of solvents added (0.5 mL) as seen in Figure 5.21. The resulting solutions are ranked in order of solubility with the most soluble on the left and least on the right. 1,4-dioxane was the best candidate and able to completely dissolve the product at this concentration, whereas the other solvents only achieved partial dissolution and both chlorinated solvents forming very fine suspensions. As a result, reaction samples were prepared by dilution of a 200 µL aliquot with 50 µL of 1,4-dioxane in a 300 µL vial for subsequent analysis. This was sufficient to keep all reactants and products in solution.

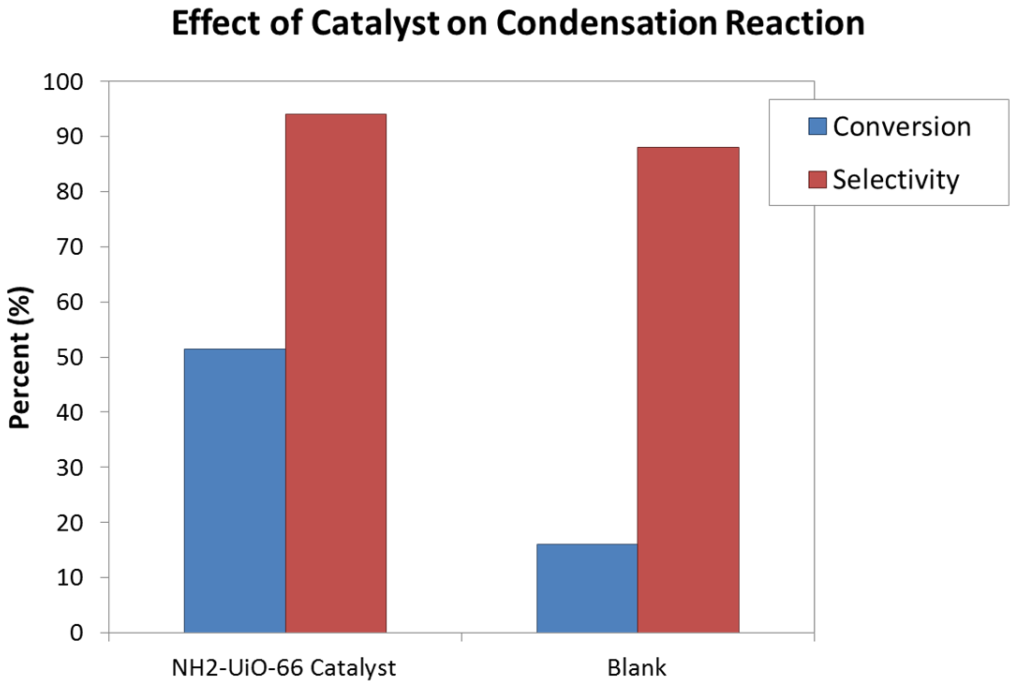

Figure 5.22 NH_2-UiO-66 catalysed and blank Knoevenagel condensation reaction (Conditions: catalyst (40 mg), cinnamaldehyde (0.1 g), malononitrile (0.1 g), chlorobenzene (0.2 g), *t*-butanol (8 mL), T = 8 hrs, t = 90 °C)

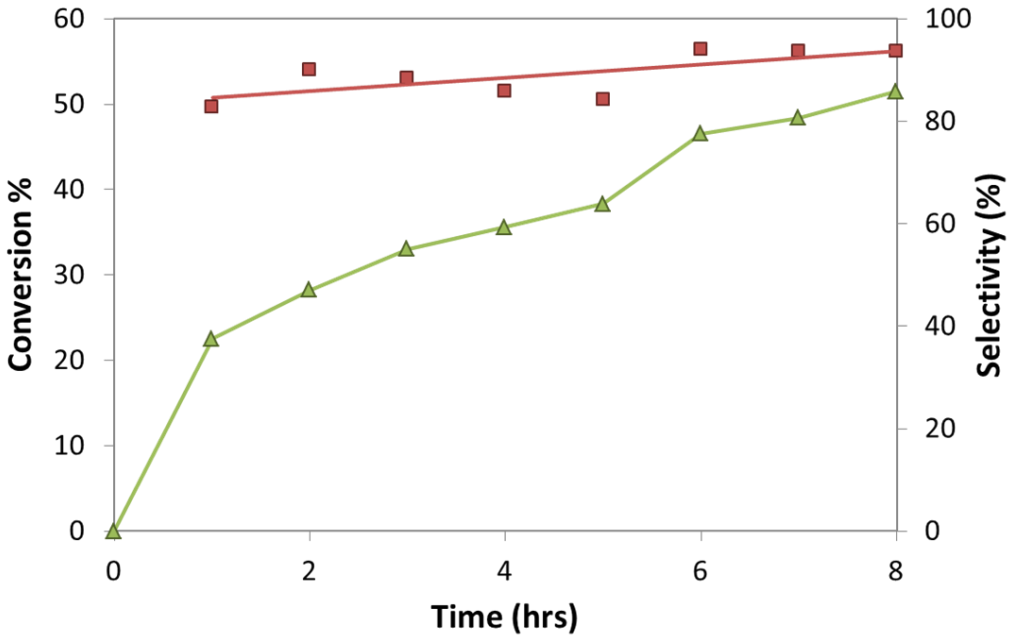

Figure 5.23 Reaction profile of NH_2-UiO-66 catalysed Knoevenagel condensation of cinnamaldehyde with malononitrile (Conditions: See Figure 5.22)

The Knoevenagel condensation of cinnamaldehyde and malononitrile was carried out in the presence of NH_2-UiO-66 as well as an equivalent blank reaction without a catalyst at 90 °C. Although a small blank background reaction with a conversion of 16 % was observed, the catalyst clearly increased the amount of conversion to over 52 % over the course of 8 hours. The reaction proceeds initially with a rate which decreases significantly over the first couple of hours to level off towards the end of the reaction (Figure 5.23). It is possible that this could be a concentration effect whereby the reduced concentration of the reactant results in reduced contact of reactants with the catalyst to form the product. The selectivity toward cinnamylidene malononitrile was consistently over 90 % over the course of the reaction, with a 95 % selectivity after 8 hours of reaction. No detectable by-products were observed by GC analysis, implying the formation of a small fraction of non-volatile and high molecular weight products. Nonetheless, a selectivity in excess of 95 % is a respectable value.

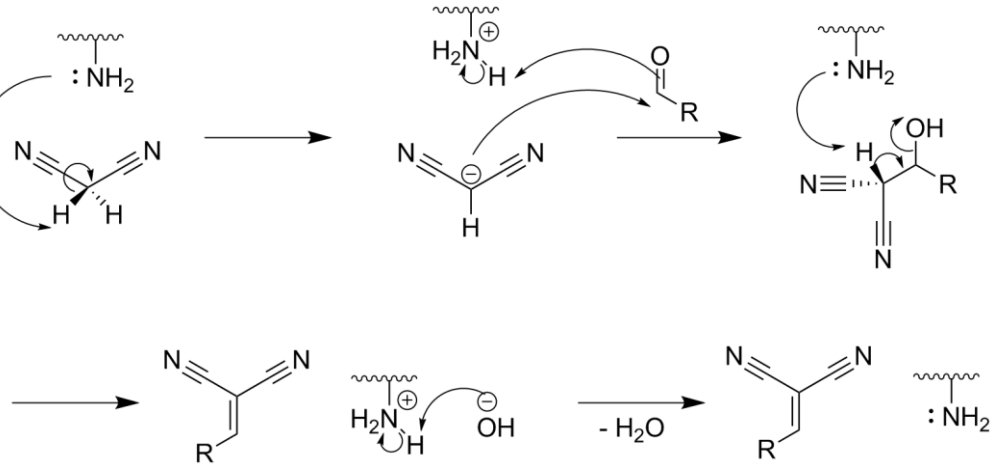

Scheme 5.4 Mechanism of amine/base catalysed Knoevenagel condensation of an aldehyde with malononitrile by abstraction of methylene hydrogen atoms

Another plausible explanation requires a more thorough analysis of the reaction mechanism. It is generally accepted that the base catalysed condensation follows the mechanism where abstraction of a hydrogen atom from the activated methylene compound occurs to form a stabilised carbanion intermediate.[83, 93] The activated intermediate can then react with the aldehyde, with a subsequent condensation step liberating water and the final product (Scheme 5.4). There are some reports[93-94] of heterogeneous amine based

catalysts which describe the formation of an imine by condensation of the aldehyde with the amine catalyst before reaction with the carbanion intermediate to form the final product. This would result in the utilisation of more active sites which would be capped by the imine for a period of time (depending on the rate limiting step), and could account for the drop in rate after the first hour. FT-IR could be used to probe the catalyst after a short reaction period to detect stretches unique to the imine functional group to confirm if this mechanism applies to the NH_2-UiO-66 as well.

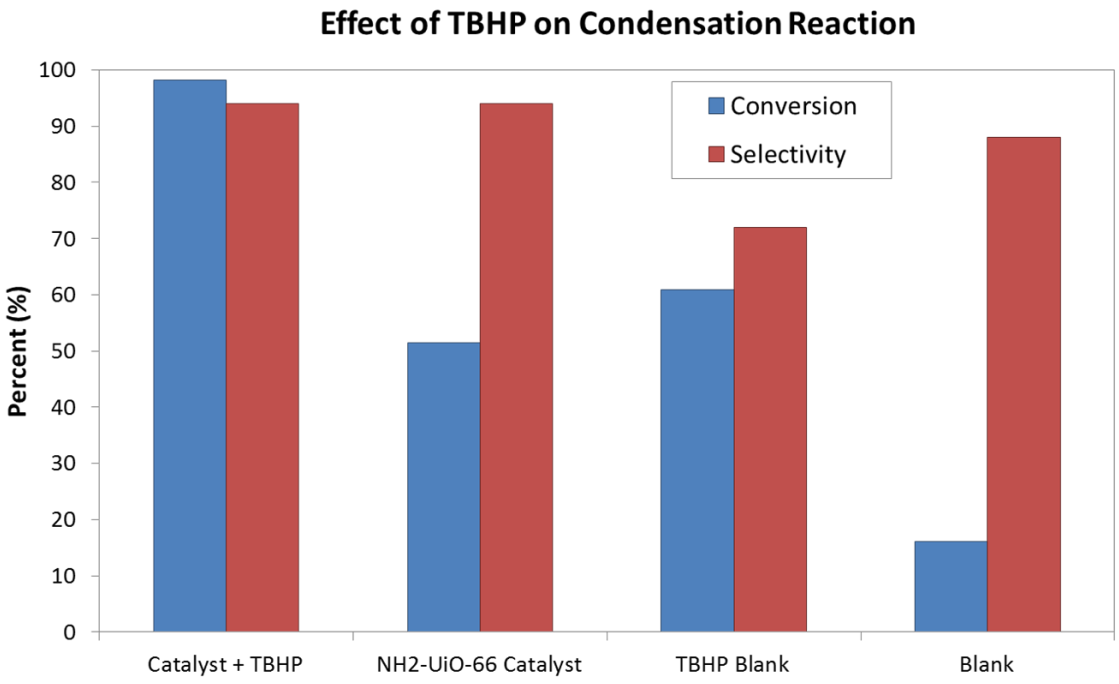

Figure 5.24 Effect of TBHP on blank and NH_2-UiO-66 catalysed Knoevenagel condensation reactions (Conditions: See Figure 5.22 with addition of TBHP (0.49 mL; 70 wt % in H_2O) where applicable)

Given that the Knoevenagel condensation reaction is designed to be carried out as a second step to the oxidation reaction, and that an excess of TBHP will be used in the oxidation step, the effect of TBHP on the Knoevenagel condensation was investigated to test for the potential effect of residual TBHP. In this study, TBHP was used in a large excess (5.3 equiv.) to exemplify the effects, although in reality, the amount of residual TBHP left in the reaction mixture is likely to be considerably less (< 1 equiv.). Figure 5.24 compares the catalytic data from the blank and catalysed reactions with and without TBHP. As can be seen, the blank reaction in the presence of an excess of TBHP

reaches higher conversions than the blank at around 60 % compared with 16 %, but the selectivity falls to less than 70 % with the main by-products being benzaldehyde, likely formed by decomposition of the reactant by TBHP. The traditional organo-catalysed Knoevenagel condensation uses the basic properties of piperidine to act as a catalyst for this reaction. The basicity of TBHP could, in this case, also be contributing to the condensation reaction in a similar manner given the high excess concentrations. Alternatively, given the propensity of TBHP to degrade by heterolytic fission to radical species, a totally different radical mechanism could be operating. It is unlikely that a radical mechanism is operating as radicals are known to be highly reactive and thus produce high rates of reaction. Unless only a tiny fraction of the TBHP has formed radical species, it is more plausible that basic properties of TBHP, and 2-electron transfer mechanics, are at play.

The NH_2-UiO-66 catalyst, although achieving slightly less conversion than an excess of TBHP, maintains high levels of selectivity. When the catalyst is used in the presence of TBHP, almost complete conversion of cinnamaldehyde is observed after 8 hours. This was unexpected given the lower selectivity observed when TBHP is present in the reaction mixture. It is possible that some synergistic effects are at play, with TBHP enhancing the rate of reaction in some way. As this study has used an excess of TBHP more than 5 times than would be present in a tandem reaction, it is expected that these effects would be scaled down by a similar factor.

5.3.3 The Tandem Oxidation-Condensation

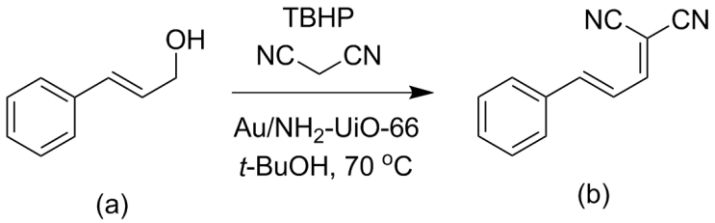

Scheme 5.5 One-pot tandem reaction of cinnamyl alcohol to cinnamylidene malononitrile using a single Au/NH_2-UiO-66 catalyst. (a) cinnamyl alcohol and (b) cinnamylidene malononitrile

The two stages of the oxidation and Knoevenagel condensation reaction, as determined in the preceding sections, were combined together in one-pot to

determine the yields achieved over a period of 1 hour. The reaction was performed at 70 °C as required for the initial oxidation reaction, with the general scheme as shown in Scheme 5.5.

A series of catalysts with single active sites (as controls) and multiple active sites were screened for activity in the tandem oxidation-condensation reaction. The Au/UiO-66 contains just metal nanoparticles and so should only provide an active site for the oxidation reaction, thus it would be expected to see the aldehyde product with little to no condensation product (apart from that which is due to the background reaction). The NH_2-UiO-66 only has basic amine groups and thus should not be active in the oxidation step. As no aldehyde is formed, no reaction should be observed in the one-pot tandem reaction. Finally, the Au/NH_2-UiO-66 contains the active metal NP surface in addition to the basic amine groups, as so it would be expected to observe the presence of some of the oxidation and condensation products in the reaction mixture.

Contrary to expectations, all three catalysts proved unsuccessful with less than 1 % conversions for the initial oxidation reaction and as a result, no conversion for the second step as no cinnamaldehyde had been produced.

Table 5.6 Catalytic data of one-pot tandem reaction on Au NP materials

Catalyst	Oxidation[a]		Condensation[b]		Yield[c] (%)
	Conversion (%)	Selectivity (%)	Conversion (%)	Selectivity[b] (%)	
Au/UiO-66	< 1	> 99	0	0	0
NH_2-UiO-66	< 1	> 99	0	0	0
Au/NH_2-UiO-66	< 1	> 99	0	0	0
Au/NH_2-UiO-66[d]	67	> 99	97	> 99	65

Conditions: catalyst (20 mg), cinnamyl alcohol (50 mg), malononitrile (50 mg), chlorobenzene (0.1 g), *t*-butanol (4 mL), TBHP (0.245 mL; 70 wt % in H_2O), T = 24 hrs, t = 70 °C. [a] Conversion of cinnamyl alcohol and selectivity to cinnamaldehyde. [b] Conversion of cinnamaldehyde and selectivity to cinnamylidene malononitrile. [c] Yield of cinnamylidene malononitrile. [d] Addition of malononitrile after 5 hours.

This was unexpected as the Au/UiO-66 has been previously shown to give high conversions of cinnamyl alcohol under similar conditions. The only difference

in the reaction conditions was the presence of malononitrile as a reactant for the second step. The reaction was repeated using the Au/NH_2-UiO-66 catalyst but with delayed addition of malononitrile until after 5 hours of reaction. The formation of cinnamaldehyde was observed with 67 % conversion of the alcohol, and almost complete conversion of the aldehyde to the final product after a total of 24 hours. This revealed that the presence of malononitrile at the beginning of the reaction was inhibiting the oxidation process, likely due to unfavourable interactions between the malononitrile and the Au NPs which are the active site for that step.

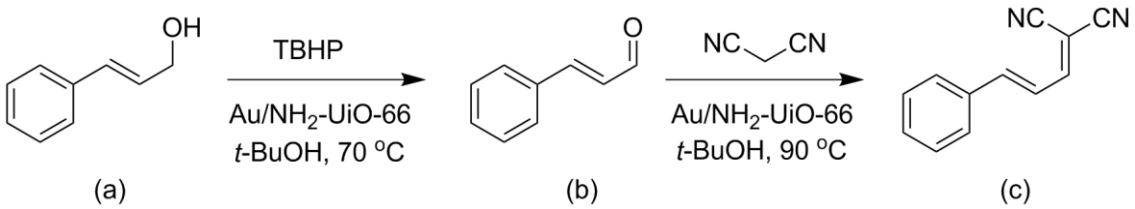

Scheme 5.6 Tandem reaction of cinnamyl alcohol to cinnamylidene malononitrile using a single Au/NH_2-UiO-66 catalyst. (a) cinnamyl alcohol, (b) cinnamaldehyde and (c) cinnamylidene malononitrile

The tandem reaction was repeated with a few minor changes. Firstly, the addition of malononitrile was delayed until 10 hours of reaction in an effort to allow the oxidation to reach higher conversions and increase the overall yield of the tandem process. The temperature was also increased from 70 °C to 90 °C to increase the rate of reaction for the condensation step. Although reasonable conversions and yields were observed initially for the condensation in the proof-of-concept attempt at the tandem reaction, the moderate conversions and high excess of TBHP are likely to have contributed to this result as identified in the previous section. The amount of TBHP was limited to 1.2 equivalents to account for some thermal decomposition of the peroxide over the course of the reaction.

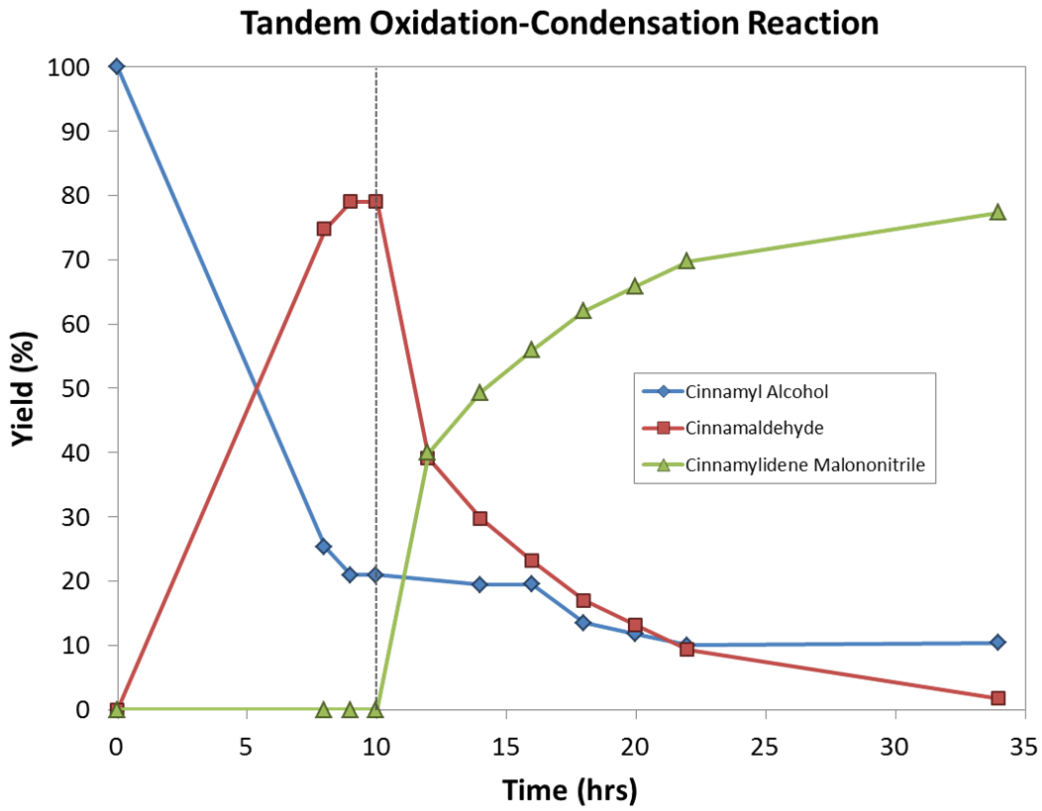

Figure 5.25 Reaction profile of tandem oxidation-condensation of cinnamyl alcohol to cinnamaldehyde and cinnamylidene malononitrile (Step 1: catalyst (40 mg), cinnamyl alcohol (0.1 g), chlorobenzene (0.2 g), *t*-butanol (8 mL), TBHP (0.124 mL; 70 wt % in H_2O) T = 70 °C, t = 0-10 hrs. Step 2: malononitrile (0.1 g), T = 90 °C, t = 10-34 hrs)

The reaction profile of the tandem reaction under these conditions (Figure 5.25) highlights that the Au/NH_2-UiO-66 is successful in achieving approximately 80 % yield of cinnamylidene malononitrile after 34 hours of reaction. The addition of malononitrile is highlighted at the 10 hour mark where a transition can be clearly observed from the formation of the aldehyde to consumption of the aldehyde to form the final product. Under these conditions, the oxidation reaction was limited to 80 % conversion as the rate of reaction declines significantly between 8 and 10 hours of reaction. This limited the overall yield, with the second step achieving close to 100 % conversion of the synthesised aldehyde. Thermal decomposition of TBHP (that could have reduced the actual molar equivalents to less than 1), as well as mass transfer limitations associated with low concentrations of the alcohol and TBHP, and

diffusion to the NP surface, may have contributed to the reduction in rate towards the end of the oxidation step.

It was also interesting to note the continued decline of cinnamyl alcohol over the course of the second step of the reaction, however the generation of more aldehyde product was not observed. Instead, small quantities of benzaldehyde and benzylidene malononitrile (the condensation product from benzaldehyde) were observed as by-products, likely due to the decomposition of the residual cinnamyl alcohol. The formation of benzaldehyde was also observed in small fractions when the individual oxidation reactions had been left for long periods of time up to 24 hours with low to moderate conversions. The mechanism for this decomposition is not known, however this could be eliminated by altering the conditions to achieve quantitative conversion of the alcohol in the oxidation step.

5.4 Conclusions and Future Work

A composite NP/MOF material has been successfully synthesised in the form of Au NPs deposited on NH_2-UiO-66, with multifunctional properties stemming from both the surface of the NPs and basic amine groups which can be utilised as active sites for catalytic processes. The method for preparing the material follows a facile synthesis for the NH_2-UiO-66 using a benzoic acid modulator to regulate the nanocrystal sizes to around 100 nm. Subsequent deposition of NPs using a simple colloidal preparation employing PVP as a polymer stabilising agent, achieved NPs with an average size of 3.7 nm. The method could be applied to both UiO-66 and the amino-functionalised NH_2-UiO-66 and, to highlight the versatility of the deposition, was demonstrated to be compatible for synthesising monometallic NP/ MOF materials with Au, Pt and Pd as well as alloyed bimetallic AuPd NPs.

The Au/NH_2-UiO-66 catalyst was then successfully applied in a one-pot tandem catalytic process involving the selective oxidation of cinnamyl alcohol with TBHP, and the subsequent transformation of cinnamaldehyde to cinnamylidene malononitrile, with an overall yield in excess of 80 %. The one-pot tandem reaction has facilitated multiple steps without the need to isolate and purify the intermediate product, which in turn could prevent potential losses in yield and reduce the overall processing time. By achieving respectable yields in the tandem process, the need for isolation and purification of cinnamaldehyde before the condensation reaction was eliminated, reducing the quantities of solvents and labour intensive processes to achieve the final condensation product. As a result, if this process were to be scaled up, this tandem process would contribute to a more sustainable process, both in terms of reduced waste and economic savings.

As a result of the unfavourable interactions of malononitrile with the Au NPs, one limitation of this process requires that the malononitrile be added after 10 hours of reaction to allow for the oxidation to progress before the condensation reaction. This is not ideal as it would be easier to add all reactants together at the start, however this was overcome with not too much difficulty with the small adaptation and the one-pot tandem process is still maintained. It is not yet fully understood how the malononitrile is inhibiting the oxidation reaction, however further study could help to reveal the

mechanisms in play. A range of less active methylene compounds such as cyanoacetates and di-esters (e.g. ethyl cyanoacetate and diethyl malonate) could help to reveal if the acidity of the reactant is a factor in this phenonmenon. The use of alternative noble metals such as Pt or Pd could provide a catalyst with similar activity which could well be resistant to interactions with malononitrile which inhibit the initial oxidation. Another possible solution would be to have a drip-feed of malononitrile over the course of the reaction, limiting the addition to match the rate of the oxidation process so that the malononitrile is never in excess in the bulk of the reaction mixture. This should allow the malononitrile to react with the aldehyde product before any interactions with the NPs can occur.

In extension to the work reported here, and in recognition of the versatility of the deposition method, it would be interesting to apply both the Pt and Pd deposited UiO-66 and NH_2-UiO-66 to the oxidation reactions and subsequent tandem steps. The comparison of noble metals from extruded NP materials in Chapters 3-4 showed compelling evidence for different activity and selectivity properties. Whilst the changes in activity were largely hypothesised to be correlated more with the degree of extrusion, the selectivity properties were unique to the composition of the NPs. This was also demonstrated for bimetallic NPs (*Section 1.2.6.2*),[95-96] where subtle changes in compositional nanostructures also demonstrated selectivity effects i.e. alloy *versus* core-shell.[97] Bulk characterisation techniques such as XPS and XAS, as applied in Chapter 4, could also be used to help validate the bulk nature of metal species across a sample and identify associated structure-property correlations in applied catalysis.

Encapsulation of NPs within the pores of UiO-66 was not successful due to difficulties preventing aggregation and large particle formation. Preliminary studies on a wet impregnation method had the most potential for encapsulation of Pt NPs, as also confirmed by a similar method reported recently in the literature,[58] however the versatility was in question with varied results when applied to the formation of Au NPs. Even with the promise of impregnation methods, NPs were observed on the surface of all materials in at least small fractions, and so selective encapsulation proved hitherto unsuccessful with these methods. Another recent report[19] has highlighted a precise ‘pore-filling’ impregnation method whereby the quantity added of

solution containing the metal salts is calculated based on the internal volume of the material. This method is however highly dependent on the crystallinity and lack of defects in the MOF support for effective and selective encapsulation.

Despite the minor limitations that arose with the application of Au/NH_2-UiO-66 materials in this tandem process, the scope of application toward a diverse combination of reaction processes is opened up using NP/MOF materials. With the diversity shown for the synthesis of these materials using a range of metal NPs, the materials should be applicable for further oxidation process on bimetallic NPs, hydrogenation reactions on Pt and/or Pd NPs, cross-coupling reactions on Pd reactions as well as others. Coupled with the potential of amine-MOFs to catalyse condensation reactions, and for the ability to functionalise them further for access to an almost unlimited amount of organocatalysed transformations, the opportunities for combining any number of these reactions in one-pot, cascade processes with these materials is vast.

5.5 References

1 N. Fairley and A. Carrick, *The Casa Cookbook*, Acolyte Science, Cheshire, **2005**.
2 M. Newville, *J. Synchrotron Radiat.,* **2001**, *8*, 322.
3 B. Ravel and M. Newville, *J. Synchrotron Radiat.,* **2005**, *12*, 537.
4 A. Dhakshinamoorthy and H. Garcia, *Chem. Soc. Rev.,* **2012**, *41*, 5262.
5 J. Juan-Alcaniz, J. Gascon and F. Kapteijn, *J. Mater. Chem.,* **2012**, *22*, 10102.
6 D. Maspoch, D. Ruiz-Molina and J. Veciana, *Chem. Soc. Rev.,* **2007**, *36*, 770.
7 G. Ferey, *Chem. Soc. Rev.,* **2008**, *37*, 191.
8 S. L. James, *Chem. Soc. Rev.,* **2003**, *32*, 276.
9 M. Ranocchiari and J. A. v. Bokhoven, *Phys. Chem. Chem. Phys.,* **2011**, *13*, 6388.
10 J. Lee, O. K. Farha, J. Roberts, K. A. Scheidt, S. T. Nguyen and J. T. Hupp, *Chem. Soc. Rev.,* **2009**, *38*, 1450.
11 J. Kim, H.-Y. Cho and W.-S. Ahn, *Catal. Surv. Asia,* **2012**, *16*, 106.
12 T. Granato, F. Testa and R. Olivo, *Micro. Meso. Mater.,* **2012**, *153*, 236.
13 P. Valvekens, F. Vermoortele and D. De Vos, *Catal. Sci. Technol.,* **2013**, *3*, 1435.
14 Y.-M. Chung, H.-Y. Kim and W.-S. Ahn, *Catal. Lett.,* **2014**, *144*, 817.
15 J. Chen, R. Liu, H. Gao, L. Chen and D. Ye, *J. Mater. Chem. A,* **2014**, *2*, 7205.
16 C. Wang, Z. Xie, K. E. deKrafft and W. Lin, *J. Am. Chem. Soc.,* **2011**, *133*, 13445.
17 P. Neves, A. C. Gomes, T. R. Amarante, F. A. A. Paz, M. Pillinger, I. S. Gonçalves and A. A. Valente, *Micro. Meso. Mater.,* **2015**, *202*, 106.
18 H. Fei and S. M. Cohen, *J. Am. Chem. Soc.,* **2015**, *137*, 2191.
19 Q.-L. Zhu, J. Li and Q. Xu, *J. Am. Chem. Soc.,* **2013**, *135*, 10210.
20 L. Shen, W. Wu, R. Liang, R. Lin and L. Wu, *Nanoscale,* **2013**, *5*, 9374.
21 M. Wen, K. Mori, T. Kamegawa and H. Yamashita, *Chem. Commun.,* **2014**, *50*, 11645.
22 H.-j. Zhang, S.-d. Qi, X.-y. Niu, J. Hu, C.-l. Ren, H.-l. Chen and X.-g. Chen, *Catal. Sci. Technol.,* **2014**, *4*, 3013.
23 I. J. Kang, N. A. Khan, E. Haque and S. H. Jhung, *Chem. Eur. J.,* **2011**, *17*, 6437.
24 S. Das, D. E. Johnston and S. Das, *CrystEngComm,* **2012**, *14*, 6136.
25 P. Guo, D. Dutta, A. G. Wong-Foy, D. W. Gidley and A. J. Matzger, *J. Am. Chem. Soc.,* **2015**, *137*, 2651.
26 J. H. Cavka, S. Jakobsen, U. Olsbye, N. Guillou, C. Lamberti, S. Bordiga and K. P. Lillerud, *J. Am. Chem. Soc.,* **2008**, *130*, 13850.
27 P. S. Bárcia, D. Guimarães, P. A. P. Mendes, J. A. C. Silva, V. Guillerm, H. Chevreau, C. Serre and A. E. Rodrigues, *Micro. Meso. Mater.,* **2011**, *139*, 67.
28 O. M. Yaghi, M. O'Keeffe, N. W. Ockwig, H. K. Chae, M. Eddaoudi and J. Kim, *Nature,* **2003**, *423*, 705.
29 N. W. Ockwig, O. Delgado-Friedrichs, M. O'Keeffe and O. M. Yaghi, *Acc. Chem. Res.,* **2005**, *38*, 176.
30 M. Kim and S. M. Cohen, *CrystEngComm,* **2012**, *14*, 4096.
31 A. Sauer, A. Kapelski, C. Fliedel, S. Dagorne, M. Kol and J. Okuda, *Dalton Trans.,* **2013**, *42*, 9007.

32 S. J. Sabounchei, M. Ahmadi, P. Shahriari, F. Hoseini-Fashami and S. Samiee, *Russ. J. Inorg. Chem.,* **2012**, *57*, 1005.
33 J. Canivet, A. Fateeva, Y. Guo, B. Coasne and D. Farrusseng, *Chem. Soc. Rev.,* **2014**, *43*, 5594.
34 P. M. Schoenecker, C. G. Carson, H. Jasuja, C. J. J. Flemming and K. S. Walton, *Ind. Eng. Chem. Res.,* **2012**, *51*, 6513.
35 A. D. Wiersum, E. Soubeyrand-Lenoir, Q. Yang, B. Moulin, V. Guillerm, M. B. Yahia, S. Bourrelly, A. Vimont, S. Miller, C. Vagner, M. Daturi, G. Clet, C. Serre, G. Maurin and P. L. Llewellyn, *Chem. Asian J.,* **2011**, *6*, 3270.
36 J. B. DeCoste, G. W. Peterson, H. Jasuja, T. G. Glover, Y.-g. Huang and K. S. Walton, *J. Mater. Chem. A,* **2013**, *1*, 5642.
37 J. E. Mondloch, M. J. Katz, N. Planas, D. Semrouni, L. Gagliardi, J. T. Hupp and O. K. Farha, *Chem. Commun.,* **2014**, *50*, 8944.
38 H. Wu, T. Yildirim and W. Zhou, *J. Phys. Chem. Lett.,* **2013**, *4*, 925.
39 B. Van de Voorde, I. Stassen, B. Bueken, F. Vermoortele, D. De Vos, R. Ameloot, J.-C. Tan and T. D. Bennett, *J. Mater. Chem. A,* **2015**, *3*, 1737.
40 Q. Yang, S. Vaesen, F. Ragon, A. D. Wiersum, D. Wu, A. Lago, T. Devic, C. Martineau, F. Taulelle, P. L. Llewellyn, H. Jobic, C. Zhong, C. Serre, G. De Weireld and G. Maurin, *Angew. Chem., Int. Ed.,* **2013**, *52*, 10316.
41 G. W. Peterson, J. B. DeCoste, F. Fatollahi-Fard and D. K. Britt, *Ind. Eng. Chem. Res.,* **2013**, *53*, 701.
42 B. Bozbiyik, T. Duerinck, J. Lannoeye, D. E. De Vos, G. V. Baron and J. F. M. Denayer, *Micro. Meso. Mater.,* **2014**, *183*, 143.
43 W.-W. Zhao, C.-Y. Zhang, Z.-G. Yan, L.-P. Bai, X. Wang, H. Huang, Y.-Y. Zhou, Y. Xie, F.-S. Li and J.-R. Li, *J. Chromatogr. A,* **2014**, *1370*, 121.
44 D. Cunha, M. Ben Yahia, S. Hall, S. R. Miller, H. Chevreau, E. Elkaïm, G. Maurin, P. Horcajada and C. Serre, *Chem. Mater.,* **2013**, *25*, 2767.
45 C. He, K. Lu and W. Lin, *J. Am. Chem. Soc.,* **2014**, *136*, 12253.
46 L. Shen, R. Liang, M. Luo, F. Jing and L. Wu, *Phys. Chem. Chem. Phys.,* **2015**, *17*, 117.
47 M. Kim, J. F. Cahill, Y. Su, K. A. Prather and S. M. Cohen, *Chem. Sci.,* **2012**, *3*, 126.
48 Y. Luan, N. Zheng, Y. Qi, J. Yu and G. Wang, *Eur. J. Inorg. Chem.,* **2014**, *2014*, 4268.
49 V. N. Panchenko, M. M. Matrosova, J. Jeon, J. W. Jun, M. N. Timofeeva and S. H. Jhung, *J. Catal.,* **2014**, *316*, 251.
50 Y. Yang, H.-F. Yao, F.-G. Xi and E.-Q. Gao, *J. Mol. Catal. A: Chem.,* **2014**, *390*, 198.
51 F. G. Cirujano, A. Corma and F. X. Llabrés i Xamena, *Chem. Eng. Sci.,* **2015**, *124*, 52.
52 M. N. Timofeeva, V. N. Panchenko, J. W. Jun, Z. Hasan, M. M. Matrosova and S. H. Jhung, *Appl. Catal., A,* **2014**, *471*, 91.
53 C. M. McGuirk, M. J. Katz, C. L. Stern, A. A. Sarjeant, J. T. Hupp, O. K. Farha and C. A. Mirkin, *J. Am. Chem. Soc.,* **2015**, *137*, 919.
54 J. Tang, W. Dong, G. Wang, Y. Yao, L. Cai, Y. Liu, X. Zhao, J. Xu and L. Tan, *RSC Adv.,* **2014**, *4*, 42977.
55 H. Fei and S. M. Cohen, *Chem. Commun.,* **2014**, *50*, 4810.
56 H. Fei, J. Shin, Y. S. Meng, M. Adelhardt, J. Sutter, K. Meyer and S. M. Cohen, *J. Am. Chem. Soc.,* **2014**, *136*, 4965.
57 L. B. Vilhelmsen and D. S. Sholl, *J. Phys. Chem. Lett.,* **2012**, *3*, 3702.
58 Z. Guo, C. Xiao, R. V. Maligal-Ganesh, L. Zhou, T. W. Goh, X. Li, D. Tesfagaber, A. Thiel and W. Huang, *ACS Catal.,* **2014**, *4*, 1340.

59 R. Wu, X. Qian, K. Zhou, H. Liu, B. Yadian, J. Wei, H. Zhu and Y. Huang, *J. Mater. Chem. A,* **2013**, *1*, 14294.
60 K. Leus, P. Concepcion, M. Vandichel, M. Meledina, A. Grirrane, D. Esquivel, S. Turner, D. Poelman, M. Waroquier, V. Van Speybroeck, G. Van Tendeloo, H. Garcia and P. Van Der Voort, *RSC Adv.,* **2015**, *5*, 22334.
61 L. Shen, S. Liang, W. Wu, R. Liang and L. Wu, *J. Mater. Chem. A,* **2013**, *1*, 11473.
62 T. W. Goh, C. Xiao, R. V. Maligal-Ganesh, X. Li and W. Huang, *Chem. Eng. Sci.,* **2015**, *124*, 45.
63 M. Zhao, K. Deng, L. He, Y. Liu, G. Li, H. Zhao and Z. Tang, *J. Am. Chem. Soc.,* **2014**, *136*, 1738.
64 Y.-Z. Chen, Y.-X. Zhou, H. Wang, J. Lu, T. Uchida, Q. Xu, S.-H. Yu and H.-L. Jiang, *ACS Catal.,* **2015**, 2062.
65 X. Li, Z. Guo, C. Xiao, T. W. Goh, D. Tesfagaber and W. Huang, *ACS Catal.,* **2014**.
66 T. Toyao, M. Saito, Y. Horiuchi and M. Matsuoka, *Catal. Sci. Technol.,* **2014**, *4*, 625.
67 M. M. Heravi, M. H. Tehrani, K. Bakhtiari and H. A. Oskooie, *J. Chem. Res.,* **2006**, *2006*, 561.
68 A. Schaate, P. Roy, A. Godt, J. Lippke, F. Waltz, M. Wiebcke and P. Behrens, *Chem. Eur. J.,* **2011**, *17*, 6643.
69 F. Vermoortele, R. Ameloot, A. Vimont, C. Serre and D. De Vos, *Chem. Commun.,* **2011**, *47*, 1521.
70 P. M. Schoenecker, G. A. Belancik, B. E. Grabicka and K. S. Walton, *AIChE J.,* **2013**, *59*, 1255.
71 D. Sun, Y. Fu, W. Liu, L. Ye, D. Wang, L. Yang, X. Fu and Z. Li, *Chem. Eur. J.,* **2013**, *19*, 14279.
72 T. T. Dang, Y. Zhu, J. S. Y. Ngiam, S. C. Ghosh, A. Chen and A. M. Seayad, *ACS Catal.,* **2013**, *3*, 1406.
73 H. Liu, Y. Liu, Y. Li, Z. Tang and H. Jiang, *J. Phys. Chem. C.,* **2010**, *114*, 13362.
74 M. Kandiah, S. Usseglio, S. Svelle, U. Olsbye, K. P. Lillerud and M. Tilset, *J. Mater. Chem.,* **2010**, *20*, 9848.
75 F. Rouquerol, J. Rouquerol and K. Sing, *Adsorption by Powders and Porous Solids: Principles, Methodology and Applicationd*, Academic Press, London, **1999**.
76 M. A. Camblor and S. B. Hong, Synthetic Silicate Zeolites: Diverse Materials Accessible Through Geoinspiration in *Porous Materials* (Eds.: D. W. Bruce, D. O'Hare, R. I. Walton), John Wiley & Sons, Ltd, Chichester, **2011**.
77 L. Valenzano, B. Civalleri, S. Chavan, S. Bordiga, M. H. Nilsen, S. Jakobsen, K. P. Lillerud and C. Lamberti, *Chem. Mater.,* **2011**, *23*, 1700.
78 B. D. Craig and D. S. Anderson, Chlorides in *Handbook of Corrosion Data*, 2nd ed., ASM International, Cincinnati, **1995**.
79 V. Guillerm, S. Gross, C. Serre, T. Devic, M. Bauer and G. Ferey, *Chem. Commun.,* **2010**, *46*, 767.
80 K. Tulig and K. S. Walton, *RSC Adv.,* **2014**, *4*, 51080.
81 C. Louis, Chemical Preparation of Gold Nanoparticles on Surfaces in *Gold Nanoparticles for Physics, Chemistry and Biology* (Eds.: C. Louis, O. Pluchery), Imperial College Press, London, **2012**.
82 A. Dhakshinamoorthy, M. Opanasenko, J. Čejka and H. Garcia, *Adv. Synth. Catal.,* **2013**, *355*, 247.

83 J. Clayden, N. Greeves, S. Warren and P. Wothers, *Organic Chemistry*, Oxford University Press, Oxford, **2001**.
84 D. Wang and Z. Li, *Catal. Sci. Technol.,* **2015**, *5*, 1623.
85 T. Toyao, M. Fujiwaki, Y. Horiuchi and M. Matsuoka, *RSC Adv.,* **2013**, *3*, 21582.
86 R. G. Eilerman, Cinnamic Acid, Cinnamaldehyde, and Cinnamyl Alcohol in *Kirk-Othmer Encyclopedia of Chemical Technology*, John Wiley & Sons, Inc., **2000**.
87 Yissum Research Development Company of the Hebrew University of Jerusalem, A. Levitzki, A. Gazit, M. Chorev and C. Gilon, **1995,** *Pharmaceutical compositions comprising benzylidene-and cinnamylidene-malononitrile derivatives for the inhibition of proliferative processes in mammalian cells, certain such novelcompounds and their preparation,* Canada Patent CA 1,334,826.
88 H. Tsunoyama, H. Sakurai, Y. Negishi and T. Tsukuda, *J. Am. Chem. Soc.,* **2005**, *127*, 9374.
89 J. C. F. Rodríguez-Reyes, C. M. Friend and R. J. Madix, *Surf. Sci.,* **2012**, *606*, 1129.
90 T. Ishida, M. Nagaoka, T. Akita and M. Haruta, *Chem. Eur. J.,* **2008**, *14*, 8456.
91 A. Abad, A. Corma and H. García, *Chem. Eur. J.,* **2008**, *14*, 212.
92 J. Muzart, *Tetrahedron,* **2003**, *59*, 5789.
93 J. Gascon, U. Aktay, M. D. Hernandez-Alonso, G. P. M. van Klink and F. Kapteijn, *J. Catal.,* **2009**, *261*, 75.
94 R. Wirz, D. Ferri and A. Baiker, *Langmuir,* **2006**, *22*, 3698.
95 M. I. bin Saiman, G. L. Brett, R. Tiruvalam, M. M. Forde, K. Sharples, A. Thetford, R. L. Jenkins, N. Dimitratos, J. A. Lopez-Sanchez, D. M. Murphy, D. Bethell, D. J. Willock, S. H. Taylor, D. W. Knight, C. J. Kiely and G. J. Hutchings, *Angew. Chem., Int. Ed.,* **2012**, *51*, 5981.
96 L. Kesavan, R. Tiruvalam, M. H. A. Rahim, M. I. bin Saiman, D. I. Enache, R. L. Jenkins, N. Dimitratos, J. A. Lopez-Sanchez, S. H. Taylor, D. W. Knight, C. J. Kiely and G. J. Hutchings, *Science,* **2011**, *331*, 195.
97 M. Morad, M. Sankar, E. Cao, E. Nowicka, T. E. Davies, P. J. Miedziak, D. J. Morgan, D. W. Knight, D. Bethell, A. Gavriilidis and G. J. Hutchings, *Catal. Sci. Technol.,* **2014**, *4*, 3120.

5.6 Appendix

5.6.1 Experimental methods

5.6.1.1 Synthesis of UiO-66, Related Materials and Methods for Loading of NPs

All standard chemicals were bought from Sigma-Aldrich, Acros Organics or VWR International and used without further purification.

Synthesis of UiO-66: In a 250 mL glass reaction bottle was measured $ZrCl_4$ (0.640 g; 2.75 mmol), terephthalic acid (0.473 g; 2.85 mmol) and N,N'-dimethylformamide (40 mL), then sonicated for 5 mins to dissolve all compounds. Benzoic acid (3.36 g; 27.50 mmol) was added and the solution sonicated for a further 5 mins until complete dissolution had occurred. The bottle was capped and placed in a preheated convection oven at 120 °C for 48 hours, then allowed to cool to RT naturally. Suspensions of the pale yellow product were collected by centrifugation at 10,000 rpm for 15 minutes. The supernatant was decanted off and the product washed twice with methanol (2x 60 mL), collecting each time by centrifugation as before. Products were then dried ready for analysis or further experiments.

Synthesis of NH_2-UiO-66: In a 100 mL glass reaction bottle was measured ZrCl4 (0.163 g; 0.70 mmol), 2-aminoterephthalic acid (0.13 g; 0.72 mmol) and N,N'-dimethylformamide (40 mL), then sonicated for 5 mins to dissolve all compounds. Benzoic acid (0.85 g; 7.00 mmol) was added and the solution sonicated for a further 5 mins until complete dissolution had occurred. The bottle was capped and placed in a preheated convection oven at 120 °C for 48 hours, then allowed to cool to RT naturally. Suspensions of the pale yellow product were collected by centrifugation at 10,000 rpm for 15 minutes. The supernatant was decanted off and the product washed twice with methanol (2x 60 mL), collecting each time by centrifugation as before. Products were then dried ready for analysis or further experiments.

Synthesis of Colloidal Au NPs: In a 150 mL round-bottom flask (RBF) was measured methanol (80 mL), $HAuCl_4$ solution (0.38 mL; 10.61 mg/mL in H_2O)

and PVP solution (0.20 mL; 6.50 mg/mL in H_2O) and stirred vigorously. To the stirred solution, a freshly prepared aqueous solution of $NaBH_4$ (0.51 mL; 0.1 M) was added drop wise over a period of 3 minutes, then left to stir for a further 2 hours.

Deposition of Colloidal Au NPs: For a 1 wt % loading of Au NPs, UiO-66 or NH_2-UiO-66 (200 mg) was added to the stirred Au NP sol and left to stir for 24 hours. The pink-purple powdered product was collected by centrifugation at 10,000 rpm for 15 minutes, the supernatant decanted and washed twice with methanol (2x 40 mL), collected by centrifugation each time as before. Products were then dried ready for analysis or further experiments.

Direct Encapsulation of NPs: In a typical experiment, a methanolic colloidal sol of AuPd (1:1) NPs was prepared as previously described in an RBF. The methanol was removed by evaporation under vacuum using a rotary evaporator until dry. The NPs were redispersed in DMF (40 mL) and sonicated for 10-15 mins until homogeneous. UiO-66 was synthesised with benzoic acid modulation as previously described using the AuPd/DMF sol as a solvent.

Oleylamine NP Encapsulation: To a 25 mL glass batch reactor was weighed benzoic acid modulated UiO-66 (100 mg) and oleylamine (5 mL). The RBF was immersed in an oil bath at 60 °C and nitrogen bubbled through the mixture with stirring for 10-15 mins. Separately in a glass vial, $HAuCl_4$ (6 mg) was dissolved in a mixture of 1-octadecene (4 mL) and oleylamine (1 mL). The gold mixture was rapidly added to the UiO-66 suspension, the temperature increased to 90 °C and the nitrogen feed raised above the surface of the mixture to stop bubbling but maintain a covering of N_2. The mixture was stirred under these conditions for 30 mins. The RBF was removed from the oil bath and cooled to RT. The purple powdered product was collected by centrifugation (15 mins @ 10,000 rpm) , washed twice with methanol (2 x 30 mL) and dried overnight in an oven at 60 °C.

Impregnation Method: First, concentrated aqueous solutions of noble metal salts were prepared; $HAuCl_4$ (5.25 mg/mL) and K_2PtCl_4 (6.89 mg/mL). In a vial was measured benzoic acid modulated UiO-66 (50 mg) to which was added concentrated metal salt solution (0.16 mL). The vial was capped and the suspension left to soak overnight (16-18 hours). The cap was removed and the

water allowed to dry naturally at room temperature to afford pale yellow and pink powders for the $HAuCl_4$ and K_2PtCl_4 loaded materials respectively. The dry materials were transferred to a glass or ceramic vessel and loaded into a tube furnace. The furnace was heated at a rate of 10 °C/min to 200 °C and held for 2 hours under a flow of 10 % H_2/N_2 and allowed to cool. Products were collected, with the Au/UiO-66 a deep purple colour and the Pt/UiO-66 a dark grey.

Cinnamylidene Malononitrile: The synthesis method was adapted from a literature reference.[67] To a glass vial (21 mL) was measured cinnamaldehyde (0.793 g; 6.0 mmol), malononitrile (0.396 g; 6.0 mmol), imidazole (0.041 g; 0.6 mmol) and dichloromethane (12 mL). The mixture was stirred at room temperature for 2 hours.

The mixture was transferred to a separating funnel, water (15 mL) was added and products extracted using 2 x 10 mL of dichloromethane and dried over $MgSO_4$. Evaporation of the solvent yielded large, yellow crystals. The product was confirmed by ^{1}H NMR (400 MHz, CDCl3) δ (ppm) 7.27 (d, 2H, J= 9.84 Hz), 7.45-7.47 (m, 3H), 7.59-7.61 (m, 3H).

5.6.1.2 Catalytic Parameters and Conditions

Catalytic Reactions: To a RBF was measured catalyst, reactants, chlorobenzene (as an internal standard) and *tert*-butanol as a solvent in pre-determined concentrations. The RBF was immersed in a preheated oil bath at 70 °C with stirring and left for the desired amount of time. Samples were extracted at varying time intervals, centrifuged and capped in a vial for GC analysis. (For specific conditions, see respective figures and tables)

Gas Chromatography (GC-FID) Analysis: All reaction samples and kinetic samples were analysed by GC-FID (flame ionisation detector) using a Perkin Elmer Clarus 480 fitted with an autosampler. Components were identified against known commercial standards (with the exception of cinnamylidene malononitrile) and quantified using an internal standard method with chlorobenzene.

The GC method employed was as follows: The autosampler was programmed to wash once with acetone before performing 2x sequential washes in the

sample and ejected to the waste. A 2 μL aliquot of the sample was then injected into the injector port and the syringe washed a further 2x in acetone for cleaning.

The injector port and detector were heated to 270 °C; helium was used as a carrier gas with a flow of 50 mL/min and a split of 20:1.

A variable temperature program was used for the oven; first, the oven was equilibrated at 80 °C and held for 1.5 min after injection of the sample. Next, the oven was ramped at a rate of 15 °C/min up to 270 °C. The total run time for the method was 14.2 minutes.

Gas Chromatography (GC-MS) Analysis: GC-MS analyses were performed using an Agilent 6890 GC with an attached HP5973 Mass Spectrometer. Components were identified against known commercial standards (with the exception of cinnamylidene malononitrile) and quantified using an internal standard method with chlorobenzene.

The GC method employed was as follows: The autosampler was programmed to wash 3x with acetone before performing 3x sequential washes in the sample and ejected to the waste. A 2 μL aliquot of the sample was then injected into the injector port and the syringe washed a further 5x in acetone for cleaning.

The injector port and detector were heated to 280 °C; helium was used as a carrier gas with a flow of 50 mL/min and a split of 50:1.

A variable temperature program was used for the oven; first, the oven was equilibrated at 70 °C and held for 2 min after injection of the sample. Next, the oven was ramped at a rate of 20 °C/min up to 230 °C. The MS detector was set with a solvent delay for 3 minutes, then automatically initiated to detect a range of ions with m/z values between 41-500.

Calibration of Standards: Commercial standards of each of the starting and product materials, with the exception of cinnamylidene malononitrile, were purchased for calibration and subsequent quantitative analysis by GC. A series of 5 samples were prepared with graduating concentrations of cinnamyl alcohol, cinnamaldehyde and cinnamylidene malononitrile in a mixed *tert*-butanol and 1,4-dioxane solvent (4:1) up to a maximum concentration of 0.75 mmol dm^{-3}. A constant quantity of chlorobenzene as an internal standard was

added to each sample (1.75 mmol dm^{-3}). Components were measured accurately to 4 decimal places.

The standards were run on the GC 3 times and the peak integrations recorded and averaged across the 3 samples to minimise the GC equipment error. Peak ratios were calculated for each of the components against the internal standard and plotted against the respective mole ratios, as demonstrated in *Section 2.2.2.1*, to calculate the response factors of each component. R_f values under this method were calculated for cinnamyl alcohol (0.8773), cinnamaldehyde (0.9967) and cinnamylidene malononitrile (0.5251) against diglyme.

5.6.2 Characterisation Equipment

Gas Physisorption Analysis: Surface areas were probed using N_2 gas adsorption at liquid nitrogen temperatures (77 K) using a Micromeritics ASAP 2020 Physisorption Analyser. Prior to analysis, samples were degassed under vacuum using the attached heating jackets to heat samples to 250 °C for UiO-66 materials and 220 °C for NH_2-UiO-66 materials.

Field Emission Scanning Electron Microscopy: SEM micrographs were collected using a JEOL JSM-7600F with an accelerating voltage of 10 kV. Powdered samples were analysed by depositing on carbon tape to a sample holder and coated in Au by a sputter-coater.

Transmission Electron Microscopy: TEM micrographs were collected using a Philips CM300 FEGTEM with an accelerating voltage of 200 kV. Samples were prepared by depositing powdered materials on a carbon film-copper mesh TEM grid from an ethanolic suspension.

Thermogravimetric Analysis: TGA analyses were performed using a Q500 analyser from TA Instruments. Typically, TGA experiments were conducted on approximately 10 mg of a sample with heating between 20-800 °C in an aerobic atmosphere (40 % air in N_2). Standard curves used a ramp rate of 20 °C/min, and high resolution curves were collected with a ramp rate of 2 °C/min.

Powder X-ray Diffraction: PXRD patterns were collected on a Bruker D2 Phaser diffractometer using K_α radiation (λ = 1.5406 Å). Samples were prepared by grinding into a fine powder and mounted in a sample holder with a small well to hold the powder in place during analysis.

Inductively Coupled Plasma – Optical Emission Spectroscopy (ICP-OES)

ICP-OES analysis was performed by MEDAC Ltd. using a Varian Vista MPX ICP-OES system. Solid samples are prepared by digestion in HF before analysis, whereas reaction solutions are used directly for analysis.

Chapter 6: Conclusions and Future Prospects

Special Acknowledgements

The following special acknowledgements recognise the direct contribution of colleagues and collaborators to the furthering of the projects outlined in this thesis

Sivan Van Aswegen: Involved in the NP/CuClP project as an undergraduate student, now a PhD student part funded to explore the use of the same materials in industrial processes

Arran Gill: For continuation of the NP/CuClP project as a PhD student, exploring further the effects of activation conditions on the structural and catalytic properties in the flow

William Webb: For further development of the NP/MOF materials in catalytic and tandem applications with new MOFs as part of his PhD studies

"Continuous effort
- not strength or intelligence -
is the key to unlocking our potential."
Sir Winston Churchill

6.1 Highly Active Metal Nanoparticle Catalysts by Extrusion

In Chapters 3 and 4, a novel method for the preparation of NP supported materials was shown for the first time by exploitation of anion exchange properties in a microporous copper chlorophosphate material. Chlorometallate anions could be incorporated into the 1D pores of the open framework by hydrothermal synthesis of the material in the presence of a precursor salt. For example, $HAuCl_4$, K_2PtCl_4 or K_2PdCl_4 could be used for *in situ* loading of square planar $[AuCl_4]^-$, $[PtCl_4]^{2-}$ or $[PdCl_4]^{2-}$ species respectively. Calcination of the as-synthesised materials in air at 500 °C were shown to reduce a small fraction of the discrete, complex anionic salts to form some NP species on the surface of the host framework by a thermal extrusion process. These calcined materials were shown to be active catalysts for the activation of molecular oxygen for the aerobic oxidation of benzyl alcohol to benzaldehyde. It was demonstrated that each of the Au, Pt and Pd/CuClP materials had varying catalytic properties, each giving different selectivity profiles and allowing opportunistic selection of the noble metal NP catalyst depending on the desired products.

In contrast to thermal extrusion by calcination for NP formation, activation by heating at lower temperatures in the presence of a reducing atmosphere containing 5 % H_2/N_2 was shown, by bulk analysis techniques including EXAFS and XANES, to be more efficient at extruding the precursor complex anions from the framework pores for NP formation. The Pt/CuClP was able to achieve complete extrusion under reducing conditions, converting all of the complex anions to surface NP species. This was further exemplified in the superior catalytic properties of the Pt/CuClP for the aerobic oxidation of vanillyl alcohol to vanillin compared with the Au and Pd/CuClP analogues. Bulk analysis of the Au and Pd/CuClP materials revealed that under identical reduction parameters to that used for the Pt/CuClP material, still only small fractions, albeit larger fractions than for the calcined materials, could be extruded to generate surface bound NPs. These structural differences could reveal the changes in interaction strengths between each of the chlorometallate anions and the framework host prior to activation by extrusion, highlighting the need for varied conditions that would be required for complete extrusion in the case of Au and Pd/CuClP.

In addition to this novel method of NP generation, the materials were applied in the selective oxidation of alcohols to aldehydes to synthesis industrially significant substrates. One of the key aims of this project was to develop catalysts that could improve on the output, sustainability and environmentally benign capacity of processes currently employed in the chemical industry. Benzylic aldehydes have been highlighted as important chemicals for the flavours and fragrances industry, with benzaldehyde and vanillin being key examples used as flavourings with aromas of almonds and vanilla respectively, as well as use as intermediates within other fine chemical or pharmaceutical industries. By utilising these new NP catalysts, O_2 was used as an oxidant for the selective oxidation of the respective alcohol substrates to these important aldehyde products in good yield. The successful use of O_2 has eliminated the need to employ stoichiometric quantities of inorganic oxidants that are traditional used on an industrial scale. The only by-product generated from the oxidant is water which is viewed as a clean, green and recyclable product. The atom efficiency is maximised by the lack of additional atoms such as metals that normally provide more reactive oxygen species but contribute to significant quantities of waste.

In the case of vanillin, O_2 is already utilised as an oxidant, however these new NP catalyst have been shown to exceed the production yields of the current process employed in industry,[1] in addition to eliminating the requirement for toxic metal promoters such as Pd and Bi. In all cases, the NP catalyst materials were shown to maintain structural integrity over the course of the catalytic reactions, with discrete and monodisperse NPs still present on the chlorophosphate support surface after reaction. Furthermore, the materials could be recycled with negligible effects on the activity and selectivity properties. These catalyst show a significant promise in developing the process which currently produces in excess of 12,000 tons of vanillin per annum as a flavouring agent,[2] by contributing not just an increase in productivity, but doing so a green and more environmentally benign manner.

6.1.1 Ongoing Work and Future Prospects

The scope of this project is vast from both a structural development and catalytic application viewpoint. This work has so far demonstrated that

complete extrusion of Pt can be achieved under reducing conditions @ 200 °C in the presence of H_2, however only the extrusion atmosphere (calcination or reduction) has been probed in detail to examine structural and resulting catalytic properties. The effect of temperature as well as activation times could be investigated in more depth to discover the conditions that could favour complete extrusion of the Au or Pd/CuClP materials. For instance, it was noted in Chapter 4 that although a slightly larger fraction of metallic Pd NPs were observed in the reduced sample compared with the calcined, a reduction in the support crystallinity was observed, with a possibility of the framework degradation contributing to this occurrence. To preserve the integrity of the chlorophosphate support, it is possible that activation under milder thermal conditions but for longer periods of time could favour the complete extrusion of the $[PdCl_4]^{2-}$ to metallic NPs of uniform small sizes. Thus a detailed study would be required to further develop the Au and Pd/CuClP materials.

Furthermore, given the propensity for the Pt/CuClP to fully extrude under the investigated conditions, the addition of Pt to either the Au or Pd/CuClP materials could also help to encourage extrusion of these materials further and generate bimetallic NP species. There has been an influx of reports over the last decade highlighting the synergistic behaviour of bimetallic nanoparticles in the oxidation of alcohols and other heteroatomic organic molecules,[3-10] and the potential toward activation of C-H bonds in non-activated hydrocarbons such as toluene.[11] In addition to the generation of monometallic NP species already demonstrated in this work, it is possible that this method could also be applied to the formation of highly active multimetallic NP species with enhanced catalytic properties. In other work, it has been identified that the synthesis conditions such as activation temperature and atmosphere, as well as choice of NP immobilisation method as outlined in *Section 1.2.4*, can affect the nanostructure of the generated NPs. One study[10] highlighted that colloidal deposition of AuPd NPs on a TiO_2 support favoured smaller alloyed particles, where as an impregnation method favoured core-shell structures. In extension, analysis of the nanostructure of bimetallic NPs generated by this new extrusion route could reveal a bias toward one particular composition.

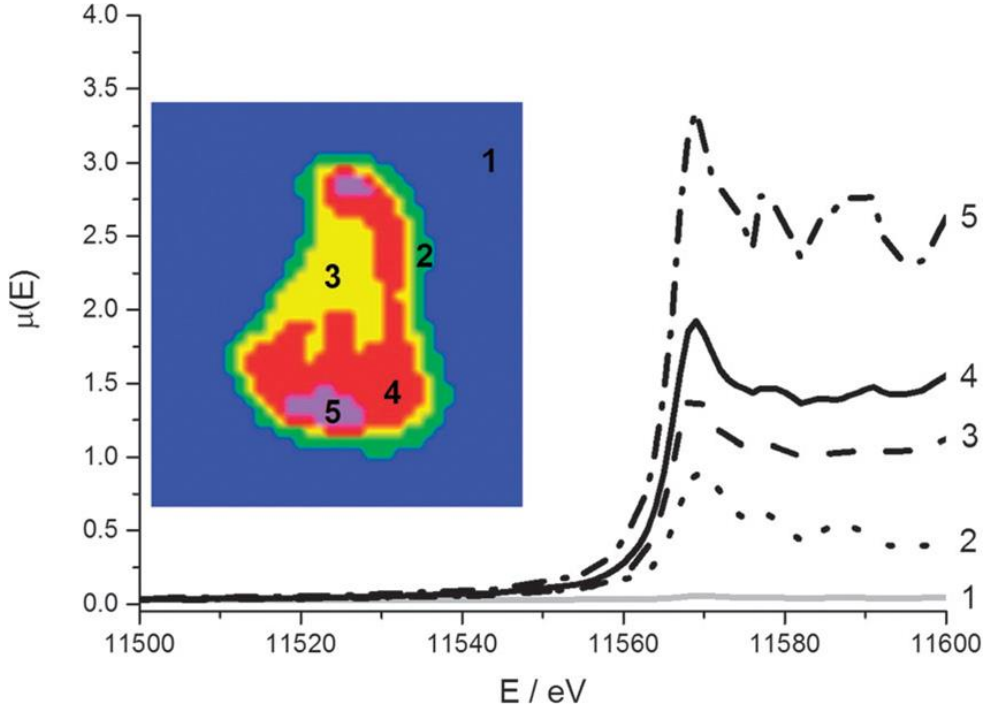

Figure 6.1 μ-XANES and 3D mapping of a catalyst particle containing different Pt species. Reproduced from Ref. 12 with permission from the PCCP Owner Societies

It would also be useful to develop a more fundamental understanding of the mechanism of the extrusion process. From the current structural investigations, we can conclude that the origin of the chlorometallate complex anions is within the pores of the framework, and that the approximately 5 nm sized NPs are predominantly located on the support surface. By deduction, it is reasonable to assume that some migration effects have caused movement of the noble metal species from the pores of the framework to the surface, which has thus far been termed 'extrusion'. It is not yet known the phases of this process and whether migration of the species occurs prior to, during or after reduction to metallic NPs. It is known that NP growth occurs generally through formation of small clusters that form nucleation points for continual growth. A new technique has recently been developed that can map the XAS, XRF and XRD data of a material across a 2D representation or 3D sample with 1-2 μm resolution (Figure 6.1).[12] As the crystal sizes of the CuClP material are between 10-50 μm, this technique should be able to measure the distribution of noble metal species across a single crystal of the material, as well as determine the chemical nature of the metals with specificity to the location of the

measurement. By analysis of materials before and after activation, any differences can be observed. Under our current model of extrusion, for the Pt/CuClP material, it would be expected to see metallic Pt species across the surface of the material, with no Pt species left within the bulk of the crystal. In contrast, for the Au/CuClP material, a distribution of Au across the whole sample would still be expected, but with further analysis of the EXAFS data showing more metallic species on the surface and more anionic chloride species within the bulk. Moreover, *in situ* experiments on the materials should provide the opportunity to map the movement of metal species over time when subjected to reduction conditions at temperature.

Understanding this process and the differences between each noble metal, in terms of cluster formation and growth in these structural and chemical environments, could be the key to understanding the differing activation parameters required. This could also aid in the continued design of the extrusion process to afford complete extrusion of Au, Pd and bimetallic analogues of the NP/CuClP materials.

To date, all experiments have thus far been carried out in traditional batch reactors, however there is an increasing interest in the use of continuous flow for production of pharmaceutical target molecules and fine chemicals.[13-14] One of the advantages of using flow reactors is the continual feed of substrate and thus collection of the product which, in theory, could continue indefinitely as long as a feed of substrate was provided. It has also been discussed that the use of flow reactors can give much better control over micromixing which can improve the efficiencies of reactions and increase yields.[14] Although the effect of mixing may not be of significant value on a small scale laboratory experiment, mass transfer effects on larger scales become significantly more important. Flow chemistry can also provide opportunities for automation and control of reaction parameters whilst the catalyst is on-stream. Given the thermal stability[15] and proven structural integrity of the NP/CuClP materials, they would be good candidates for heterogeneous packed bed flow reactions in the liquid or gas-phase. As the catalysts have proven to be active in oxidation reactions, they could easily be tested for other substrates such as the oxidation of KA-oil (the product of cyclohexane oxidation) to cyclohexanone and adipic acid – the precursor for nylon-6,6. The Pt/CuClP

catalyst could be tested for hydrogenation/reduction reactions[16-21] in the flow as well as some cross-coupling reactions[22-23] as previously reported in the batch.

Nonetheless, it would be important to probe the high-pressure batch reactions in more depth to attain a more detailed comprehension of mechanistic and kinetic factors in the catalytic process. Investigation of the effects of pressure on catalytic activity would disclose the mass-transfer properties of O_2 in the system, with respect to dissolution within *t*-butanol (or alternative solvents) and adsorption to the catalyst surfaces. Further analysis of the substrate concentration effects would also better help in understanding the mechanism of action, and whether the reaction more closely follows Langmuir-Hinshelwood or Eley-Rideal type mechanisms as hypothesised for the Au/UiO-66 materials in *Section 5.3.1.* To contrast the different catalysts synthesised in this thesis, comparisons of the NP/CuClP in the oxidation of cinnamyl alcohol and other functional groups would shed light on the comparative selectivity properties with the NP/UiO-66 materials for alcohol oxidation, and resistance to reaction with other functionality. Organic reactions on complex molecules often require protection and deprotection of functional groups to attain selective processes. If theses catalysts could achieve selectivity without the need for protective groups, this could increase prospective yields and reduce the chemical components required for the reaction.

6.2 MOF Supported Nanoparticle Catalysts

The choice of NP support is of vital significance for successful synthesis of stable and resistant catalyst materials, as well contributing factors to the activity of the NPs for a desired application. In the case of the earlier work in Chapter 3-4, the porous support was utilised for the formation of uniform small NPs *in situ* by reduction of supported metal salts in addition to strong interactions that maintain the integrity of the catalyst over the course of multiple catalytic cycles.

In the latter part of the project, UiO-66 and NH_2-UiO-66 were utilised for the first time toward support of NPs by colloidal deposition for selective catalytic oxidation and related tandem reactions. In contrast to the copper chlorophosphate framework in Chapters 3 and 4, the role of the support in this section was to facilitate colloidal deposition of NPs in addition to utilising the amine functionality of the MOF to facilitate a tandem reaction. As such, a novel process using an Au/NH_2-UiO-66 composite material applied to the tandem oxidation-condensation was successfully achieved with yields in excess of 80 %. The reaction studied involved the oxidation of cinnamyl alcohol to cinnamaldehyde and subsequent Knoevenagel condensation with malononitrile to form cinnamylidene malononitrile. Both products have significance as a cinnamon flavouring agent[24] or anti-cancer therapeutic agent respectively.[25] Mechanistically, a similar mode of action is expected to be occurring as with adsorption and dehydrogenation of alcohol species that is expected for the NP/CuClP materials. The main difference originates in the presence of the PVP stabilising ligands on the NPs in the colloidal deposition route, in contrast to the bare NPs generated by thermal extrusion from the CuClP frameworks. Preliminary mechanistic investigations have indicated that the process is diffusion limited, rather than limited by surface reaction on the NPs, due to the marked increase in activity (measured by TONs) observed when the concentration of the substrate is increased. If surface reactions were the limiting step, no change in the activity of the catalyst would be expected. To test the maximum capacity of the catalyst, a solvent free process could be attempted in order to eliminate bulk diffusion limitations and restrict the rate of reaction only by adsorption of the substrate, desorption of the products or

surface reactions such as the β-hydride abstraction from metal-alcoholate species or removal of surface hydrides by the oxidant.

Through careful design of a multifunctional catalyst such as this - containing multiple active sites that can achieve multi-step reactions in one-pot - the need for isolation and purification of the intermediate product is eliminated. Not only does this provide an economic benefit by reducing the amount of resources and manpower required to attain the final product, yields can be maximised and it also addresses the need for sustainability (a core aim of this project) by reducing the waste produced in the process. As isolation and purification is not necessary, the quantities of solvents used are reduced and no fresh solvent is required for the second step. In addition, a simple peroxide in the form of TBHP is used for the oxidation step, liberating *t*-butanol which is already engaged as the solvent for the reaction; this further reduces waste and potential detrimental effects to the environment if the process were to be scaled-up.

6.2.1 Ongoing Work and Future Prospects

As highlighted, the bifunctional Au/NH_2-UiO-66 material was demonstrated to be a successful catalyst for a tandem process involving a two-step oxidation-condensation reaction. The use of NP supported materials as catalysts for oxidation,[3, 7, 9, 26-31] hydrogenation[16, 32-34] and coupling reactions[35-38] coupled with the demonstrated applications of amine-MOFs in a variety of condensation reactions,[39-44] acetalisations[45] and others,[46] highlights the potential scope of these materials to be applied to any combination of these reactions. The fine-chemical and pharmaceutical industries often employ multi-step reactions to afford target molecules, and NP/MOFs have shown potential for application in a multifunctional process that could increase productivity on a vast array of different reactions and molecules.

In the current project, the conditions could be optimised further to achieve close to maximum yields for the final product, by tailoring the oxidant levels and time at which the second step is initiated through addition of the malononitrile. It would be prudent to examine further the interaction of the malononitrile with the Au NPs to establish the reasons behind the inhibition of

the first step and prevention of malononitrile being added at the start of the reaction. To survey the wider application of the catalysts to the tandem reaction involving the Knoevenagel condensation, a range of activated methylene compounds could be screened that contain esters in place of the nitrile groups. These compounds are considered less reactive due to a reduction in inductive effects of the electron-withdrawing groups (and indirectly measured by the pKa values of the methylene protons), which could result in reduced rates of reaction compared with malononitrile. Also, the lower reactivity of the condensation reactant could be less inhibiting on the first step and allow for addition of all components at the beginning of the reaction.

As TBHP, a liquid oxidant, is used for this tandem process, regular laboratory glassware is sufficient to facilitate this reaction. With the necessary high-pressure batch reactor equipment, the application of the NP/UiO-66 type materials could also be investigated for the activation of abundant and environmentally benign molecular oxygen as for the NP/CuClP catalysts. It would be interesting to compare the catalytic profiles of the MOF supported NP catalysts for the oxidation of O_2 against peroxides. These data could also be compared with the aerobic oxidation of cinnamyl alcohol using NP/CuClP catalysts to probe deeper any effects that the support may have toward the oxidation reaction, and whether the supports act purely as an inactive host or contribute to enhance the overall activity of the NP catalyst material.

The colloidal deposition method on UiO-66 type materials was shown to be versatile in generating similarly monodisperse Pt, Pd and AuPd nanoparticles. Therefore, it would be interesting to monitor the changes in catalytic activity of these metals for the oxidation and subsequent tandem reaction. Studies on the NP/CuClP materials demonstrated varying selectivity properties between the noble metals, whilst data reported elsewhere has highlighted the different properties still of bimetallic AuPd[10, 47-48] in oxidations of benzylic alcohols. Composition, as well as synthesis method, could be integral for the NP/UiO-66 materials for selectivity not just for cinnamyl alcohol oxidation, but benzylic alcohols as used in Chapters 3-4 and other substrates. Moreover, it may be that the physical properties of alternative metallic particles could be resistant to detrimental interactions with malononitrile, facilitating a one-pot reaction that could proceed with all reactants present at the start of the process.

The composite catalyst used for the tandem reaction was synthesised using a deposition method which had the benefits of facile preparation and good integrity for the catalytic reaction. Although encapsulation of NPs was unsuccessful in this project, there have been reports of NP encapsulation in other MOFs[49-52] as well as UiO-66[53] (although controversially difficult to reproduce). If selective encapsulation could be reproducibly achieved, NP/UiO-66 materials could be employed in size-selective catalytic processes which are hitherto not reported. UiO-66 and NH_2-UiO-66 have relatively small pore windows compared with other MOFs, at approximately 6 Å, which could prove to be an advantage when high degrees of size-selectivity is required for reactions with small molecules.

6.3 References

1 Rhodia Chimie, P. Metivier, **2001,** *Method for preparing a 4-hydroxybenzaldehyde and derivatives,* US Patent 6,184,421.
2 J.-P. Vidal, Vanillin in *Kirk-Othmer Encyclopedia of Chemical Technology*, John Wiley & Sons, Inc., **2006**.
3 D. I. Enache, J. K. Edwards, P. Landon, B. Solsona-Espriu, A. F. Carley, A. A. Herzing, M. Watanabe, C. J. Kiely, D. W. Knight and G. J. Hutchings, *Science,* **2006**, *311*, 362.
4 A. J. Frank, J. Rawski, K. E. Maly and V. Kitaev, *Green Chem.,* **2010**, *12*, 1615.
5 M. Chen, D. Kumar, C.-W. Yi and D. W. Goodman, *Science,* **2005**, *310*, 291.
6 N. Dimitratos, A. Villa, D. Wang, F. Porta, D. Su and L. Prati, *J. Catal.,* **2006**, *244*, 113.
7 H. Zhang and N. Toshima, *Catal. Sci. Technol.,* **2013**, *3*, 268.
8 M. S. Holden, K. E. Nick, M. Hall, J. R. Milligan, Q. Chen and C. C. Perry, *RSC Adv.,* **2014**, *4*, 52279.
9 P. Qiao, S. Xu, D. Zhang, R. Li, S. Zou, J. Liu, W. Yi, J. Li and J. Fan, *Chem. Commun.,* **2014**, *50*, 11713.
10 M. Morad, M. Sankar, E. Cao, E. Nowicka, T. E. Davies, P. J. Miedziak, D. J. Morgan, D. W. Knight, D. Bethell, A. Gavriilidis and G. J. Hutchings, *Catal. Sci. Technol.,* **2014**, *4*, 3120.
11 L. Kesavan, R. Tiruvalam, M. H. A. Rahim, M. I. bin Saiman, D. I. Enache, R. L. Jenkins, N. Dimitratos, J. A. Lopez-Sanchez, S. H. Taylor, D. W. Knight, C. J. Kiely and G. J. Hutchings, *Science,* **2011**, *331*, 195.
12 S. W. T. Price, K. Ignatyev, K. Geraki, M. Basham, J. Filik, N. T. Vo, P. T. Witte, A. M. Beale and J. F. W. Mosselmans, *Phys. Chem. Chem. Phys.,* **2015**, *17*, 521.
13 A. Kirschning, W. Solodenko and K. Mennecke, *Chem. Eur. J.,* **2006**, *12*, 5972.
14 R. L. Hartman, J. P. McMullen and K. F. Jensen, *Angew. Chem., Int. Ed.,* **2011**, *50*, 7502.
15 E. R. Williams, R. M. Leithall, R. Raja and M. T. Weller, *Chem. Commun.,* **2013**, *49*, 249.
16 H.-j. Zhang, S.-d. Qi, X.-y. Niu, J. Hu, C.-l. Ren, H.-l. Chen and X.-g. Chen, *Catal. Sci. Technol.,* **2014**, *4*, 3013.
17 K. Na, S. Alayoglu, R. Ye and G. A. Somorjai, *J. Am. Chem. Soc.,* **2014**, *136*, 17207.
18 T. Maji, S. Banerjee, M. Biswas and T. K. Mandal, *RSC Adv.,* **2014**, *4*, 51745.
19 Z. Guo, C. Xiao, R. V. Maligal-Ganesh, L. Zhou, T. W. Goh, X. Li, D. Tesfagaber, A. Thiel and W. Huang, *ACS Catal.,* **2014**, *4*, 1340.
20 J. Zhu, T. Wang, X. Xu, P. Xiao and J. Li, *Appl. Catal., B,* **2013**, *130–131*, 197.
21 S. Cheong, J. D. Watt and R. D. Tilley, *Nanoscale,* **2010**, *2*, 2045.
22 R. Narayanan and M. A. El-Sayed, *Langmuir,* **2005**, *21*, 2027.
23 R. Narayanan, *Molecules,* **2010**, *15*, 2124.
24 R. G. Eilerman, Cinnamic Acid, Cinnamaldehyde, and Cinnamyl Alcohol in *Kirk-Othmer Encyclopedia of Chemical Technology*, John Wiley & Sons, Inc., **2000**.

25 Yissum Research Development Company of the Hebrew University of Jerusalem, A. Levitzki, A. Gazit, M. Chorev and C. Gilon, **1995,** *Pharmaceutical compositions comprising benzylidene-and cinnamylidene-malononitrile derivatives for the inhibition of proliferative processes in mammalian cells, certain such novelcompounds and their preparation,* Canada Patent CA 1,334,826.
26 T. Balcha, J. R. Strobl, C. Fowler, P. Dash and R. W. J. Scott, *ACS Catal.,* **2011**, *1*, 425.
27 P. Venkatesan and J. Santhanalakshmi, *Chin. J. Catal.,* **2012**, *33*, 1306.
28 J. Mielby, J. O. Abildstrøm, F. Wang, T. Kasama, C. Weidenthaler and S. Kegnæs, *Angew. Chem., Int. Ed.,* **2014**, *53*, 12513.
29 P. Fristrup, L. Johansen and C. Christensen, *Catal. Lett.,* **2008**, *120*, 184.
30 M. Turner, V. B. Golovko, O. P. H. Vaughan, P. Abdulkin, A. Berenguer-Murcia, M. S. Tikhov, B. F. G. Johnson and R. M. Lambert, *Nature,* **2008**, *454*, 981.
31 F. Zhang, F. Jiao, X. Pan, K. Gao, J. Xiao, S. Zhang and X. Bao, *ACS Catal.,* **2015**, *5*, 1381.
32 B. Sarkar, C. Pendem, L. N. S. Konathala, T. Sasaki and R. Bal, *J. Mater. Chem. A,* **2014**, *2*, 18398.
33 M. R. Knecht and D. B. Pacardo, *Anal. Bioanal. Chem.,* **2010**, *397*, 1137.
34 D. Zhang, F. Ye, Y. Guan, Y. Wang and E. J. M. Hensen, *RSC Adv.,* **2014**, *4*, 39558.
35 Z. J. Wang, S. Ghasimi, K. Landfester and K. A. I. Zhang, *Chem. Mater.,* **2015**, *27*, 1921.
36 B. Cornelio, A. R. Saunders, W. A. Solomonsz, M. Laronze-Cochard, A. Fontana, J. Sapi, A. N. Khlobystov and G. A. Rance, *J. Mater. Chem. A,* **2015**, *3*, 3918.
37 G. Collins, M. Blömker, M. Osiak, J. D. Holmes, M. Bredol and C. O'Dwyer, *Chem. Mater.,* **2013**, *25*, 4312.
38 S. Sarina, H.-Y. Zhu, Q. Xiao, E. Jaatinen, J. Jia, Y. Huang, Z. Zheng and H. Wu, *Angew. Chem., Int. Ed.,* **2014**, n/a.
39 Y. Yang, H.-F. Yao, F.-G. Xi and E.-Q. Gao, *J. Mol. Catal. A: Chem.,* **2014**, *390*, 198.
40 J. Gascon, A. Corma, F. Kapteijn and F. X. Llabrés i Xamena, *ACS Catal.,* **2014**, *4*, 361.
41 T. Toyao, M. Fujiwaki, Y. Horiuchi and M. Matsuoka, *RSC Adv.,* **2013**, *3*, 21582.
42 L. T. L. Nguyen, K. K. A. Le, H. X. Truong and N. T. S. Phan, *Catal. Sci. Technol.,* **2012**, *2*, 521.
43 M. Hartmann and M. Fischer, *Micro. Meso. Mater.,* **2012**, *164*, 38.
44 A. Dhakshinamoorthy, M. Opanasenko, J. Čejka and H. Garcia, *Adv. Synth. Catal.,* **2013**, *355*, 247.
45 X. Li, Z. Guo, C. Xiao, T. W. Goh, D. Tesfagaber and W. Huang, *ACS Catal.,* **2014**.
46 Y.-M. Chung, H.-Y. Kim and W.-S. Ahn, *Catal. Lett.,* **2014**, *144*, 817.
47 J. Pritchard, M. Piccinini, R. Tiruvalam, Q. He, N. Dimitratos, J. A. Lopez-Sanchez, D. J. Morgan, A. F. Carley, J. K. Edwards, C. J. Kiely and G. J. Hutchings, *Catal. Sci. Technol.,* **2013**, *3*, 308.
48 V. Peneau, Q. He, G. Shaw, S. A. Kondrat, T. E. Davies, P. Miedziak, M. Forde, N. Dimitratos, C. J. Kiely and G. J. Hutchings, *Phys. Chem. Chem. Phys.,* **2013**, *15*, 10636.

49 Y.-Z. Chen, Y.-X. Zhou, H. Wang, J. Lu, T. Uchida, Q. Xu, S.-H. Yu and H.-L. Jiang, *ACS Catal.,* **2015**, 2062.
50 M. Zhao, K. Deng, L. He, Y. Liu, G. Li, H. Zhao and Z. Tang, *J. Am. Chem. Soc.,* **2014**, *136*, 1738.
51 M. Wen, K. Mori, T. Kamegawa and H. Yamashita, *Chem. Commun.,* **2014**, *50*, 11645.
52 P. Hu, J. V. Morabito and C.-K. Tsung, *ACS Catal.,* **2014**, *4*, 4409.
53 R. Wu, X. Qian, K. Zhou, H. Liu, B. Yadian, J. Wei, H. Zhu and Y. Huang, *J. Mater. Chem. A,* **2013**, *1*, 14294.